

SCOUTDROID: Inspection Pocket Drone

Design of a small, quickly deployable unmanned aerial vehicle suitable for indoor inspection:

SCOUT Drone for Reconnaissance of Out- and Indoor Danger zones

H.N. Basien	4207653	E.J. Kroon	4157958
D.S.A. ten Brink	4106873	V.A. Pereboom	4150554
R. Cirera Rocosa	4228987	N.D. Potdar	4206371
G.I. Földes	4211553	C.H.C. Vlemmix	4157095
S.C. Hungs	4133889	S.E.C. Voorhoeve	4228766

Final Report
Design Synthesis Exercise



Preface

The Design Synthesis Exercise (DSE) is the final project of the Bachelor of Aerospace Engineering program at the Delft University of Technology. This report presents a revolutionary, user-friendly, safe and elegant aerial rescue and support service vehicle called the Inspection Pocket Drone. This paper contains the research done and the system designed by DSE group 18, along with the methods used and design decisions made along the way. It is a result of 11 weeks of hard work and three previous technical reports that can be used for further development of the product.

Readers who are particularly interested in the detailed system description, including the descriptions of the vehicle and the Ground Control Station can find this in Chapter 12. Readers who are principally interested in the concurrent engineering method used which describes the way the design procedure is conducted can find this also in Chapter 12. The theories used for the propulsion design, hardware, airframe design and software can be found in Chapter 5, Chapter 6, and Chapters 7 & 8 respectively. Lastly, future work and plans on putting the design into effect are presented in Chapter 14.

We would like to extend our thanks to our principal tutor, Christophe De Wagter, and our DSE coaches, Jan Rohac and Zhi Hong for all the guidance and help they have offered during this period. We are very grateful for their feedback and endless support. Moreover, special thanks goes to the the whole DSE Organizing Committee (OSCC), Joris Melkert, Vincent Brügemann, Erwin Mooij, Nando Timmer and Wim Verhagen. We are also grateful for the work and dedication of the OSSA Student Assistants.

Summary

This report shows that Unmanned Aerial Vehicles can be used for the benefit of the public by rescue & support services such as the fire department. The present investigation reveals that indoor inspection of precarious buildings such as ones on fire or affected by an earthquake is possible without the direct involvement of rescue teams.

The presented design is a ring shaped flying surveillance system with a flight time of 10 minutes equipped with a visual and a thermal camera. A contra-rotating rotor design is located in the center of the ring and is carefully housed to prevent lacerations to people. The hull surrounding the rotors gives space for the placement of subsystems and acts as a straight diffuser. Plus, the sides of the vehicle are padded meaning that operations in the vicinity of people can be safely conducted. It is also designed to accommodate the needs and preferences of rescue teams: the mass of the vehicle is a remarkable 533 grams, and the total mass of the system including a portable Ground Control Station is 5 kg. Moreover, for the control of the vehicle a double swashplate system was designed. Each rotor has its own swashplate system which allows for roll and pitch control. By varying the rpm per motor yaw control can be achieved. By increasing or decreasing the rpm of both motors simultaneously direct control over altitude is gained. Two battery packs connected in parallel ensure that the system has enough energy to fly for ten minutes. They can quickly be changed to allow for more inspection time on site.

The mission of the vehicle consists of both an outdoor and indoor segment. Firstly, the operator deploys the system, after which the vehicle lifts off and searches for a suitable entrance to the building. Upon entry, the vehicle sweeps the rooms and sends video and thermal images to the operator who can determine whether the rescue team should enter the area. Afterwards, the vehicle leaves the building and returns to the Ground Control Station.

A detailed research was carried out to discover a user-friendly and easy-to-use interface. The Ground Control Station consists of a tablet plus video glasses with motion tracker, a handheld controller device and an omnidirectional antenna system, easily deployable from a small portable suitcase. To fulfill the mission, the vehicle is equipped with two cameras: a 5 megapixels visual light camera for still images and a compressed video stream, and an infrared camera for thermal imaging. A NavStik board running the Paparazzi platform provides the on-board computing power and, together with sonar sensors for distance measurement, aids in the control. The combination of sonar sensors and the thermal camera allow for inspection in smoky or dimmed lighting conditions, further increasing the operational range of the system.

To ensure all the data can be communicated between the drone and ground while indoors, the antennae were designed to allow communications over at least 260m through a reinforced concrete wall. High gain, high power antennae will be used to guarantee a robust link capable of transmitting the live video stream and control and command data.

Further development of the system includes prototyping, testing, assessment by regulatory bodies, sales and after-sales. The system is expected to be operational by early 2016, with after-sales continuing to August 2016. The development costs are estimated to be €242.000,-.

In conclusion, an innovative product is created that has the potential to increase the effectiveness of rescue services and drastically increase the amount of people to be saved while giving the rescue crew a clearer and detailed overview of the situation inside and the layout of the danger zone.

Nomenclature

List of Symbols

a	Porosity [-]
a_{dif}	Difference in acceleration [$\frac{m}{s^2}$]
a_{ref}	Set reference acceleration [$\frac{m}{s^2}$]
a_{refz}	Set reference acceleration along the z-axis [$\frac{m}{s^2}$]
a_x	Acceleration along the x-axis [$\frac{m}{s^2}$]
A	Area [m^2]
A_{ci}	Area of cell i of the cross section [m^2]
A_{head}	Acceleration of a head upon impact [-]
A_i	Cross sectional area of element i
A_{inner}	Sweep area of the inner diameter of the complete vehicle
A_{prop}	Propeller sweep area [mm^2]
A_{strut}	Cross-sectional area of the strut [m^2]
b_1	Damping coefficient of the strut [$\frac{Ns}{m}$]
b_2	Damping coefficient of the protective foam [$\frac{Ns}{m}$]
B	Bandwidth [Hz]
BR_{up}, BR_{down}	Data bit-bate uplink and downlink [bit/s]
C	Battery discharge rate [C]
C_d	Drag coefficient of the complete vehicle [-]
C_{d0}	Rotor drag coefficient at zero angle of attack [-]
$C_{l\alpha}$	Lift curve slope [$\frac{1}{\circ}$]
C_{Lmax}	Maximum lift coefficient [-]
C_{m0}	Moment coefficient at zero angle of attack [-]
C_T	Thrust coefficient [-]
d	Fence wire diameter [mm]
d_i	i^{th} hull cross section dimension [m]
$d_{min\,distance}$	Minimum allowable distance from wall
d_{wall}	Distance from wall
D	Drag of the complete vehicle [N]
D_{inner}	Inner diameter of the hull [m]
E, E', E''	Young's, storage and loss modulus [MPa]
E_b	Energy per bit [J]
E_{bat}	Battery energy [Wh]
E_{req}	Required energy from the battery system [Wh]
E_{spec}	Specific energy
f_{pp}	Full power percentage [%]
F	Prandtl tip loss factor [-]
F	Force [N]
$F_{allowable}$	Allowable impact force on a head [N]
F_{imp}	Impacting force [N]
F_{imp}'	Half of the impacting force [N]
F_m	Pressure loss coefficient [-]
FM	Figure of merit [-]
F_{rot}	Rotational force [N]
g	Gravitational acceleration [$9.81 \frac{m}{s^2}$]
G	Shear modulus [Pa]
$G_{Tx,a}, G_{Rx,a}$	Transmitting and receiving antenna gains [dB]
h_{cs}	Cross-section height [m]
HIC	Head injury criterion [-]
I	Area moment of inertia [mm^4]
I_{max}	Maximum current the system needs [A]
$I_{max,bat}$	Maximum current battery can deliver [A]
I_{xx}	Area moment of inertia with respect to the x axis [m^4]
$I_{xx,i}$	Area moment of inertia of element i with respect to the x axis [m^4]

I_{xy}	Product of inertia [m^4]
I_{yy}	Area moment of inertia with respect to the y axis [m^4]
$I_{yy,i}$	Area moment of inertia of element i with respect to the y axis [m^4]
J	Mass moment of inertia [$kg\ m^2$]
k	Ideal power correction factor [-]
k	Equivalent spring stiffness [$\frac{N}{m}$]
k_1, k_{ve}	Spring constant of the protective foam [$\frac{N}{m}$]
k_2	Spring constant of the strut [$\frac{N}{m}$]
k_B	Boltzmann constant [J/K]
k_{int}	Interference power factor [-]
L	Lift [N]
L_{beam}, l_{beam}	Beam length [m]
L_d	Diffuser length [mm]
LM	Link margin [W]
L_{path}, L_{fsl}	Transmission and free space path loss [dB]
L_{strut}	Length of the strut [m]
$L_{Tx,c}, L_{Rx,c}$	Transmitting and receiving cable losses [dB]
$(L/D)_{max}$	Maximum lift to drag ratio [-]
m	Distance between fence wires [mm]
m_{bat}	Total battery mass [g]
$m_{bat,one}$	Single battery mass [g]
m_h	Mass of the hull structure plus the included subsystems [kg]
m_{head}	Mass of a head
m_i	Mass of subsystem i [g]
m_{prop}	Mass of the complete propulsion subsystem [kg]
$m_{propulsion}$	Engine mass [g]
m_{uav}	Mass of the complete vehicle [kg]
M	Moment [Nm]
M_B	Redundant moment [Nm]
$M_{p,max}$	Maximum moment generated by the propulsion system [Nm]
M_x	Moment acting in the x direction [Nm]
$M_{x,strut}$	Moment applied on the hull in the x direction by the strut [Nm]
M_y	Moment acting in the y direction [Nm]
$M_{y,hull}$	Moment in the y direction caused on the hull by its own weight [Nm]
M_z	Moment acting in the z direction [Nm]
$M_{z,strut}$	Moment applied on the hull in the z direction by the strut [Nmm]
M_θ	Moment as a function of polar position [Nm]
n	Path loss exponent [-]
n_{sides}	Number of sides [-]
N	Noise power [W]
N_0	Noise intensity [J]
N_P	Total number of batteries needed in parallel [-]
N_{P_E}	Number of batteries needed in parallel for energy [-]
N_{P_i}	Required number of batteries in parallel for current [-]
N_S	Total required number of batteries in series [-]
P_{avg}	Average power required [W]
P_{crit}	Critical load for buckling [N]
P_{fp}	System power consumption full power [W]
P_{hover}	Hover power [W]
P_{ideal}	Ideal power [W]
P_{impact}, P_i	Impact load [N]
P_{max}	Maximum power to be delivered by the battery system [W]
P_{mp}	System power consumption while maneuvering [W]
$P_{propulsion}$	Propulsion power [W]
P_{Rx}, P_{Tx}	Receiving and transmitting power [W]
q	Shear flow [$\frac{N}{m}$]
q_0	Constant component of the shear flow in a closed cross section [$\frac{N}{m}$]
q_b	Open cross section shear flow due to shear forces [$\frac{N}{m}$]
q_s	Shear flow due to shear forces [$\frac{N}{m}$]
q_t	Shear flow due to torque [$\frac{N}{m}$]
Q	Battery capacity [Ah]
r	Blade radius [m]
r	Radius of the stiffening ring [m]

r_{path}	Transmission range [m]
r_{servo}	Servo arm length [m]
R	Radius [m]
R	Maximum blade radius [mm]
R_B	Redundant force load [N]
Re	Reynolds number
R_{link}	Maximum transmission range [m]
$R_{strut,inner}$	Inner radius of the strut [m]
s	Distance along cross sectional element [m]
s_{Rx}	Receiver sensitivity [W]
S	Surface of the complete vehicle perpendicular to the airflow [mm ²]
S_{front}	Frontal surface area of the complete vehicle [mm ²]
S_{impact}	Impact load [N]
S_{top}	Top surface area of the complete vehicle [mm ²]
S_x	Force applied in the x direction [N]
$S_{x,strut}$	Force applied on the hull in the x direction by the strut [N]
S_y	Force applied in the y direction [N]
$S_{y,strut}$	Force applied on the hull in the y direction by the strut [N]
$S_{z,strut}$	Force applied on the hull in the Z direction by the strut [N]
S_z	Force applied in the z direction [N]
t	Thickness [m]
t_{fp}	Full power mission time [s]
t_i	Thickness of element i of the hull cross section [m]
t_{max}	Maximum flight time [s]
t_{mp}	Manoeuvre power mission time [s]
$t_{settling}$	Settling time till error has dissipated [s]
t_{strut}	Strut thickness [m]
T	Thrust per propeller [N]
T_{duct}	Duct thrust [N]
t_{impact}	Duration of impact [s]
T_{max}	Maximum thrust [N]
T_{rotor}	Rotor thrust [N]
T_{total}	Total thrust [N]
U_{bat}	Output voltage battery [V]
U_{req}	Required output voltage battery system [V]
ν	Kinematic viscosity [$\frac{m^2}{s}$]
v_h	Ideal induced velocity [$\frac{m}{s}$]
v_i	Induced velocity [$\frac{m}{s}$]
V	Airspeed [$\frac{m}{s}$]
$V_{0,h}$	Initial velocity of the hull structure [$\frac{m}{s}$]
$V_{0,prop}$	Initial velocity of the propulsion subsystem [$\frac{m}{s}$]
V_{bat}	Battery volume [m ³]
V_{dif}	Difference velocity [$\frac{m}{s}$]
V_h	Horizontal velocity component [$\frac{m}{s}$]
V_{ref}	Set reference velocity [$\frac{m}{s}$]
V_v	Vertical velocity component [$\frac{m}{s}$]
w_{cs}	Cross-section width [m]
W_{hull}	Weight of the hull [N]
x	Position [m]
\dot{x}	Velocity [$\frac{m}{s}$]
\ddot{x}	Acceleration [$\frac{m}{s^2}$]
x_c	x coordinate of the centroid location [m]
x_{cg}	Lateral center of gravity position [mm]
x_h	Displacement of the hull structure plus the included subsystems [m]
x_i	Lateral position of subsystem i [mm]
x_i	Longitudinal position of subsystem i [mm]
x_{sc}	x coordinate of the location of the shear centre [m]
x_{uav}	Horizontal displacement of the vehicle [m]
y_c	y coordinate of the centroid location [m]
y_{cg}	Longitudinal center of gravity position [mm]
y_{sc}	y coordinate of the location of the shear centre [m]

α	Angle of attack [$^{\circ}$]
α_s	Stall angle of attack [$^{\circ}$]
β	Atmospheric specific attenuation [dB/m]
β_{node}	Clockwise angular position of component (node) in hull [rad]
$\gamma_{F_{imp}'}$	Deflection of the stiffening ring at the impacting force
δ_p	Stress-strain phase difference [rad]
$\delta\alpha_{servo}$	Angular servo deflection from neutral position
δ_{tip}	Tip deflection blade [mm]
Δa	Axial displacement [m]
Δb	Lateral displacement [m]
Δh_{servo}	Servo rod deflection [m]
Δm_{prop}	Mass difference between propellers [kg]
ΔP	Pressure drop [Pa]
Δx	Displacement [m]
ε_{PW}	Power to weight ratio [-]
η_{motor}	Motor efficiency [%]
η_{shaft}	Shaft efficiency [%]
θ	Angle of twist [$^{\circ}$]
θ	Polar position on the stiffening ring [rad]
θ	Body pitch angle of the UAV [rad]
θ_d	Diffuser angle [$^{\circ}$]
θ_{max}	Maximum pitch angle [$^{\circ}$]
Θ	Angle between the displacement Δx and the axis of the strut [rad]
λ	Inflow ratio [-]
λ_{link}	Wavelength [m]
ρ	Density [kg/m^3]
ρ_{air}	Air density [kg/m^3]
ρ_{energy}	Energy density
σ	Blade solidity [-]
σ_{axial}	Axial stress [Pa]
$\sigma_{bending}$	Bending stress [MPa]
σ_d	Diffuser expansion ratio [-]
σ_{KE}	Kinematic correction factor [-]
σ_{MO}	Momentum correction factor [-]
σ_{normal}	Normal stress [Pa]
σ_{tens}	Tensile stress [MPa]
σ_{yield}	Yield stress [Pa]
τ	Shear stress [Pa]
φ	Hull rotation [$^{\circ}$]
ω	Rotational speed / angular frequency [rad/s]

Abbreviations

AES	Advanced Encryption Standard
AHP	Analytical Hierarchical Process
AWG	American Wire Gauge
BEC	Battery Eliminator Circuit
BER	Bit Error Rate
BVLOS	Beyond Visual Line Of Sight
CAS	Collision Avoidance System
CBS	Cost Breakdown Structure
CFRP	Carbon Fibre Reinforced Polymers
CPU	Central Processing Unit
DES	Data Encryption Standard
DSE	Design Synthesis Exercise
EASA	European Aviation Safety Agency
EOM	Equation Of Motion
ESC	Electronic Speed Controller
FBS	Functional Breakdown Structure
FFD	Functional Flow Diagram
FM	Figure of Merit
FPS	Frames Per Second
FPV	First Person View
FSK	Frequency Shift Keying
GCS	Ground Control Station
GPS	Global Positioning System
HC	Helicopter
HUD	Head-up Display
I2C	Inter-Integrated Circuit
IMU	Inertial Measurement Unit
IPD	Inspection Pocket Drone
IR	Infrared
JPEG	Joint Photographic Experts Group
LED	Light Emitting Diode
LIDAR	Light Detection and Ranging
LiPo	Lithium Polymer
LOS	Line-of-Sight
LWIR	Long-wave Infrared
MNS	Mission Need Statement
NASA	National Aeronautics and Space Administration
NiCd	Nickel Cadmium
NiMH	Nickel-Metal Hydride
OBC	On-Board Computer
OFDM	Orthogonal Frequency Division Multiplexing
OSSC	DSE Organization Committee
POS	Project Objective Statement
PSK	Phase Shift Keying
RGB	Red Green Blue
RPAS	Remotely Piloted Aircraft System
Rx	Communication Receiver
SNR	Signal-to-Noise Ratio
TKIP	Temporal Key Integrity Protocol
Tx	Communication Transmitter
UAV	Unmanned Aerial Vehicle
USB	Universal Serial Bus
USP	Unique Selling Point
VFR	Visual Flight Rules
VLOS	Visual Line Of Sight
VR	Virtual Reality
WAF	Wall Attenuation Factor

Contents

1	Introduction	1
2	Mission Description	2
2.1	Functional Flow Diagram	2
2.2	Functional Breakdown Structure	4
2.3	Mission Requirements	5
3	Market Analysis	10
3.1	General Market Description	10
3.2	Applications and End Users of UAV Systems	10
3.3	Market Structure	11
3.4	Product Differentiation and Market Gap	12
3.5	Legislation	14
4	Design and Iteration Strategy	15
5	Subsystem Design: Propulsion	17
5.1	Thrust Calculations	17
5.2	Coaxial Rotor Design	20
5.3	Rotor Head Design	21
5.4	Propeller Design	23
5.5	Power Calculations	26
6	Subsystem Design: Electronics	27
6.1	Payload	27
6.2	On Board Computer	31
6.3	Payload and OBC hardware configuration	35
6.4	Communications	37
6.5	Power	50
6.6	Hardware Interface	54
6.7	Ground Control Station	57
7	Subsystem Design: Structures	60
7.1	Sizing for Loads	60
7.2	Impact Resistance	66
7.3	Occupational Health & Safety considerations	78
7.4	Vibrational Analysis	79
8	Data Handling & Hardware-Software Interaction	84
8.1	Data handling	84
8.2	Software Design	86
9	Control and Stability	88
9.1	Actuation flow	88
9.2	Flight Controller	89
9.3	Alterations to the Paparazzi software	90
9.4	Summary	93
10	Verification and Validation	94
10.1	Verification of Propulsion Calculations	94
10.2	Validation of Propulsion Design	95
10.3	Verification and Validation of the Structural Design	95
10.4	Verification and Validation of Communication Calculations	97

11 Sustainable Solutions	98
11.1 Social sustainability	98
11.2 Economical Sustainability	99
11.3 Environmental sustainability	100
12 Systems Engineering	102
12.1 Resource Allocation and Budget Balance	102
12.2 Risk Assessment	104
12.3 Subsystem Allocation	109
12.4 Design Iteration Summary	110
12.5 Sensitivity Analysis	116
12.6 Inspection Pocket Drone: description of the integrated system	118
13 Requirement Compliance Matrix & Feasibility Analysis	120
13.1 Requirement Compliance Matrix	120
13.2 Feasibility Analysis	120
14 Further Development	124
14.1 Project Design and Development Logic	124
14.2 Development Gantt Chart	125
14.3 Cost Breakdown Structure	127
14.4 Operations and Logistics Concept	127
15 Conclusion	130
16 Recommendations	132
A Work distribution	137
B Propulsion Example Calculation	138

1 | Introduction

This report concludes and contains discussion on the first two design phases in the development of the ‘Inspection Pocket Drone’ system, a reliable and easily deployable unmanned aerial vehicle system designed for indoor inspection and flying in Dutch weather conditions.

UAVs are becoming increasingly present in everyday life. These aerial robots have the capability to perform tasks such as inspection and surveillance in areas that are difficult or dangerous for humans to enter or reach. A few examples of such possible UAV applications include:

1. Scanning of fragile structures that are in danger of collapsing, in search for survivors, during or in the aftermath of a disaster (e.g. fire, earthquakes, and hurricanes).
2. Risk-limited reconnaissance of hostage-taking situations.

From a technological point of view the maturity of drones has reached a state such that these applications are feasible in theory. Companies and research institutions increasingly focus on UAV systems and applications. Therefore DSE Group 18, comprised of 10 students of the faculty of Aerospace Engineering of the TU Delft, set the goal to research and design an innovative vehicle that will enable emergency services to inspect buildings.

The report starts with a mission description by means of a functional flow diagram and a functional breakdown structure, which can be found in Chapter 2. In Chapter 3, one can find market analysis on the current state of the UAV market and the positioning of the IPD in this market was performed to establish the best options for potential customers. Also, elaboration on the relevant legislation is found in this chapter.

Definition of a clear mission description, market analysis and a chosen final concept allows for the commence of the detailed design phase. In Chapter 5 the theories and design of the propulsion system are explained. Then, in Chapter 6 all electronic components are treated such as payload, communications and the ground control station. To house the propulsion system and payload, a structure is needed. This structure will be designed and analysed in Chapter 7.

Chapter 8 will explain how the data of the UAV is handled and will show its software layout and flight controller, this chapter will also discuss the control and stability of the UAV. Now all calculations are performed, the results have to be verified and validated in Chapter 10. Social, economical and environmental sustainable solutions will be discussed in Chapter 11.

Chapter 12 will give an overview of every system engineering tool used to result in the given design options to be used. These include the design and iteration strategy, resource allocation and budget balance, risk assessment, payload allocation, iteration summary and a description of the integrated system. With the complete design of the system a requirement compliance matrix is created and a feasibility analysis is performed in Chapter 13.

In Chapter 14 gives an overview how further development of the project will appear. It also shows a cost break down structure and the operations and logistics concept of the mission itself. Finally, recommendations regarding the work done and the work to be done can be found in Chapter 16.

2 | Mission Description

In this chapter the mission description is shown by means of a functional flow diagram and a functional breakdown structure of the system. Also all requirements are listed in this chapter. Section 2.1 presents the functional flow diagram, which represents the functions to be performed during operation. Section 2.2 elaborates on the functional breakdown structure, which summarises the functions that the UAV must perform in order to be operational. Section 2.3 gives an overview of all requirements imposed on the system.

The functional flow diagram and breakdown structure are based on the Mission Need Statement and Project Objective Statement. The Mission Need Statement and Project Objective Statement are as follows:

Mission Need Statement:

"Emergency services are in need for a portable, quickly-deployable, user friendly, innocuous, unmanned outdoor and indoor inspection system for danger zones"

Project Objective Statement:

"Design a backpack-sized UAV (and its corresponding ground station) equipped with a visual inspection system, enabling users to identify objects of interest, that is operational within one minute for safe use outdoors and indoor confined places for a duration of at least 10 minutes; the task is to be performed by 10 students before 2-7-2015."

So in the event of a fire in a high-rise building, the system will provide the emergency services with the capability of visually inspecting the inside of the structure. In order to do so, the aerial segment will be able to fly in the prevailing weather conditions outdoors and locate a suitable entry point to the building. It will then enter the building and proceed to gather and transmit visual data to the user operating the ground station. While maneuvering indoors the vehicle will endure the environmental conditions encountered inside the building (collisions, water, particulates, etc) and be safe to people. In case a suitable entry point can not be found, the system will be able to inspect the building by looking through the windows.

2.1 Functional Flow Diagram

In order to show all the different functions of the project in a structured manner, a Functional Flow Diagram (FFD) is made, which is depicted in Figure 2.1. The FFD shows the functions, depicted as blocks of the whole mission from start to end on-site. The functions before and after a mission are not shown in the diagram but explained in the text below. The FFD is divided in to seven main phases: Deployment, Take-off, Entering area of interest, Reconnaissance/Inspection, Return to the ground control station, Replacement of energy source, End of mission. Each of these phases is broken down into more detail, as far as possible with current knowledge on the design.

Before one can leave to the location of interest the UAV has to be picked up from storage and the energy sources disconnected from the charger and packed into the backpack. Once arrived at the location of interest the UAV has to be deployed. Firstly, the UAV has to be unpacked and assembled, then the ground station has to be set up. After the system is turned on and the connection is established, the UAV is ready for take off.

Before the actual take-off is done, the take-off direction has to be determined and checked, this prevents the vehicle from crashing into objects. Once the take-off procedures are done the UAV can go airborne and fly to the area of interest.

At the area of interest, the UAV will scan for openings to fly through, either autonomously or by the help of the operator. Once an opening is found it will be determined whether the UAV can fly through.. If the opening is large enough the UAV will enter. If it is concluded that it is not, the vehicle will search for another opening or the ground team can create an opening for it.

Once the UAV is indoors, it can start the actual inspection of the building. During the inspection phase, the UAV provides a live feed to the ground control station. If the UAV gets a command to take a picture of an

object, it will stop and stabilise to take the picture. As soon as the mission ends, it proceeds to the 'Return to ground control station' phase.

When the UAV receives the command that the mission is finished or that the energy level runs low it will return back to the ground control station. Once arrived at the exit it will check whether it is still a suitable opening to fly through. If not, it will look for a new exit. If yes, it will fly through and land at the ground station.

If the mission has to continue, the soundness of the UAV will be examined and the energy source will be replaced if it is still able to continue the mission. Once this is done the phases explained in the previous paragraphs will be followed once more. If the mission is ended the system will be turned off and packed again. After each mission, an evaluation will occur by looking at abnormalities seen during the inspection, what could have gone better and which improvements should be made for the next mission. Once back at the base, the UAV gets its regular maintenance and fixes in case the UAV was damaged. After this activity, the UAV can be stored again and the energy sources can be recharged.

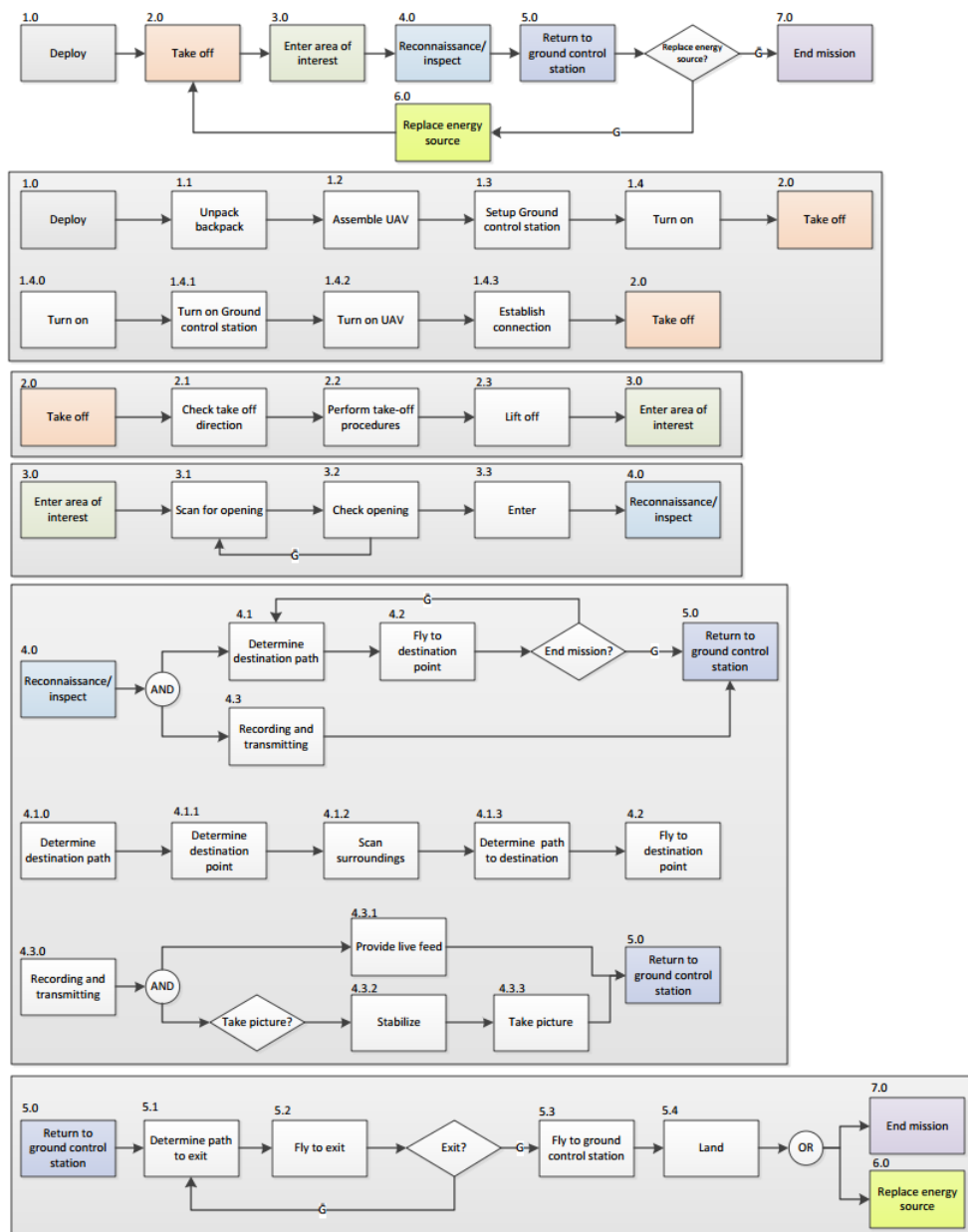


Figure 2.1: The functional flow diagram for the Inspection Pocket Drone project

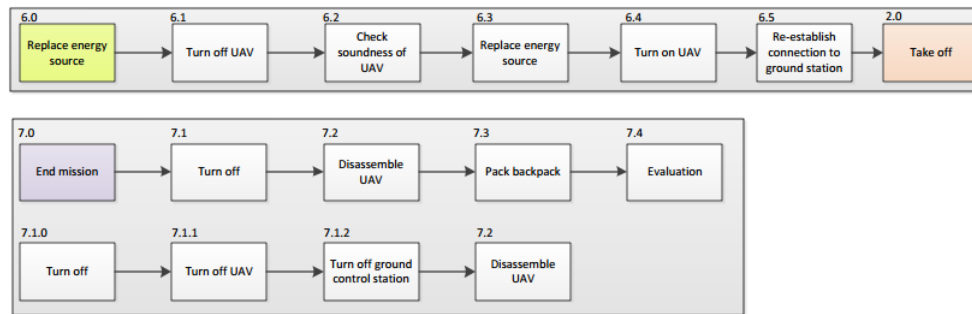


Figure 2.2: The functional flow diagram for the Inspection Pocket Drone project

2.2 Functional Breakdown Structure

In order to find out all sub-functions that are needed for the UAV to fulfill its mission, a functional breakdown structure (FBS) is made. A FBS is an "And" tree, which means that a function is the sum of the functions below it. The FBS for this mission is shown in Figure 2.3. The main functions to be performed are to fly, to communicate, to record, to provide power and to provide a user interface. The first four functions are performed by the UAV itself while the last function is done by the Ground Control Station (GCS).

In order to fly, the UAV must provide lift, thrust, stability and control. The lift and the thrust are fundamental functions since without lift the UAV will not fly, and without thrust it cannot move about. The stability is placed under the function sensing and processing. Control is necessary to steer the vehicle to its desired position. It shall be controlled by either direct control inputs from the user interface or by an autopilot providing autonomous flight.

Sensing and processing deal with environmental influences on the UAV, such as stability and obstacle avoidance. The stability is done by sensing disturbances in every direction and correcting for them.

The communication performed by the UAV shall be split into providing a live feed, receiving control inputs and transmitting video data and pictures. The live feed, data and pictures are transmitted by communication from the UAV to the GCS. The live feed is used to pilot the vehicle around during operations using manual control and is used to inspect the area of interest. The data and pictures can be used to analyse certain areas in more detail without the additional time pressure from the limited flight time. The control inputs are divided into flight controls and camera controls: flight controls to fly the UAV and camera controls to look in a different direction than the aircraft or to take a picture.

The inspection phase consists of the generation of the live feed, taking pictures and collecting data. Generating the live feed is very important, since this live feed is needed to navigate the vehicle through a building. The ability to take pictures greatly increases the UAV's reconnaissance capabilities since not everything has to be analysed during the (short) flight. To make best use of these features the camera must be able to be pointed into a desired direction, by rotating the UAV. Different data acquisition will also add inspection functionality. Although sensing and inspecting might sound like they are the same, there is a significant difference: the sensing is done by the UAV to keep itself flying properly, whereas the inspection is done for the user.

To keep everything operational, power input to the subsystems is required. Power must be provided to four subsystems: propulsion, control, payload and the GCS. These four groups can be traced back to the other functions in the FBS. Power to the propulsion group is needed for the lift and thrust functions. The control group consists of the control and the sensing and processing functions. Communication and recording are covered by the input power for the payload group and GCS also has a separate power allocation. The required power for different groups can come from the same source, e.g. a battery, however the possibility of assigning a separate power supply for each subsystem is still probable.

The last function is to design a user interface. This user interface must show the live feed that is used to fly the UAV when it is out of sight. It must also have means to give control inputs to the vehicle, these cover both flight and camera controls. The data from the UAV must be processed in a way that the delivered information is in a desired format.

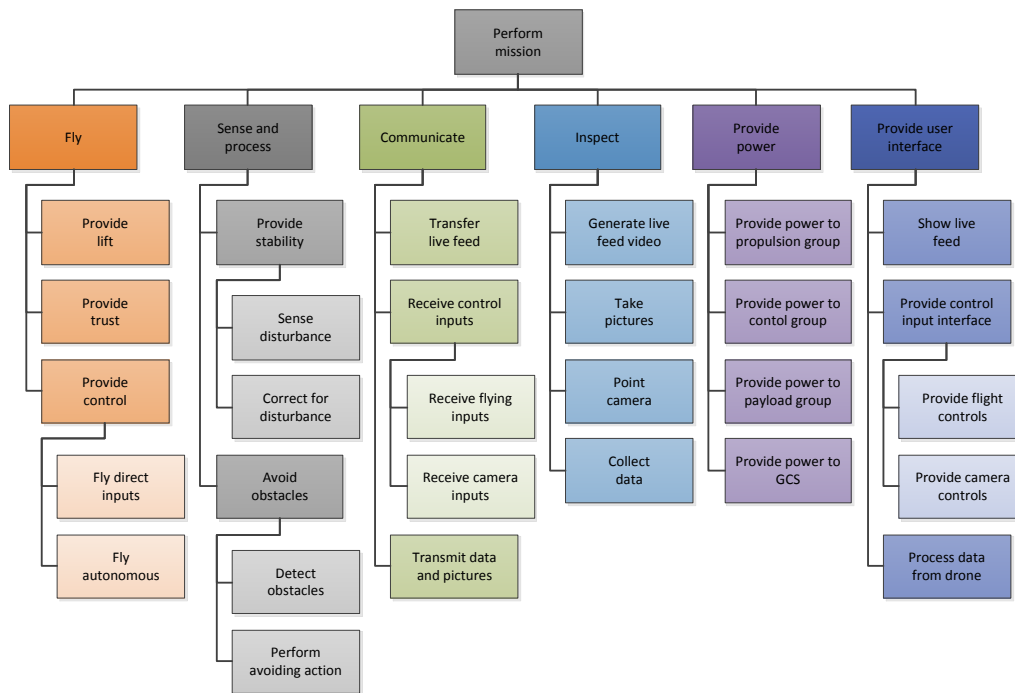


Figure 2.3: The functional breakdown diagram for the Inspection Pocket Drone project

2.3 Mission Requirements

In this section the list of requirements of the system is stated. These requirements are based on the customer requirements and the mission that has to be performed. These requirements are found using an extensive requirements discovery tree. The list of requirements is split up in 9 smaller lists based on segments of the mission containing the requirement code and the requirement itself in full sentences. The 9 lists are as follows:

Transportation Requirements

- IPD-AAoI-Transport [1,D,K]: A single firefighter shall be able to carry the entire system on his own.
- IPD-AAoI-Transport-A [2,D,K]: The maximum stored size of the total system shall be 35x25x10cm.
- IPD-AAoI-Transport-B [3,D]: The maximum total system mass shall be 2kg.

Deployment Requirements

- IPD-AAoI-Deploy [1,D]: The system shall be deployable.
- IPD-AAoI-Deploy-A [1,D,K]: The total system shall be deployable and operational in under 60 seconds.
- IPD-AAoI-Deploy-B [3]: No tools shall be necessary for the deployment of the system.
- IPD-AAoI-Deploy-C [3]: No more than 5 tools shall be necessary to replace a part of the system in the emergency zone.
- IPD-AAoI-Deploy-D [2]: Replacement of energy source of the system shall be conducted under 60 seconds.

Reach Area of Interest Requirements

- IPD-AAoI-Reach [1,D,K]: The vehicle shall be able to reach the area of interest.
- IPD-AAoI-Reach-A [1,D]: The vehicle shall be able to fly to the area of interest..
- IPD-AAoI-Reach-A-1 [1]: The vehicle shall generate the required lift to complete its mission.
- IPD-AAoI-Reach-A-1-A [1]: The vehicle shall provide the required power to the lift generation subsystem.
- IPD-AAoI-Reach-A-2 [1]: The vehicle shall generate the required thrust to complete its mission.
- IPD-AAoI-Reach-A-2-A [1]: The vehicle shall provide the required power to the thrust subsystem.

- IPD-AAoI-Reach-A-3 [1,D,K]: The system shall be able to operate in 90% of Dutch weather conditions at an altitude of 10 meters.
- IPD-AAoI-Reach-A-3-A [1,D]: The vehicle shall be able to perform its mission in maximum wind speeds of $11 \frac{m}{s}$.
- IPD-AAoI-Reach-A-3-B [1,D]: The vehicle shall be able to perform its mission in maximum gust speeds of $17 \frac{m}{s}$.
- IPD-AAoI-Reach-A-3-C [1,D]: The vehicle shall be able to perform its mission in maximum of 2.6mm of rain per hour.
- IPD-AAoI-Reach-A-3-D [1]: The vehicle shall be able to perform its mission in minimum temperatures of $-5^{\circ}C$.
- IPD-AAoI-Reach-A-3-E [1]: The vehicle shall be able to perform its mission in maximum outdoor temperatures of $25^{\circ}C$.
- IPD-AAoI-Reach-A-4 [1]: The vehicle shall be stable.
- IPD-AAoI-Reach-A-4-A [1]: The vehicle shall be directionally stable.
- IPD-AAoI-Reach-A-4-B [1]: The vehicle shall be longitudinally stable.
- IPD-AAoI-Reach-A-4-C [1]: The vehicle shall be laterally stable.
- IPD-AAoI-Reach-A-5 [1]: The vehicle shall be able to withstand flight loads without experiencing any damage that compromises the mission.
- IPD-AAoI-Reach-A-5-A [1,D]: The vehicle shall be able to withstand static flight loads without experiencing any damage that compromises the mission.
- IPD-AAoI-Reach-A-5-B [1,D]: The vehicle shall be able to withstand dynamic flight loads without experiencing any damage that compromises the mission.
- IPD-AAoI-Reach-A-5-C [1]: The vehicle shall be able to withstand flight induced vibrations loads without experiencing any damage that compromises the mission.
- IPD-AAoI-Reach-A-6 [1]: The vehicle shall be able to sense its state properties.
- IPD-AAoI-Reach-A-6-A [2,D]: The vehicle shall be able to sense its state properties at lighting conditions of $0 \frac{cd}{m^2}$.
- IPD-AAoI-Reach-A-6-B [1]: The vehicle shall determine its attitude.
- IPD-AAoI-Reach-A-6-C [1]: The vehicle shall determine its relative position to the surroundings.
- IPD-AAoI-Reach-A-6-D [2]: The vehicle shall determine its absolute position.
- IPD-AAoI-Reach-A-6-E [1]: The vehicle shall determine its velocity.
- IPD-AAoI-Reach-A-6-F [3]: The vehicle shall record its housekeeping data.
- IPD-AAoI-Reach-A-7 [1,D,K]: The vehicle shall fly safely.
- IPD-AAoI-Reach-A-7-A [1]: The vehicle shall enter autonomous position hold when no input commands are received.
- IPD-AAoI-Reach-A-7-B [1,D,K]: The vehicle shall not cause trauma to people upon impact.
- IPD-AAoI-Reach-A-8 [2,D,KL]: The system shall be able to operate in 75% of Dutch weather conditions at an altitude of 100 meters.
- IPD-AAoI-Reach-A-8-A [2,D,KL]: The vehicle shall be able to perform its mission in maximum wind speeds of $21 \frac{m}{s}$.
- IPD-AAoI-Reach-A-8-B [2,D,KL]: The vehicle shall be able to perform its mission in maximum gust speeds of $24 \frac{m}{s}$.

Enter Area of Interest Requirements

- IPD-AAoI-Enter [1,D,K]: The vehicle shall be able to enter the area of interest.
- IPD-AAoI-Enter-A [2,D]: The vehicle shall be able to detect a suitable entrance into the area of interest.
- IPD-AAoI-Enter-A-1 [2,D]: The vehicle shall be able to break a tempered double-glass window.

- IPD-AAoI-Enter-A-2 [2,D]: The vehicle shall be equipped with a visual inspection system to be able to detect a suitable entrance.
- IPD-AAoI-Enter-B [1,D,K]: The vehicle shall be able to traverse the entrance of the area of interest.
- IPD-AAoI-Enter-B-1 [2]: The vehicle shall be able to determine its relative position with respect to the entrance to the area of interest with an accuracy that prevents it from colliding with the boundaries of the entrance.
- IPD-AAoI-Enter-B-2 [1,D,K]: The vehicle shall be able to go through a 61x60 *cm* opening during operational conditions.
- IPD-AAoI-Enter-B-3 [1,D]: The vehicle shall remain stable while entering the area of interest.
- IPD-AAoI-Enter-B-3-A [2,D,KL]: The vehicle shall be able to enter the area of interest in maximum wind speeds of $21 \frac{m}{s}$.
- IPD-AAoI-Enter-B-3-B [2,D,KL]: The vehicle shall be able to enter the area of interest in maximum gust speeds of $24 \frac{m}{s}$.
- IPD-AAoI-Enter-B-4 [1,D]: The vehicle shall sustain impacts upon entering the area of interest.

Payload Requirements

- IPD-GI-Payload [1,D,K]: The vehicle shall have payload.
- IPD-GI-Payload-A [1]: The vehicle shall be able to provide power to the payload.
- IPD-GI-Payload-B [1,K]: The payload shall be able to gather visual data.
- IPD-GI-Payload-B-1 [2,K]: The payload shall be able to capture video.
- IPD-GI-Payload-B-1-A [2,K]: The payload shall be able to provide a video quality sufficient to recognise persons at 5*m* distance.
- IPD-GI-Payload-B-1-B [3]: The camera of the payload shall provide video with a minimum frame rate of 24 frames per second.
- IPD-GI-Payload-B-2 [1,K]: The payload shall be able to capture still images.
- IPD-GI-Payload-B-2-A [1,K]: The payload shall be able to provide a still image quality sufficient to recognise persons at 5*m* distance.
- IPD-GI-Payload-B-2-B [2,K]: The payload shall be able to take at least 3 MP still images.
- IPD-GI-Payload-B-3 [3]: The minimum view angle of the payload cameras shall be 80 degrees.
- IPD-GI-Payload-C [2,K]: The payload camera system shall operate in lighting conditions down to $0 \frac{cd}{m^2}$.
- IPD-GI-Payload-D [2]: The payload shall be able to capture sound.
- IPD-GI-Payload-E [2]: The vehicle shall keep the visual measurement instruments stable.
- IPD-GI-Payload-E-1 [2]: The vibration of the payload cameras shall not exceed an amplitude of 5 pixels.
- IPD-GI-Payload-E-2 [2]: The frequency of the vibration of the payload cameras shall not exceed half of the video frame rate.
- IPD-GI-Payload-E-3 [2]: The drift of the payload cameras shall not blur the images taken.
- IPD-GI-Payload-F [2,K]: The payload shall gather temperature data of the surroundings.
- IPD-GI-Payload-G [2,D]: The vehicle shall be able to withstand payload loads without experiencing any damage that compromises its mission.
- IPD-GI-Payload-H [2,K]: The payload shall gather gas concentration data of the surroundings.

Manoeuvrability Requirements

- IPD-GI-Maneuver [1,D]: The vehicle shall be able to maneuver through the area of interest.
- IPD-GI-Maneuver-A [1]: The vehicle shall have a means of propulsion for indoor maneuvering.
- IPD-GI-Maneuver-A-1 [1]: The vehicle shall provide the required power to the propulsion subsystem.
- IPD-GI-Maneuver-B [1]: The vehicle shall be able to sense its state properties.
- IPD-GI-Maneuver-B-1 [2,D]: The vehicle shall be able to sense its state properties at lighting conditions of $0 \frac{cd}{m^2}$.

- IPD-GI-Maneuver-B-2 [1]: The vehicle shall determine its attitude.
- IPD-GI-Maneuver-B-3 [1]: The vehicle shall determine its relative position to the surroundings.
- IPD-GI-Maneuver-B-4 [2]: The vehicle shall determine its absolute position.
- IPD-GI-Maneuver-B-5 [1]: The vehicle shall determine its velocity.
- IPD-GI-Maneuver-B-6 [3]: The vehicle shall record its housekeeping data.
- IPD-GI-Maneuver-C [1,D,K]: The vehicle shall be able to maneuver safely.
- IPD-GI-Maneuver-C-1 [1]: The vehicle shall enter autonomous position hold when no input commands are received.
- IPD-GI-Maneuver-C-2 [1,D,K]: The vehicle shall not cause trauma to people upon impact.
- IPD-GI-Maneuver-D [1,D]: The vehicle shall be able to maneuver in the indoor environmental conditions of the mission..
- IPD-GI-Maneuver-D-1 [2,D]: The vehicle shall have liquid ingress protection to a maximum water flow rate of $35 \frac{l}{m^2h}$.
- IPD-GI-Maneuver-D-2 [1,D]: The vehicle shall withstand impact loads caused by its collision with stationary objects under nominal flying conditions.
- IPD-GI-Maneuver-D-3 [2,D]: The vehicle shall withstand impact loads caused by moving objects under nominal flying conditions.
- IPD-GI-Maneuver-D-4 [3,KL]: The vehicle shall be able to perform its mission in maximum indoor temperatures of $400^{\circ}C$.
- IPD-GI-Maneuver-D-5 [3]: The vehicle shall have level 5 solid particle protection of the IP Code.
- IPD-GI-Maneuver-E [2]: The vehicle shall automatically avoid collisions with the surroundings.
- IPD-GI-Maneuver-F [3]: The vehicle shall be manually controllable.
- IPD-GI-Maneuver-F-1 [3]: The vehicle shall be controllable to a minimum of 3 degrees of freedom.
- IPD-GI-Maneuver-F-2 [3]: The CAS shall be turned on/off from the GCS.
- IPD-GI-Maneuver-F-3 [3]: The vehicle shall have a settling time of 1 second upon control
- IPD-GI-Maneuver-G [1]: The vehicle shall be stable.
- IPD-GI-Maneuver-G-1 [1]: The vehicle shall be directionally stable.
- IPD-GI-Maneuver-G-2 [1]: The vehicle shall be longitudinally stable.
- IPD-GI-Maneuver-G-3 [1]: The vehicle shall be laterally stable.

Communication Requirements

- IPD-Communicate-A [1]: The vehicle shall provide power to the communication subsystem.
- IPD-Communicate-B [3]: The communication link shall be secure.
- IPD-Communicate-C [3]: The system shall be able to communicate with persons inside the building.
- IPD-Communicate-D [2,K]: The GCS user interface shall be readable under lighting conditions of $96000 \frac{cd}{m^2}$.
- IPD-Communicate-E [1,D]: The vehicle shall transmit the collected mission data to the GCS.
- IPD-Communicate-E-1 [2]: The delay of the mission data stream shall be less than 0.1 sec.
- IPD-Communicate-E-2 [2]: The vehicle shall be able to stream video.
- IPD-Communicate-E-3 [1]: The vehicle shall be able to transmit the still images.
- IPD-Communicate-E-4 [2]: The vehicle shall transmit sound data to the GCS.
- IPD-Communicate-E-5 [2]: The vehicle shall transmit temperature data of the surroundings to the GCS.
- IPD-Communicate-E-6 [2]: The vehicle shall transmit gas concentration data of the surroundings to the GCS.
- IPD-Communicate-F [1,D]: The vehicle shall communicate control data to and from the GCS.
- IPD-Communicate-F-1 [3]: The vehicle shall communicate control feedback to the GCS.

- IPD-Communicate-F-1-A [3]: The frequency of the control feedback transmission shall be at least $10Hz$.
- IPD-Communicate-F-1-B [3]: The vehicle shall transmit its velocity readings to the GCS.
- IPD-Communicate-F-1-C [3]: The vehicle shall transmit its attitude readings to the GCS.
- IPD-Communicate-F-1-D [3]: The vehicle shall transmit its relative position relative to the surroundings to the GCS.
- IPD-Communicate-F-1-E [3]: The vehicle shall transmit its absolute position to the GCS.
- IPD-Communicate-F-1-F [3]: The delay of the control feedback data stream shall be less than 0.1 sec.
- IPD-Communicate-F-2 [1,D]: The vehicle shall be able to receive control input data from the GCS.
- IPD-Communicate-F-2-A [2]: The delay of the control input data stream shall be less than 0.1 sec.
- IPD-Communicate-G [2]: The vehicle shall transmit its housekeeping data to the GCS.
- IPD-Communicate-H [2,D]: The system communication range shall be $150m$.
- IPD-Communicate-H-1 [2,D]: The vehicle shall be able to communicate with the GCS from a range of $100m$ through 2 brick walls.
- IPD-Communicate-H-2 [2,D]: The vehicle shall be able to communicate with the GCS from a range of $100m$ through 1 reinforced concrete wall.

Miscellaneous Requirements

- IPD-Misc-A [2,D,K]: The vehicle shall have a maximum weight of 500 grams.
- IPD-Misc-B [2]: The vehicle shall have an operational range of $200m$.
- IPD-Misc-C [2]: The vehicle shall have an operational ceiling of $100m$.
- IPD-Misc-D [2,K]: The system shall be operational for at least 10 minutes.
- IPD-Misc-E [2,K]: The maximum material cost of the total system shall be €15000.
- IPD-Misc-F [2,K]: The system shall comply with the Dutch legislation.
- IPD-Misc-G [2,D,K]: 80% of the system mass shall be recyclable at the end of life.
- IPD-Misc-H [2]: The vehicle shall have a safe-mode.
- IPD-Misc-H-1 [2]: The vehicle shall switch to safe-mode in case of GCS failure.
- IPD-Misc-H-2 [2]: The vehicle shall switch to safe-mode if communication with the GCS is lost.
- IPD-Misc-I [3]: The system radiation shall be lower than $20 \frac{Sv}{year}$.
- IPD-Misc-J [3]: The system shall not contain any poisonous materials that can come into contact with the user.
- IPD-Misc-K [3]: The system shall not contain any irritant materials that can come.
- IPD-Misc-L [3]: The vehicle shall not emit noise higher than 85 dB at source.

DSE Requirements

- IPD-DSE-A [1,K]: The system design shall be completed before 2nd July 2015.
- IPD-DSE-B [3]: The system design shall be completed by the contribution of no more than 10 team members.
- IPD-DSE-C [3]: The system design process shall be conducted without the use of prototype testing.

To summarize the mission was first described by means of a functional flow diagram and a functional breakdown structure. The last part of the chapter states all requirements applicable to the mission.

3 | Market Analysis

A market analysis was performed to identify the current state of the UAV market and to identify the position of the Inspection Pocket Drone. Section 3.1 gives a brief overview of the market followed by Section 3.2 describing current and future applications and end users of UAV systems. The market structure that identifies the market's state, supply chains, dominant players is discussed in Section 3.3. Section 3.4 presents positions of current products and identifies possible gaps. Lastly, Section 3.5 explains the legislation of UAVs.

3.1 General Market Description

In the past years, unmanned aerial vehicles or drones gained a lot of public attention worldwide. The UAV market can be split into military and civilian use, of which the first part takes up 89% of the total revenue, surpassing 6 billion dollars in total in 2014. The civilian market however is expected to experience high growth in the upcoming years.¹ Because of the technological advancements in batteries, GPS systems, Inertial Measurement Unit (IMU) chips and payload devices like cameras, the systems available on the consumer market are becoming increasingly sophisticated, of high quality and affordable. Especially multi-rotor systems like quadcopters are popular because of their capability to hover and take-off vertically, making them flyable in areas with limited space, combined with higher stability than single rotor systems.² The popularity of small UAV's gives a large impulse to the market, accelerating development and innovation. The commercial use of such systems is increasing as well. UAV's provide a very versatile platform to efficiently perform a large range of tasks, which contributes to their popularity. For instance reaching remote areas and dangerous locations, collecting data and performing inspection and surveillance missions.³ Considering the global scale, the UAV market in 2013 resided for 77% in the US and Europe, of which the US holds the largest share of military uses.⁴

3.2 Applications and End Users of UAV Systems

Considering the civilian UAV market, the end users have various uses for UAV systems, therefore the customer profile of this market has been analysed. Figure 3.1 identifies end users in two major groups, the public and private sector. Within the private sector, there are both commercial and non-commercial applications and UAVs can be used by individuals or organisations. Figure 3.2 identifies current and potential uses of UAV's.

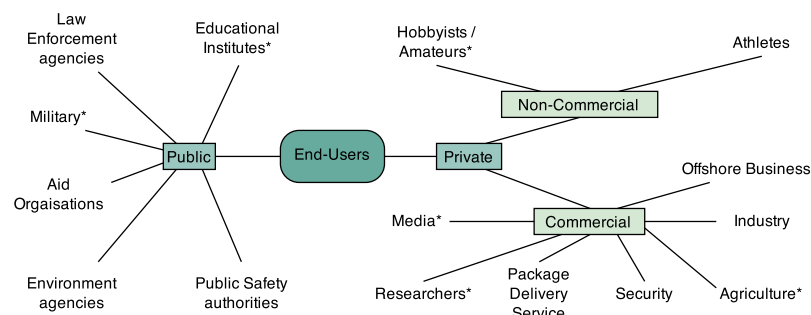


Figure 3.1: Current and potential end-users of UAV systems, asterisk indicate groups that currently have the largest user base

¹URL:<http://www.tealgroup.com/index.php/about-teal-group-corporation/press-releases/118-2014-uav-press-release>

²URL:<http://singularityhub.com/2015/01/27/drones-will-be-everywhere-watching-listening-and-planting-millions-of-trees/>

³URL:<http://singularityhub.com/2014/08/11/top-10-reasons-drones-are-disruptive/>

⁴URL:<http://www.slideshare.net/terrai/global-commercialandciviluavmarketguide20142015>

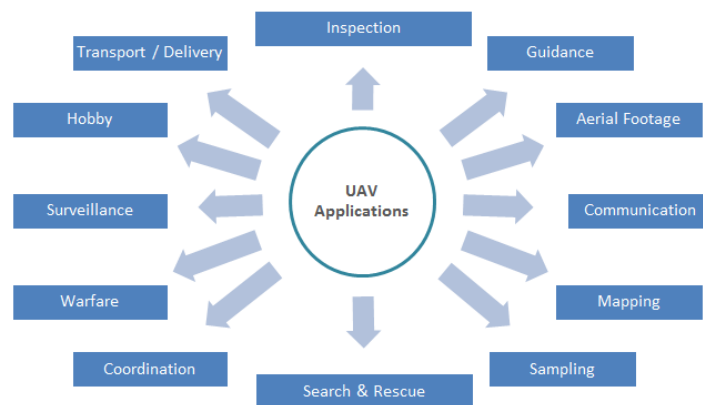


Figure 3.2: Current and potential applications of UAV systems by users

UAVs are being used by different types of users with many particular applications. It is not possible to distinguish all use cases by specific end users, however, UAVs are increasingly being developed for specific applications. For example, in the media recently there are the U.S. Department of Defence General Atomics Predator drones for (armed) reconnaissance missions⁵. Additionally, aid organisations have utilised UAVs for damage assessment during 2013's Typhoon Haiyan [1] and the health care services can potentially use the TU Delft Ambulance Drone⁶ as a rapid-response fleet for emergencies. Businesses have also started to use UAVs, for example in Japan and the US, UAVs are being utilised by farmers for crop management to obtain a higher quality yield⁷.

As the market grows and research is carried out on potential applications, a variety of individuals and businesses are being exposed to the technology, and it is likely that the user base will increase. The list of applications and users is endless and UAVs could even become a household item in the future. However, the analysis considered in this report is limited to the current/near future market and topics related to the design of the IPD. Current focus lies on research of potential applications by end users, hence fully developed systems have not been proven and deployed by the public and private sectors. More future applications will be developed over time, but research is still necessary on UAV infrastructure and regulations. When these aspects are improved, UAV usage will likely increase as the supporting assets are in place to introduce UAVs for regular use.

3.3 Market Structure

The dynamics of the UAV market for civilian use is influenced by different industries influencing technological progress and innovation.

Within the UAV market, several types of businesses can be defined:

- UAV Development & Manufacturing companies
- Component manufacturers (other industries)
- Control and navigation software and hardware manufacturers and developers
- Service companies using UAVs
- Payload manufacturers (other industries)
- Integrated development & UAV service companies

3.3.1 Market suppliers

The commercial UAV market is relatively new, which means many businesses are still developing and launching new products. As UAVs are becoming more affordable, the market is moving away from directly selling to

⁵URL:http://www.militaryfactory.com/aircraft/detail.asp?aircraft_id=46

⁶URL:<http://www.io.tudelft.nl/onderzoek/delft-design-labs/applied-labs/ambulance-drone/>

⁷URL:<http://www.wired.com/2013/05/the-business-of-putting-robots-in-the-sky/>

customers to using distributors and retailers to appeal more to the mass-market⁸, an example is the Parrot AR Drone which has found its way to many (online) stores globally⁹.

The current manufacturing and marketing method of commercial market leaders is that they utilise off-the-shelf components and proprietary software to develop their UAV. The software usually runs on an off-the-shelf micro-controller, such as the Arduino platform¹⁰ that has been stripped down to only the necessary features. Major structural components are usually manufactured in-house to meet the design requirement and smaller, more standardized parts such as joints and propeller can usually be bought from other suppliers. In general, suppliers for most other subsystems such as communication (antennas), power (batteries, wiring) and propulsion (servos, motors) already exist and have technologies readily available for use in relatively small vehicles.

Innovative products such as custom software or subsystems are being developed by research universities or businesses when the current market suppliers are not offering the desired software or component. Products are more rapidly entering the commercial market due to increasing research and investment in the sector and lack of stringent regulations and certifications which usually take up a lot of time before launch to market.

3.3.2 Revenue models

Various revenue models can be distinguished related to UAV systems and applications.

- One-time system purchase
- Fee-for-service
- Fee-for-use
- Lease structure
- Long-term (periodic) service contracts
- Direct purchase combined with service contract (pilot training / setup e.g.)
- Customized development and manufacturing contract

In the current commercial market for private use, most often UAVs are sold in the form of a one time purchase through a reseller or distributor. However, when considering more specific applications like inspection missions, in a business to business environment, revenue models tend towards fee-for-service contracts or structures where aspects like pilot training and equipment setup and servicing is considered.

3.4 Product Differentiation and Market Gap

Businesses developing and selling UAVs position and differentiate themselves in the market by marketing their product's specifications as unique selling points (USPs). The list below summarises the main specifications and features of an entire UAV system and highlights important aspects for differentiating the IPD and defining unique selling points. Table 3.1 is divided into specifications that are directly quantifiable and features that can be described in a more qualitative way. The important distinction is that features are not necessarily quantifiable. The ordering of specifications and features reflect the items that the market mostly differentiates their product by (the USPs) and are mostly the main area of innovation and research.

⁸URL:<http://dronelife.com/2015/01/24/drone-sales-figures-2014-hard-navigate/>

⁹URL:<http://www.parrot.com/>

¹⁰URL:<http://www.arduino.cc/>

Table 3.1: UAV system specifications and features

Quantifiable specifications	Qualitative features
Payload mass and dimensions	Operability (ease of use)
Endurance	Safety
Range	Quality
Reliability	Durability
Operational cost	Maintainability / Serviceability
Price to customer	Portability (User impression of mobility)
Availability	Use diversity
Vehicle dimensions	Having multiple use cases
Non-vehicle system dimensions (for example GCS)	Sustainability
	Aesthetics

The current market trend is towards giving more attention to operability and safety aspects of UAVs. Especially the strong public opinion regarding the safety of UAVs has been subject to discussion, hence the urgency for regulatory bodies such as the European Aviation Safety Agency (EASA)¹¹, to draft new air worthiness and operational regulations regarding UAV systems. Manufacturers of UAVs generally market the payload carrying capability, endurance and range of their UAVs. Since the market is growing, competition increases with several businesses offering the same product, hence price is becoming an ever more important aspect when differentiating products. The other specifications and feature, though important, have not been the primary focus of innovation and differentiation of products by firm.

Despite the rapid growth pace of the general UAV market, the niche market for UAVs for specific use in an indoor environment, where dimensions, ease of use and operability are of high importance, is currently not developed yet. Considering the wide range of indoor uses for UAVs with a high level of autonomy, operability and attention to safety aspects, developing solutions addressing this market has much upside potential.

Some areas of innovation in the UAV market related to the IPD include the following:

Ease Of Use

Most current UAVs have a relatively steep learning curve when it comes to mastering the controls; users require training and several hours of practice before they can confidently fly a UAV. Many manufacturers, such as the Parrot AR Drone¹² have introduced active control to stabilise the UAV, however flying it, avoiding collision and performing manoeuvres is largely dependent on the users capability. There is an opportunity to introduce a system that is more readily flyable where the training required is minimal. The system should be easily integrable in a organisation's current or future activities and the implementation time period should be short avoiding an extensive training program and costly supporting infrastructure.

Indoor flying capabilities

UAVs for specific indoor usage are scarce and the market is still empty. The ability to fly indoors imposes several restrictions on the control, stability and sensing aspect of the drone as it is necessary to avoid and/or be tolerant to obstructions. Flying through small openings also requires good precision control and accurate manoeuvres and further research in this area is necessary. There is an opportunity to introduce smaller, high accuracy drones to the market that are able to maneuver indoor and avoid or be tolerant to impacts.

Safety

Considering the current public opinion towards UAVs and the safety aspects, designing a system that is safe to fly near humans and does not cause harm in case of mechanical or operational failure would provide a very favourable competitive edge.

Inspection capabilities

Regarding the intended end user, the capabilities of the system to inspect and gather information in dangerous areas and communicating this data to the pilot should at least come close to the capabilities of a person inspecting the same area.

The IPD is designed to innovate in the areas identified to close the current market gaps. These innovations will make the IPD unique and competitive when compared to the current market products. Users may also identify novel uses of the IPD when the product is brought to the market which can help drive research in this field.

¹¹URL:<https://www.easa.europa.eu/unmanned-aircraft-systems-uas-and-remotely-piloted-aircraft-systems-rpas>

¹²URL:<http://www.parrot.com/>

3.5 Legislation

In the last couple of years, the sudden increase in the usage of RPAS's has led to a situation where the regulations for these aircraft were often unclear or inadequate. For recreational use of remotely piloted aircraft, the "Regeling modelvliegen" is applicable. This law uses the term "modelluchtvaartuig" (model airplane) when an unmanned airplane is used recreationally without benefit and without compensation. When an unmanned aircraft is used occupationally the government uses the term "licht onbemand luchtvaartuig" (small unmanned aircraft). The usage of this was prohibited, unless an exemption had been granted.

Under future law, in effect on July 1, 2015, licenses can be obtained to use an RPAS commercially, under strict conditions. These include that the UAV is used within visual line of sight, not more than 500m from the operator (or an observer), and at least 150m horizontally from a crowd, buildings, or traffic; within visual flight rules and within the universal daylight period (approximately sunrise to sunset). The restrictions on buildings can be lessened if the owner of the building agrees with that, or if there is a compelling reason on grounds of common interest. Additional lessening on the regulations for drones weighing less than 4 kg will not be applicable to this product because it will not be able to fly near buildings and crowds without certification

Additionally, the Minister of Transport wants to allow emergency services such as police and firefighters to use an RPAS without the restrictions on vicinity to people and buildings, however still within Visual Flight Rules (VFR) (but possibly outside the daylight period). This significantly reduced the legal issues for the usage of the system. Operators (the pilot in command) still need to complete a training process to obtain an RPA-L license.

For the RPAS under consideration, one major restriction still applies: it can only be used within (extended) visual line of sight operations. This means that the operator or an observer has to see the drone. The law also specifies Beyond Visual Line Of Sight (BVLOS) operations, however the government has no intentions to use this provision in the near future. In short, while in airspace, the drone has to be in sight. However, when the drone is inside a building, it strictly speaking is not flying in airspace. Hence, the regulations do not apply and the system can be remotely operated without having explicit sight of the UAV.

To conclude, under current legislation, the system can be used by licensed emergency service operators to perform their occupational duties. If a non-government service wants to use it to inspect a building, this is still possible as long as the building owner agrees with it; in that case the operator can obtain an exemption. In all cases, when outside of buildings, the UAV should be in sight.

The market analysis summarises the current state of the UAV market, challenges faced by most UAV businesses, the competition and possible gaps in the market. Finally legislative aspects of UAVs are discussed because the current regulations are catching up to the rapid pace of the UAV market. The regulations are still being drafted and keep changing, hence it is an area of attention to make sure the IPD can be certified for operations.

4 | Design and Iteration Strategy

The detailed design involves multiple iterations of the different subsystem designs before a final product design is achieved. In this chapter, the procedure to be followed in the detailed design phase is presented.

The process to be followed in the detailed design phase consists of different steps involving subsystem design and requirement verification. The procedure is presented in Figure 4.1. The aim of the process is to first obtain a feasible design that complies with all the primary requirements. Once this is achieved, the process is continued trying to improve the design in order to fulfill as many secondary and tertiary requirements as possible.

Until a final design that complies with all the primary requirements has been achieved, only the primary requirements and the current design state will have an effect on the design steps being performed. The first step of the process is to design the payload and the sensors subsystems. Next, the On-board Computer will be designed. When the OBC design is set, the communications subsystem will be addressed. After the communications subsystem the power subsystem will be designed. Subsequently, the structure is constructed and the propulsion subsystem design concludes the procedure. The last three steps, power, structures and propulsion design will be repeated until the design process converges into a feasible design solution.

Once a solution has been found it will be assessed against the requirements to check how well the design complies with the requirements. If all the primary requirements are met this design will be saved as a possible final design. Then the design process will begin again with the design of the payload and the sensors, taking into consideration not only the current design state and the primary requirements, but also the secondary and tertiary requirements.

In case not all the primary requirements are met the cause of it will be examined and a corrective action will be taken. The only possibility in the first design process iteration is that two or more of the primary requirements are contradicting hence driving the design in opposite ways. In this case, a compromise between the two requirements must be reached, and then the design process can start over. In later design process iterations it might also be possible that all the primary requirements are not met due to contradictions with secondary and tertiary requirements. In this case priority, must be given to the primary requirements and the design process can be restarted.

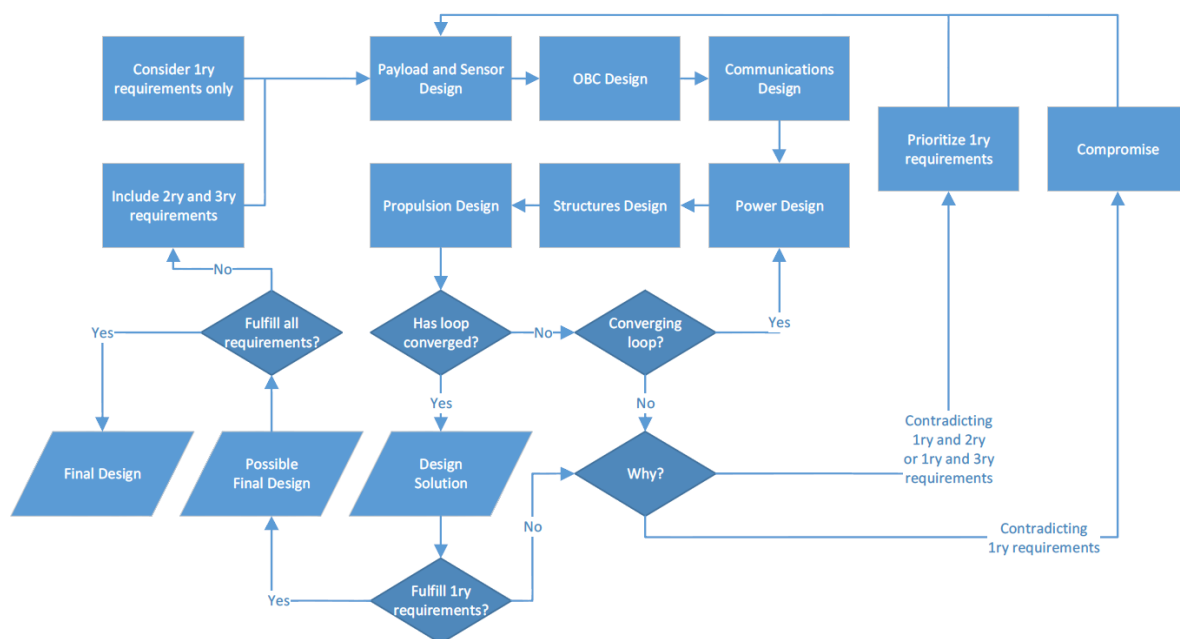


Figure 4.1: Flowchart of the detailed design process

There is the possibility that at any iteration of the design process, the loop iteration of the power, structures and propulsion subsystems design will not converge into a design solution. If so, the reason behind this divergent

behaviour must be found and accounted for. This will be assessed in the same way that the non-compliance with the primary requirements was addressed.

If at some point during the design process a design solution is found to fulfill all the primary, secondary and tertiary requirements the process will stop and this design solution will be taken as the final design. If, on the other hand, the time allocated for the detailed design phase is over before a solution fulfilling all the requirements is found, a trade-off will be performed to choose the best performing possible solution encountered during the process. This solution will then be taken as the final design.

To summarize, the detailed design process will first aim to obtain a design that fulfills all the primary requirements. Then the design will be improved in order to comply with secondary and tertiary requirements as well. Of all the solutions that satisfy the primary requirements, the best performing one will be chosen as the final design.

5 | Subsystem Design: Propulsion

In this chapter the amount of required thrust and power will be determined and how much thrust can be generated will be explained. Firstly, the required thrust is treated in Section 5.1. Secondly, the thrust generated is calculated using Blade Element Momentum Theory (BEMT) in Section 5.2. Thirdly, the design of the rotor head is described in Section 5.3. Then, the propellers is designed in Section 5.4. And finally, the required power for flight is calculated in Section 5.5.

5.1 Thrust Calculations

The impact of the duct is most noticeable in the reduction in blade tip losses and the low pressure field around the inlet which generate thrust. This thrust is dependent on the total thrust of the entire uav and the shape of the duct. To calculate the total thrust of the UAV first simple trigonometry is used.

The total amount of thrust is dependent on the required lift and the drag. The lift (L) is equal to the weight (W) of the UAV which is defined in Equation 5.1.

$$L = W = m_{uav}g \quad (5.1)$$

As can be seen L is thus only dependent on the mass of the UAV (m_{uav}) and the gravitational constant (g) which is $9.81 \frac{m}{s^2}$. For the mass of the UAV which is $533g$ this then results in a L of $5.229N$.

The drag (D) is calculated using Equation 5.2 where C_d is the drag coefficient of the UAV, ρ_{air} is the density of air at sea level conditions, V is the speed of the air around the UAV and S is the surface area of the UAV perpendicular to the airflow.

$$D = C_d \frac{1}{2} \rho_{air} V^2 S \quad (5.2)$$

In Equation 5.2 V is a design goal. It is set that the UAV can fly in an airspeed of $13 \frac{m}{s}$ and ρ_{air} is a constant with the value of $1.225 \frac{kg}{m^3}$. C_d can not be calculated and generally is found using either Computation Fluid Dynamics (CFD) or experimental data. As CFD is not an option due to time and computational power restrictions previous CFD calculations on a similar shape were found and used. In Figure 5.1 C_d against inclination angle for both a hollow cylinder and a solid cylinder is shown for a Reynolds number of 10000 which is closest to the Reynolds number of the UAV. The Reynolds number is calculated in Equation 5.3. Where x is the distance over which the airflow is located in this case assumed to be the diameter of the UAV of $237mm$ and ν the kinematic viscosity of $15.11 \cdot 10^{-6} \frac{m^2}{s}$. This results in a Reynolds number of $2 \cdot 10^5$. From Figure 5.1 the C_d for a hollow cylinder, which is the closest approximation for the UAV design, at an inclination angle of 45 degrees is found to be 1.1.

$$Re = \frac{Vx}{\nu} \quad (5.3)$$

The surface area S in Equation 5.2 is calculated using the frontal surface area (S_{front}), the top surface area (S_{top}), and the pitch angle (θ_{max}) of the UAV as seen in Equation 5.4. However the pitch angle is dependent on the drag as can be seen in Equation 5.5 and as such an iteration loop needs to be used with an initial guess for the pitch angle. To clarify, the pitch angle is defined as the angle between the z-axis and the thrust as can be seen in Figure 5.2. S_{front} is a rectangular defined by the outer diameter of the UAV (D_{outer}) and the height (h). S_{top} is a ring defined by the outer diameter (D_{outer}) and the inner diameter (D_{inner}).

¹URL:http://www.engineeringtoolbox.com/air-properties-d_156.html

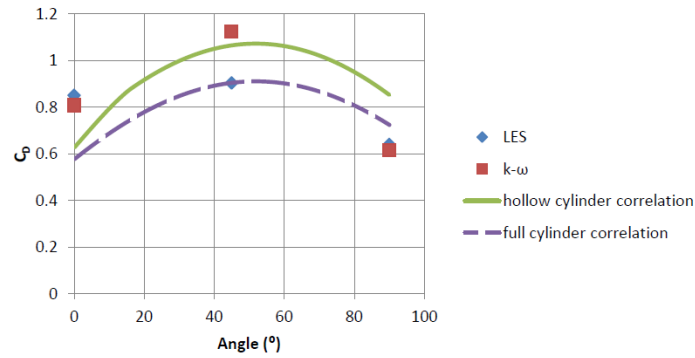


Figure 5.1: C_d against inclination angle for hollow and solid cylinder $Re = 10000$ [2]

$$S = S_{front} \cos \theta_{max} + S_{top} \sin \theta_{max} \quad (5.4)$$

$$\theta_{max} = \arccos \frac{D}{L} \quad (5.5)$$

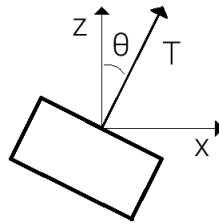


Figure 5.2: The pitch angle of the UAV

With an initial pitch guess of 30 degrees a pitch angle of 45 degrees was found and with a height of 115mm, an outer and inner diameter of 278mm and 188mm S was found to be 45900mm². This then results in a drag of 5.222N.

The total thrust can now be calculated using Pythagoras' theorem and the lift and drag as seen in Equation 5.6. And with the values for lift and drag calculated before to be 5.229N and 5.222N the total thrust is calculated to be 7.39N.

$$T_{total} = \sqrt{L^2 + D^2} \quad (5.6)$$

5.1.1 Duct Design

Now with the total thrust the thrust generated by the rotors and the thrust generated due to the effect of the duct can be calculated using Equations 5.7 and 5.8 [3], and the expansion ratio σ_d can be calculated with Equation 5.9 [4].

$$T_{rotor} = \frac{T_{total}}{2\sigma_d} \quad (5.7)$$

$$T_{duct} = T_{total} - T_{rotor} \quad (5.8)$$

$$\sigma_d = \left(1 + 2 \frac{L_d}{D_{inner}} \tan \frac{\theta_d}{2} \right)^2 \quad (5.9)$$

The variables in Equation 5.9 are the parameters of the duct of the UAV as depicted in Figure 5.3. As can be seen in Figure 5.3 L_d is the length of the diffuser and θ_d is the diffuser angle. It was found that with the recommended values of 10mm, 178m, and 10 degrees according to [4] this results in an expansion ratio of 1.02. This value

is so close to the value of a straight duct without diffuser, which is 1, that it was decided to use a straight duct only. This reduced the height of the UAV and thus the drag. From this a rotor thrust of $3.69N$ was found.

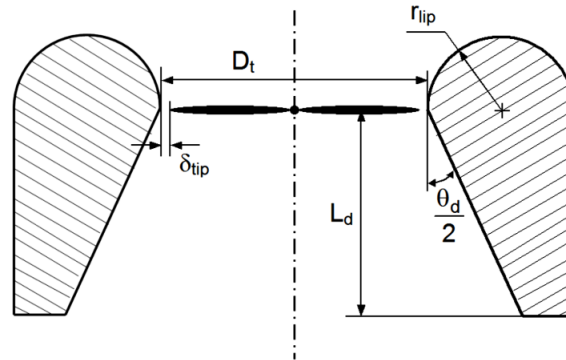


Figure 5.3: Duct design parameters [4]

5.1.2 Protective Fence

To calculate the effect of the protective fence on the thrust the pressure drop over the fence (ΔP) is calculated using Equations 5.10 and 5.11 [5] for the pressure loss coefficient.

$$\Delta P = \frac{1}{2} \rho_{air} F_m (v_i + V_v)^2 \quad (5.10)$$

$$F_m = \left(\frac{\sigma_{MO}}{\sigma_{KE}} \frac{7.125}{Re_{fence}} + \frac{0.88}{\log(Re_{fence} + 1.25)} + 0.055 \log Re_{fence} \right) \left(\frac{1 - a^2}{a^2} \right) \quad (5.11)$$

In Equation 5.10 v_i and V_v are the induced velocity and the vertical velocity component. The vertical velocity component only has a value when the UAV is trying to climb and the induced velocity has different values for the fence on the top of the UAV and on the bottom. The induced velocity for the upper fence is calculated using Equation 5.13 [3] where the ideal induced velocity v_h is calculated in Equation 5.14. The induced velocity of the lower fence is calculated using Equation 5.15 [3]. In Equation 5.11 σ_{MO} and σ_{KE} are the momentum and kinetic energy correction factors which are 1.333 and 2 respectively for a pipe form [6]. Re_{fence} is the Reynolds number specific for the fence. It is calculated using Equation 5.3 and replacing x with the diameter of the fence wire (d) and using $v_i + V_v$ for the airflow speed. a is the porosity of the fence and can be calculated using Equation 5.12 [6].

$$a = (1 - md)^2 \quad (5.12)$$

$$\frac{v_i}{v_h} = \frac{V_v}{2v_h} (\sigma_d - 2) + \sqrt{\left(\frac{\sigma_d V_v}{2v_h} \right)^2 + 1} \quad (5.13)$$

$$v_h = \sqrt{\frac{\sigma_d T_{total}}{\rho_{air} A_{prop}}} \quad (5.14)$$

$$v_i = \frac{\lambda}{\omega R} \quad (5.15)$$

As can be seen in Equation 5.12 the porosity is only dependent on d , the fence wire diameter of $4mm$ and m , the distance between each wire. For the 5 bar fence this distance is equal to a fifth of the circumference of the inner diameter or $118mm$. This results in a porosity of 0.998. In Equation 5.13 A_{prop} is the propeller sweep area. With a propeller diameter of $178mm$ this results in a propeller sweep area of $99500mm^2$. This results in an ideal induced velocity of $15.6 \frac{m}{s}$ and an induced velocity of $15.6 \frac{m}{s}$ for when the UAV is in forward flight or hover. Equation 5.15 is used to calculate the induced velocity below the lower rotor and as such uses the inflow ratio λ of the lower rotor which is calculated in Section 5.2. An average value of 0.36 for the inflow

ratio is used. ω is the radial velocity which is $1414 \frac{rad}{s}$ or $13500rpm$. With the propeller radius R of $89mm$ this results in an induced velocity of $45.4 \frac{m}{s}$ for the lower fence.

The Reynolds number for the fences was calculated to be 4000 and 13000 for the upper and lower fence. This resulted in pressure loss coefficients of 0.0011 and 0.0012 and pressure drops of $0.16Pa$ and $1.5Pa$

When ΔP is known the loss of thrust can be calculated using momentum theory as seen in Equation 5.16.

$$T_{loss} = \Delta P A_{inner} \quad (5.16)$$

Here A_{inner} is the sweep area of the inner diameter of the uav of $188mm$. This results in thrust losses of $0.004N$ and $0.04N$. These losses of thrust will be added to the rotor thrust calculated in Subsection 5.1.1 and the combination will later be compared to the rotor thrust as calculated using BEMT for coaxial rotors in the next section.

5.2 Coaxial Rotor Design

The thrust that the rotors provide were calculated using Equations 5.17 through 5.20 [3], where the subscripts u and l denote the upper and lower rotor of the coaxial design.

$$C_{T_u} = \frac{1}{2} \int_0^R \sigma_u C_l r^2 dr \quad (5.17)$$

$$C_{T_l} = \frac{1}{2} \int_0^R \sigma_l C_l r^2 dr \quad (5.18)$$

$$T_u = C_{T_u} \rho_{air} A (\omega R)^2 \quad (5.19)$$

$$T_l = C_{T_l} \rho_{air} A (\omega R)^2 \quad (5.20)$$

The blade solidity σ_u and σ_l are calculated in Equation 5.21 as a function of the radius r . C_l , the lift coefficient, can be calculated using a lift slope C_{l_α} of 0.117 and the angle of attack of the blades. Equation 5.22 [3] calculates the angle of attack and when plugging this into Equations 5.17 and 5.18 Equations 5.23 and 5.24 are found.

$$\sigma = \frac{N_b c r}{A} \quad (5.21)$$

$$\alpha = \theta - \frac{\lambda}{r} \quad (5.22)$$

$$C_{T_u} = \frac{1}{2} \int_0^R \sigma_u C_{l_\alpha} \left(\theta_u - \frac{\lambda_u}{r} \right) r^2 dr \quad (5.23)$$

$$C_{T_l} = \frac{1}{2} \int_0^R \sigma_l C_{l_\alpha} \left(\theta_l - \frac{\lambda_l}{r} \right) r^2 dr \quad (5.24)$$

In Equations 5.23 and 5.24 the 4 unknowns are the twist distributions as a function of radius θ_u and θ_l and the inflow ratios λ_u and λ_l . The twist distribution is a design value and how it is obtained will be explained in Subsection 5.4.2. The inflow ratios can be calculated in Equations 5.25 through 5.27 [3]. These ratios account for the effect of the upper rotor on the lower rotor in a coaxial design.

$$\lambda_u = \sqrt{\left(\frac{\sigma_u C_{l_\alpha}}{16F} - \frac{\lambda_\infty}{2} \right)^2 + \frac{\sigma_u C_{l_\alpha}}{8F} \theta_u r} - \left(\frac{\sigma_u C_{l_\alpha}}{16F} - \frac{\lambda_\infty}{2} \right) \quad (5.25)$$

$$\lambda_l = \sqrt{\left(\frac{\sigma_l C_{l_\alpha}}{16F} - \frac{\lambda_u}{2} \right)^2 + \frac{\sigma_l C_{l_\alpha}}{8F} \theta_l r} - \left(\frac{\sigma_l C_{l_\alpha}}{16F} - \frac{\lambda_\infty - (A/A_c)\lambda_u}{2} \right) \quad (5.26)$$

$$\lambda_l = \sqrt{\left(\frac{\sigma_l C_{l_\alpha}}{16F} - \frac{\lambda_u}{2} \right)^2 + \frac{\sigma_l C_{l_\alpha}}{8F} \theta_l r} - \left(\frac{\sigma_l C_{l_\alpha}}{16F} - \frac{\lambda_\infty}{2} \right) \quad (5.27)$$

Important to note is that Equations 5.26 and 5.27 are both used to calculate the inflow ratio of the lower rotor. This is because Equation 5.26 is used to calculate the inflow ratio when the lower rotor is in the wake of the upper rotor when $r < r_c$ where r_c is the radius of the blade inside the wake. This also means that A_c is the propeller sweep area inside the wake. Equation 5.27 calculates the inflow ratio for when $r > r_c$. F is the Prandtl tip loss factor calculated using Equations 5.28 and 5.29 [3]. λ_∞ is the inflow ratio of the free stream velocity located above the rotors. It is calculated in Equation 5.30 [3] which has been improved on using theory from Seddon[7] to also account for forward flight.

$$F = \frac{2}{\pi} \arccos e^{-f} \quad (5.28)$$

$$f = \frac{N_b}{2} \left(\frac{1-r}{\lambda} \right) \quad (5.29)$$

$$\lambda_\infty = \frac{V_v \cos \theta + V_h \sin \theta + v_i}{\omega R} \quad (5.30)$$

It can be seen from Equation 5.29 that the Prandtl tip loss factor is dependent on the inflow ratio that is calculated using the Prandtl tip loss factor. As such the calculations need to be iterated until convergence occurs. An initial value for F of 1 is set for the iterations. V_v and V_h are the vertical and horizontal velocity components of the airflow the UAV is in and v_i is the induced velocity.

As most calculations in this section require numerical methods due to iteration or complicated integrals an example calculation is shown in Appendix B.

5.3 Rotor Head Design

In this section the rotor head will be designed. First an overview is given on how the UAV will be controlled and secondly an explanation is given of how the propellers are designed.

5.3.1 Control System

To control the UAV a control system on the rotor blades is necessary. The UAV can be controlled by rotating the individual blades using a swashplate mechanism, of which a sketch can be seen in Figure 5.4. By tilting the swashplate the pitch of the blades will change, leading to a change in lift produced. So for example if the UAV has to fly forward the swashplate will be tilted such that the aft blades have an increase in pitch, hence producing more lift and thus inducing a forward moment.

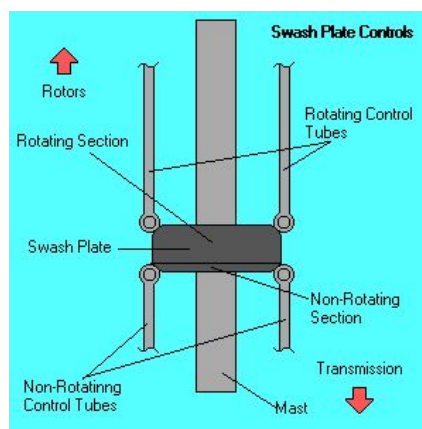


Figure 5.4: Sketch of a swashplate rotor head system²

For this project it was decided to design a new control system. The reason for this is that there are no off the shelf components which are so compact as needed for this system, mainly due to the height constraints.

²URL:<http://www.helicopterpage.com/images/swash.gif>

What also adds complexity is that a coaxial system is used, so it is not enough to just control one propeller; both need a variable pitch to control the UAV.

The designed control system can be described as follows. The whole structure is connected by three bars and a plate in the middle. In the middle of the system three servos are placed on the plate to control both swashplate systems. They are both linked to the same rods and will thus get exactly the same control inputs. Each propeller has its own engine placed underneath and above the the plate. Around this the swashplate mechanism is placed. In Figure 5.5 a rendering of the rotor head is found. The servos are not yet connected in this figure.

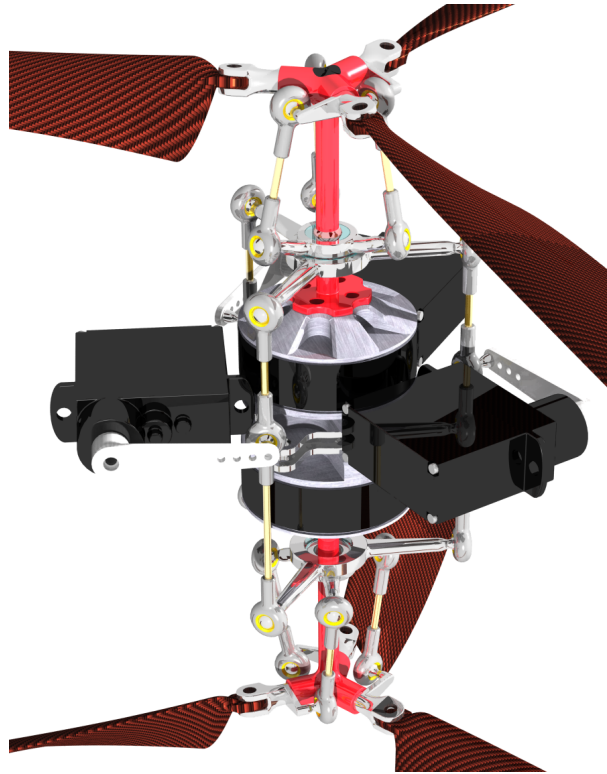


Figure 5.5: Rotor head of the Inspection Pocket Drone

Servo Selection

To select the proper servos for the control some properties have to be taken in to account. First of all the servos should of course be lightweight and as small as possible. Next, the modulation of the servo should be digital, should have metal or titanium gears to avoid slipping and increase reliability, should have a high speed to increase controllability of the UAV. By using these properties and making a selection online³, the Power HD DSM 44 Servo was selected. Details of this servo can be found in Table 5.1.

Table 5.1: Properties of the Power HD DSM 44 Servo ⁴

Properties	Value
Modulation	Digital
Torque	1.2 Kg/cm at 4.8 V
Speed	0.09 sec/60deg at 4.8 V
Weight	5.8 g
Dimensions	LxWxH: 22.0x8.7x22.0 mm
Motor type	Coreless
Gear type	Metal

³URL:www.servodatabase.com

⁴URL:<http://www.servodatabase.com/servo/power-hd/dsm-44>

5.4 Propeller Design

The propellers which are attached to the rotor head are designed in the following manner: First of all an airfoil is selected by making a trade-off between the airfoils stated in an experiment by NASA [8]. Then the propellers are sized using the calculations in Section 5.2 and also the twist is calculated. Finally a material is selected and the tip displacements of the propellers are calculated.

5.4.1 Airfoil Selection

For the airfoil selection an experiment of NASA is used: An Experimental Study of Dynamic Stall on Advanced Airfoil Sections [8]. In this experiment eight different airfoils, from which six are specially made for helicopter propellers, are tested. The eight airfoils can be found in Figure 5.6.

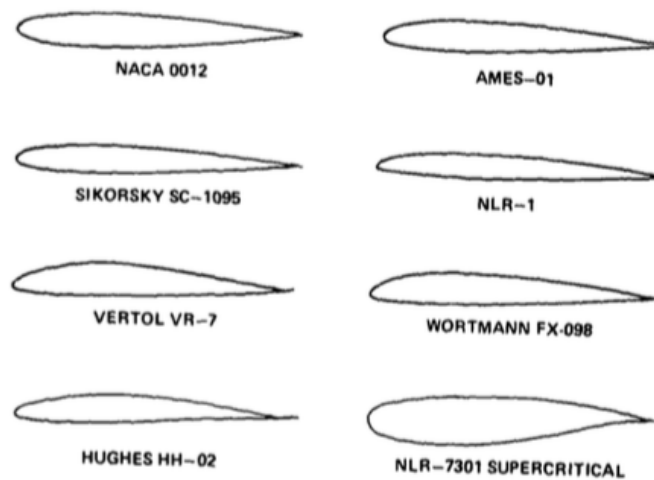


Figure 5.6: Eight airfoils from the experiment by NASA used for the airfoil trade-off [8]

From these airfoils a trade-off is done by looking at parameters that are relevant for the design. These parameters are the following: The lift curve slope C_{l_α} for high lift, the moment coefficient at zero angle of attack C_{m0} which has to be close to zero to reduce forces in the structure, a high maximum lift coefficient $C_{L_{max}}$ for obvious reason, a high stall angle of attack α_s , a high lift to drag ratio $(L/D)_{max}$ and finally a low value of the drag coefficient at zero angle of attack C_{d0} to reduce the drag forces and increase the efficiency of the propellers. [9]

The values of these parameters can be found in Table 5.2. For each parameter the airfoil with the best number is marked light grey and with the worst number is marked dark grey. Looking at the numbers it looks like the NLR-7301 super critical airfoil would be the best. However it was decided not to use this airfoil for three reasons. Firstly, the moment coefficient at zero angle of attack C_{m0} is very high, which will induce much unwanted force in to our system. Secondly, the airfoil has never been used on other helicopters, so it is not a proven design. And finally, it is stated in the technical report of the experiment that the measurement uncertainties are quite high due to the high camber. Therefore it is decided to go the Vertol VR-7 airfoil, which scored relatively good on all parameters.

Table 5.2: Trade-off table of the eight airfoils from the NASA experiment [8]

Data	C_{l_α}	C_{m0}	$C_{L_{max}}$	α_s	$(L/D)_{max}$	C_{d0}
NACA0012	0,109	-0,007	1,33	13,7	90	0,01
Ames A-01	0,111	-0,005	1,45	13,6	100	0,01
Wortmann FX-098	0,109	-0,026	1,43	13,1	94	0,01
Sikorsky SC-1095	0,110	-0,027	1,46	13,5	98	0,01
Hughes HH-02	0,114	-0,002	1,42	13,2	92	0,01
Vertol VR-7	0,117	-0,016	1,51	12,6	107	0,01
NLR-1	0,102	-0,025	1,29	12,4	87	0,01
NLR-7301 super critical	0,117	-0,083	1,83	17,2	89	0,01

5.4.2 Propeller Sizing & Twist Distribution

The main parameters for the propeller size are the chord length, the radius, and the cut-off radius. These 3 parameters are design values and are changed during the design phase in an iterative way until enough thrust is provided for the uav to fly. The twist distribution is calculated by first calculating the angle of relative velocity the propeller experiences over the entire radius of a propeller. This was plotted and a polynomial was placed over it. The order of the polynomial was changed iteratively until a sufficiently smooth and accurate function was found. It was decided to use a polynomial as the lower rotor has a large kink in the angle of relative velocity where the lower rotor transitions from the wake area to the non-wake area. This kink can't be used to select the twist distribution as it would be impossible to manufacture. Therefore smooth polynomials were used to generate rotors that can be manufactured. To generate the twist distribution the same polynomials were used and a flat angle of attack was added to the polynomial. This results in the twist distribution that is used for the propeller design. These twist distributions were checked for both full thrust and hover mode to have no negative lift or stall on the blades. In Figure 5.7 plots with the twist distribution, the angle of relative velocity and the angle of attack the blade experiences are shown for full thrust. In these plots the radius includes the cut-off radius.

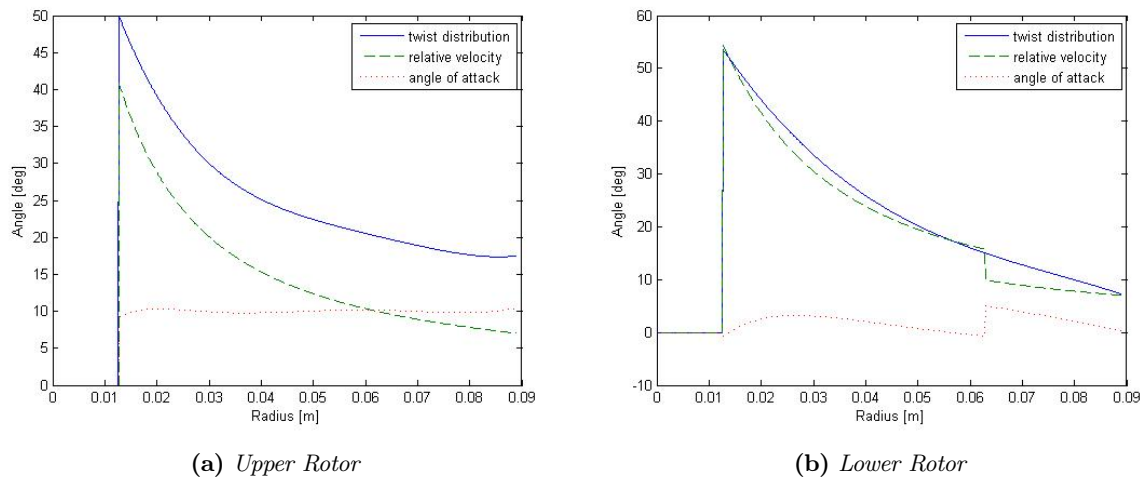


Figure 5.7: Twist distribution, angle of relative velocity, and angle of attack for the upper and lower rotor

5.4.3 Material Selection & Tip Displacement & Stress Calculations

First a material has to be selected for the blade before further calculations can be done on the tip displacement and stress. In Table 5.3 an overview of possible materials for the blades can be found. A good material for the blades has a low density to reduce the overall weight and has a high Young's Modulus (E) to reduce the tip deflection of the blades. By looking at the values in the table it is chosen to use Carbon Reinforced Polymers (CFRP) for the blades of the UAV. CFRP has a low density, absorbs vibrations well, has high strength and stiffness to cope with the loads, and reduces the tip deflection. Next to this CFRP is widely used in the radio controlled helicopter world and are proven to be the best blades on the market.

Table 5.3: Possible materials for the blades [10]

Material	Yield strength[MPa]	Tensile strength[MPa]	Young's modulus[GPa]	Density[kg/m ³]	Cost[€/kg]
Aluminium 1100	34	90	69	2710	2.45
Aluminium 6061	276	310	69	2700	7.55
Aluminium 356	164	228	72.4	2690	2.97
Polycarbonate	62.1	62.8	2.38	1200	9.35
PEEK	91	70.3	1.10	1310	80.00
E-glass fiber epoxy	-	40	12	2100	44.4
CFRP	-	503	65	1540	48.8
Torayca T300	-	76	135	1760	115.4
Torayca M40J	-	53	230	1770	N/A

With the Young's modulus of CFRP the tip displacement of the propellers can be calculated. This is done with standard standard beam bending theory. Equation 5.31 is the equation for the tip displacement.

$$\delta_{tip} = \frac{1}{E} \cdot \frac{M}{I} \quad (5.31)$$

Where E is the Young's modulus of the material, M is the moment of the blade and I is the moment of inertia. The moment is calculated in a numerical way by summing the moments of each element on the blade with Equation 5.32

$$M(i) = M(i-1) + dL(i) \cdot dr(i) \quad (5.32)$$

This equation is run from the tip of the blade to the root. Where $M(i-1)$ is the moment of the previous part, dL is the sectional lift and dr is the arm from the tip.

The moment of inertia of the airfoil is found by using Equations 5.33, 5.34 and 5.35.⁵

$$A = \int_0^c [Z_u - Z_l] dx \quad (5.33)$$

$$\bar{z} = \frac{1}{A} \int_0^c \frac{1}{2} [Z_u^2 - Z_l^2] dx \quad (5.34)$$

$$I = \int_0^c \frac{1}{3} [(Z_u - \bar{z})^3 - (Z_l - \bar{z})^3] dx \quad (5.35)$$

Having the airfoil data points of the Vertol VR-7⁶ and the rotation matrix in Equation 5.36, in which θ is the angle of twist, the inertia can be calculated for each section. With the inertia for each section the tip deflection can now easily be calculated.

$$\begin{bmatrix} \cos(\theta(i)) & -\sin(\theta(i)) \\ \sin(\theta(i)) & \cos(\theta(i)) \end{bmatrix} \quad (5.36)$$

It was found that the tip deflection at the end of the upper blade was 0.33 mm and for the lower blade 0.28 mm. These are small values, but the rotor blades are very stiff due to the use of CFRP, the forces are small and the rotor blades are short.

Finally the stresses at the root of the blade due to the centrifugal force and lift force will be calculated. For each blade the tensile force due to the rotation of the blades can be calculated with Equation 5.37.

$$F_{rot} = M_{blade} \omega R \quad (5.37)$$

Where ω is the rotation in radians per second, M_{blade} the moment at the root and R the radius of the blade. The stress can now be calculated with Equation 5.38, where A is the area of the point attaching the airfoil to the rotor head.

$$\sigma_{tens} = F_{rot} / A \quad (5.38)$$

Using an attachment area of only 1 mm^2 , which is the production limit, it is found that the tensile stress is 283.2 MPa for both blades. This is well below the tensile strength of CFRP of 501 MPa.

Not only tensile stresses act on the blade, but also bending stresses due to the lift generated. These stresses are calculated using the moment on the blade M, the distance to the neutral line y and the moment of inertia I at the root as seen in Equation 5.39.

$$\sigma_{bending} = \frac{My}{I} \quad (5.39)$$

⁵URL:<http://ocw.mit.edu/courses/aeronautics-and-astronautics/16-01-unified-engineering-i-ii-iii-iv-fall-2005-spring-2006/systems-labs-06/sp110b.pdf>

⁶URL:<http://airfoiltools.com/airfoil/details?airfoil=vr7-il>

To calculate the actual stresses the area and moment of inertia of the attachment part are needed. This part is designed by looking at the production possibilities and stresses that would occur. The final design including sizing can be found in Figure 5.8. Using the values depicted in this figure a tensile stress at the root is found of 70.8 MPa for both the upper and lower blade. These stress is well below the tensile strenght of CFRP, which is 501 MPa. For the bending stress of the upper blade a stress of 14.7 MPa is found and for the lower blade a stress of 10.7 MPa, both well below the Young's Modulus of CFRP, 65 GPa.

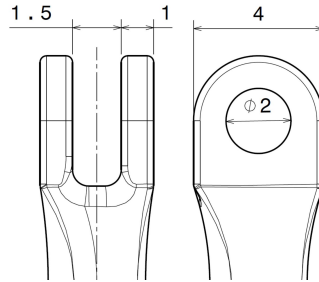


Figure 5.8: Sketch of the blade holder. Values are in mm

5.5 Power Calculations

The power required to fly can be calculated using the Figure of Merit (FM) and the ideal power. A FM of 0.588 is calculated using Equation 5.40 [3].

$$FM = \frac{C_T^{\frac{3}{2}}}{\sqrt{2} \left(k_{int} k \frac{C_T^{\frac{3}{2}}}{\sqrt{2}} + \frac{\sigma C_{d_0}}{8} \right)} \quad (5.40)$$

Where C_T is the thrust coefficient of the total thrust calculated in Equation 5.41 [3], k_{int} is the interference power factor with a value of 1.219 [3], k is the ideal power correction factor with a value of 1.15 [3], σ the blade solidity for 1 rotor calculated using Equation 5.42 and C_{d_0} the rotor drag coefficient which may be assumed to be 0.01 [3].

$$C_T = \frac{T_{total}}{\rho_{air} A_{prop} (\omega R)^2} \quad (5.41)$$

$$\sigma = \frac{N_b c R}{A_{prop}} \quad (5.42)$$

In Equations 5.41 and 5.42 A_{prop} is the propeller sweep area, R is the propeller radius, c is the mean propeller chord, N_b is the number of propeller blades in the rotor and ω is the radial velocity. Using a radius of 89mm this results in a propeller sweep area of $24.8 \cdot 10^3 \text{ mm}^2$, with a mean propeller chord of 15mm, 3 propeller blades and a radial velocity of $1414 \frac{\text{rad}}{\text{s}}$ results in a σ of 0.161 and a C_T of 0.015. This results in a FM of 0.588.

The ideal power (P_{ideal}) can be calculated using Equation 5.43 [3]. When dividing the ideal power by the FM the actual required power for flight can be found. Thus using the previous calculated values an ideal power of 57.6W is found and this results in the actual required power of 97.9W.

$$P_{ideal} = \frac{T_{total}^{\frac{3}{2}}}{\sqrt{4\sigma d \rho_{air} A_{prop}}} \quad (5.43)$$

This chapter has dealt with all aspects of the propulsion system. The calculations to determine the thrust delivered by the ducted rotors are explained and the Vertol VR-7 airfoil has been chosen for the rotors. A twist distribution has been made as well as a material choice, which is CFRP. Lastly the required power that must be put into the system is calculated.

6 | Subsystem Design: Electronics

A large part of the performance and reliability of the UAV system depends on the configuration of the electronic components and software inside the drone. This chapter discusses the hardware and software architecture of the payload, on board computer and communication elements included in the UAV design.

6.1 Payload

The payload section of the UAV includes all components related to generating the required data needed to successfully perform the mission.

6.1.1 Payload Requirements

Considering the payload, the initial primary requirement was that the system should be capable of providing visual data to the operator. This can be in form of still images or video. Besides that, the UAV should be able to determine its attitude and relative position to its surroundings in order for the control system to keep the UAV stable and easy and safe to operate. Secondary requirements include functionality to record sound and video, determine temperature of the UAV surroundings and detect dangerous gas concentrations. The state determination of the UAV should be possible to be performed in zero lighting conditions (0 cd/m^2).

Because the UAV will for a large part of the mission operate outside the line-of-sight with the operator, the choice is made to add first-person view (FPV) functionality to the UAV. First-person View functionality means that the UAV is controlled from an on-board perspective by means of an on-board camera with a direct video link to the ground station. This will enable the user to fly and manoeuvre the system without requiring full autonomous behaviour and navigation, which is complicated, costly and requires a large amount of on-board processing power. Including a video feed with downlink to the GCS however adds further requirements to the on board computer and communication hardware. The video and image quality as received by the ground station should be sufficient to recognize persons.

Regarding likely operational environments for the UAV, it is possible that there will be significant presence of smoke and dust particles in the air. This makes several types of payload devices less suitable for use in the system.

6.1.2 General Considerations with respect to Payload

There are several payload configurations that offer the functionality needed to comply with these requirements. Besides making the straightforward choice of using separate video for FPV flight and ranging sensor data for automatically avoiding collisions with objects, it is as well possible to use computer vision techniques like stereo vision or RGB-D vision by means of an IR laser, IR camera and a regular camera to create a detailed three dimensional rendering of the UAV surroundings. By using computer vision algorithms, the UAV can be designed to react to its surroundings in a more efficient and smooth manner. [11][12]

Regarding the choice of payload elements, it is of main importance to include the architecture that fulfills the technical requirements in the most efficient manner, together with ease of development and related costs of the integrated system. The following sections discusses the process of choice of all payload elements and their respective properties.

Camera modules

The on-board camera is the most essential payload hardware component in the UAV as it enables the operator to fly the device as soon as the direct line-of-sight is obstructed. Furthermore, the camera is needed to perform the recognition mission for people based on a live video feed and have the ability to make stills of the environment,

preferably with a high resolution ($> 3\text{MP}$) in order to fulfil the secondary requirements. The camera should, according to Section 2.3, have a minimum view angle of 80 degrees and the video feed should have a minimum frame rate of 24fps and be able to operate in minimum lighting conditions of $5\text{cd}/\text{m}^2$.

Based on the requirement to have a minimum resolution needed to be able to recognize persons from the video feed at a distance of 5 meters from the camera, a test is performed to determine what video resolution is sufficient. Combined with the maximum communication data link budget, as described in Section 6.4.6, the usable resolution is limited to 576×324 pixels. As can be seen in Figure 6.1, this resolution is sufficient to fulfill the requirement.



Figure 6.1: A person at a distance of 5 meters from the camera with 576×324 pixel resolution

In order to make FPV flight by means of a direct video link possible, the camera should be compatible with the desired way of data compression and communication link budget restrictions as described in Section 6.4.

The image can be compressed by a factor 40 to a medium quality JPEG using the on-board computer (OBC).¹

There is a wide range of small cameras available for these purposes, however, special attention is directed towards the compatibility with the OBC hardware and functionality.

The eCam56 Gumstix Overo 5MP camera is chosen to be included in the payload configuration. It is a plug-and-play device working with all Gumstix Overo COM's. The camera board is built around an OmniVision OV5640 image sensor[13]. Using a 27-pin ISP OMAP connection, it can directly be connected to the Texas Instruments OMAP processor series on the Overo board for quick processing.

Table 6.1 provides an overview of the eCam56 5MP camera properties.²

Table 6.1: eCam56 5MP Gumstix Overo camera properties

Max. Image Transfer Rate	VGA - 30fps HD(720p)-30fps 5MP - 7fps
View Angle	70 deg
Focus Type	Auto Focus
Module Dimensions (mm)	15 x 58 x 6.75
Connection	27-pin ISP OMAP
Supply Voltage	3.7V
S/W Driver	Linux V4L2 camera driver

Inertial Measurement Unit (IMU)

In order for the UAV to determine the attitude and acceleration of the system in all three axes of motion, an Inertial Measurement Unit (IMU) needs to be included as part of the hardware configuration. The IMU is needed for autonomous stabilisation and sends measurements of the acceleration and orientation of the UAV for

¹URL:http://www.ou.edu/class/digitalmedia/articles/CompressionMethods_Gif_Jpeg_PNG.html

²URL:<http://www.e-consystems.com/5MP-Gumstix-Camera.asp>

all three axes back to the central processing unit which determines the UAV's attitude and, by means of feedback control, sends the right outputs to the servos and electronic speed controllers. Especially in unstable aircraft, an IMU combined with feedback control is essential in order for the pilot to be able to operate the aircraft or UAV.

In case of the NavStik flight controller, the IMU is part of the hardware and discussed in further detail in Section 6.2.

Ranging Sensors

With respect to ranging devices and sensors, sonar is often used in robotics as a basic but robust way to accurately measure distances to objects. Other options for generating ranging data include lidar, infrared laser ranging hardware or using a dual vision camera setup with on board image processing. Lidar is a very accurate and omni-directional but costly, heavy, and power intensive way to measure distances to the UAV surroundings. Furthermore, both systems behave inaccurately in reduced visibility conditions as with the presence of smoke and dust particles in the air. Therefore, sonar sensors are chosen to be included in the design as they have a sufficient reliability in environments with smoke attenuation.[14]

As multiple ultrasonic ranging sensors are used on one vehicle for continuous distance measurements they may interfere with each other which largely reduces the accuracy of the distance readings. This can for instance occur if one of the sensors transmits a signal while another sensor is in receiving mode and reads a reflected signal from the other sensor. Occurrence of this problem is indicated by noise in the voltage readings at regular intervals.

If the sensors are not synchronized and wired to operate at continuous measurement speeds, eventually due to small differences in operating speeds they will diverge from their synchronous behaviour. There are ways of ensuring interference free operation by controlling the sensors to send signals simultaneously or in sequence. The simultaneous sensing is preferred as this increases the maximum achievable sensing rate per sensor.

The choice is made to work with Maxbotix EZ sonar ranging sensors able to determine distances to objects from $20cm$ up to $210cm$ with an accuracy of $1cm$, operating at a voltage of $3.3V$. These sensors provide a low power and lightweight solution.[15] The sensors are connected to the IvyPro interface board of the Navstik flight controller by means of one I2C connection. All six sonar sensors can be connected to the same I2C port on the interface board as indicated in Figure 6.2.

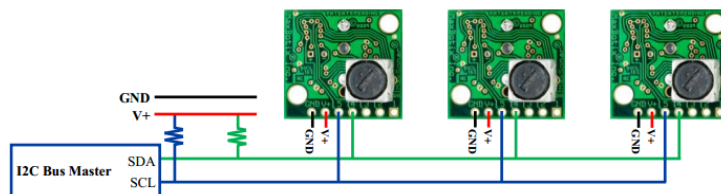


Figure 6.2: Connection illustration of sonar sensors³

The MaxBotix sonar sensors have a reading rate of up to $40Hz$, or every $25ms$. Having a maximum range up to $210cm$ means that the maximum time it takes for a signal to bounce off objects and can be received by the sensor is $6.2ms$. Therefore, it is safe to assume that synchronized sensing with all six sensors at $40Hz$ will cause no interference during operation.

Temperature sensors and thermal camera modules

For measuring the temperature of the UAV surroundings, both directional and non-directional options can be chosen. Basic temperature sensors exist for many purposes and in many types. Besides a basic local temperature measurement, it is also an option to use an IR camera to create a much more detailed temperature reading of the environment. As nowadays very compact and lightweight thermal cameras are available it will be possible to incorporate this element into the UAV payload architecture and assess the surroundings during the course of the mission in greater detail. Measuring temperature belongs to the secondary requirements regarding the mission.

³URL:http://www.maxbotix.com/documents/I2CXL-MaxSonar-EZ_Datasheet.pdf

A thermal camera enables the operator to still recognize persons in case of reduced visibility conditions such as smoke or low lighting in which the normal camera will not provide sufficient contrast or image quality to perform the inspection mission.

A thermal camera for this mission needs to meet various stringent constraints. The wavelength used shall be suitable to detect the temperature ranges for this application, sufficient to tell a person apart from its surroundings, and when possible also higher temperatures to aid in detecting fire hotspots. Furthermore the signal power shall not be attenuated too much by smoke particles. Finally, the module should have a low mass to fit in the mass budget. These constraints call for a camera using long-wave infrared (LWIR) technology: this is the correct wavelength to see the required temperature differences and does not require cooling (unlike for instance short and medium wave infrared) reducing size and mass of the component. Also, LWIR does not suffer from attenuation by smoke, not even over hundreds of meters.⁴

In the current state of the art, there was just one component suitable for this particular mission, which is the FLIR Lepton module. It has a resolution of 80 x 60 px, sufficient to recognize persons, and the camera and breakout board together have a mass of 6 grams. The choice was made for the shuttered edition, as this eases temperature readings: the shutter (which is at ambient temperature which is known from another sensor) provides a reference to calibrate the temperature readings on-the-fly, significantly reducing (but not abolishing) absolute temperature error⁵. Using programmatic tools this camera can be used to display both differential and absolute temperature data. For instance, the lowest and highest temperature could be displayed on a scale, and temperatures can be seen using false colors in between these temperatures.

GPS receivers

GPS receivers become standard equipment in UAVs for mission planning and execution. Most GPS receivers are very small in size but powerful enough to provide accurate position readings within a range of several meters. For the inside part of the mission, GPS might not be necessary but it will still provide a large functionality enhancement while flying outside and makes it possible to let the UAV navigate itself by means of waypoints. NavStik recommends using the MAX-6Q GPS receiver from uBlox which offers a 5Hz navigation update rate and a horizontal position accuracy of 2.5 meters (CEP, 50%, 24 hours static, -130dBm).[16] This is a lightweight solution that is integrated on the NavStik main board. A GPS antenna patch can be connected through the micro-coax connector to the NavStik main board. The uBlox module will be used in combination with the Sangshin 1580MHz RF 18mm Antenna patch.

Microphone and speaker hardware

In order to communicate with people in the direct environment of the UAV during the mission, or to get a better understanding of the UAV surroundings, sending and receiving sound can be added to the UAV system. However, because of the noise and vibrations created by the propulsion system, especially the rotors, obtaining a clear sound from a microphone is expected to be not feasible in this design stage as testing is required for further development.

Other components and peripherals

Other components which can be added to the system include a gas detector and a window-breaking mechanism in the form of a spring-loaded point impact device which are not further assessed in this development stage due to the expected large weight increase and time constraints. Four white high brightness LED lights are included in the design to be mounted near the camera for operation in low lighting conditions. Furthermore, two blinking LED's are incorporated on the sides of the drone for awareness and a red and green OBC status LED are mounted near the on/off switch.

The further combination of components in the payload configuration is discussed in Section 6.3

⁴URL: <http://www.mut-group.com/fire-detection/lwir-key-features.html>

⁵URL:http://www.flir.com/uploadedFiles/CSV_Americas/Cores_and_Components_NEW/Products/Uncooled_Cores/Lepton/FLIR-Lepton-DataBrief.pdf

6.2 On Board Computer

The on board computer hardware functions as the central 'brain' of the UAV. It performs processing of the data coming from the sensors, accelerometers, gyroscopes and payload devices. Furthermore, it interprets and processes all user input signals coming from the ground station and sends back the required data like video, attitude and system status. The on board computer is also responsible for providing the control feedback based on the IMU data to the motors and rotor actuators. The inclusion of needed additional processing units in the OBC hardware architecture is discussed as well.

6.2.1 OBC hardware requirements

Regarding the requirements for the entire UAV, it is of high importance that the OBC system is lightweight and has a low power consumption while providing sufficient computational power and speed.

To make implementation and future use of the chosen OBC system efficient, the hardware should also provide a suitable development platform for the internal software and be compatible with all attached hardware components. In case higher levels of in-flight autonomy are needed, increasing the level of required computing power, the OBC architecture should allow the expansion of the system and addition of functionality without the need for a redesign of the complete hardware setup. Therefore it is preferred to make use of off-the-shelf components as it largely decreases development time and costs and have proven their reliability and performance.

To comply with the requirements, the UAV should be able to determine its attitude and provide directional, longitudinal and lateral stability combined with autonomous position hold in case no user inputs are received. This is needed to provide the end user with an easy and safe to operate system.

For implementation of these requirements, essential hardware components include at least 3-axis accelerometer, a 3-axis gyroscope and sufficient connectivity options for the described ranging sensors as well as a sufficient number of PWM outputs for the rotor actuator servos and electronic speed controllers as described in this section. This needs to be combined with enough processing power to execute the needed stabilization and flight algorithms and handle the data stream coming from the on-board camera, as described in Section 6.1.

6.2.2 Hardware platforms and possible configurations

Various platforms can be used as a basis for the on board computer hardware setup of the UAV. Several of these platforms are widely used in the field of robotics and suitable for application in UAVs. The following platforms are considered for use in the UAV system:

Paparazzi

Paparazzi is a system of open source hardware and software designed for use with many types of unmanned aerial systems like fixed-wing craft, helicopters and multicopters.⁶ There is a range of available Paparazzi compatible hardware components and various options of adding additional sensors and functionality. Because of the open-source character of the platform, the Paparazzi software can be tailored and expanded according to the needs of the user. It is based on Linux architecture and has modules for both the ground control station as the airborne segment of the UAV system.

Considering hardware, the Paparazzi environment includes several very small and lightweight autopilot boards and sensor equipment.⁷ The TU Delft MAVLab is an active contributor to the Paparazzi user community and implements the Paparazzi architecture successfully in their projects.[17]

The Paparazzi Lisa/M v.2 is, besides the Lisa/S flight controller, one of the lightest available autopilot systems in the Paparazzi range of hardware options. It has an on-board 3-axis IMU and 3-axis magnetometer, barometer and does not require an interface board for connection with PWM devices or other interface options.

Other Paparazzi compatible flight controller hardware includes the NavStik, which is a very small and lightweight board with a very modular architecture and various on-board sensors. It can be combined with one out of three

⁶URL:<http://wiki.paparazziuav.org>

⁷URL:<http://wiki.paparazziuav.org/wiki/Autopilots>

different interface boards to connect the flight controller to sensors and external processing units.⁸ Compared to other available Paparazzi flight controllers, NavStik is one of the more powerful and modular options within the Paparazzi spectrum with built-in connectivity to COM devices from Gumstix.

Intel Edison and Arduino

The Intel Edison is a small and powerful processing board recently developed by Intel for quick prototyping of connected and "smart" devices.⁹ The board can be combined with many integrated development environments like Arduino. The Arduino hardware consists of a series of microcontroller boards with a very versatile range of IO options. Arduino offers a range of off-the-shelf boards and compatibility with a range of additional sensors, components and other platforms.[18] [19]

One of the features of the Intel Edison platform is the large amount of computational power, with a dual-core CPU, a single core microcontroller and on-board data storage based on a Linux environment. However, one needs an expansion board to use the Intel Edison on any type of application. It is fully compatible with the Arduino platform to create sufficient IO functionality to connect all sensors, servos, ESCs and cameras used in the UAV. Upsides of this configuration are the high level of modularity of both the choice of expansion boards as well as the processors used in the Edison board itself. The Intel Edison runs Linux and supports C/C++, Python, Node.js and Javascript for software and application development.

Raspberry Pi and Arduino

The Raspberry Pi is a small, versatile and powerful computer module with flexible functionality. It can be combined with for instance Arduino hardware or other expansion boards. A Raspberry Pi is designed to function as a stand alone PC which makes the Raspberry Pi boards relatively heavy and bulky, especially if more IO functionality is needed.¹⁰ As the Raspberry Pi is a fully functional computer, it contains a lot of processing power. However, to apply it in the UAV system, the standard IO functionality is not sufficient and should be expanded using for instance an Arduino board, for which a different hardware interface is required. Besides that, the Raspberry Pi contains many functions and hardware options that are not needed for the functionality of the UAV.

Other platforms and options

There are many autopilot systems available on the market that deliver good hardware and functionality. Examples are OpenPilot¹¹ with the CC3D board, PixHawk and APM2 from 3D Robotics¹² and ArduPilot¹³ which is based on the Arduino platform. However, all these systems have a closed development environment and limited compatibility with other platforms or require inefficient expansion boards. Therefore, these systems are not considered to be feasible options throughout the further design process.

Next to the available off-the-shelf solutions, another option is to develop custom hardware specific for the desired use in the UAV system. However, developing such hardware and software combinations requires a substantial amount of time and development costs which is why this is not further considered and included in the design process.

6.2.3 OBC Hardware selection and Trade-Off

The selection of the on board computer hardware is based on the following criteria:

1. Weight of the initial setup
2. Dimension of initial setup
3. Computational power

⁸URL:<http://wiki.navstik.org/doku.php>

⁹URL:<http://www.intel.nl/content/www/nl/nl/do-it-yourself/edison.html>

¹⁰URL:<https://www.raspberrypi.org/products/raspberry-pi-2-model-b/>

¹¹URL:<https://www.openpilot.org/>

¹²URL:https://store.3drobotics.com/products/3dr-pixhawk?taxon_id=34

¹³URL:<http://ardupilot.com/>

4. Usability and development costs
5. Availability of existing S/W and H/W interface options
6. Modularity and expansion flexibility

Table 6.2 shows the compliance of the four platform incorporated in the trade-off with the above mentioned criteria.

Table 6.2: Compliance with trade-off criteria of four considered platforms

	Intel Edison + Arduino	Paparazzi Lisa/M v.2	Paparazzi Navstik	Raspberry Pi + Arduino
Weight est. of minimal setup (g)	≈ 50	11	13	≈ 75
Dimensions of main board (mm)	35.3 x 25 x 3.9	34 x 60 x 10	18 x 59 x 4	85 x 56 x 15
CPU clock speed	500MHz + 100MHz	72MHz	168MHz	1GHz
Cores	2 + 1	1	1	4 + graphics core
Usability and development costs	+-	+	+	+-
Availability of existing S/W and H/W interface options	++	-	+	++
Modularity and expansion flexibility	+	+-	+	+

Considering weight of the initial setup, both the Intel Edison as well as the Raspberry Pi setup have a very high weight. This is as well due to the fact that sensors and the inertial measurement unit are not included on the main hardware board. The Paparazzi hardware components are very lightweight as their design is focused on use in UAVs.

The same is true looking at the dimensions of the minimal required setup. This means that the Raspberry Pi, combined with an Arduino interface will be too large for use in the UAV.

Regarding the usability and software development costs, the Paparazzi framework is favoured because of the open-source character of the platform. Various modules are readily available and can be extended according to the system needs. This results in lower development costs than when for instance the Intel Edison platform is used, for which the software for both the ground station and airborne segment needs to be developed from the ground up.

Advantages of the Intel Edison and Raspberry Pi setups are the large amount of internal computational power, allowing for more advanced on-board data processing and broadening the range of applicable sensor and computer vision modules. Both paparazzi boards need additional processing power, for instance by incorporating a COM like the Gumstix Overo in the setup. The Navstik has an integrated interface for this, while the Lisa/M does not have such an option.

Both platforms which are compatible with Arduino have access to a large range of IO options and available sensor modules. The Paparazzi platform does allow access to a broad range of hardware options as well, however limited compared to the Arduino platform. The Navstik board allows for more expansion options and modularity.

Based on the described characteristics, the choice is made to work with the Paparazzi based NavStik hardware and the IvyPro breakout board. This provides the best balance between having a very compact hardware layout combined with sufficient modularity and interface options to equip the UAV system with the needed functionality and keep options open for further expansion of the system.

6.2.4 OBC hardware

This section discusses the further properties of all OBC hardware components and interaction with other systems.

NavStik and IvyPro interface board

Based on the Paparazzi platform, NavStik is a micro navigation and control board. In a highly modular format, it delivers a very lightweight solution tailored for use in UAVs and providing access to a rich variety of sensors

and interfaces with other components. The basic hardware consists of a main board and an interface board, needed for making the NavStik interfaces accessible for the user and connecting sensors, PWM devices like servos and ESCs and a transmitter/receiver connection.

The main board includes an InvenSense MPU-6050 IMU (3-axis accelerometer and 3-axis gyroscope)[20], together with a Honeywell HMC5883L 3-axis magnetometer, a Bosch BMP180 barometer, hardware temperature sensor and micro-coax GPS connector and differential pressure sensor. The main board is equipped with a 32-bit, 168MHz Cortex-M4 microcontroller. The interface board, in this case the IvyPro, also features UART, I2C micro USB ports for interfaces and debugging. A Micro-SD card slot is included for on-board data storage. The NavStik main board has an interface for Gumstix Overo COM's to include additional computational power for image and sensor data processing.

Table 6.3 gives an overview of all hardware specifications of the NavStik flight controller¹⁴ and Table 6.4 provides an overview of all specifications and connectivity options if the IvyPro interface board.¹⁵

Table 6.3: *NavStik flight controller board specifications*

NavStik Main board	
Processor	Cortex-M4
Base clock speed	168MHz
Memory	16MB SPI Flash
On-Board Sensors	InvenSense MPU-6050 3-axis gyroscope and 3-axis accelerometer
	3-axis Honeywell HMC5883L magnetometer
	Bosch BMP180 static pressure sensor
	Temperature sensor
Connectivity	GPS antenna connector
	Gumstix Overo interface

Table 6.4: *IvyPro interface board specifications*

IvyPro Interface board	
Connectivity	6+6 PWM Channels
	Micro-SD Card Support
	TelemetryPort (UART)
	Spektrum Port (UART)
	2 USB port and an UART port for Gumstix Overo
Other	Current Measurement
	Battery Voltage Monitor
	ESD and Short-Circuit Protection
Weight	8.6g
Size	41mm x 35mm
Input Voltage	4.5V ~ 14.0V

Gumstix Overo Earthstorm COM and expansion board

Gumstix is a manufacturer of Computer-On-Module (COM) hardware. The Gumstix Overo series are very small, lightweight but high-performance COM modules.

To ensure the required functionality of a video downlink to the ground station, on-board video data compression is needed to stay within the available bandwidth of the transmitter/receiver connection. As image processing requires a substantial amount of processing power, the NavStik module and interface board performance is insufficient to perform this task. Including the Gumstix Overo Earthstorm model in the hardware configuration, the 1GHz Cortex-A8 processor can be used.

The Gumstix Overo Earthstorm has a single core ARM Cortex-A8 processor with a base clock speed of 800MHz, 512MB of RAM and a Micro SD card slot for storage expansion. There is a designated OMAP ISP interface for connection with a camera. The Gumstix hardware runs Linux and is fully compatible with the NavStik

¹⁴URL:http://wiki.navstik.org/doku.php?id=hw:main_board

¹⁵URL:<http://wiki.navstik.org/doku.php?id=hw:ivypro>

hardware through a high speed USB interface. The weight of the Gumstix module is 5.6 grams which is very favourable for the UAV system.[21]

In order to access all needed interfaces from the Gumstix Overo, an expansion board is needed which includes connectors for the thermal camera and transceiver unit. The Gumstix Summit board will provide this functionality and is used in the system. It is connected to the Gumstix Overo using the 70 pins connector.¹⁶

Table 6.5 provides an overview of all hardware specifications and connectivity options of both the Gumstix Overo Earthstorm and the Gumstix Summit expansion board.

Table 6.5: *Gumstix Overo Earthstorm and Gumstix Summit specifications*

Gumstix Overo Earthstorm		Gumstix Summit expansion	
Processor	ARM Cortex A8	Connectivity	2x UART
Base clock speed	800MHz		2x SPI
Max clock speed	1GHz		Stereo audio in/out
Memory	512MB RAM		3 to 6 pins GPIO
			1x I2C
Connectivity			2x PWM
Camera	OMAP ISP		
Storage	Micro SD slot	Weight	17 g
V input	3.3 - 4.2 V		
Weight	5.6 g		
Operating temp (C)	0 C - 85 C		

6.3 Payload and OBC hardware configuration

Over the course of the design process, several hardware configurations were established and evaluated based on compliance with the primary and secondary requirements. An overview of these configurations is stated in this section.

6.3.1 Hardware configuration for first design iteration

For the initial design, it is first of all important to fulfill all primary requirements related to the payload configuration. The most efficient way to do this is by including only a camera capable of taking video footage with the desired resolution and create a video downlink to the GCS. In this way the camera enables FPV flight and provides the operator with an indication of the relative distance to objects and surroundings. Table 6.6 provides an overview of all payload and OBC components as used in the first design iteration and their respective properties.

Table 6.6: *First hardware configuration for payload and OBC*

Component name	Number of units	Weight [g]	Total Weight [g]	Dimensions [mm]			Supply Voltage [V]	Current draw [A]	Total Power consumption [W]
				W	L	H			
NavStik Main Board	1	4	4	18	59	4	3,7	0,15	0,2
IvyPro interface board	1	8,9	8,9	35	41	8	4,5 - 14	0,05	0
Gumstix Overo Earthstorm	1	5,6	5,6	17	58	4,5	3,7	0,4	1,48
Gumstix Summit expansion board	1	17	17	39	80	6	3,7	-	-
e-CAM56_37x module	1	10	10	15	58	6,75	3,7	0,14	0,518
On/Off switch	1	3	3	5	10	8	-	-	-
High brightness LED	4	0,1	0,4	5,4	3	0,9	3	0,2	0,6
LED L-36BSRD-B Flashing	2	0,5	1	3	5	3	3	0,05	0,3
Status LED's (red+green)	2	0,4	0,8	3	5	3	3	0,05	0,15
Total			50,7						3,2

It is chosen to work with the E-con systems 5MP (eCam56) camera which is directly compatible with the Gumstix Overo COM's by means of a 27 pin connector. This direct link between the camera and the COM

¹⁶URL:<https://store.gumstix.com/expansion/overo-expansion/summit.html>

enables faster data transfer and reduces latency throughout the video connection. Compression of the video data is performed directly on the Gumstix Overo board.

The high brightness LEDs are included to ensure that the camera can be operated in very low lighting conditions.

6.3.2 Hardware configuration for second design iteration

For the second design, after one iteration, attention is paid to fulfilling secondary requirements as well. In order to determine the absolute position to the UAV surroundings, sonar sensors are chosen to be included in the design. Sonar ranging sensors are applied at four places on the UAV; One pointing in flight direction to the front, two pointing to the left and right respectively and one pointing downwards.

The camera as described in the first design configuration is kept the same. A GPS receiver antenna patch is included in the design to enable more exact positioning and broaden the scope of applications of the UAV. The used GPS receiver is the uBlox MAX-6Q module as recommended by NavStik.

Furthermore, the FLIR Lepton thermal camera module and corresponding breakout board are included in the configuration as a way to better assess the UAV environment during the mission and detect persons and fire hotspots in low visibility conditions. The FLIR Lepton camera is connected to the Gumstix Overo Summit breakout board over an SPI connection.

Table 6.7 provides an overview of all payload and OBC components as used in the second design iteration and their respective properties.

Table 6.7: *Second hardware configuration for payload and OBC*

Component name	Number of units	Weight [g]	Total Weight [g]	Dimensions [mm]			Supply Voltage [V]	Current draw [A]	Total Power consumption [W]
				W	L	H			
NavStik Main Board	1	4	4	18	59	4	3,7	0,15	0,2
IvyPro interface board	1	8,9	8,9	35	41	8	4,5 - 14	0,05	0
Gumstix Overo Earthstorm	1	5,6	5,6	17	58	4,5	3,7	0,4	1,48
Gumstix Summit expansion board	1	17	17	39	80	6	3,7	-	-
e-CAM56_37x module	1	10	10	15	58	6,75	3,7	0,14	0,518
I2CXL-MaxSonar EZ	4	5,6	22,4	22,1	19,9	25,11	5	0,0044	0,022
Flir Lepton w/ breakout board	1	6	6	25	24	25	3,3	0,061	0,2
uBlox MAX-6Q GPS module + Sangshin 1580MHz antenna patch	1	2	2	10,3	9,7	2	3	0,011	0,033
On/Off switch	1	3	3	5	10	8	-	-	-
High brightness LED	4	0,1	0,4	5,4	3	0,9	3	0,2	0,6
LED L-36BSRD-B Flashing	2	0,5	1	3	5	3	3	0,05	0,3
Status LED's (red+green)	2	0,4	0,8	3	5	3	3	0,05	0,15
Total			82,1						3,8

6.3.3 Final payload and OBC hardware configuration

Table 6.8 gives an overview of the combination of the final payload hardware components and their properties. Included are as well the total weight and power consumption of the system. The payload and OBC architecture have a combined weight of 93,3 grams excluding wiring and a power consumption in full operation of 3.8 Watt.

Changes with respect to the previous configuration include the use of two extra sonar sensors, adding an additional weight of 11 grams. Including two extra sensors enables the use of four sensors in the horizontal plane and two in the vertical plane. The front sensor measures in flight direction, the backward sensor measures in rearward direction and two sensors measure at 90 degree angles towards the left and right sides. The last two sensors measure distances upward and downward distances. The placement of the sonar sensors among all other components is given in Figure 12.17b.

Table 6.8: Overview of Payload and OBC hardware components and properties

Component name	Number of units	Weight [g]	Total Weight [g]	Dimensions [mm]			Supply Voltage [V]	Current draw [A]	Total Power consumption [W]
				W	L	H			
NavStik Main Board	1	4	4	18	59	4	3,7	0,15	0,2
IvyPro interface board	1	8,9	8,9	35	41	8	4,5 - 14	0,05	0
Gumstix Overo Earthstorm	1	5,6	5,6	17	58	4,5	3,7	0,4	1,48
Gumstix Summit expansion board	1	17	17	39	80	6	3,7	-	-
e-CAM56 37x module	1	10	10	15	58	6,75	3,7	0,14	0,518
I2CXL-MaxSonar EZ	6	5,6	22,4	22,1	19,9	25,11	5	0,0044	0,026
Flir Lepton w/ breakout board	1	6	6	25	24	25	3,3	0,061	0,2
uBlox MAX-6Q GPS module + Sangshin 1580MHz antenna patch	1	2	2	10,3	9,7	2	3	0,011	0,033
On/Off switch	1	3	3	5	10	8	-	-	-
High brightness LED	4	0,1	0,4	5,4	3	0,9	3	0,2	0,6
LED L-36BSRD-B Flashing	2	0,5	1	3	5	3	3	0,05	0,3
Status LED's (red+green)	2	0,4	0,8	3	5	3	3	0,05	0,15
Total			93,3						3,8

For a more detailed overview of the entire hardware configuration and interface layout of the UAV please refer to 6.6. For the exact payload and OBC hardware arrangement in the fuselage, refer to 12.3.

6.4 Communications

This section will explain the approach taken to decide which method of communication would be most convenient to use in the UAV. Then a component selection will be made followed by a performance analysis.

A communications subsystem is necessary to be able to send commands to and receive the video feed from the UAV. This can be achieved using a wired or a wireless connection. Since a wired connection would increase the weight and decrease the range and manoeuvrability of the UAV, it was deemed impractical. Therefore, a direct wired communications link between the ground station and the UAV was not considered. A wireless connection on the other hand offers a broad spectrum of possible system designs, depending on frequency, bandwidth, transmission power and more. These factors of influence will be discussed in Subsections 6.4.1 through 6.4.5. To find what the properties of the optimal wireless communications subsystem have to be, a program was written to consider the data rate constraints and compute the link budget for the link. More elaboration and program results are discussed in Subsection 6.4.6.

6.4.1 Mission requirements on communications

This section aims to elaborate on the mission requirements pertaining to the communications subsystem. First only the primary requirements were considered. In later iterations, also secondary and tertiary requirements were taken into account to ensure the final solution to be an optimal fit.

The primary requirements on the communications subsystem are shown in Section 2.3. Although few, these indicate exactly where the focus lies in the first design of the communications subsystem; the subsystem needs power to be able to function, it has to be able to transmit collected mission data to the ground control station and it has to be able to communicate control data to and from the ground control station. It is important to notice that the requirement to transmit a live video stream is only considered to be of secondary importance. Therefore, this requirement was not taken into account until later design iterations. A different approach was taken on secondary but driving requirements. Due to their driving nature, these were already considered during the first design iteration. Tertiary requirements were also first considered during the second iteration.

6.4.2 Communication Data Analysis

The purpose of the communication subsystem is to transmit data, therefore, a computation of the uplink (BR_{up}) and downlink (BR_{down}) data rate was performed. In Chapter 8 the flow of data will be discussed in more detail. For the sizing of the communication subsystem, an analysis of the data rate was performed based on the payload selection in Section 6.1.

Hardware video compression

Media usually has a high data rate and the UAV will be capable of streaming live video. Therefore, the data rate requirement set is important for communication design. As mentioned the live video feed will be downscaled and compressed to H.264 format to reduce the data rate. In H.264 compressed video, every video frame is not sent, but rather only pixel (px) data that changes from frame to frame. Video is generally recorded at 16:9 aspect ratio in YUV4:2:2 pixel format, which is 16bits/px¹⁷, at 24FPS to stream natural motion real-time video. The H.264 compressed data rate can be calculated by equation 6.1 based a on method proposed by Ameransinghe[22].

$$BR_{video} = w_{px} \cdot h_{px} \cdot FPS \cdot K_{movement} \cdot 0.07 \quad (6.1)$$

The w_{px} and h_{px} represent the frame pixel width and height, FPS is the frames per second and $K_{movement}$ is a factor for the amount of movement in the image. The article [22] suggests a $K_{movement}$ factor of 1,2 and 4 for low (minimal change in image), medium (general slow movement) and high motion (rapid action movie type). A factor of 2 was chosen for calculations as the expected scene for the UAV's camera is general slow movement. Table 6.9 shows the BR_{video} for some common 16:9 aspect resolutions.

Table 6.9: Data rate of uncompressed and H.264 compressed 16:9 video

Frame pixel dimension (width x height) [px]	Bitrate [Mbps]	
	Uncompressed YUV4:2:2	H.264
416 x 234	37.4	0.3
576 x 324	71.7	0.6
960 x 540	199.1	1.7
1280 x 720	353.9	3.5
1920 x 1080	796.3	7.0

It becomes apparent that compression reduce the data rate down to $< 1\%$ of the original stream. This is important regarding communication because higher quality feeds can be transmitted the better the compression using the same maximum data rate. A choice was taken to use the 576 x 324px resolution as that would be the best quality stream possible as will become clear in the proceeding sections.

Data budget

Almost all communications modules use a serial interface to communicate with the host and transmit data. These modules generally use asynchronous bidirectional communication whereby a common frequency is used for transmitting (Tx) and receiving (Rx) using an agreed upon protocol for timing the switch between the two modes Tx and Rx. The Asynchronous Serial Format consists of data words where each word has a start, stop and parity (error checking) bit including the actual data bits¹⁸. Assuming one start, stop and parity bit (together referred to as framing bits) for every 8 data bits, a word of 11 bits is constructed, therefore, the raw data rate increases by 37.5% to include the framing bits. Table 6.10 summarises the uplink data to the UAV and downlink data from the UAV with framing included where Float Single-Precision and Char is a 32 and 8-bit data type respectively.

Table 6.10: Uplink and Downlink Data for 10ms transmission.

Uplink	Type	Data [bits]	Downlink	Type	Data [bits]
4 DOF control	Float SP	128	Main video feed 576x324px 24FPS H.264	-	62706
Flight mode	Char	8	FLIR Thermal image 80x60px RGB24 to JPEG	-	2880
Framing	-	51	Internal Temp.	Float SP	32
Total BR_{up} [bits/0.1s]	-	187	3 axis Attitude	Float SP	96
			6 Sonar sensor info.	Float SP	192
			Battery level	Float SP	32
			Light On/off state	Char	8
			GPS receiver latitude/longitude	Float SP	96
			Pressure reading	Float SP	32
			Framing	-	24777
			Total BR_{down} [bits/0.1s]	-	90851

Note that this is the worst case where all data is sent at 10Hz to and from the GCS. The video feed and FLIR thermal image data rates are post-compression rates. During the initial design of the communication subsystem,

¹⁷URL:<http://www.fourcc.org/yuv.php>

¹⁸URL:<http://nl.mathworks.com/help/instrument/serial-port-overview.html>

a data rate of 850kbps was assumed as a less accurate estimate of the data rates was available. However, the final design which will later be presented with an accompanying performance analysis in Section 6.4.8 does perform at the data rate presented in Table 6.10.

6.4.3 Operating Frequency

The most important property to be determined is the operating frequency. A multitude of factors have an influence on the available operating frequencies, all of which will be discussed in this section.

Power and Attenuation

The transmission of a signal takes power. However, the power consumption of the communications subsystem is negligible compared to that of other subsystems, i.e. propulsion and is therefore considered to be of low importance. However, the power the signal transmits to the receiving end is a very important factor in wireless communication. To analyse the influence of power, range and frequency, a link budget analysis was performed [23][24], which will be explained later. Both the range between sending and receiving end and obstructions along the signal's path affect the signal in a negative way[25]. Another important factor is the noise introduced; this largely depends on the quality of the components used and the operational environment [26]¹⁹.

High-frequency signals are generally more prone to negative attenuation due to obstruction. Figure 6.3 shows this for attenuation due to the atmosphere and a concrete wall. The atmosphere attenuates the signal due to the moisture in the air resulting in an attenuating factor [27]. Since the atmospheric attenuation is a function of distance, even though the effect of moisture in the air is very low, when the range increases it does become a factor of influence which should be taken into account. Therefore, a low-frequency signal seems more convenient in terms of maximum range. Figure 6.3a shows the specific attenuation as function of frequency from experimental data [27]. A requirement on communication through two brick walls was set but compared to reinforced concrete walls, the attenuation is significantly less [28].

In terms of attenuation by reinforced concrete walls, the same applies. Higher frequencies suffer a higher signal power loss and are therefore less practical. The signal power loss due to a reinforced concrete wall is very high [29], and is the main contributing factor of signal power loss for an operational range of 150 meters. In Figure 6.3b, the level of attenuation of a concrete wall for certain frequencies can be found based on experimental research [29]. Information was not available for the 2 to 3 GHz band, however, the figure shows that even below 2GHz, the attenuation is considerable. The graph gives a good indication of the effect of frequency on reinforced concrete wall attenuation. The mesh size and bar thickness used corresponds to dimensions commonly used in Dutch buildings, which is a mesh width and height of 140x140 mm, and a bar thickness of 19mm, with a wall thickness of 203mm [28][30][31].

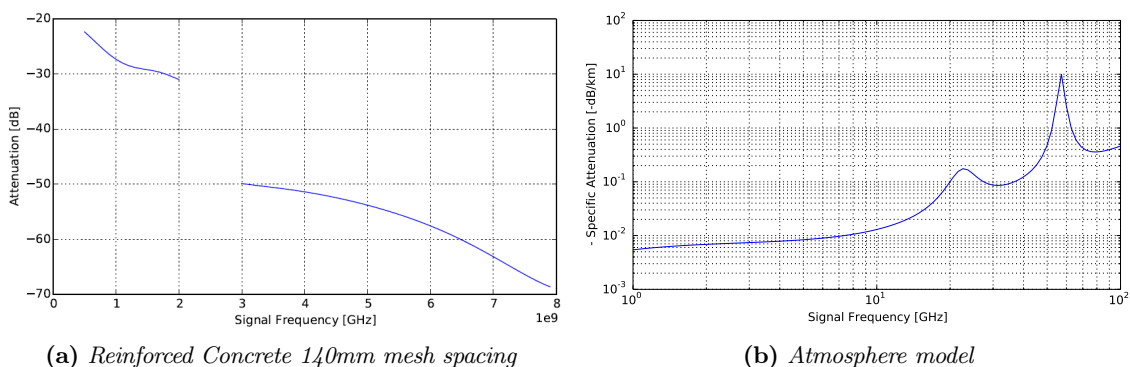


Figure 6.3: Signal attenuation from wall obstruction and atmospheric gases

Legal restrictions

Sending out a signal into the environment is simple, but local and global governments have put restrictions on certain frequencies to regulate the signal traffic in an orderly fashion. Some frequencies are free to use,

¹⁹URL: http://www.engineeringtoolbox.com/resistivity-conductivity-d_418.html

some require a license, and some are restricted to certain agencies. In Europe in general the unlicensed band is 863-870MHz²⁰. Only Dutch regulations were taken into account based on [32]. These regulations divide the available spectrum into section available for certain goals, some of which require a license to use.

6.4.4 Modulation and Bit Error Rate

The second decision made was the modulation type used on the data signal. Modulation describes the way the information is relayed onto a carrier signal. A trade-off was performed based on bandwidth efficiency, complexity, and power efficiency. A good early indicator of a modulation methods performance is the Baud rate, this is a measure for symbol rate, and is expressed as symbols per second (not to be confused with the bitrate, bit/second[33]). Generally, a high Baud rate is preferred. The modulation types considered and associated relation between bit and Baud rate can be found in Table 6.11. For QAM and OFDM, many different combinations are possible with varying bit-Baud relations.

Table 6.11: Modulation types with associated Bit-Baud relations [23]

Modulation Type	Baud rate	Bit rate	Units	Bandwidth [Hz]
BASK (Binary Amplitude Shift Keying)	N	N	Bit	-
OFSK/BFSK (Binary Frequency Shift Keying)	N	N	Bit	2N
BPSK (Binary Phase Shift Keying)	N	N	Bit	2N
DPSK (Differential Phase Shift Keying)	N	N	Bit	2N
QPSK (Quadrature Phase Shift Keying)	N	2N	Dibit	N
MSK (Minimum Shift Keying)	N	N	Bit	1.5N
GMSK (Gaussian Minimum Shift Keying)	N	-	Bit	-
OFDM (Orthogonal Frequency Division Multiplexing)	-	-	-	-
QAM (Quadrature Amplitude Modulation)	-	-	-	-

Once a signal is sent it has to be demodulated by the receiver and to achieve this a minimum Signal-to-Noise Ratio (SNR) per bit (E_b/N_0) is necessary to demodulate and detect the data signal. The E_b/N_0 value depends on the Bit-Error Rate BER (the fraction of erroneous bits of the total bits transferred) and its relation is plotted in Figure 6.4.

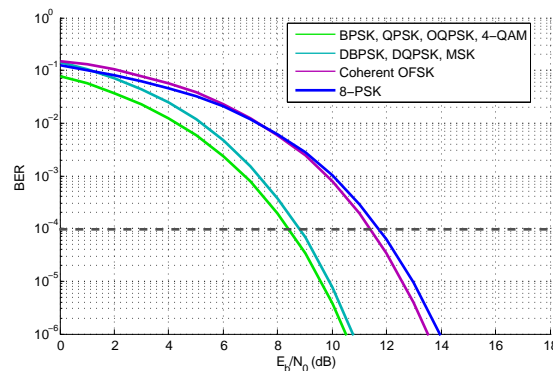


Figure 6.4: Minimum E_b/N_0 for given BER for different common modulation types.

For the transmission of real-time video, a BER of 10^{-4} is deemed sufficient to not compromise on the quality of the signal [34]. A minimum BER was set to the aforementioned value for the design of the subsystem.

A thorough literature study was performed to find the benefits and downsides of each modulation type [35][36][37][38]. Based on this gathered knowledge, OFDM was concluded to have optimal characteristics for the mission in terms of bandwidth usage, effect on range, sensitivity to obstruction and datarate.

What makes OFDM stand out as a modulation technique is the fact that the signal is divided across multiple sub-carriers. These sub-carriers use conventional modulation techniques, and each only contains a small portion

²⁰URL:<http://itu.int/go/ITU-R/RWP1B-SRD-UWB-14>

of the total signal. Since this introduces a low symbol rate per signal, it is possible to make use of guard intervals. A guard interval makes sure there is no interference between signals. Also, splitting the signal over multiple carriers (a so-called 'diversity scheme') improves the reliability of the signal by providing a higher overall gain and, therefore, a higher signal-to-noise ratio. This improvement is achieved by the reduction of fading and reduced chance of error bursts, a direct consequence of using a diversity scheme.

6.4.5 Data Encryption

To ensure the data signal cannot be seen by anyone but the drone operator, and to ensure no control commands can be sent to the drone by anyone but the drone operator, the communication channel is encrypted. Encryption means altering the signal sent to and from the ground control station in a structured manner. This introduces network latency and might interfere with the live video feed requirement.

Several usable encryption methods could be identified, these include:

- TKIP
- AES (multi-bit)
- DES
- RSA

It is important to note that TKIP is an integrity check, and not an encryption algorithm²¹. Of these four options, AES is considered to offer the most robust security. DES only has a 56-bit decryption key size, and is therefore easier to crack than the 128-bit or even 256-bit AES²². RSA is very hardware dependent and is, therefore, predictable when the hardware configuration is known.[39] TKIP is also easily crackable and is therefore deemed to offer insufficient security to implement[40].

AES emerged as the optimal encryption method to be employed on the UAV communications signals. Also, most transceivers can readily transmit using AES(128bit) encryption as they contain hardware chips capable of accelerating the process.

There are three key sizes for AES encryption: 128, 192 and 256 bits. The number of bits indicates the length of the encryption key, however, doubling of the bit length does not equate to doubling the security effectiveness of the method, but in general a higher number of bits indicates a more secure system. However, since methodically cracking an AES 128 encrypted message has not yet been achieved, the 128 bits key can be considered safe enough for the communications signal of the UAV. Also, it is capable of handling real-time video transmission requiring a high bit rate[41].

Having established the encryption method, it is important to know what kind of latency this encryption might introduce to the system. According to a research performed on this very subject, the maximal latency experienced when using AES 128 encryption was 0.01 ms[42], depending on the block size. This is an acceptable and almost negligible addition to the latency of the system. Whether this latency can be achieved with the currently selected on-board computer is still to be determined. Even though the specifications of the OBC indicate sufficient processing power, research and testing must be performed to guarantee optimal results.

6.4.6 Link Budget Analysis and Subsystem Design Constraints

Prior to component selection, a link budget analysis was performed to identify minimum performance specifications necessary to establish a reliable communication link. The design drivers of the communication system consist of three important factors:

1. Minimal Transmission Range (R_{link}) of 150m through reinforced concrete wall.
2. Data Bitrate uplink (BR_{up}) and downlink (BR_{down}) UAV. An average value of 850kbps was chosen.
3. Bit Error Rate (BER) for data transmission of 10^{-4} .

As mentioned, the goal of conducting a link budget analysis was to choose an operating frequency capable of transmitting data 150m through a reinforced concrete wall while minimising required transmission power. The subsystem will also be able to transmit the data in a timely manner with sufficient quality. To satisfy the design goals, a two-step process was used that first determines the minimum system specifications followed by

²¹URL:<https://learningnetwork.cisco.com/thread/11207>

²²URL:<http://cs-exhibitions.uni-klu.ac.at/index.php?id=263>

a step that analyses the performance based on the system specifications of the chosen transmitter (Tx)/receiver (Rx) module and configuration. The design process is schematised in Figure 6.5.

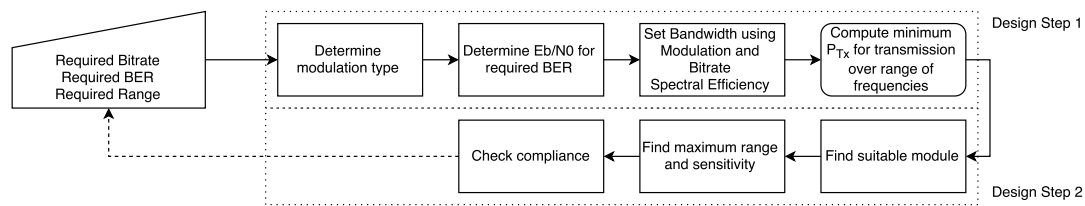


Figure 6.5: Two step optimisation of Communication subsystem

The most challenging aspect of estimating radio propagation was the UAV’s operation in built-up areas and inside buildings; this adds a lot of complexity to the situation regarding the communication aspect. The complexity is a result of the diffraction, refraction and reflection taking place as the signal moves through multiple obstacles and reflects off surfaces. These physics are difficult to simulate so an appropriate program/model was chosen and developed to simulate the signal. First a description of the communication link is provided followed by an explanation of the path loss in more detail.

Link Description and Signal Power

The complete link, from leaving the antenna port on the transmitting communication module to entering the equivalent port on the receiving end has been schematised in Figure 6.6

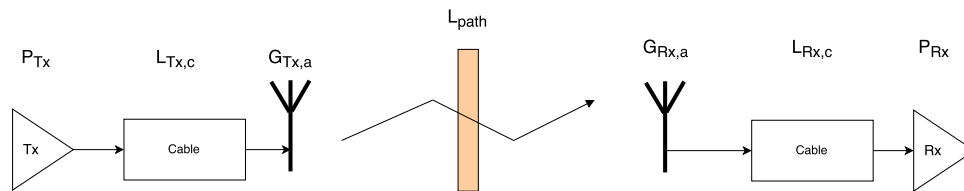


Figure 6.6: Communication link model showing gains and losses during transmission

The power at the receiving end, the signal power, (P_{Rx}) is modelled in decibels by equation 6.2

$$P_{Rx}[dB] = P_{Tx} - L_{Tx,c} + G_{Tx,a} - L_{path} + G_{Rx,a} - L_{Rx,c} \quad (6.2)$$

The transmitting power is P_{Tx} with the L and G representing losses and gains respectively for cables (c) and antennae (a). The L_{path} represents the power loss resulting from wireless propagation loss.

Wireless Signal Propagation Path Loss (L_{path}) Model

When modelling signal propagation, the signal power always reduces as a result of physical phenomena [43], the main contributors include;

Attenuation: Power loss due to propagation through different media.

Free space (path) loss: Dispersion of the signal with increasing distance from the Tx.

Multi-path: A result of reflection, diffraction and scattering of the signal resulting in the signal reaching the receiving antenna from two or more paths.

Fading: Multi-path resulting in a time varying signal power and phase causing destructive interference.

Noise: Natural disturbances and thermal noise from the different media modelled as Band-limited White Noise; noise that is limited to the bandwidth of the transmitted signal.

For modelling the signal propagation for free space path loss, several well-known models were considered from which a selection was made that best fit the situation for the designed system [44].

Simplified Friis equation model is an unobstructed Line-of-Sight (LOS) model based on the power law whereby the signal power decreases with the range squared. [43].

Ray Tracing represents signal wavefronts as particles and uses the physics of electromagnetic radiation to model the reflection and possibly also the diffraction and refraction of the signal. This model is more accurate than the Friis equation as it is a more fundamental model, however, it requires significant computational power to model.

Two path Model is similar to the Friis model, however in addition to the LOS path, a path with one reflection between the Tx and Rx is also considered. However, this model is generally not accurate for built-up or indoor areas [43].

Empirical Models simplify the problem to equations applicable to specific environmental conditions. These models usually build upon the models above or presents very specific solutions with limited applicability.

A decision was made to use the simplified Friis equation that have been adapted for indoor and built-up area propagation based on empirical models of indoor propagation. Ray tracing was ruled out as it is a computationally expensive and time-consuming model that would take considerable time to program and verify. The two-path model was not chosen as it would not be applicable for the operational conditions considered (indoor flight).

The equation modelling the path loss L_{path} with distance r_{path} between Tx and Rx is given by equation 6.3 and is known as the Log-Distance model [45].

$$L_{path}(r_{path}) = L_{path}(r_{path,0}) + 10 \cdot \log_{10} \left(\frac{r_{path}}{r_{path,0}} \right)^n + \beta \cdot r_{path} + \sum_{i=0}^M WAF_i \quad (6.3)$$

Here $r_{path,0}$ is a reference distance which is normally taken at 1m [45]. The path loss is represented by exponent n which is normally 2 for free space, but is different depending on the operational environment of the communication subsystem. The WAF is the wall attenuation factor in dB and summed for transmission through M walls. For this subsystem, transmission through one reinforced concrete wall is considered as explained in Section 6.4.3. Atmospheric attenuation is included by β which is the specific attenuation of the atmosphere in dB/m as shown in Figure 6.3a. The term $L_{path}(r_{path,0})$ is the free space loss at distance $r_{path,0}$, given by equation 6.4 where λ_{link} is the signal wavelength in meters.

$$L_{path}(r_{path,0}) = L_{fsl} = 10 \cdot \log_{10} \left(\frac{4\pi r_{path,0}}{\lambda_{link}} \right)^2 \quad (6.4)$$

The choice of the path-loss exponent n depended highly on the environmental situation. As mentioned, the UAV will operate in built-up outdoor and indoor areas hence obstacles and their effect on the signal propagation adds a lot of complexity to predicting the received signal power. The Ray Tracing model could account for most of these factors, however, results will vary greatly with different obstacle configurations, so many computationally intensive simulations would have to be carried out to get accurate results. The simple Log-Distance model (or sometimes referred to as Median Path Loss model) uses empirical results to set a value for the path-loss exponent n , this value is computed from extensive tests conducted in different categories of environments and measuring the signal losses [25][43][46]. Table 6.12 summarises the path-loss exponents for different environments.

Table 6.12: Path loss exponent n for different operational environments [43]

Environment	n
Free-Space	2
Flat Rural	3
Rolling Rural	3.5
Suburban, Low rise	4
Dense Urban, Skyscrapers	5

Research conducted by Seidel on path loss prediction models for indoor communication showed that for the four buildings he researched which included a grocery, retail and two office buildings, in general the path loss exponent n was 3.14 [45]. Given the buildings on which the research was conducted closely reflect the building types the UAV will enter, and as the value n corresponded well with the statistical values from Table 6.12,

calculation for the UAV's communication subsystem design were performed using this value. Noteworthy is that Seidel mentions a large uncertainty in the received power which is modelled as a log-normal distribution with a standard deviation of 16.3dB in received power for all transmission ranges (1 to 100m) tested. Therefore, the theory is only good for a first-order prediction and tests will be necessary to verify and validate the subsystem design under operational conditions.

Noise Power and Signal-to-Noise Ratio

Using the equations previously presented, the signal power for the Rx can be computed. In addition to signal power, there is received noise with specific power which is modelled as band-limited white noise (BLWN) [47]. BLWN has a constant noise intensity N_0 [W/Hz] across the bandwidth B of the signal. The ratio of signal power P_{Rx} to noise power N (SNR) is an important factor for detection of data from a modulated signal and the minimum SNR mostly depends on the modulation method used to modulate the signal as mentioned in Section 6.4.4. BLWN power is calculation with equation 6.5 where T_{sys} is the system noise temperature which has a typical value of 290K for analysis [23] and k_B is the Boltzmann constant.

$$N = N_0 B = k_B T_{sys} B \quad (6.5)$$

The SNR per bit denoted by E_b/N_0 is computed by equation 6.6 where E_b is the received power per bit of data and N_0 is the noise power per bit. BR is the bitrate of the data transmission in bits/s.

$$SNR = \frac{E_b}{N_0} = \frac{P_{Rx}}{BR \cdot N_0} \quad (6.6)$$

Receiver Sensitivity and Link Margin

Once the received power and SNR is calculated, the performance of the communication link can be defined. Every Rx has a Rx sensitivity (s_{Rx}) which is the minimum P_{Rx} required to be able to decode and detect the data signal. The link margin LM given by equation 6.7 is the surplus received signal power; a surplus allows for fluctuating and unforeseen link attenuating factors that could reduce the received power and also helps in maintaining a safety margin by design.

$$LM = P_{Rx} - s_{Rx} \quad (6.7)$$

The primary reason for unforeseen attenuation is Fading from Multi-path as previously described. Fading can significantly reduce P_{Tx} so it is important to take it into consideration and always have some link margin [48].

Design Step 1: Determining minimum transmitter power and limiting design space

Based on the theory presented, the minimum system specification was computed to define the Rx sensitivity (s_{Rx} and associated minimum Tx power (P_{Tx})). The estimated 850kbps data downlink rate from the UAV drove the communication subsystem design as explained in Subsection 6.4.2. The upper and lower design boundaries when choosing modulation type and omni-directional antennae are defined by assuming two communication setups with BER of 10^{-4} and data rate of 850kbps.

1. Worst case: OFSK modulation - highest minimum SNR for detection 11.5dB (see Figure 6.4) and bandwidth equal to twice the data bitrate (see Table 6.11). Antennae assumed isotropic, no gain.
2. Best case: QPSK modulation - lowest minimum SNR for detection 8.2dB (see Figure 6.4) and bandwidth equal to the data bitrate (see Table 6.11). Antennae assumed simple 3dBi gain ²³.

A calculation for the minimum Tx power (no Link Margin) for the 'best case' at 868MHz is done which is repeated, but not fully described here, for the 'worst case'. Note that the Equations 6.2 to 6.7 take P_{Tx} as input to solve for P_{Rx} , the equations are reversed so that the minimum P_{Tx} is calculated using the minimum P_{Rx} to detect the signal. This method is based on a method outlined in [23].

²³URL:<https://www.ncjrs.gov/pdffiles1/nij/185030b.pdf>

First the Noise Power N is computed based on the baseband null-to-null bandwidth B which is equal to the magnitude of the bitrate (850kbps), hence 850Hz [23]²⁴.

$$N = k_B T_{sys} B = 1.38 \cdot 10^{-23} \cdot 290 \cdot 8.5 \cdot 10^5 = 3.40 \cdot 10^{-15} \text{W} = -114.7 \text{dBm}$$

The Rx noise floor is the thermal white noise N plus a Noise Figure (NF) as a result of noise introduced by the Rx; typical value is 10dB ²⁵.

$$\text{Rx Noise Floor} = N + NF = -114.7 + 10 = -104.7 \text{dBm}$$

The E_b/N_0 for QPSK modulation is 8.2dB (6.6) as seen in Figure 6.4 which is associated with a total SNR.

$$SNR = (E_b/N_0) \cdot (BR/B) = 6.6 \cdot 1 = 6.6 \equiv 8.2 \text{dB}$$

The minimum Rx power / Rx sensitivity is then computed which is the power to be received such that the signal can just be successfully demodulated and the data can be read.

$$P_{Rx} = s_{Rx} = \text{Rx Noise Floor} + SNR = -104.7 + 8.2 = -96.5 \text{dBm}$$

The path loss is computed for the 868MHz wave at 0.345m wavelength for a range of 150m (as per specification) using the specific atmospheric attenuation of $4.99 \cdot 10^{-6} \text{dB/m}$ and reinforced concrete wall attenuation 26.18dB .

$$\begin{aligned} L_{path} &= 20 \cdot \log_{10} \left(\frac{4\pi}{\lambda_{link}} \right) + 10 \cdot \log_{10} (r_{path})^{3.14} + \beta \cdot r_{path} + \sum_{i=0}^N WAF_i \\ &= 20 \cdot \log_{10} \left(\frac{4\pi}{0.345} \right) + 10 \cdot \log_{10} (150)^{3.14} + 4.99 \cdot 10^{-6} \cdot 150 + 26.18 = 125.7 \text{dB} \end{aligned}$$

The minimum Tx power is then computed by rearranging equation 6.2.

$$P_{Tx} = P_{Rx} + L_{Rx,c} - G_{Rx,a} + L_{path} - G_{Tx,a} + L_{Tx,c} = -96.5 \text{dBm} + 0 \text{dB} - 3 \text{dBi} + 125.7 \text{dB} - 3 \text{dBi} + 0 \text{dB} = 23.2 \text{dBm}$$

Power is measured in dBm where 23.3dBm is equal to 209mW . The terms can be added as dBm represent power while the dB and dBi represent gains and losses [23]. This calculation is done over a range of transmission frequencies. Figure 6.7 shows how the minimum Tx power changes with transmission frequency.

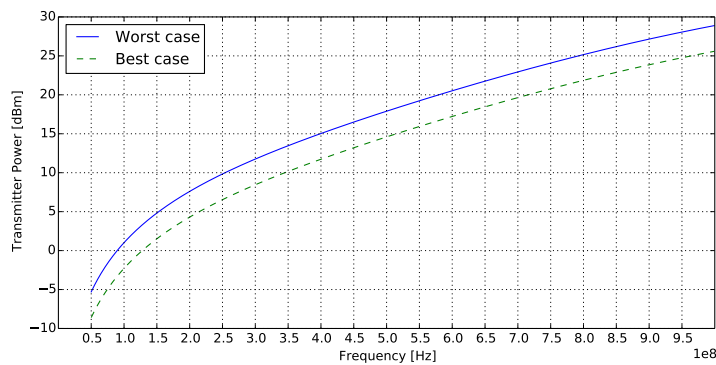


Figure 6.7: Minimum Tx power with varying transmission frequency at 850kbps , 10^{-4} BER and 150m range through reinforced concrete wall

The Tx power roughly grows exponentially with frequency, hence it is better to transmit at lower frequencies to minimise power requirements. The growth in power required is a result of increasing loss due to free space, and increasing wall and atmospheric attenuation at higher frequencies as previously discussed. The drawback of lower frequencies is that the bandwidth available is usually more limited, hence achievable data rates are lower. Most regulations limit transmission powers to a maximum of 30dBm (1W) for safety and health reasons [23], hence from Figure 6.7 it becomes apparent that only the Sub-1 GHz band is a viable option in the design space.

²⁴URL:<http://jugandi.com/ebooks/Wireless/05%20Phase%20Modulation.htm>

²⁵URL:http://www.eetimes.com/document.asp?doc_id=1272302

As previously discussed in Section 6.4.3 there are limited frequency bands available for unlicensed use and, therefore, two contenders stand out for the operational frequency. The 863-870 and 902-928MHz bands are both viable options as they are two bands for which manufacturers produce transceiver modules and are unlicensed in many parts of the world. Modules typically have the option to operate at 868 and/or 908MHz within these bands and will need a minimum P_{Tx} range, from the worst to the best case, for the 868 and 908 MHz frequencies of 23.2-26.5dBm and 24.0-27.3dBm respectively (all less than 550mW). Taking the best case, which is still conservative as better antennae with higher than 3dBi gain exist, and as QPSK is widely used in many modules, a sensitivity analysis was performed to see how P_{Tx} would be affected by changing individually the maximum range and data bit-rate.

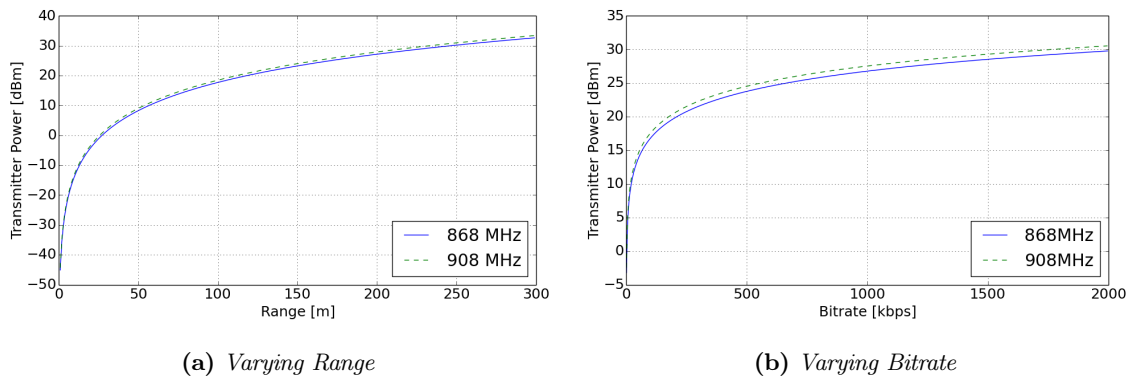


Figure 6.8: Minimum Tx Power sensitivity to changes in bitrate and range for 868 and 908MHz

From Figure 6.8 it is clear that the minimum Tx power varies exponentially with range and bit-rate. Given that Tx power is limited to 30dBm for safety, Table 6.13 summarises the maximum range and bit rate for the chosen frequencies.

Table 6.13: Maximum operational performance for 868 and 908MHz frequencies

Frequency [MHz]	Min. Tx Power [dBm]	Max. Range [m]	Max. Bitrate [kbps]	Max. Bandwidth [MHz]
868	23.2	240	2000	2.0
908	24.0	230	1700	1.7

6.4.7 Component selection process

Once the optimal system properties were found, a search for components to fulfil the task begins. During this process also components commonly used in FPV flying were investigated, even though these components might not fulfil any or all requirements. This is done to gain a good understanding of state-of-the-art systems, and to identify major design differences which might pose a challenge to fulfil.

The communications subsystem consists of a part on the UAV and a part on the GCS. These parts both need multiple components to establish a communication stream. Since this design is only limited to the communications subsystem, the components necessary are limited to a transceiver system and an accompanying antenna. Any peripherals needed to establish a link between the OBC and the communications subsystem, including components for video compression and signal modulation, fall within the scope of the OBC design.

Transmitter and receiver

Both the UAV and ground station must be able to transmit and receive signals. Therefore, they both need a transmitter and receiver, or a combination: a transceiver. The latter offers the convenience of combining two systems on one board, decreasing the total subsystem size.

To find existing transmitters, receivers and transceivers, a search was performed using various sources including the Internet where shops dedicated to model aircraft flying offered many off-the-shelf communication systems²⁶

²⁶URL:<http://www.readymaderc.com/store/>

²⁷ ²⁸ ²⁹. Another good source of possible boards were datasheets from component manufacturers (such as Freakduino [49], Texas Instruments [50], Adaptive Network Solutions [51] and LSR[52]). During this search, a decision was made to consider experimental, commercially available components in the final trade-off as well, as long as the experimental results are reliable and the design has potential to get FCC/EASA approval.

Table 6.14: Feasible communication transceiver modules with data-sheet information

Transceiver	Manufacturer	Power rating	Tx Power [dBm]	Rx Sensitivity [dBm]	Bitrate [kbps]	Module dimension	Mass [g]	Frequency
Freakduino v2.1a	Freaklabs	5V	27		1000	6.70 x 7.95cm		Both 868/900MHz
SiFLEX02-R2	LSR	3.6V 300mA	24	-110	1000	2.29 x 4.14cm	10	868 or 900MHz
SiFLEX02-R2-HP	LSR	3.6V 300mA	29	-110	1000	2.29 x 4.14cm	10	868 or 900MHz
DNT900	muRata		30		500	52.07 x 34.54 x 7.24 mm		900MHz
n920	Microhard		30	-100	1200	2 x 1.25 x 0.25in	18	900MHz
@ANY900-2 RF	ANS	3.6V 26mA	10	-110	1000	40 x 13.5 x 2 mm	2	Both 868/900MHz
NT Series	Linx Technologies	5.5V 40mA	12.5	-113	300	0.630 x 1.150 x 0.131in		868 or 900MHz
AW900MSP1	AvaLAN	0.75W	21	-97	1540	7.5 x 51 x 7 mm		900 Mhz
STEVAL-IKR001V8D	ST		27	-123	500			868Mhz
FL-AT86RF212-CC1190	Freaklabs		27		1000			Both 868/900MHz
Zulu 2km Radio	RF solutions		20		56			868 or 900Mhz
Zulu M	RF solutions		13		56			868 or 900Mhz
Ubiquiti SR9	Ubiquiti	3.3V 800mA	23	-70	54000			900MHz
Xbee-Pro 900HP	digi	3.6V 229mA	24	-101	200			900MHz
SX1276 Lora module 14dB	Semtech	3.7 120mA	14	-139	300	27.3 x 24.51mm		Both 868/900MHz
SX1276 Lora module	Semtech	3.7 120mA	20	-139	300	27.3 x 24.51mm		Both 868/900MHz

Once sufficient information on components was collected, a trade-off was performed on the components outlined in Table 6.14. This led to a small selection of possible boards, from which the final design component can be selected. From the trade-off, the SiFLEX02-R2-HP module was identified to be the most suitable module as it is versatile and met all minimum specification requirements presented in Table 6.13. No iterations were performed as the module was sufficient for the specified data budget. The other transceiver options either did not meet the minimum specifications or were limited to only the 900MHz operations (which is not allowed for unlicensed use in The Netherlands).

The SiFLEX02-R2-HP is a dual antennae transceiver module enabling half-duplex serial communication. It has a built-in Low Noise Amplifier that allows it to operate at low Rx sensitivities, and a Tx amplifier allowing it to transmit at up to 29dBm [52]. The module's chip supports Antenna Diversity allowing it to use both antennae for transmitting or receiving (the module can be customised to enable this feature). The built-in switch allows one of two antennae to be used for Tx and allows both to be used for Rx (refer to data-sheet for more information [52]). The chipset supports both European (868Mhz) and American (900MHz) bands and the vendor can deliver the module in either configuration when customised. Subsection 6.4.8 will present more technical data of this module.

Antenna

To select the optimal antenna for this design, an overview of possible antennae had to be established first. From a literature study³⁰, the following antennae were taken into consideration

- Short Dipole
- Dipole
- Half-wave Dipole
- Monopole
- Loop
- Patch
- Helical
- Parabolic reflector
- Yagi-Uda
- Horn

Due to size restrictions, the Yagi-Uda, Horn, Parabolic, Helical and Loop antennae are not considered for the UAV. However, they might turn out to be a good fit for the ground control station.

Where the dipole and monopole antennae are omnidirectional, the patch antenna offers directional signal transmission. This is convenient since directional antennae offer higher gain. However, it does mean the antenna has to be pointed roughly in the direction of the ground control station at all times. The mechanism needed to turn the antenna in the right direction will add complexity and weight to the UAV.

²⁷URL:<http://www.fpvflying.com/categories/FPV-UAV-RC-modelplanes/>

²⁸URL:<http://www.getfpv.com/>

²⁹URL:<http://www.hobbyking.com/hobbyking/store/index.asp>

³⁰URL:<http://www.antenna-theory.com/antennas/main.php>

For the UAV, the antenna choice was heavily restricted by size and weight constraints, and simplicity in both operation and replacement was an important contributing factor. For these reasons, the final decision was made for a quarter-wavelength monopole antenna known as Random Wire Antenna or Long-wire antenna³¹. It offers sufficient gain for the smallest size and lowest weight when compared to other options. Since the antenna will be on the outside, it is very susceptible to collisions. Having a flexible antenna model would be very beneficial for this reason. The options are then restricted to having a wire for an antenna or a whip antenna. A wire offers good performance for low weight, where a whip antenna offers a minor increase in performance for a slightly higher weight. Since weight is an important factor for this design, the wire antenna is the better choice. The optimal length for this wire is a quarter of the signal wavelength[53], which is 86.4mm for the 868MHz frequency. Antenna gain for Random Wire Antenna is difficult to predict and model so for the analysis it is assumed to be similar to a quarter-wavelength monopole which has a gain of around 5.2dBi [54]. For redundancy, multiple antennae can be placed on the UAV, between which the system can switch according to optimal signal strength. With only one antenna, the situation of the UAV being in the transmission path will occur multiple times during the mission: by placing two antennae with on either side of the UAV, this will not occur since the system can switch to the unobstructed antenna when necessary. A clarifying depiction of the antenna placement is shown in Figure 6.9. The red bars indicate the antenna placement on both sides of the UAV and give an indication of the antenna length compared to the hull size. The antennae will be placed on a slightly curved surface, which increases the width of the radiation pattern in the horizontal direction.

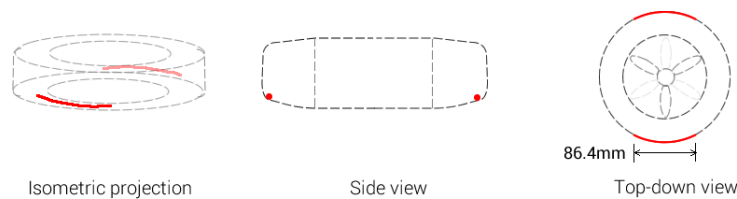


Figure 6.9: *Random Wire Antennae placement on downward slanted edge of UAV*

During the mission, the UAV will always be higher than the GCS, therefore, a signal aimed downward at a slight angle is suitable resulting in the antenna placement on the downward slanted edge. The radiation pattern of a quarter wavelength monopole antenna is depicted in Figure 6.10. The middle figure shows the radiation pattern in the XY-plane, which corresponds to the side-view image in Figure 6.9. The only concern is possible blind spots left and right to the UAV (when seen from Top-down view); to correct for that the two antennae can be placed perpendicular to each other on the bottom edge of the UAV. The perpendicular placement will allow coverage towards the front, back, left and right of the UAV. Another option may be to vertically place antennae to allow for better coverage towards the sides, however, blind spots directly below the UAV are a problem. Tests with different antennae placement is recommended to determine the best antennae positioning. The goal would be to minimise blind spots in the regions where the GCS would be positioned, hence, a semi-spherical isotropic coverage down from the UAV would lead to the best coverage.

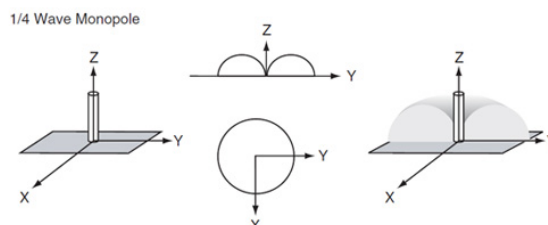


Figure 6.10: *The radiation pattern of a quarter-wave monopole antenna*

Keeping in mind that weight, cost and complexity are important factors, a decision was made to implement two omnidirectional 1.25 wavelength dipole antennae on the ground control station for receiving communications, of which one switches between transmitting and receiving. These antennae have a high gain of 5.2dBi [55]. Since power is less of an issue on the GCS, higher signal amplification can be applied to increase performance.

³¹URL:<http://udel.edu/~mm/ham/randomWire/>

Making the antennae foldable or telescopic will aid in deployability of the GCS. More information on this can be found in Section 6.7.

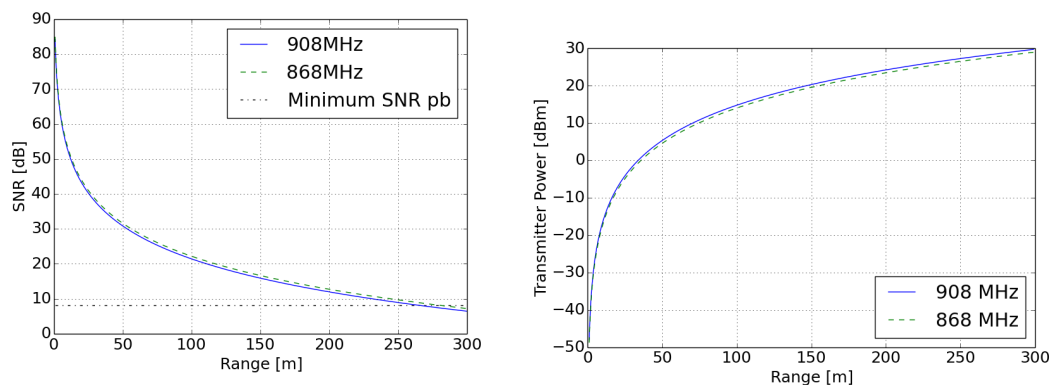
6.4.8 Performance Analysis and Data Sequencing

The SiFLEX02-R2-HP module will be operated in the settings summarised below [52][56]:

- **Frequency:** 868 or 908MHz (Vendor customisable module)
- **Transmission Data rate (BR) and modulation:** 1Mbps, proprietary OQPSK based with Direct Sequence Spread Spectrum spreading. Bandwidth (B) is equal to BR. For 10^{-4} BER, the minimum SNR per bit (E_b/N_0) is 8.2dB.
- **Host Data rate:** 921.6Baud equivalent to 921.6kbps
- **Tx Power P_{Tx} :** Approximately 29dBm (750mW)
- **Rx Sensitivity s_{Rx} :** -95dBm
- **UAV Tx/Rx Antennae Gain $G_{Tx,Rx,a}$:** 5.2dBi
- **GCS Tx/Rx Antennae Gain $G_{Tx,Rx,a}$:** 5.2dBi

Design Step 2: Subsystem performance analysis

Based on the configuration and inputs presented in Section 6.4.8, equation 6.2 is used to calculate the P_{Rx} and equation 6.6 to calculate E_b/N_0 which given indication of the module's performance. The losses in the cables are negligible given that the wiring distances in the UAV are small. The minimum E_b/N_0 (Minimum SNR per bit) at the receiver must be 8.2dB for the signal to be detectable. Given that 1Mbps is sufficient for the required data transmission, the most important performance measure is the maximum achievable range through a reinforced concrete wall, this is shown in Figure 6.11. The SNR of the link over the range, as in Figure 6.11a, is calculated by equation 6.2. The terms in equation 6.2 are calculated with equations 6.3 to 6.6 for both the 868 and 908MHz. The terms for these equation are presented in the configuration list at the beginning of Section 6.4.8. Figure 6.11b is produced by the same procedure as presented in Section 6.4.6, Design Step 1, using the SiFLEX's configuration presented before. This computation of the minimum P_{Tx} is done for both the 868 and 908MHz frequency.



(a) SNR per bit (E_b/N_0) of Rx for given range with minimum value indicated

(b) Minimum P_{Tx} for given transmission range

Figure 6.11: SiFLEX02-R2-HP range and sensitivity to P_{Tx} for communication through reinforced concrete wall with 5.2dBi gain Tx and Rx antennae

From Figure 6.11a, for the current configuration, the maximum achievable range using 868MHz is 278.3m and 908MHz is 263.2m. At this range, there is no link margin so the signal is susceptible to loss. Other performance characteristics are given in Table 6.15. The signal should, therefore, be detectable with the given link margin and should the UAV go beyond the 150m limit, the signal should still be detected.

Table 6.15: *SiFLEX02-R2-HP performance analysis summary*

Frequency [Hz]	Max. Range [m]	Max. Range (free space) [m]	Min. P_{Tx} 150m range [W]	Link margin at 150m range [dBm]
868	278.3	1896	19.6	9.4
908	263.2	1843	20.3	8.7

Data Timing for Transmission

The initial data rate analysis in Subsection 6.4.2 showed that the maximum directional data rate would be 850kbps from the UAV to the GCS. Given that the SiFLEX02-R2-HP operates at 1Mbps directional and adopts half-duplex communication (bidirectional asynchronous serial), timing has to be allocated to make sure the UAV and GCS are in the correct mode (Tx or Rx) at the right time. From Subsection 6.4.2 the rate of switching between Tx and Rx mode is every 0.1s to facilitate the 10Hz data update requirement. The remaining majority of the time the UAV will send data to GCS to achieve a live video stream, however, this will be disrupted every 0.1s for the GCS to send data to the UAV. The time it takes for the GCS to send data to the UAV should, therefore, be minimal so that the video feed is not visibly broken every 0.1s.

Provided the data rates for video and control/housekeeping data, an estimate is made for data timing. Assuming the GCS to UAV data is time critical, the timing is designed to meet its requirements first. Table 6.16 shows the data rates and allocated Tx time with the maximum possible data transfer within the Tx time. This data timing sequence repeats every 100ms indefinitely until the communication link is broken.

Table 6.16: *Data timing for 100ms transmission between GCS and UAV and maximum supported data*

Data Direction	Data with Framing [bit]	Tx time [ms]	Max. Tx Data in 10ms [bits]	Margin on Tx Data [bits]
GCS to UAV	187	0.19	187	0
UAV to GCS	90851	99.81	99813	8962

The table shows that even with the current data load, there are 8962bits of unused bandwidth per 10ms which can be used in case data has to be resent or additional data has to be sent. The communication data cycle scheme is designed such that if erroneous data is sent by the GCS to UAV, then when the UAV starts communicating to the GCS it sends a reply flagging the event or sends an 'ok' message. Then the UAV continuously sends to the GCS with no reply from the GCS until the cycle completes after 100ms and transceiver modes switches. When erroneous data is sent by the GCS to the UAV, the UAV will maintain the previous control input and wait till the next input after a full 100ms cycle. Upon loss of connection, the UAV enters its 'hold' mode. The Tx time for the GCS to UAV communication is negligible with respect to data delay of the UAV to GCS transmission hence there will be no observable delay in the video stream. The data rates were also checked against the host data rate and the module is capable of transferring the data.

Considering the complete performance analysis, the SiFLEX02-R2-HP module would be capable of meeting the minimum requirements while maintaining a margin of safety on the design to allow for unforeseen changes to data rates during production and testing.

6.5 Power

The power subsystem has the sole function to power all the other electronics on board of the UAV. The largest power budget required comes from the propulsion group. The electric motors require a lot of power (more than ninety percent) to keep the drone aloft and therefore drive the battery choice. The motors convert the electrical energy from the battery in mechanical energy to drive the rotors. Between the motors and the batteries will be the electronic speed controllers, that will receive control inputs from the on-board computer. The focus of this design is not on the electronics, and because of that off-the-shelf components are used.

6.5.1 Mission requirements on power subsystem

From the overall mission requirements each subsystem gets its own set of requirements. For the power system these specific requirements can be summarised very briefly. The power subsystem shall provide power to all other

subsystems. The power subsystem shall be able to operate in the specified indoor and outdoor environmental conditions. In general the batteries are some of the heaviest components so they should be as light as possible in order to make the entire drone reach the 500 gram requirement. The batteries shall be easy to place and replace with only five or less tools within one minute. The battery power level shall be measured and transmitted to the GCS.

6.5.2 Motors

The propulsion group has calculated a certain power that must be put into the system by the motors. The maximum power that the motors must be capable of delivering is 49.0 watt per motor, at an RPM of 13500. Based on these two requirements a matching motor is found. To ensure that all options are included a spreadsheet is constructed to be used as a motor database. In this database the power ranges from 5 to 930 watt. The maximum RPM is calculated by multiplying the K_v value with the maximum voltage. K_v ranges from 980 to 7000 RPM/V, while the maximum voltage ranges from 3.7 to 22.2 volt, with steps of 3.7 volt (nominal output voltage for LiPo battery cells). Mass and dimensions are also included. 22 motors have been included in this spreadsheet. If two motors are able to provide the same RPM and power output, mass is the driving factor to choose one over the other. In this way the choice for the motors has come to the DYS Quanam MT Series 1806. Its specifications are listed in Table 6.17

Table 6.17: *DYS Quanam MT Series 1806 specifications*³²

Kv	2300 rpm/V	Shaft diameter	2 mm
Weight	19 g	Motor length	15 mm
Maximum Current	7.6 A	Motor diameter	24 mm
Maximum Voltage	12 V	Can Length	6 mm
Power	85 W	Total Length	20 mm

6.5.3 Electronic Speed Controller

From the motor requirements and specs the electronic speed controllers (ESC) can be selected as well. The driving criterion for the speed controllers is the current they can handle. To minimize the maximum current the voltage in the system is chosen the highest the motors can handle, 11.1 volt. With the maximum power of 49.0 watt this results in a current of 9.5 amps. By making a spreadsheet database for ESCs a choice can be made. This spreadsheet includes the values on maximum continuous current that an ESC can withstand. These range between 6 and 20 amps. Their operating voltage is between 7.4 and 22.2 volt. Masses and dimensions are included as well. Some of the available ESCs have an integrated battery eliminator circuit (BEC). This BEC can provide a steady voltage and current to other components than the motors. The BEC voltage is 5 volt if there is a BEC, the current from it ranges between 0.5 and 4 amps. Again mass is the most important parameter for choosing between two similar ESCs. 27 ESCs have been compared. With this the choice of ESC has lead to the Flycolor 15 Amp Multi-rotor ESC, see Table 6.18.

Table 6.18: *Flycolor 15 Amp Multi-rotor ESC specifications*³³

Constant Current	15 A	Length	48 mm
Maximum Burst Current	18 A	Width	19 mm
Input Voltage	7.4 11.1 V, max 12.6 V	Height	10 mm
BEC	5V - 2A	Mass	12 g

6.5.4 Battery

Now the battery must be chosen. The process that is used to do that is described below. The final battery choice is described with all its specifications in the end.

³²URL:http://www.hobbyking.com/hobbyking/store/_66404__Quanam_MT_Series_1806_2300KV_Brushless_Multirotor_Motor_Built_by_DYS.html

³³URL:http://www.hobbyking.com/hobbyking/store/_58262__Flycolor_15_Amp_Multi_rotor_ESC_2_3S_with_BEC.html

Type of battery

The most commonly used types of batteries in small aerial vehicles are the NiCd, NiMH and LiPo types [57]. NiCd are the most mature option of the three and are relatively inexpensive. They need to be fully discharged after use or they will lose capacity drastically (cell memory), and they have a lower energy density than the other two. Due to the cadmium part of this battery disposal can be troublesome. NiMH batteries have significantly higher capacities than NiCd cells, while fitting in approximately the same size. They do not suffer from cell memory, so their maintenance is much easier with respect to NiCd. LiPo batteries maintain a higher and more constant voltage during their operational cycle, what results in much smaller and lighter batteries with the same capabilities. They must be monitored during charging, as charging a bad cell or overcharging cells can cause fire hazards. More details about this are given below. For storage it is best to keep LiPo batteries at a cool (refrigerated, but not freezing [58]) place with about half charge. However, because the IPD is designed to be used during emergencies this last bit is not possible. This reduces capacity, but when the batteries are stored in a refrigerator this is only as much as six percent per year. The cost of these off-the-shelf batteries is low, so if needed they can be easily replaced.

Method to find a suitable battery

Since off the shelf batteries are used in this design a large spreadsheet was made with the available options. 110 batteries are included, all with different parameters. Some are battery packs with two, three or four cells connected in series, while the rest are single cell batteries. Their capacity ranges from 60 to 1800 mAh. The smaller ones require over thirty packs to comply with the specifications, which makes them unfeasible to actually implement. The nominal discharge rates vary between 10 and 65 C. A higher C rate means that the battery can support higher currents for the same capacity, so as long as the systems current draw does not exceed the battery specifications a low C rate does not have to be a limiting factor. The mass of single batteries is between 1.72 and 138 gram. The lighter ones also have the smaller capacities, so more of them are needed to comply with the power demands of the system, which mostly results in heavier battery systems. The battery spreadsheet can be used as follows. The payload and propulsion groups provide the power group with a minimum amount of power that must be delivered in order to be fully functional. It is assumed that the payload operates at full power throughout the entire mission. For the propulsion group a mission profile is outlined. This is a really basic outline, consisting of a certain percentage of flight time with full power and flying at indoor manoeuvre power for the rest of the time. From the full power requirement (combined with the RPM requirement) a motor is selected. This poses a voltage limit for the power group. The voltage is chosen as close to that voltage limit as possible to keep the currents small to prevent unnecessary heat production. This leads to an output voltage of 11.1 V. As a result all battery packs consisting of 2 or 4 cells in series can be ignored, since multiples of these will not yield 11.1 V. Single cell batteries of 3.7 V can be combined to become a 3 cell battery. A description of how to do that is given below. In this way it is determined how many batteries are needed in series. If more are needed, they are assumed to be one battery pack from this point on.

The maximum required current can be determined by dividing the maximum power by the output voltage. The maximum current that the battery can provide can be calculated by multiplying the capacity with the nominal discharge rate. The number of required batteries in parallel is calculated by dividing the required current by the current one battery can provide and round that up to the nearest integer. This rounding leads to some contingency in the final design.

The energy that needs to be stored in the batteries can be calculated from the mission profile as well. Adding the maximum power times the total flight time at full power with the power at manoeuvre power times the total time at manoeuvre power gives the total amount of watt-hour needed for the entire mission. The total energy that a battery can provide can be calculated by multiplying its output voltage with its capacity. The battery is discharged for eighty percent, discharging further can lead to serious battery damage and loss of capacity. Dividing the required energy by the available energy and rounding up gives the number of batteries that must be linked in parallel in order to provide enough power. Again, the rounding means there is some contingency introduced. The additional energy stored in the battery can be used to extend the mission flight time if needed. Therefore the maximum flight time is calculated as well. The required batteries in parallel due to the current and due to the energy might differ. In this case the largest number is required, because both criteria cannot be violated.

With the number of cells in series and in parallel and the mass of each cell the total battery mass can be calculated. Because of the dimensions of the circular hull it is not practical to have only one battery. This is accounted for when the choice of battery was made. During each iteration the battery choice was revised to make sure that the optimal solution was used.

Example of the calculations

To illustrate the calculation described above an example is given here. This is not an optimised solution, but it is used to illustrate the process. The mission profile is 600 seconds flight time of which 40 percent is flown at full power. At full power 90 W is needed and at manoeuvre power 75 W is needed. The motors can handle 11.1 V, so that is what is designed for. The battery cell parameters used for this example are shown in Table 6.19.

Table 6.19: Battery parameters used for the example

Voltage	Capacity	Nominal Discharge Rate	Mass
3.7 V	750 mAh	35 C	18 g

The number of batteries required in series is calculated as follows.

$$N_S = \frac{U_{req}}{U_{bat}} = \frac{11.1}{3.7} = 3 \quad (6.8)$$

From this point in the calculations the batteries are assumed to be in battery packs of three batteries connected in series. Next, the number of these battery packs needed in parallel to handle the systems maximum current is determined.

$$N_{P_I} = \frac{I_{max}}{I_{max,bat}} = \frac{P_{max}/U_{req}}{Q*C} = \frac{90/11.1}{0.750*35} = 0.31 \quad (6.9)$$

N_{P_I} must be rounded up to the nearest integer, so it becomes equal to 1. To check how many battery packs are necessary in parallel to provide enough energy to fulfil the mission the total energy required is calculated. The number of packs is then calculated by dividing the total required energy by the amount of energy in a single pack (of three batteries in this case), while taking a maximum discharge of eighty percent into account.

$$E_{req} = P_{fp} * t_{fp} + P_{mp} * t_{mp} = 90 * \frac{240}{3600} + 75 * \frac{360}{3600} = 13.5 Wh \quad (6.10)$$

$$N_{P_E} = \frac{E_{req}}{N_S * U_{bat} * Q} = \frac{13.5}{0.8 * 3 * 3.7 * 0.750} = 2.03 \quad (6.11)$$

This result must be rounded up to the nearest integer, resulting in N_{P_E} being equal to 3. This is the more than required to handle the maximum current, so this is the number to continue the calculations with. As can be seen in equation 6.11, two battery packs are just not enough to provide enough energy to the system, resulting in a large additional flight time. In this case it would be wise to try to use less power, or to shorten the mission duration, so two battery packs in parallel are sufficient. The energy overshoot percentage is calculated as well.

$$t_{max} = \frac{E_{bat} * 0.8}{P_{avg}} = \frac{N_S * U_{bat} * N_P * Q * 0.8}{P_{fp} * f_{pp} + P_{mp} * (1 - f_{pp})} = \frac{3 * 3.7 * 3 * 0.750 * 0.8}{90 * 0.4 + 75 * (1 - 0.4)} * 3600 = 888s \quad (6.12)$$

As can be seen the mission duration can be extended almost for five minutes. Extending the mission even longer leads to more than eighty percent discharge which can lead to serious battery damage. Finally the mass of all batteries required is calculated.

$$m_{bat} = N_P * N_S * m_{bat,one} = 3 * 3 * 18 = 162g \quad (6.13)$$

Battery pack assembly

To combine single cells into battery pack it is not enough to just wire them in series. This is because LiPo batteries are very sensitive to overcharging and undercharging. A single cell should not drop below three volts, but if three cells are wired in series and the total output is nine volts it might be the case that one of the three cells is actually on a lower voltage than the minimum allowed three volts. This can result in a bad cell inside the

pack that reduces the capacity of the entire pack. The same goes for charging. If the total pack is at its required voltage it might be the case that one cell is at a higher voltage while the other two are lower. To ensure this does not happen a balance plug needs to be wired into the battery pack. How this is done can be seen in Figure 6.12. This balance plug allows the charger to monitor the voltages of each cell and can correct deficiencies when needed. This ensures that all cells are at the same voltage, which in turn can extend battery life.

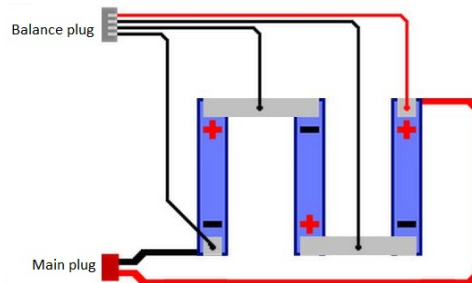


Figure 6.12: *Wiring in a three cell LiPo battery with a balancing plug*

Final battery choice

The method described above has been applied on every iteration, and the best option was picked by sorting the spreadsheet for mass. The lightest solution was not always considered the best, as they gave problems to balance the drone because of the number of batteries required. The final choice is the Zippy Flightmax 800 mAh pack. This has three cells in series which gives 11.1 volts. Two of these packs are needed in parallel to provide enough energy to ensure long enough flight time. An overview of this battery pack and its properties are given in Table 6.20. This pack is already assembled with the wiring as described in the previous section.

Table 6.20: *Zippy Flightmax specifications*³⁴

Capacity	800 mAh	Mass	62 g
Output Voltage	11.1 V	Length	56 mm
Nominal Discharge Rate	20 C	Width	22 mm
Burst Discharge Rate	30 C	Height	33 mm
Charge Rate	2 C	How Many Required	2

6.6 Hardware Interface

Figure 6.13 provides an overview of the entire hardware architecture of the airborne segment of the UAV system including interface types and electrical connections. This combines the payload, OBC, communication and propulsion hardware incorporated in the design.

The solid lines indicate power supply, the dashed lines indicate data and control connections. For a more detailed description and view of the data interfaces between all components, refer to Figure 8.1.

³⁴URL: http://hobbyking.com/hobbyking/store/..41710..ZIPPY_Flightmax_800mAh_3S1P_20C_EU_warehouse_.html

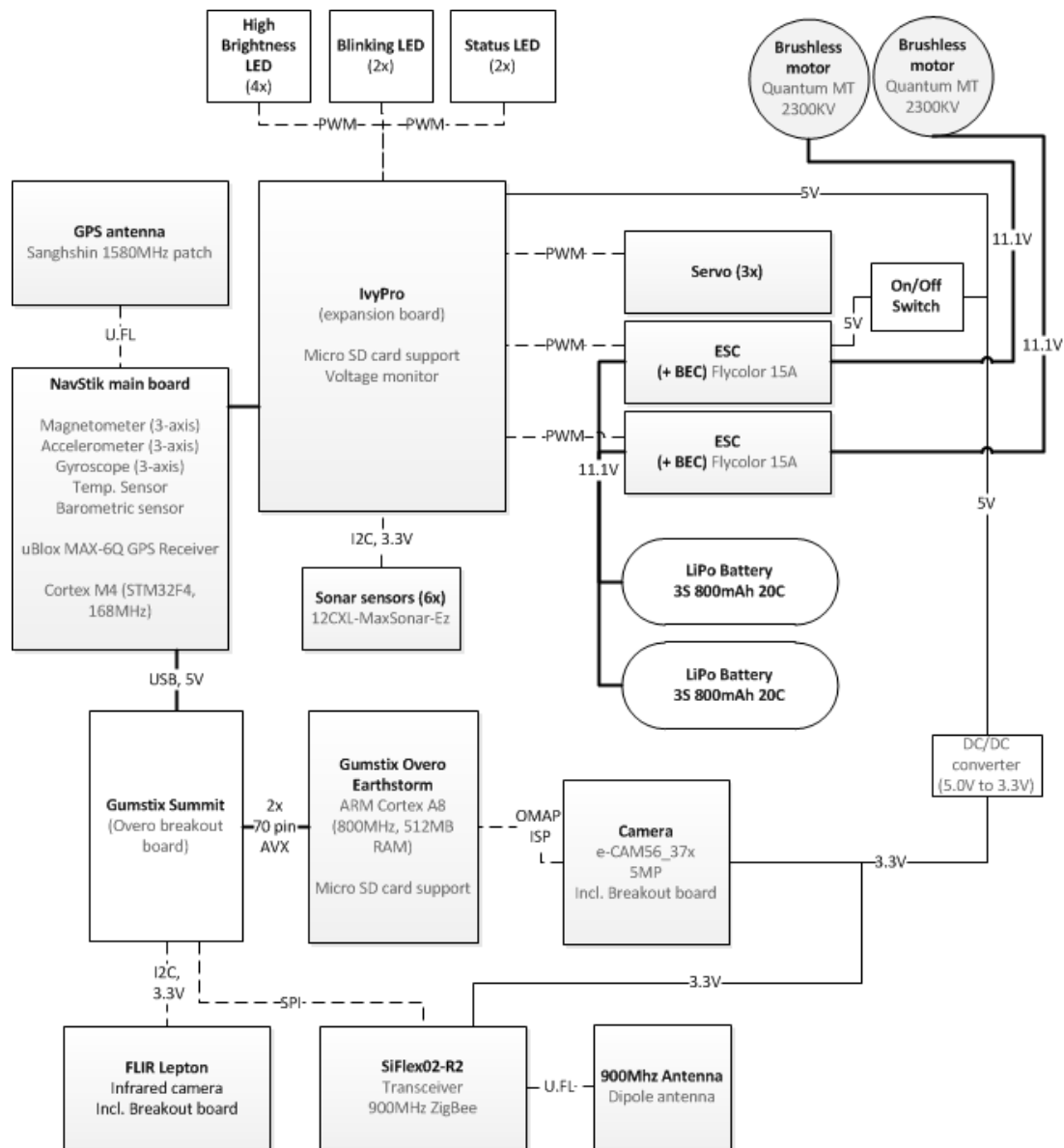


Figure 6.13: Electronics diagram of the airborne segment of the UAV system

Two main elements can be defined. The NavStik flight controller combined with the IvyPro interface board take care of the servo and ESC controls through the six PWM outputs on the IvyPro interface board. The RC receiver port on the IvyPro is used to operate the high brightness, awareness and status LED's through PWM output. The six sonar sensors are connected to the IvyPro interface board through an I2C connection which also provides the 3.3V input voltage.

The second module includes the Gumstix Overo Earthstorm COM and the corresponding Summit expansion board. The Gumstix Overo Earthstorm COM is interfaced with the e-Cam camera by means of a 24 pin OMAP ISP interface. The Flir Lepton thermal camera is connected through the Summit board as well with an ISP interface. The transceiver module is connected to the Gumstix Overo by means of an SPI connection through the Summit expansion board.

The two 3S (11.1V) batteries are connected in parallel to both electronic speed controllers. The voltage supplied to the motors is regulated by the ESC's, controlled over a PWM connection with the IvyPro interface board. The ESC's include a battery elimination circuit (BEC) to power the IvyPro and Navstik boards and the Gumstix modules. Through the BEC, the camera and SiFlex transceiver module are powered as well over a 3.3V connection.

The UAV can be switched on and off by means of a switch between the BEC output of the ESC and the IvyPro interface board.

Hardware wiring estimation

Figure 6.13 shows how hardware components interface with each other. An estimation of the wiring mass is performed assuming solid copper cables, with 0.4mm thick PVC insulation³⁵, capable of carrying the maximum current expected in the cable. Wire dimensions are defined according to the American Wire Gauge (AWG) that classifies wires according to their diameter and associated maximum current capacity³⁶. For special wires that consist of several sub-wires, such as the Universal Serial Bus (USB) and Inter-Integrated Circuit (I2C), each sub-wire was considered as an individual wire. The hardware configuration is divided into nodes, which are the hardware components itself, and connections between nodes that are divided into N_{wire} wires. The mass of all wires between two nodes (m_{node12}) is calculated by equation 6.14 and then summed for all node pairs to compute the total mass.

$$m_{node12} = 1.5 \cdot N_{wire} \left(\frac{|\beta_{node2} - \beta_{node1}|}{2\pi} \right) \pi D_{midhull} \cdot \frac{\pi}{4} \left((D_{wire} + 0.08)^2 \rho_{PVC} + D_{wire}^2 (\rho_{copper} - \rho_{PVC}) \right) \quad (6.14)$$

The equation computes the wire mass based on the arc length between two nodes (node 1 and 2) positioned on the hull at β_{node} radians clockwise positive from the front (front defined as the position of the main camera module). For a schematic of subsystem layout refer to Figure 12.17b. $D_{midhull}$ is the diameter at half the hull thickness which is $0.108m$. The wire's diameter is denoted by D_{wire} and depends on the AWG classification (type) chosen which is based on the current in the wire. The density of copper (ρ_{copper}) is $8960kg/m^3$ ³⁷ and of PVC is (ρ_{PVC}) $1450kg/m^3$ ³⁸. The principle behind equation 6.14 is to take the arc length between two nodes and multiply that by the copper's and PVC's cross sectional areas with their associated densities; necessary unit conversions to SI units are performed. A design factor of 1.5 on the wire arc length is taken to account for non-perfectly arced wire placement and necessary extra wire that may be necessary when placing the hardware in the UAV. For the connections to the motor and servo (at the UAV's centre), the wire along the strut to the centre is accounted for by adding the inner hull radius of $0.094m$ is to the length calculation. The dimensioning of all wiring and subsystem location is given in Table 6.21.

Table 6.21: Wiring mass estimation based on wire current capacity and AWG classifications

Node 1	Node 2	Number of wires	Current capacity [A]	Node 1 position [deg]	Node 2 position [deg]	AWG type	Diameter [mm]	Length [m]	Mass wires [g]
Battery 1	ESC 1	2	9	-90	-135	21	0.72	0.127	1.69
Battery 1	ESC 2	2	9	270	135	21	0.72	0.382	3.56
Battery 2	ESC 1	2	9	90	225	21	0.72	0.382	3.56
Battery 2	ESC 2	2	9	90	135	21	0.72	0.127	1.69
ESC1	Motor 1	3	9	-135	-180	21	0.72	0.268	4.08
ESC2	Motor 2	3	9	135	180	21	0.72	0.268	4.08
IvyPro	ESC 1	3	0.09	54	225	40	0.080	0.483	0.31
IvyPro	ESC 2	3	0.09	54	135	40	0.080	0.229	0.28
IvyPro	Servos	9	0.09	54	54	40	0.080	0.141	0.79
IvyPro	LED HB 4x	2	0.86	54	0	30	0.25	0.153	0.46
IvyPro	LED Blink Right	2	0.09	54	90	40	0.080	0.102	0.17
IvyPro	LED Blink Left	2	0.09	54	-90	40	0.080	0.407	0.20
IvyPro	LED Status 2x	4	0.09	54	180	40	0.080	0.356	0.40
IvyPro	Sonar 2x Right 1x Top	4	0.09	54	180	40	0.080	0.356	0.39
IvyPro	Sonar 2x Left 1x Bottom	4	0.09	54	-90	40	0.080	0.407	0.40
IvyPro/BEC	Camera	2	0.17	54	0	37	0.11	0.153	0.22
IvyPro/BEC	Transceiver	2	0.7	54	180	31	0.23	0.356	0.56
NavStik Main	GPS	2	0.09	54	0	40	0.080	0.153	0.17
Gumstix Summit	FLIR Lepton	4	0.09	-5	0	40	0.080	0.014	0.33
Gumstix Summit	SiFLEX02	1	0.09	-5	-180	40	0.080	0.495	0.10
Gumstix Overo	Camera	1	0.09	-5	0	40	0.080	0.014	0.08
SiFLEX02	Antenna 1	2	0.53	180	180	32	0.20	0.0	0.0
SiFLEX02	Antenna 2	2	0.53	180	0	32	0.20	0.509	0.57
NavStik Main	Gumstix Summit	4	0.5	54	-5	32	0.20	0.167	0.74
Total		67						6.049	24.83

The total wiring mass is 24.83g with total wire length of 6.049m. Note that the Sonar sensors use a common bus (wire) so only wire lengths to the furthestmost two sensors are taken. The mass of connecting pins/connectors is neglected in the calculations as estimates for those were not available. By using the 1.5 factor, the mass of connectors would be accounted for.

³⁵URL: <http://www.markelcorporation.com/downloads/StrandingandWallThk.pdf>

³⁶URL: <http://hyperphysics.phy-astr.gsu.edu/hbase/tables/wirega.html>

³⁷URL: <http://www.rsc.org/periodic-table/element/29/copper>

³⁸URL: <http://www.vinidex.com.au/technical/material-properties/pvc-properties/>

6.7 Ground Control Station

This section of the report offers information on the final Ground Control Station (GCS) design and the reasoning behind it. To do this in a clear and concise way, the section is split up in three parts. The first to explain the requirements imposed on the GCS, and the second to explain the chosen design. The last part explains the chosen transportation container for the UAV and the GCS.

6.7.1 Requirements on GCS

There are not a lot of requirements relating directly to the GCS. Direct requirements include the total system mass (2kg) and the readability of the display (readable under direct sunlight conditions). However, a lot of requirements on the system impose requirements on the GCS; for instance, the communications range, the ability to control the UAV through first-person view video as well as the video characteristics like resolution and framerate, and the fact that the remaining energy level has to be displayed on the system. A detailed discussion on the requirements and the extent to which they are met is given in Chapter 13.

6.7.2 GCS Design

An assessment of the necessary components of the Ground Control Station is made to gain a better overview of what needs to be designed. These components are: audiovisual feedback system for the operator, control system for the operator, a communications system, a data handling system and a power supply. These components are discussed below with according chosen solution.

The first component is the audiovisual feedback system for the operator. This system must consist of a combination of displays and speakers, and must be practical in use. Existing systems that were considered are (amongst others) tablet computers, laptop computers and video glasses. One big difference between the systems is the fact that video glasses can be used in any situation, whereas tablets and laptops either need a stand or have to be held. This means the hands of the operator will not be free to give control inputs, unless the controls are integrated with the device and can be operated while also carrying the device. This restricts design options, while the use of video glasses offers the same performance without the restrictions. A downside of using video glasses is that the operator can only see from the UAV's perspective. To compensate for this, a built-in camera on the video glasses can send a live feed to the display, enabling the operator to see what's in front of him while still controlling the UAV by using a screen-in-screen method (having a small part of the monitor displaying a secondary feed). To account for the auditive part, the glasses must be outfitted with earphones. This is a standard feature of most video glasses, and is therefore not difficult to find.

The second component is the control system for the operator. Many different controllers exist in different shapes and sizes, all with their own application. Three standard controller layouts were considered in this selection process: a regular RC controller, a joystick, and a gamepad. The joystick is a common control device for aircraft, and offers intuitive attitude control. However, it would have to be placed on a stable surface from which it can be comfortably controlled. This means a table or other raised surface must be available at all times, and this is impractical. The RC controller and a gamepad remain. Keeping complexity in mind, the RC controller, with its cascade of options and settings, was deemed too complicated for regular use. Gamepads on the other hand are specifically designed to be as simple and ergonomically comfortable as possible, and offer high software flexibility to be able to interface with almost all computer driven systems. For this reason, gamepads are not uncommon in for example military control applications^{39,40}. Therefore, a gamepad was chosen as a control input system. The most common gamepads with the highest level of technological and ergonomic advancement are those developed and made by Microsoft and Sony, which differ mostly in button placement and controller shape. Since controller preference is user-dependant, the choice of controller is left to the operator.

The third component is the communications system. The features of the communications system of the ground station are heavily restricted and mostly predetermined by the properties of the communications system on board the UAV. To reduce GCS design complexity, a decision was made to use the same transceiver module on the ground control station, with two omnidirectional dipole antennas. One will be switching between receive

³⁹URL:<http://www.dailymail.co.uk/sciencetech/article-3082276/War-games-Russia-reveals-latest-tank-controlled-PLAYSTATION-controller.html>

⁴⁰URL:<http://www.army-technology.com/projects/xm1216-small-unmanned-ground-vehicle-sugv/>

and send mode, the other is fixed in receive mode. Which antenna is switching between Tx/Rx-mode depends on which antenna receives the best signal.

The fourth component, a data handling system, is responsible for taking control inputs and translating these into signals to be sent by the communications subsystem, and for taking the signals from the UAV and converting this into data to be sent to the audiovisual system. Basically, any system with sufficient computing power will suffice, and for this reason the choice was made to use a tablet computer for this purpose. It adds the advantage of having another screen on which information can be displayed in addition to the video glasses, so that non-operators can still see what's happening. It is also small and lightweight, so it's ideal for carrying around. An important point to keep in mind is to select a tablet with a sufficient amount of communication ports. For the choice of tablet, an analysis of current state-of-the-art technology must be performed. Since computer technology is advancing constantly, this selection is best to be performed once software demands are known.

6.7.3 Transportation container

The GCS and UAV will have to be transported to the mission area prior to deployment. This indicates a need for a container to hold one or both of these items. Having the UAV and GCS in the same container would be very convenient, although this does pose a challenge in terms of available space. A conversation with a fireman granted a few pointers as to which methods of transportation would be convenient for the GCS. Emphasis was placed on accessibility and deployability of the container in which the GCS and UAV would be held. A fireman wearing gloves should be able to transport the GCS and UAV to the location of interest along with his other gear. Also, the container should offer a simple layout. This speeds up the deployment process by decreasing the time it would take to look for certain components. The container should be sturdy and easily stackable to fit on the fire truck, and lightweight so it doesn't encumber the firefighter. As an example, the standard fireman cloth medic pouch was discussed. With a standard layout, the sought-after item can be located with ease in situations where fast handling is necessary. Its small size makes it very portable and integrable into the standard fireman kit. A downside is having to open many lids and covers before the item can be taken out, and some of these pockets are difficult to handle while wearing glove due to the small size. A solution to this would be having rigid compartments instead of the soft cloth pockets, but that would reduce mobility.

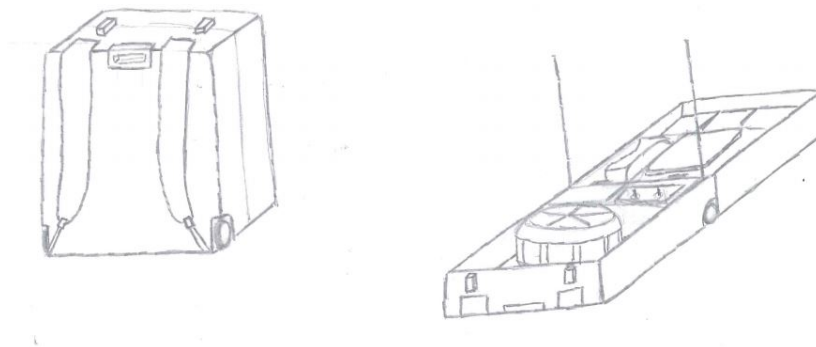


Figure 6.14: *Sketch of the ground control station*

The most commonly used containers in everyday life are backpacks, suitcases and trolleys. The differences between the three groups lie in rigidity and carrying mechanism, all with their own benefits and drawbacks. A combination of the three would offer a choice to the person carrying it and therefore be adaptable to every situation; the trolley wheels reduce the effort to carry the container so that the operator can take more other items with him. When the ground is not suitable for wheels, the container can be carried by hand or on the back, depending on whether the back is occupied by other gear. Since a simple and unchanging layout is considered beneficial, the UAV and GCS will have to be held in place by some means. This sparked the idea of having a compartmentalized rigid case, featuring straps to hold the different deployables in their place.

A sketch of this idea is shown in Figure 6.14. This design also offers the possibility of partially integrating the GCS into the case, such as the power source, antennae, wiring and spare parts. This reduces deployment complexity and duration, and therefore saves time. The rectangular shape of the case makes it easily stackable, and together with the straps also protects the contents during transit. To guarantee sturdiness and durability

of the case while still being lightweight, it will be made out of hard plastic. This also makes it waterproof, and keeps the weight to a minimum.

This chapter discussed the selection of payload and on board computing hardware, together with the determination of the link budget and corresponding hardware. The required battery properties based on the power budget are determined as well on which the choice of batteries is based accordingly.

7 | Subsystem Design: Structures

The structure subsystem houses, protects and joins the different subsystems of the UAV so that they can operate together in order to perform the UAV's mission. This relation with the rest of the subsystems imposes constraints on the structure regarding size and load bearing capabilities. For example, the structure houses the payload, therefore a constraint on the minimum structure dimensions is given by the dimensions of the payload.

The structure also needs to fulfill certain requirements in order for the UAV to perform its mission successfully. As an example, one of the most important requirements for the structure is that it must allow the drone to endure collisions with its surroundings.

The structure of the Inspection Pocket Drone consists of two main parts. The first one is the hull. This part of the structure houses and protects the payload, OBC, Communications and Power subsystems. The hull surrounds and protects the propellers as well. Moreover its inner side acts as a duct, increasing the efficiency of the propulsion subsystem. The second part of the structure consists of three struts that connect the hull to the propellers in the middle of the duct.

Given the constraints of the different subsystems a geometry for the structure was outlined. This is presented in Figure 7.1. It is important to note that the hull geometry of the first design iterations was different, but it will not be discussed here since it is not related to the final design.

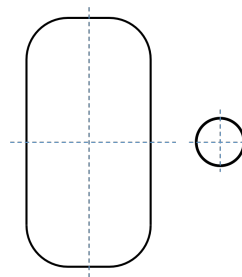


Figure 7.1: *Geometry of the hull cross section (left) and the strut's cross section (right)*

The geometry of the inner side of the hull was given by constraints from the propulsion subsystem. In addition, the hull needed to have a closed cross section in order to protect the payload. For the sake of simplifying the design and the stress calculations, the outer side of the cross-section was mirrored from the inner side and the bottom was mirrored from the top. For the strut cross section, it was considered to use airfoil shaped beams or circular beams. The interference was low in both cases, and even though the flow interference was lower with the airfoil cross section, the circular cross section was chosen in order to simplify the stress calculations. It is important to note that only the geometry of the structure was fixed, but the dimensions varied in different designs and iterations, to adapt the structure to the payload and the loads present.

7.1 Sizing for Loads

Since the geometry of the structure was set, the only decisions made during the design concerned the dimensions. The design of the hull and of the struts was performed separately. Subsections 7.1.1 and 7.1.2 present the design process of the hull and the struts respectively.

7.1.1 Hull structure design

The hull consists of 8 elements shown in Figure 7.2. Due to symmetry, the dimensions that define the hull structure, as shown in Figure 7.2, are the constant thickness of the cross section and 3 size dimensions, leaving a total of 6 variables: d_1 , d_2 , d_3 and t .

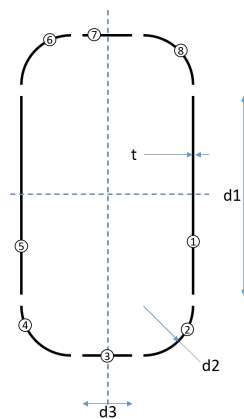


Figure 7.2: Hull cross section elements and dimensions

In every design, the minimum size dimensions required were chosen, in order to reduce the structural weight as much as possible. The size dimensions used in iteration 11 of the design are presented in Table 7.1. Then a value was chosen for the thickness and it was checked whether the structure was strong enough to cope with the applied loads without experiencing damage. If the structure was strong enough, the thickness was reduced. If the structure was not strong enough the thickness was increased. The process followed to check if the stresses present in the structure were too high is presented in the next paragraphs, accompanied by examples of the calculations. The calculation of the stresses was performed using a script written by the design team.

Table 7.1: Length of the size dimensions of the hull cross section used in design iteration 11

Dimension	d1	d2	d3
Magnitude [mm]	40	1	26

The first step in order to analyze the stresses in the hull structure is to determine the loads acting on it. The loads acting on the hull are shown in Figure 7.3. These loads are a combination of the worst case scenario loads present under vertical climb flight, horizontal forward flight, impact and during manoeuvres.

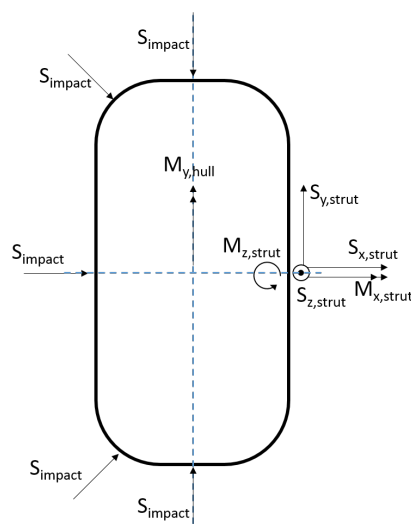


Figure 7.3: Loads applied on the hull

The maximum $S_{y,strut}$ present in the cross section is equal to the force that one strut applies on the hull when the thrust is maximum, i.e. one third of the maximum thrust or $S_{y,strut} = \frac{T_{max}}{3}$. The $M_{x,strut}$ and $M_{z,strut}$ are the moments that the strut applies on the hull due to the effect of the swash plate on the propellers. The maximum values of $M_{x,strut}$ and $M_{z,strut}$ are assumed, as a worst case scenario, to be the maximum moment generated by the propellers, $M_{p,max}$. The force $S_{x,strut}$ is the axial force that the strut applies to the hull. This force appears when the UAV is at a pitch angle and is responsible for counteracting the component of the weight of the hull

that is perpendicular to the thrust axis. The weight of the hull is carried by the three struts, however in this case it is assumed that one strut carries all the hull weight as a worst case scenario. The magnitude of the horizontal force is then $S_{x,strut} = W_{hull} \cdot \sin(\theta_{max})$, where W_{hull} is the weight of the hull including all the subsystems housed in it, and θ_{max} is the maximum pitch angle of the drone. Another load related to the weight of the hull is $S_{z,strut}$. This is the load that the strut applies on the hull in order to compensate for its weight when the strut is in horizontal position. The magnitude is $S_{z,strut} = W_{hull} \cdot \cos(\theta_{max})$. In this case a moment $M_{y,hull}$ is also present, caused by the weight of the hull located between two contiguous struts. The magnitude of this moment is $M_{y,hull} = 0.5 \cdot D_{inner} \cdot (1 + \cos(30)) \cdot W_{hull} \cdot \sin(\theta_{max})$, where D_{inner} is the inner diameter of the hull. The impact load S_{impact} was modelled as a point load applied either centred at the top or bottom of the cross section, at the centre of the side of the cross section, or at the two outer corners, always acting perpendicular to the surface of the cross section. The process to calculate its magnitude is described in Section 7.2. The calculations of the stresses were performed for the case where all the previous loads are applied simultaneously, and for the 5 different locations of the impact load. The values of the loads in iteration 11 are presented in Table 7.2. Moreover during the calculations the shear loads $S_{x,strut}$, $S_{y,strut}$ and S_{impact} were translated to act through the shear centre. Extra moments around the x,y and z axis were added to compensate for this translation.

Table 7.2: Magnitude of the loads depicted in Figure 7.3 in design iteration 11

$S_{x,strut}$ [N]	$S_{y,strut}$ [N]	$S_{z,strut}$ [N]	S_{impact} [N]	$M_{x,strut}$ [Nm]	$M_{y,hull}$ [Nm]	$M_{z,strut}$ [Nm]
2.81	3.00	2.91	278.30	0.13	0.12	0.13

The next step to calculate the stresses on the cross section is to determine the centroid location. Since the cross section is symmetric, the centroid is located on the intersection of the axis of symmetry. Measuring from the centre of element 3, the centroid location in the horizontal direction is $x_c = 0$ and in the vertical direction $y_c = d2 + \frac{d1}{2}$.

The following step in the calculations involves determining the moments of inertia of the cross section about its centroid. Due to symmetry the product of inertia I_{xy} is zero. The other two moments of inertia, I_{xx} and I_{yy} were calculated by adding up the individual contributions of each element of the cross section, as shown in Equations 7.1 and 7.2.

$$I_{xx} = \sum_{i=1}^{i=8} I_{xx,i} = 3.6294 \cdot 10^{-8} m^4 \quad (7.1)$$

$$I_{yy} = \sum_{i=1}^{i=8} I_{yy,i} = 1.9794 \cdot 10^{-8} m^4 \quad (7.2)$$

In Equations 7.1 and 7.2, $I_{xx,i}$ and $I_{yy,i}$ are the moments of inertia of the i^{th} element of the cross section with respect to the centroid's x axis and y axis respectively. The values of $I_{xx,i}$ and $I_{yy,i}$ in iteration 11 are presented in Table 7.3.

Table 7.3: Moments of inertia of the elements of the hull cross section about the centroid in iteration 11

Element	1	2	3	4	5	6	7	8
$I_{xx,i} [10^{-9} m^4]$	5.33	0.67	11.47	0.67	5.33	0.67	11.47	0.67
$I_{yy,i} [10^{-9} m^4]$	7.84	0.29	1.46	0.29	7.84	0.29	1.46	0.29

With all the calculations regarding the centroid and the moment of inertia sorted out, the normal stress due to bending, $\sigma_{bending}$, can be calculated. The formula for $\sigma_{bending}$ is given in Equation 7.3 [59].

$$\sigma_{bending} = \frac{-M_y \cdot x}{I_{yy}} + \frac{M_x \cdot y}{I_{xx}} \quad (7.3)$$

Equation 7.3 gives the normal stress in Pascals at the point located at (x, y), with x and y measured from the centroid. In order to find the stress distribution over the cross section, a list of x and y locations belonging to the elements needs to be made. Every pair of x and y on the list is then used as input in Equation 7.3. A total of 632 points were used in the script.

Another contribution to the normal stress is due to the load $S_{z, strut}$. This load induces the stress σ_{axial} , given by Equation 7.4.

$$\sigma_{axial} = \frac{S_{z, strut}}{\sum_{i=1}^{i=8} A_i} \quad (7.4)$$

Equation 7.4 gives as a result a constant. This constant is added to the normal stress calculated using Equation 7.3 on the 551 points to obtain the total normal stress distribution over the cross section, $\sigma_{normal} = \sigma_{bending} + \sigma_{axial}$.

Apart from normal stress σ_{normal} , shear stress τ is also present in the cross section. In order to calculate the shear stress distribution, the shear flow q on the cross section needs to be calculated. Then using Equation 7.5 the shear stress can be calculated at every location on the cross section, if the local thickness t is known [59].

$$\tau = \frac{q}{t} \quad (7.5)$$

The shear flow q has two main contributions: the shear flow due to shear forces, q_s , and the shear flow due to torque, q_t . For a closed section such as the one being considered, the shear flow q_s has two components as well, a varying, so called "basic" shear flow q_b obtained by "cutting" the cross section at a certain location and assuming the cross section is open, and a constant, "zero" shear flow q_0 which equals the value of the shear flow at the location of the cut made to obtain q_b .

In the hull cross section, the cut was made at the middle of elements 3 as seen in Figure 7.4. The resulting cross section was divided into segments, each delimited by a number in every end. This can be seen in Figure 7.4 as well. The basic shear flow between points 1 and 2 is denoted $q_{b,1-2}$. The same format is used all around the cross section. The expression for the basic shear flow between point i and point j for a thin-walled structure is given in Equation 7.6 [59].

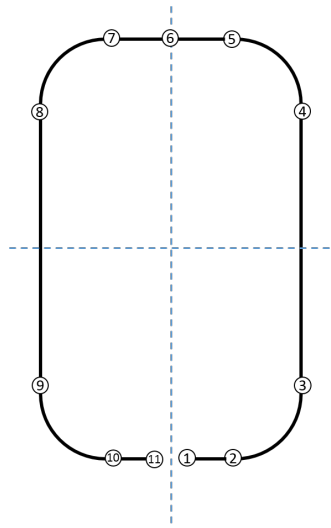


Figure 7.4: Cross section division for the calculation of the basic shear flow q_b

$$q_{b,i-j} = q_{b,i} - \frac{S_x}{I_{yy}} \int_0^s t x ds - \frac{S_y}{I_{xx}} \int_0^s t y ds \quad (7.6)$$

In Equation 7.6, s is the lengthwise direction of segment $i-j$ from i to j , $q_{b,i}$ is the shear flow at point i , t is the thickness of the structure between the points i and j , x is the distance from the centroid in the x direction on the segment $i-j$, y is the same but in the y direction. Equation 7.6 was applied at the cross section, beginning at the cut points assuming that $q_{b,1} = 0$ and following the order 1-2, 2-3, 3-4, etc. until 11. If the calculations are performed correctly, $q_{b,11} = 0$.

The constant shear flow q_0 acting on the cross section is shown in Figure 7.5. In order to determine the magnitude of q_0 Equation 7.7 was solved. This equation specifies that since the shear forces act through the shear centre, the cross section does not experience twist [59].

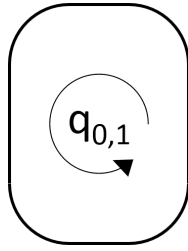


Figure 7.5: Location and direction of the constant shear flow q_0

$$0 = \frac{1}{2A_c G} \oint_{cell1} \frac{q_s}{t} \quad (7.7)$$

In Equation 7.7, q_s is the shear flow due to shear forces, comprised of the basic component q_b already known, and the constant shear flow q_0 that is being solved for. Moreover, A_c is the enclosed areas of the cross section and G is the shear modulus of the material of the cross section.

The next shear flow to be solved for is q_t . Before it can be determined, the torque around the shear centre must be determined. In order to do so the location of the shear centre needs to be determined. Due to symmetry, the shear centre location is the same as the centroid location, from the centre of element 3 $x_{sc}=0$, $y_{sc}=d2+\frac{d1}{2}$. With this values, the total torque around the shear centre can be found using Equation 7.8.

$$M_z = M_{z, strut} + S_y(x_{S_y} - x_{sc}) - S_x(y_{S_x} - y_{sc}) \quad (7.8)$$

In Equation 7.8, x_{S_y} and y_{S_x} are the x and y coordinated of the point of action of the total shear loads S_x and S_y . With the value of M_z known q_t can be determined with Equation 7.9. [59].

$$q_t = \frac{M_z}{2A_c} \quad (7.9)$$

With q_t determined, the total shear flow can be found by adding all of the components up, and the shear stress τ can be found using Equation 7.5.

Knowing the normal and the shear stress distribution over the cross section, the von Mises stress, Vm can be calculated. The von Mises stress is given by Equation 7.10 [60].

$$Vm = \sqrt{\sigma_{normal}^2 + 3\tau^2} \quad (7.10)$$

If the maximum von Mises stress Vm is lower than the tensile yield stress of the cross section material σ_{yield} , the structure will not fail. A safety factor of 1.5 was used in the calculation of the von Mises stress, before comparing it with σ_{yield} .

As stated previously, if the von Mises stress was too high, the thickness of the cross section was increased, if Vm was lower than σ_{yield} , t was decreased. The process described in the previous paragraphs was then followed again. For iteration 11 the resulting thickness was $t=1\text{ mm}$.

7.1.2 Struts structure design

The cross section of the three struts connecting the propellers to the hull is shown in Figure 7.6. The cross section is a hollow circle, with dimensions $R_{strut, inner}$ and t_{strut} . As seen in the figure as well, the part of the strut where the propellers are located is assumed to be clamped. The maximum loads acting on the strut are presented in Figure 7.7. The highest loads are: S_y is equal to one third of the maximum thrust, $S_y = \frac{T_{max}}{3}$, S_x is equal to the weight of the hull, $S_x = W_{hull}$, S_z is axial component of the hull weight, $S_z = W_{hull} \sin(\theta_{max})$, M_x is the moment that the S_y generates on the strut at the maximum distance L from the propellers, plus the maximum moment generated

by the propellers, $M_x = S_y L + M_{p,max}$, M_y is the moment that the strut must apply on the hull to compensate for the moment on that direction on the hull due to its weight, $M_{y,hull} = 0.5 \cdot D_{inner} \cdot (1 + \cos(30)) \cdot \frac{1}{3} W_{hull} \cdot \sin(\theta_{max})$, finally M_z is equal to the maximum moment that the propellers can generate, $M_z = M_{p,max}$. An additional impact load S_{impact} is present, that can either act in place of S_y , if divided by 3, or in place of S_z . This S_{impact} is given by the mass of the propulsion subsystem and the maximum g load experienced upon impact, $S_{impact} = m_{prop} g_{max}$. Some assumptions regarding the loads need to be noted. The shear force S_y is assumed to act through the shear centre of the cross section, located on the centroid due to symmetry. The axial force S_z is also assumed to act through the centroid. The magnitude of the loads can be seen in Table 7.4.

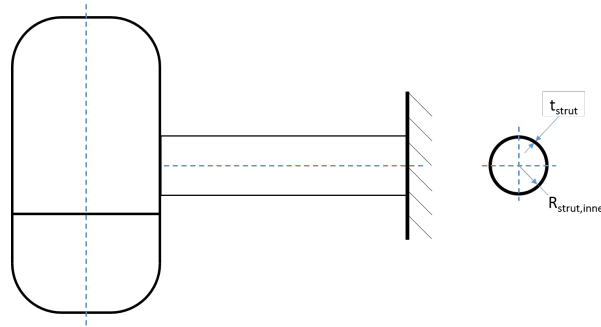


Figure 7.6: Strut cross section and end clamping conditions

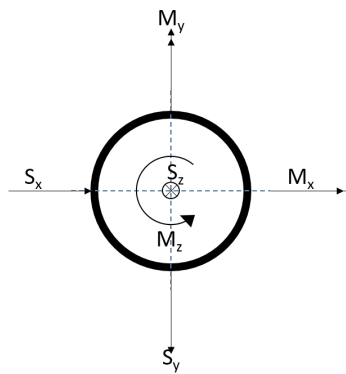


Figure 7.7: Loads applied on the strut

Table 7.4: Magnitude of the loads acting on the a strut in iteration 11 as presented in Figure 7.7

$S_x [N]$	$S_y [N]$	$S_z [N]$	$M_x [Nm]$	$M_y [Nm]$	$M_z [Nm]$	$S_{impact} [N]$
3.92	3	2.73	0.41	0.16	0.13	57.38

A similar process to the one followed with the calculations for the hull stresses was followed for the struts. The dimensions of the lightest strut cross section that did not result in structural failure were $R_{strut,inner} = 4.6mm$ and $t_{strut} = 1.1mm$. However, another failure type needed to be investigated, buckling. Due to the high compressive loads caused by impacts, the strut could buckle and fail.

For the buckling analysis, it was assumed that the strut was simply supported on both ends, as shown in Figure 7.8. The critical compressive load at which the strut fails is given by Equation 7.11 [59].

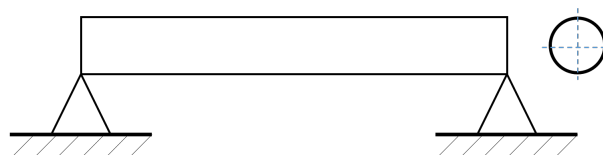


Figure 7.8: Set up assumed for the buckling analysis of the struts

$$P_{crit} = \frac{\pi^2 EI}{L_{beam}^2} \tag{7.11}$$

In Equation 7.11, P_{crit} is the critical load at which the strut fails under buckling, E is the Young’s modulus of the material the strut is made out of, I is the smallest of the moments of inertia I_{xx} and I_{yy} , given in Equation 7.12, and L_{beam} is the length of the strut. A safety factor for the critical load of 1.5 was used in the equation. To determine if the strut would buckle, the values of the design were substituted in the equation and the critical load P_{crit} was compared to the actual applied load. The values in iteration 11 are presented in Table 7.5.

$$I_{xx} = I_{yy} = \frac{\pi((R_{strut,inner} + t_{strut})^4 - R_{strut,inner}^4)}{4} \tag{7.12}$$

Table 7.5: Values used to calculate the critical buckling load in iteration 11

$E[Pa]$	$I[m^4]$	$L_{beam}[m]$
$1.55 \cdot 10^9$	$4.77 \cdot 10^{-10}$	0.094

The critical load with the values presented in Table 7.5 is $P_{crit} = 826N$.

For the case of iteration 11, for an axial load of 57.38 N it was thus determined that the struts would not buckle.

7.2 Impact Resistance

Two primary requirements mentioned in Section 2.3, namely IPD-AAoI-Enter-B-4 and IPD-GI-Maneuver-D-2 pertain to the vehicle’s ability to withstand impact loads. Therefore, it is of primary importance that this increased high load situation is designed for. In this section, several solutions will be presented and traded-off in order to arrive at the optimum solution. The goal is to design an impact resistance subsystem that introduces the least amount of additional weight into the structure, eases assembly and environmentally friendly. First, the system model will be introduced, followed by elaboration on the concepts. Finally, the chosen concept is presented.

The design team took a decision based on controllability issues that the highest achievable translational speed that the vehicle will experience is $3 \frac{m}{s}$. This figure is based on the maximum velocity the UAV will traverse at within or in the vicinity of a building or obstacle. Therefore, it has to be able to withstand impact loads at that speed. The vehicle is modelled as 2 masses connected together with a spring and a damper with one of the spring and damper connected between one of the masses and the environment. One of the masses is the propulsion subsystem, the other mass connected with the environment is the total hull housing the payload and other subsystems. This model is schematised in Figure 7.9. In this model, it was assumed that the hull is rigid, hence, it does not deform. This allowed to model the hull as a point mass. It is also assumed there is no damping between the two masses as the already connecting struts (made of HDPE material) do not have significant damping properties.

Figure 7.9: Impact resistance model to examine relative displacements of the hull and the propulsion unit

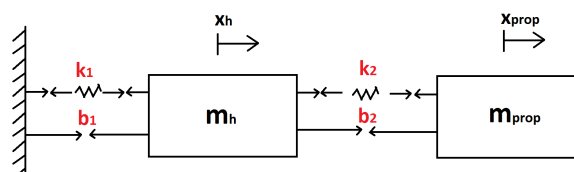


Figure 7.9 helps to develop a state-space system to examine the situation, so the next step in the process is to set up this state-space model which is done using Equation 7.13 to Equation 7.17 [61]. In these equations x_h corresponds to the positive horizontal displacement of the hull, whereas x_{prop} defines the horizontal displacement of the propulsion subsystem.

$$\ddot{x}_h m_h = k_2(x_{prop} - x_h) - k_1(x_h) + b_2(\dot{x}_{prop} - \dot{x}_h) - b_1(\dot{x}_h) \quad (7.13)$$

$$\ddot{x}_{prop} m_{prop} = b_2(\dot{x}_h - \dot{x}_{prop}) + k_2(x_h - x_{prop}) \quad (7.14)$$

$$x_1 = x_h \quad \text{and} \quad x_2 = \dot{x}_1 = \dot{x}_h \quad \text{and} \quad \dot{x}_2 = \ddot{x}_h \quad (7.15)$$

$$x_3 = x_{prop} \quad \text{and} \quad x_4 = \dot{x}_3 = \dot{x}_{prop} \quad \text{and} \quad \dot{x}_4 = \ddot{x}_{prop} \quad (7.16)$$

$$\begin{bmatrix} \dot{x}_1 \\ \dot{x}_2 \\ \dot{x}_3 \\ \dot{x}_4 \end{bmatrix} = \begin{bmatrix} 0 & 1 & 0 & 0 \\ \frac{-k_1 - k_2}{m_h} & \frac{-b_2 - b_1}{m_h} & \frac{k_2}{m_h} & \frac{b_2}{m_h} \\ 0 & 0 & 0 & 1 \\ \frac{k_2}{m_{prop}} & \frac{b_2}{m_{prop}} & \frac{-k_2}{m_{prop}} & \frac{-b_2}{m_{prop}} \end{bmatrix} + \begin{bmatrix} 0 \\ 0 \\ 0 \\ 0 \end{bmatrix} u \quad (7.17)$$

As can be seen, there is no input acceleration to the state-space system, however, it is best to model the system specifying an initial velocity input on both the hull and the propulsion subsystem. These initial conditions are defined in Equation 7.18. These velocity inputs were given a negative magnitude since they are opposite to the positive displacements of the system defined earlier. Additionally, the spring constant k_2 of the stiffening strut can be modelled as an axially loaded beam as it is shown in Equation 7.19. [62]

$$x_0 = \begin{bmatrix} V_{0,h} \\ V_{0,prop} \end{bmatrix} = \begin{bmatrix} -3 \\ -3 \end{bmatrix} \frac{m}{s} \quad (7.18)$$

$$k_2 = \frac{E_{strut} A_{strut}}{L_{strut}} = \frac{1.55 * 10^9 * 6.3 * 10^{-5}}{0.095} = 1.03 * 10^6 \frac{N}{m} \quad (7.19)$$

In this situation, the cross-sectional area of the strut is a hollow cylinder with an inner radius of 4 mm and an outer radius of 6 mm. One also has to model the impact resisting foam that is attached to the outer side of the hull, namely, one has to calculate k_1 and b_1 . These values are introduced in Subsection 7.2.2 below, and their values are $12282 \frac{N}{m}$ and $89.074 \frac{Ns}{m}$. Also, the mass of the hull is set to be 537.5 grams and the mass of the propulsion subsystem is set to be 121.5 grams. The state-space matrix with the substituted values can be seen in Equation 7.20.

$$\begin{bmatrix} \dot{x}_1 \\ \dot{x}_2 \\ \dot{x}_3 \\ \dot{x}_4 \end{bmatrix} = \begin{bmatrix} 0 & 1 & 0 & 0 \\ \left(\frac{-12282 - 1.03 * 10^6}{0.5375} \right) & \frac{-0 - 89.074}{0.5375} & \frac{1.03 * 10^6}{0.5375} & \frac{0}{0.5375} \\ 0 & 0 & 0 & 1 \\ \frac{1.03 * 10^6}{0.1215} & \frac{0}{0.1215} & \frac{-1.03 * 10^6}{0.1215} & \frac{-0}{0.1215} \end{bmatrix} + \begin{bmatrix} 0 \\ 0 \\ 0 \\ 0 \end{bmatrix} u \quad (7.20)$$

The results of the state-space simulation show that the maximum difference between the displacements of the hull and the propulsion subsystem is a negligible $3.6 * 10^{-5}$ m. The insignificance of this value lies in the fact that the struts that connect the hull to the propulsion subsystem are very stiff.

To lower the average impact load on the hull and, therefore, reduce the necessity of strengthening its structure, the use of a buffer or impact reducing/absorbing layer was introduced to the design. Both concepts were only introduced in iteration 4, as will be explained in Section 12.4.2, and analysed for relative performance and one was selected to be introduced into the final design. The design state at iteration 4 was a UAV mass of 0.516kg with an outer radius of 0.119m.

7.2.1 Impact load reduction using spring buffer

The impact load reducing spring buffer concept does not dissipate the kinetic energy (KE) from impact, but rather reduces the average impact load by converting (KE) to elastic potential energy (EPE) and then back to (KE) over time. By allowing deformation of a spring, the rebound time of the UAV is lengthened resulting in a reduced average load. As traditional springs will be bulky and add too much weight, a wave strip spring concept was thought of as shown in Figure 7.10.

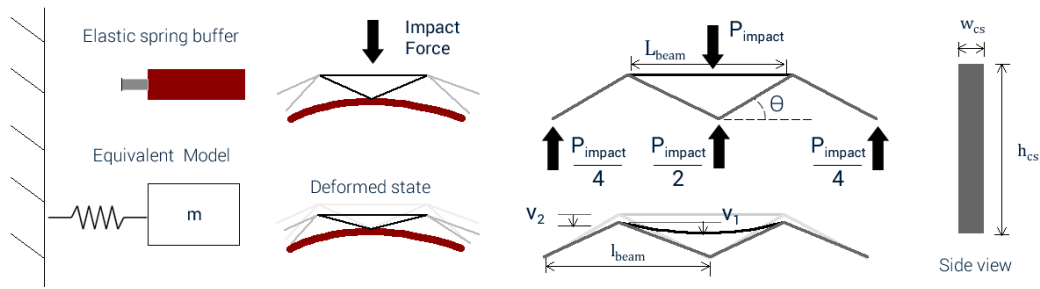


Figure 7.10: Wave strip spring buffer on outer edge of UAV (UAV mass m) hull

As seen in Figure 7.10, upon impact the spring will deform to convert KE to EPE. The rebound velocity will be equal to the impact velocity of $3m/s$ as in elastic collision the total KE is conserved¹. The strip spring is modelled as a conventional spring with stiffness k_{spring} by computing the deformation mechanics of the buffer upon loading. The deformation of a centrally loaded straight beam is given by equation 7.21 [63].

$$v_{def} = \frac{P_{impact} L_{beam}^3}{48EI} \quad (7.21)$$

Assuming that the top horizontal beam is loaded centrally by P_{impact} and the left triangular element is centrally loaded by $\frac{P_{impact}}{2}$ as half the impact load is carried by the right, and half by the left, triangular section, then there are two centrally loaded beams. The triangular section is modelled as a equivalent straight beam with length l_{beam} given by equation 7.22.

$$l_{beam} = \frac{L_{beam}}{\cos\theta} \quad (7.22)$$

The total displacement of the buffer system is the sum of the displacement of both beams (the top horizontal and triangular element) as given by equation 7.23. Equation 7.21 is the deflection of any centrally loaded beam, now that there is a top horizontal beam and equivalent straight beam (the triangular section) both centrally loaded, the deflection of both are summed. The total deflection, given by equation 7.21, is equation 7.21 summed when substituting the loads on the horizontal L_{beam} and equivalent straight beam l_{beam} .

$$v_{total} = v_1 + v_2 = \frac{P_{impact} L_{beam}^3}{48E_1 I_1} + \frac{P_{impact} l_{beam}^3}{2 \cdot 48E_2 I_2} = \frac{P_{impact} L_{beam}^3}{48} \left(\frac{1}{E_1 I_1} + \frac{1}{2\cos^3\theta E_2 I_2} \right) \quad (7.23)$$

E and I represent the material's Young's modulus and beam's area moment of inertia respectively for the horizontal beam (1) and equivalent straight beam (2). The area moment of inertia is computed assuming a rectangular cross section [63] and is calculated with equation 7.24 where w_{cs} and h_{cs} are beam cross section width and height respectively. These dimensions are perpendicular and parallel to the impact face as shown in Figure 7.10.

$$I = \frac{w_{cs}^3 h_{cs}}{12} \quad (7.24)$$

Given that the spring displacement relation is $P_{impact} = k_{spring} \cdot v_{total}$ the spring stiffness for the spring buffer is given by equation 7.25.

$$k_{spring} = \frac{48}{L_{beam}^3} \left(\frac{1}{E_1 I_1} + \frac{1}{2\cos^3\theta E_2 I_2} \right)^{-1} \quad (7.25)$$

An impact is modelled as a unforced half wave response of a spring because when the spring deform and the deformation v_{total} returns to zero, the UAV losses contact with the object it impacts. The spring model was implemented in a *MATLAB* program that solved the response from a simple spring equation of motion (EOM) where the initial conditions of position was $v_{total}(0) = 0m$ and velocity $V_{impact} = -3m/s$. Important to note is that the load transferred into the UAV at each joint is half the average load of P_{impact} as shown in Figure 7.10.

Material selection and design

For this concept, it is best to have the k_{spring} as low as possible and maximising the deformation v_{total} . This lengthens the period of the oscillation hence reducing the average load on the UAV. The peak load is not considered because the structural response to very short high loads (impulses) is beyond the scope of this research.

¹URL:<http://hyperphysics.phy-astr.gsu.edu/hbase/elacol.html>

Given the interior layout of payload in the hull, a nonagon configuration ($n_{sides} = 9$) of the spring around the hull was chosen so that there would be 9 discrete points of load introduction into the hull. The maximum spring deflection $v_{total,max}$, and beam dimensions were set such that the average g load did not exceed the set 23g. The length L_{beam} is computed by equation 7.26 where $R_{outer,hull}$ is the outer radius of the hull.

$$L_{beam} = 2(R_{outer,hull} + v_{total,max}) \cdot \tan \frac{\pi}{n_{sides}} \quad (7.26)$$

This computation is carried out for several materials and the result is presented in Section 7.2.3.

7.2.2 Impact absorption using viscoelastic buffer

One of the major drawbacks of an elastic buffer is that the rebound velocity is equal to the impact velocity as explained in Section 7.2.1. A viscoelastic buffer is a material that demonstrates both elastic and viscous behaviour when deformed, hence, total KE is not conserved [64]. The concept of a viscoelastic buffer uses a block of viscoelastic material on the UAV's outer hull to absorb the impact energy and therefore reducing the average load. Figure 7.11 shows the concept and equivalent spring-dashpot system used to model the viscoelastic material's behaviour.

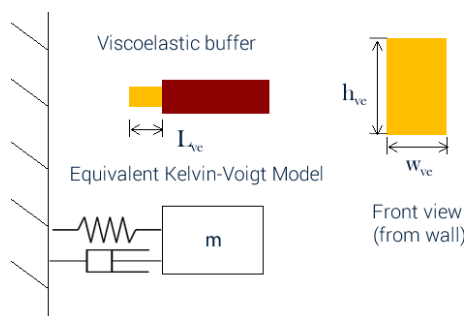


Figure 7.11: Viscoelastic buffer on outer edge of UAV (UAV mass m) hull

The equivalent spring-dashpot model is known as the Kelvin-Voigt material model; for a first-order analysis of viscoelastic material this model can describe the material's behaviour under loading with adequate accuracy [65]. In [66] by C.P. Chen and R.S. Lakes a procedure is suggested to calculate the response of viscoelastic impact absorbers which has been used in this research. For a free spring damper system with the general damped solution $x = x_0 e^{j\omega t}$ the Equation 7.27 gives the EOM for the UAV.

$$m_{UAV} \ddot{x} + (k + j\omega c)x = 0 \quad (7.27)$$

k and c are the material's equivalent stiffness in N/m and damping coefficient in Ns/m and ω the angular frequency of oscillation in rad/s . The displacement x is negative when the buffer is compressed. The article states that by assuming that the mass of the viscoelastic buffer is considerably less than that of the UAV, the term $k + j\omega c$ can be written in terms of the buffer properties by Equation 7.28 [66]. This assumption is valid as most materials used for impact absorption are polymeric foams or light rubbers.

$$m_{UAV} \ddot{x} = -E^*(j\omega) \frac{w_{ve} h_{ve}}{L_{ve}} x \quad (7.28)$$

The dimensions of the foam are represented by w_{ve} , h_{ve} and L_{ve} as depicted in Figure 7.10. The $E^*(j\omega)$ is a complex dynamic modulus which is a function of the frequency of vibration. Analogous to the Young's Modulus for elastic materials, the $E^*(j\omega)$ for viscoelastic materials characterises the stiffness and damping of such materials [66]. $E^*(j\omega)$ is defined by a storage modulus E' and loss modulus E'' , given by equation 7.29, which are related to the phase offset between the stress and strain response of the materials indicated by δ_p [65]. As the stress-strain relation is non-linear, the strain usually lags the stress so the maximum stress does not occur at the same time as the maximum strain [65].

$$E^*(j\omega) = E' + jE'' = E'(1 + j \tan \delta_p) \quad (7.29)$$

The value of $\tan\delta_p$ is an indication of the level of damping where high values equal greater damping. The value is related to the logarithmic decrement (Λ) of the response by equation 7.30 ².

$$\Lambda = \pi \tan\delta_p \quad (7.30)$$

When substituting $E^*(j\omega)$ in equation 7.28 as done in equation 7.31, the storage modulus E' is equivalent to the Young's modulus of a material and therefore the term $\frac{E' A_{ve}}{L_{ve}}$ is equivalent to a spring stiffness k_{ve} where A_{ve} is the buffer's cross sectional area. The same can be said for the loss modulus E'' which is equivalent to a complex spring stiffness k_{ve}^* .

$$m_{UAV}\ddot{x} = -\frac{E' A_{ve}}{L_{ve}}x - j\frac{E'' A_{ve}}{L_{ve}}\dot{x} \equiv -k_{ve}x - k_{ve}^*\dot{x} \quad (7.31)$$

Having this analogy in mind, the solution to the EOM 7.31 is given by equation 7.32 where the initial conditions is zero displacement and initial velocity is V_{impact} which is the impact velocity of $-3m/s$ (compressive displacement is negative) [66].

$$x(t) = \frac{V_{impact}}{\beta_{ve}\omega_0} \sin(\beta_{ve}\omega_0 t) e^{-\alpha_{ve}\omega_0 t} \quad \begin{aligned} \alpha_{ve} &= (1 + \tan^2\delta_p)^{1/4} \sin\frac{\delta_p}{2} \\ \beta_{ve} &= (1 + \tan^2\delta_p)^{1/4} \cos\frac{\delta_p}{2} \\ \omega_0 &= \sqrt{\frac{E' A_{ve}}{m_{UAV} L_{ve}}} \end{aligned} \quad (7.32)$$

Derivatives of the solution are taken to find the velocity and acceleration from which the P_{impact} can be computed. This process was all programmed in *MATLAB* to simulate responses for different buffer designs. The best designs have a low stiffness k_{ve} to lower the average load and high $\tan(\delta_p)$ values to absorb greater energy from the impact [66].

Material selection and buffer design constraints

Viscoelastic materials do not respond to loading like conventional elastic materials to loading as the stress-strain response is not linear [66]. Figure 7.12 shows a general response of viscoelastic material to compression, what is important to note is that the material is only useful for shock absorption up to 50-70% strain ³.

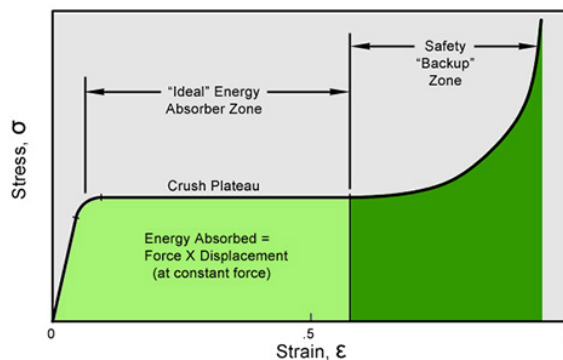


Figure 7.12: Stress-strain plot for compressed viscoelastic material showing non-linear behaviour and deformation limits ⁴

In the backup zone, the material degrades and loses performance much faster, therefore for the design, a maximum block deformation of 50% was set maintaining a margin of safety should the block deform more than 50% upon higher velocity impacts. As mentioned a low stiffness (low Young's Modulus) and high damping (high $\tan(\delta_p)$) is preferable; polymeric foams are the best of both hence all block designs considered this category of materials[67]. Setting the maximum deformation, the buffer blocks were sized to reduce the average impact load to 23g. The number of blocks (n_{blocks}) uniformly spaced angularly on the outer hull is calculated using

²URL:<http://silver.neep.wisc.edu/~lakes/VENotes.html>

³URL:<http://www.ergaerospace.com/Energy-Absorbition.html>

⁴URL:<http://www.ergaerospace.com/Energy-Absorbition.html>

equation 7.33 which is based on the design choice that if impact should occur between blocks, they both should both be able to deform 50% before the wall contacts the UAV hull.

$$n_{blocks} = \frac{\pi}{\cos^{-1}\left(\frac{R_{outer,hull}}{R_{outer,hull} + 0.5 \cdot L_{ve}}\right)} \quad (7.33)$$

7.2.3 Results and evaluation of spring and viscoelastic buffer concepts

Several materials and configurations for both concepts were considered and an analysis of the extra mass added to the UAV was done. The concepts were designed for a 23g load (116.5N) with a UAV mass of 0.516g and impact velocity of 3m/s.

Spring buffer design

Using several low-density rigid material, 3 designs were produced with the results given in Table 7.6. Machining of materials limited the dimensions to an integer multiple of 1mm so the average loads were lower than the 23g load which was set as the goal to design for.

Table 7.6: Spring buffer design options with average impact load $P_{i,avg}$ and total spring mass

Ref.	Material	$P_{i,max}$ [N]	L_{beam} [mm]	$v_{total,max}$ [mm]	$w_{cs,1}$ [mm]	$h_{cs,1}$ [mm]	$w_{cs,2}$ [mm]	$h_{cs,2}$ [mm]	E_1 E_2 [GPa]	Density [kg/m ³]	$P_{i,avg}$ [N]	$P_{i,avg,ver}$ [N]	Mass [g]
1	CFRP	356.5	96	13	4	2	4	3	65	1540	222.6	226.0	43.8
2	Aluminium	367.3	96	13	4	2	4	3	69	2712	229.2	232.8	77.1
3	HDPP	353.8	96	13	10	6	10	6	1.6	906	221.0	224.3	144.4

CFRP is Carbon Fibre Reinforced Plastic [10] and HDPP is High-Density Polypropylene (PP-C)⁵. Only a few designs were made because it became apparent that this concept would add a lot of mass to the UAV. Note that the average load on the UAV is half of $P_{i,avg}$ as previously described in Section 7.2.1; this was because the spring concept distributes the load and introduces at two points into the hull. To verify the *MATLAB* simulated average force calculations, the average force $P_{i,avg,ver}$ was calculated using Newton's Second Law of linear momentum and the calculated rebound velocity and time; the results from the simulation and theory were very close as seen in Table 7.6.

Viscoelastic polymeric foam design

Using polymeric foams currently available in the market, nine design choices were produced with the results given in Table 7.7. Machining of materials limited the dimensions to an integer multiple of 1mm so the average loads were lower than the 23g load.

Table 7.7: Viscoelastic buffer design options with average impact load P_{avg} and total blocks mass

Ref.	Material	P_{max} [N]	L_{ve} [mm]	h_{ve} [mm]	w_{ve} [mm]	E' [MPa]	$\tan\delta_p$	Density [kg/m ³]	$P_{i,avg}$ [N]	$P_{i,avg,ver}$ [N]	Mass [g]
1	IMPAXX 300	240.1	20	40	7	0.868	1	38.5	105.5	105.8	1.71
2	IMPAXX 500	240.0	20	40	5	1.224	1	40.4	105.9	105.9	1.28
3	IMPAXX 700	241.7	20	40	4	1.67	1	44.7	110.7	110.6	1.11
4	Ethafoam Duralite FR	242.5	20	40	25	0.248	1	28.8	106.6	106.4	4.56
5	Plastazote LD15FM	239.2	20	40	29	0.208	1	15.0	105.2	105.3	2.78
6	Plastazote LD45FM	239.4	20	40	19	0.318	1	45.0	105.2	105.3	5.45
7	Plastazote LD24FM	242.7	20	40	27	0.230	1	24.0	106.7	107.0	4.11
8	Plastazote MP15FR	243.1	20	40	35	0.178	1	15.0	106.8	107.0	3.32

The height (h_{ve}) and width (w_{ve}) were kept constant so that all designs would require 8 blocks separated by 45° angular separation allowing for comparison of material. The rebound velocity for all designs is 0.816m/s and the

⁵URL:<http://www.matbase.com/material-categories/natural-and-synthetic-polymers/commodity-polymers/>

rebound time (half wave/half period) is around 18ms. Information on the loss tangent ($\tan\delta_p$) value was not available so a nominal value of 1 was assumed which is typical for polymeric foams [67]. Verification of the average force was done similar to the spring buffer design. Verification of the program is later discussed in Section 10.3.1. The IMPAXX series of polystyrene based foam are manufactured by The DOW Chemical company and have been used in NASCAR cars for impact absorption ⁶ [68]. The Ethafoam are Low-Density Polyethylene (LDPE) foams also manufactured by DOW ⁷. The Plastazote LDPE series are manufactured by Zotefoams and are already being used in aircraft for padding and soft trims; also the FM series is fire retardant giving it an advantage over other foams^{8 9}.

Impact buffer selection

After considering both the spring and viscoelastic buffer concept, the viscoelastic buffer concept had a clear and large mass advantage. Other aspects on which the viscoelastic buffer outperforms includes;

- Insulation benefit - foam can insulate the hull from the environment.
- Cost - Foam materials are cheaper than metals, composites and heavy plastics ¹⁰
- Total solution - Foam cover allows for multi-angle impact while for a spring concept multiple springs would be required to allow multi-direction impact coverage.

From the polymeric foams for the viscoelastic buffer, Plastazote MP15FR was chosen to be the best option as it was one of the lighter designs that is flame-retardant [69] (Full details and tests on material can be found on Zotefoam's website ¹¹). Given that the UAV may enter warm (above room temperature but below $100^\circ C$) areas and possibly be exposed to a flame, a material that will not ignite is essential as it can delay the heating of internal components and provide some protection. Plastazote foams are also non-toxic, odourless, good against ultraviolet exposure and will not absorb water as a result of its closed cell structure ¹². The IMPAXX series was not chosen as it is susceptible to degrading at high temperatures and cannot be exposed to flames [68].

The final design chosen is similar to Ref. 8 of Table 7.7. The height (h_{ve}) and width (w_{ve}) were modified to 42 and 27mm respectively; the height had to be modified so the foam block height would match the UAV's final design hull height. Ten foam blocks separated at 36° will be placed on the UAV's outer hull. In addition to the foam blocks, the top and bottom of the UAV will be fully covered by a shaped foam with a maximum thickness of 33.5mm at the inner hull edge. This top and bottom foam covers will serve both as an inlet and outlet for the propulsion subsystem's duct, and as impact resistance in case the UAV impacts an obstacle from above or below. More details on the dimensions of this foam is provided in Section 12.4.3 in Figure 12.17a. A CAD model of the foam was created to obtain an accurate estimate of the foam volume from which the total foam mass was calculated using the material density provided in Table 7.7. The complete foam impact buffer design, for a UAV mass (without foam) of $0.504g$, is given in Table 7.8. The additional top and bottom foam cover adds 26.5grams in addition to the 10 foam blocks mass of 2.9g resulting in a total foam mass of 29.4grams. Figure 7.13 shows the response of the foam to the $3m/s$ impact. All calculation were performed using the method outlined in Section 7.2.2.

Table 7.8: Final design foam buffer with foam block and total foam cover mass

Material	$P_{i,max}$ [N]	L_{ve} [mm]	h_{ve} [mm]	w_{ve} [mm]	E' [MPa]	$\tan\delta_p$	Density [kg/m^3]	$P_{i,avg}$ [N]	Rebound time [ms]	Compression [%]	Mass blocks [g]	Mass total [g]
Plastazote MP15FR	234.6	17	42	27	0.178	1	15.0	103.2	18.6	60	2.9	29.4

⁶URL:<http://www.dow.com/en-us/markets-and-solutions/products/impaxx/impaxxenergyabsorbingfoams/>

⁷URL:<http://www.qualityfoam.com/ethafoam.asp>

⁸URL:<http://www.qualityfoam.com/plastazote.asp>

⁹URL:<http://www.kewell-converters.co.uk/aerospace-materials--components>

¹⁰URL:http://www-materials.eng.cam.ac.uk/mpsite/interactive_charts/strength-cost/basic.html

¹¹URL:<http://azote.zotefoams.com/item/all-categories/molding-grade/mp15fr>

¹²URL:<http://www.polyformes.co.uk/plastazote.html>

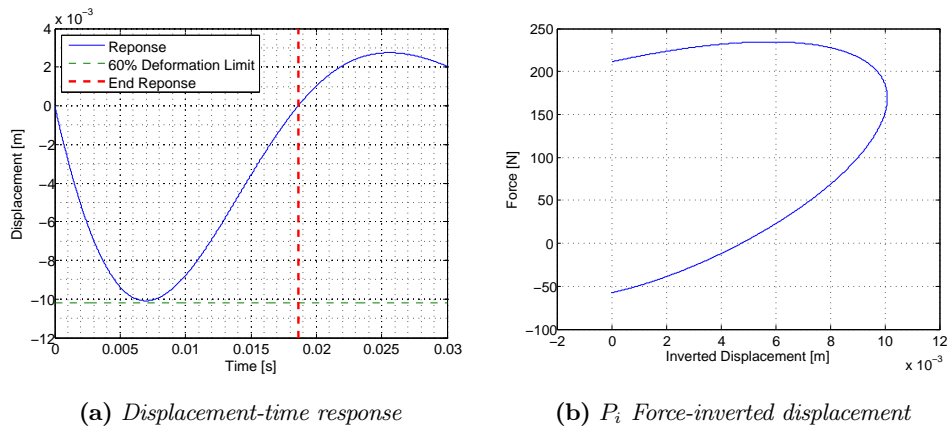


Figure 7.13: *Plastazote MP15FR 42×27×17mm buffer block half-wave response to 3m/s impact*

Some compromise was made on the design to allow for the changes in the final UAV design. Each block will be able to compress 60% upon impact which is still within the material’s allowable strain limits as discussed in Material selection of Section 7.2.2. If impact occurs between blocks, the blocks will be allowed to deform only 50% which is acceptable as the load is distributed between the blocks so it will not deform this much at 3m/s impact. The hull design is able to sustain the impact load as will be explained in the sections that follow.

7.2.4 Impact resistance using the stiffening ring concept

In the previous sections, it was mentioned that the amount of g loads that act on the structure upon impact can be greatly reduced by using either a spring buffer structure or a foam padding. However, using this concept still cannot reduce the impacting force enough that the original structure can cope with it. Therefore, a means of reinforcement of the architecture is essential. This section introduces the so-called "stiffening ring" concept. Firstly, the theory behind the concept will be elaborated on. Then, 2 prospective solutions will be compared.

The stiffening ring concept makes use of a stiffening circular shape that follows the contour of the payload housing hull and has a rectangular cross-section as it can be seen in Figure 7.14. This reinforcing ring would be made out of high strength, but low weight materials. It is important to note that the stiffening ring has to both be able to cope with the impact loads, and be able to deflect by a minimal amount.

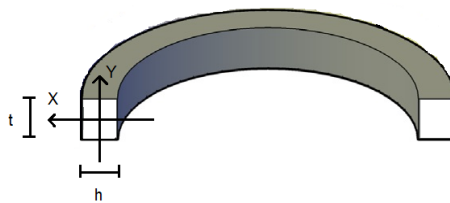


Figure 7.14: *Model representation of the stiffening ring concept as a solution for impact resistance*

In order to investigate the behaviour of such a structure, one has to model the ring as an indeterminate half ring which is clamped on both ends. The reason behind this assumption is that the ring is symmetric. This indeterminate system can be seen on Figure 7.15. In order to calculate deflections, Castigliano’s theorem will be used. [59]

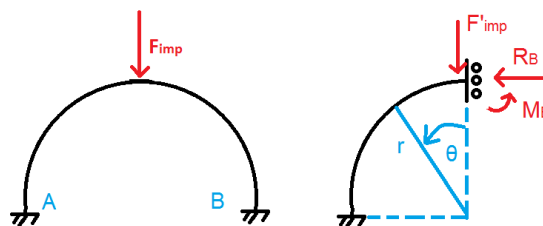


Figure 7.15: *Model representation of the stiffening ring concept as a solution for impact resistance*

As it can be seen, a point load (impacting load) acts on the structure. However, to do so, one has to simplify the model (using symmetry) by introducing redundant loads R_B and M_B as shown on the right-hand side of Figure 7.15. It can also be seen that in the middle of the half ring where the impact load F_{imp} is applied, the slope of the structure always remains zero. Accordingly, the model can be halved and the behaviour of the right-hand side is a guided cantilever. It can provide a left-right force reaction, a moment reaction, but it does not provide a vertical reaction. The next step in the process is to define the moment acting in the quarter circle. It is shown in Equation 7.34.

$$\text{for } \frac{\pi}{2} \leq \theta \leq \pi \quad M(\theta) = R_B r (1 - \cos(\theta)) - F_{imp}' r \sin(\theta) + M_b \quad (7.34)$$

Also, the deflection due to R_B is zero while the slope due to M_B is zero. Three partial derivatives have to be used in the process and they can be seen in Equation 7.35, Equation 7.36 and Equation 7.37.

$$\frac{\partial M(\theta)}{\partial R_B} = r(1 - \cos(\theta)) \quad (7.35)$$

$$\frac{\partial M(\theta)}{\partial M_B} = 1 \quad (7.36)$$

$$\frac{\partial M(\theta)}{\partial F_{imp}'} = -r \sin(\theta) \quad (7.37)$$

Then, deflections due to R_B and M_B can be calculated. It is important to note that these deflections are zero, this is the reason for the zeros in Equation 7.38 and Equation 7.39.

$$\delta_{R_B} = 0 = \int_0^{\frac{\pi}{2}} M(\theta) \frac{\partial M(\theta)}{\partial R_B} r \, d\theta \quad (7.38)$$

$$\delta_{M_B} = 0 = \int_0^{\frac{\pi}{2}} M(\theta) \frac{\partial M(\theta)}{\partial M_B} r \, d\theta \quad (7.39)$$

Afterwards, one has to set up the deflection due to the impact force F_{imp}' . It has to be mentioned that due to the extensive calculations and rearrangements necessary to arrive at the final results, the scientific tool Maple 18 was used. Both the starting situation and the expanded view are shown in Equation 7.40. It is important to notice that the largest deflection will be at 90°, therefore the θ values will be replaced by $\frac{\pi}{2}$.

$$\begin{aligned} \delta_{F_{imp}'} &= \frac{1}{EI} \int_0^{\frac{\pi}{2}} M(\theta) \frac{\partial M(\theta)}{\partial F_{imp}'} r \, d\theta \\ &= -\frac{1}{2} \frac{r^2 F_{imp}' (\pi^2 \cos(\frac{\pi}{2}) \sin(\frac{\pi}{2}) - \pi^2 \frac{\pi}{2} - 2\pi \cos(\frac{\pi}{2})^2 - 4\pi \cos(\frac{\pi}{2}))}{(\pi^2 - 8)EI} \\ &\quad - \frac{1}{2} \frac{r^2 F_{imp}' (8\cos(\frac{\pi}{2})^2 - 8\cos(\frac{\pi}{2}) \sin(\frac{\pi}{2}) + 6\pi + 8\cos(\frac{\pi}{2}) + 8\frac{\pi}{2} - 16)}{(\pi^2 - 8)EI} \end{aligned} \quad (7.40)$$

This equation allows for the calculation of the stiffening ring's deflection due to the impact load. In order to calculate the deflection, one first has to calculate the moment of inertia of the cross section. The cross-section can be seen in Figure 7.15. The moment of inertia for a rectangular cross-section is calculated using Equation 7.41. In order to show the calculation method with numerical results, a sample cross-section is created with a height of 5.5 mm and a thickness of 5 mm.

$$I_{yy} = \frac{h^3 t}{12} = \frac{0.0055^3 \cdot 0.005}{12} = 6.9323 \cdot 10^{-11} \, m^4 \quad (7.41)$$

Now, the deflection of the beam can take place. As the sample example, a force of 116 N will be applied on a Carbon Fibre Reinforced Polymer with a Young's modulus of 65 GPa and a density of $1540 \frac{kg}{m^3}$ with a ring

radius of 95 mm. The next step is to substitute these values into Equation 7.40. In Equation 7.42, the constant is the simplified version of Equation 7.40

$$\delta_{F_{imp}'} = -\frac{r^2 F}{EI} 0.0233 = -\frac{0.095^2 111}{65 * 10^9 \cdot 6.93 * 10^{-11}} 0.0233 = -0.0054 \text{ m} = -5.4 \text{ mm} \quad (7.42)$$

Even though the deflection can already be calculated, one has to also check whether the ring is able to cope with the tensile and shear loads that are present in the structure. One of the primary loads is a compressive stress due to a bending moment. The highest bending moment is calculated at the clamps that are shown in Figure 7.15 where the radius contribution is the highest. The bending moment can be calculated using Equation 7.43. [59]

$$\sigma_{ring} = \frac{M}{I_{yy}} x \quad (7.43)$$

Also, the shear load that acts on the structure has to be computed and is done using Equation 7.44. [59]¹³

$$\tau_{ring} = \frac{F_{imp}' h^2}{8I} \quad (7.44)$$

In order to end up with a feasible design, one has to account for the von Mises stresses in the structure which are the highest stresses that can occur as a combination of all the stresses that act on the structure. Equation 7.45 gives the general expression for the von Mises stress, while Equation 7.46 and Equation 7.47 shows the von Mises stresses at for the two critical points. Equation 7.46 shows the maximum compressive stress due to bending at location "A" in Figure 7.15 while Equation 7.47 presents the maximum shear stress at the position where the impact force is applied. Both these equations are multiplied by a safety factor of 1.5, which is a commonly used value in the aerospace community. [59]

$$\sigma_y = \sqrt{\frac{1}{2}[(\sigma_x - \sigma_y)^2 + (\sigma_y - \sigma_z)^2 + (\sigma_z - \sigma_x)^2] + 3\tau_{xy}^2 + 3\tau_{yz}^2 + 3\tau_{xz}^2} \quad (7.45)$$

$$\sigma_{ring} = 1.5 \sqrt{\frac{1}{2} \left(\frac{F_{imp}' r \frac{h}{2}}{I} \right)^2} = \frac{0.095 * 116 * \frac{0.0055}{2}}{6.93 * 10^{-11}} = 1.5 \sqrt{\frac{1}{2} (4.373 * 10^8)^2} = 4.638 * 10^8 \text{ Pa} \quad (7.46)$$

$$\tau_{ring} = 1.5 \sqrt{3 \left(\frac{F_{imp}' h^2}{8I} \right)^2} = \tau_{ring} = 1.5 \sqrt{3 \left(\frac{116 * 0.0055^2}{8 * 6.93 * 10^{-11}} \right)^2} = 1.644 * 10^7 \text{ Pa} \quad (7.47)$$

One major assumption that has been made is that at position "A" of Figure 7.15, only the compressive stress is considered and at the position where the impact force is applied, only the shear stress is considered. The validity of this assumption lies in the fact that the magnitude of the shear stress is 1, sometimes 2 magnitudes lower than the compressive stress as it will be seen in Subsection 7.2.5.

The next step in the process is to calculate whether the stiffening struts that connect the foam and the stiffening ring can actually survive the compressive load. The stiffening struts will have a rectangular cross-section to allow for easy variations of the moment of inertia. For the calculations, it is assumed that the impact load acts directly in the middle of the rectangular cross-section. The cross-section will have the exactly the same shape (with different dimensions) as the one seen in Figure 7.14. As it was already discussed in Subsection 7.1.2, the struts are more likely to buckle before compressive failure would occur, therefore only the buckling case will be considered to find the limit of the concept. Equation 7.48 shows the expression for the buckling load. [70]

$$F_{imp}' = \frac{\pi^2 E_{strut} I_{strut}}{L_{strut}^2} \quad (7.48)$$

For the sample calculation, it has to be noted that the impact load is already known (116 N) along with the strut length (33.5 mm) and the inertia of the 1.5x1.5 mm strut is equal to $4.22 * 10^{-13} \text{ m}^4$. Rearranging the equation results in finding the proper Youngs' modulus as it can be seen in Equation 7.49 where a safety factor of 1.5 is applied.

$$E_{strut} = 1.5 \frac{F L_{strut}^2}{\pi^2 I_{strut}} = 1.5 \frac{116 * 0.0335^2}{\pi^2 4.22 * 10^{-13}} = 4.69 * 10^{10} \text{ Pa} = 46.9 \text{ GPa} \quad (7.49)$$

¹³URL:http://fp.optics.arizona.edu/optomech/references/OPTI_222/OPTI_222_W10.pdf

7.2.5 Material selection for the stiffening ring concepts

The stiffening ring concepts presented in the previous subsection are prospective additional features of the vehicle. It means that additional weight would be added to the structure which has to be minimised. It is also required next to stiffening the structure to keep the additional weight minimal. Therefore, a trade-off has to be made between several materials based on their strength, mass, occupied volume in the hull, cost and environmental friendliness. Eight different materials were collected and examined for each of the above-mentioned criteria. Moreover, two stiffening ring concepts are being introduced. Firstly, the stiffening ring would be housed inside the payload carrying hull, more specifically it would be attached to the inner wall of the hull as shown in Figure 7.16. It can also be seen that stiffening struts are attached to the foam and the stiffening ring. The presence of these struts is essential in order to avoid direct load transfer into the hull structure.

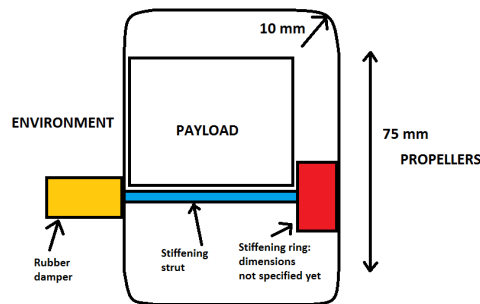


Figure 7.16: Stiffening ring with stiffening struts attached to the inner side of the hull as a means of impact resistance solution

Figure 7.17 shows the second stiffening ring concept. Here, the ring is attached to the outer wall of the hull, therefore the foam is directly attached to it and the use of additional struts is unnecessary.

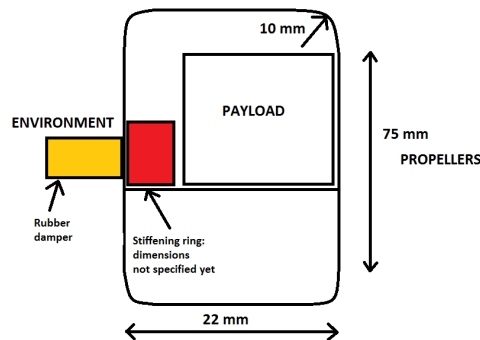


Figure 7.17: Stiffening ring attached to the outer side of the hull as a means of impact resistance solution

In order to carry out the comparison on these concepts, several assumptions in the design had to be made. It has to be mentioned that this is not the finalised situation, this is only a suitable condition to compare the two stiffening ring concepts. Change in their final parameters might be possible in later design stages and will be addressed in Section 12.4. The first assumption was based on the load case when the vehicle collides with a wall at $3 \frac{m}{s}$ and an expanded polystyrene layer is attached to the outer side of the structure. These conditions were already presented in Subsection 7.2.2. The polystyrene layer would reduce the g load acting on the structure to 23 g's. Also, after extensive discussions with the propulsion design team, it was concluded that the maximum allowable deflection of the stiffening ring, and hence the hull is 5 mm. It means that there is at least 5 mm clearance between the propellers and the inner wall of the hull. Then, it is also assumed that in case the ring with stiffening struts are used, 8 struts will be present in the structure (one strut every 45 degrees) as mentioned in Subsection 7.2.3. As for the ring stiffener at the outer hull concept (Figure 7.17), the polystyrene foam is directly attached to the ring. It is also assumed that the impact on the vehicle acts in the middle (cross-sectional center of gravity) of the strut or at the neutral axis of the ring.

The next step in the process is to list the prospective materials that could primarily cope with the loads without breaking or deflecting enough that the duct wall reaches the propellers which would lead to system failure. Table 7.9 contains eight selected materials that will be examined for the impact resistance solutions. Material costs were based on distributor prices. Also, these prices are based on large quantity orders (900 kg), since most materials are sold in bulk lots. Unfortunately, it was impossible to obtain material prices for lower quantities. The collection date of the pricing information is January 2007. The prices that were measured in US dollars, however, they were converted to Euros based on the mid-market rates on 14/06/2015 when the cost of 1 USD was 0.8878 EUR.¹⁴ Moreover, the prices that were measured in GBP were converted to Euros based on the mid-market rates on 14/06/2015, when the cost of 1 GBP was 1.3979 EUR.¹⁵

Table 7.9: *Material properties for the stiffening ring with and without struts impact resistance concepts*

Material name	Yield strength [MPa]	Tensile strength [MPa]	Young's modulus [GPa]	Density [kg/m ³]	Elongation at failure [%]	Cost [EUR/kg]	Relative cost
Aluminium 1100	34	90	69	2710	40	2.45	1
Aluminium 6061	276	310	69	2700	17	7.55	3.1
Aluminium 356	164	228	72.4	2690	3.5	2.97	1.2
Aramid RA11 ¹⁶	-	147	68.6	1270	2	35	14.3
Aramid RA13 ¹⁷	-	139	68.6	1275	2	35	14.3
E-glass fiber epoxy	-	40	12	2100	2.3	44.4	18.1
CFRP ¹⁸	-	503	65	1540	-	48.8	20
Torayca T300 ¹⁹	-	76	135	1760	1.3	115.4	47.1
Torayca M40J ²⁰	-	53	230	1770	1.1	115.4	47.1

In the table, CFRP corresponds to Carbon Fibre Reinforced Polymer and Al 1100 corresponds to an aluminium alloy. As it can be seen, aluminium alloys cost the least out of the listed materials, however since cost was determined as a secondary requirement (Section 2.3) and impact resistance is a primary requirement, materials with high stiffness and low weight are considered more favourable. Low weight is benign since additional weight might cause a significant snowball effect in the weight of the total vehicle (propulsion system & power system weight increase). Calculations with all the materials on the model presented in Subsection 7.2.4 and the results are shown in Table 7.10.

Table 7.10: *Stiffness and dimensional parameters of the stiffening ring concept at the inner hull wall*

Material	Applied force [N]	Ring thickness [mm]	Ring height [mm]	Max. deflection [mm]	Max. bending stress [MPa]	Max. shear stress [MPa]	Ring mass [g]
Al 1100	116.5	13	15	0.1	32.2	1.34	322
Al 6061	116.5	5	7	2.2	272	12.9	54
Al 356	116.5	6.5	8	1.1	160	8.73	82
Fibra RA11	116.5	6.5	8.5	1	142	8.2	41
Fibra RA13	116.5	6.5	9	0.9	132	7.62	44.5
E-glass fiber epoxy	116.5	12.5	12	1	37	3.03	199
CFRP	116.5	5	5.5	4.9	441	16.5	23.5
Torayca T300	116.5	9	10	0.2	74	5	94.5
Torayca TM40J	116.5	15	10	0.1	44.5	3	158.5

The properties of prospective struts can be found in Table 7.11. It has to be mentioned that the same materials were used for the struts and the ring. One can easily see that all types of struts are very small both in size and in mass, therefore one can choose any of the materials. Nonetheless, it is favourable to choose the same material as the ring since production and assembly of the system is more straightforward. Also, in case the same material is used for the strut and the ring, they can be manufactured as one part, which is beneficial for load translation from the strut to the ring. Provided that one chooses to do this, the mass properties mentioned in Table 7.10 would increase by a maximum of 2 grams.

¹⁴URL:<http://www.xe.com/currencyconverter/convert/?From=EUR&To=USD>

¹⁵URL:<http://www.xe.com/currencyconverter/convert/?From=GBP&To=EUR>

Table 7.11: Comparative design parameters of impact resistance struts for different materials

Material	Buckling load [N]	Strut thickness [mm]	Strut height [mm]	Mass of 9 struts [g]
Al 1100	116.5	1.5	1.5	1.5
Al 6061	116.5	1.5	1.5	1.5
Al 356	116.5	1.5	1.5	1.5
Aramid RA11	116.5	1.5	1.5	0.7
Aramid RA13	116.5	1.5	1.5	0.7
E-glass fiber epoxy	116.5	1.5	2	2
CFRP	116.5	1.5	1.5	0.9
Torayca T300	116.5	1.5	1.5	1
Torayca TM40J	116.5	1.5	1.5	1
HPDE	116.5	2	4	1.9
PA 640-GSL	116.5	2	3.5	1.4

In case one opts for the ring at the outer hull wall, the results in Table 7.12 are found for the stiffening ring. It has to be emphasised, that these values are comparable to the values mentioned in Table 7.10 and Table 7.11. Since the ring is on the outer side of the hull (outer-most position on the vehicle), it is longer than the one in the inside, therefore more material and larger dimensions are necessary to cope with the bending loads and increased deflections as mentioned in Subsection 7.2.4. This results in higher masses for each material as it can be seen in Table 7.12. Therefore, it can be concluded that it is preferable to use a stiffening ring on the inside of the hull with stiffening struts rather than using a ring on the outside. The reasoning is twofold: the inner ring introduces less additional mass into the structure and there is less extra space necessary to be allocated (in the hull) for the impact resistance system. In this way, the outer stiffening ring concept will not be further considered as a solution for impact resistance.

Table 7.12: Stiffness and dimensional parameters of the stiffening ring concept at the outer hull wall

Material	Applied force [N]	Ring thickness [mm]	Ring height [mm]	Max. deflection [mm]	Max. bending stress [MPa]	Max. shear stress [MPa]	Ring mass [g]
Al 1100	116.5	13	13.5	0.1	32.4	2.6	329
Al 6061	116.5	6.5	7	1.7	259	10	86.5
Al 356	116.5	8	8	0.9	157.7	7.1	121.5
Fibra RA11	116.5	9	8	0.8	140	6.3	64.5
Fibra RA13	116.5	9	8	0.8	139	6.3	65
E-glass fiber epoxy	116.5	15	12.5	0.8	33	2.4	272
CFRP	116.5	5.5	5.5	4.4	497	15	32
Torayca T300	116.5	11	10	0.2	72	4.1	136
Torayca TM40J	116.5	15	10	0.1	53	3	187

This chapter presented several solutions for the impact resistance of the system. It can be concluded that all solutions would be suitable for the vehicle, however, decisions have to be made in order to keep the UAV mass minimal. Therefore, as it will be seen in Section 12.4 the vehicle will make use of a protective foam layer introduced in Subsection 7.2.2 with a thickened hull structure as shown in Section 7.1. The combination of these two solutions produces the least amount of additional material to the system.

7.3 Occupational Health & Safety considerations

This section primarily assesses the safety of the system towards the environment. It is of primary importance to design a system that carries the least amount of risk, mainly due to the fact that civilian people might be involved in the operations. In this way, Occupational Health & Safety considerations have to be accounted for. Several primary requirements address this issue and can be broken down to two separate parts, namely the prevention of injury upon collision and prevention of lacerations upon impact.

The system makes use of contra-rotating propellers which pose a huge risk to the casualties that might be involved, therefore, it is important to protect them from lacerations. Fortunately, the propellers are guarded against the environment on the sides but are still not covered on the top and the bottom. Consequently, a protective fence has to be placed on the top and bottom of the vehicle. In order to find the required refinement of the mesh, one has to investigate the worst-case situation where a civilian accidentally has his or her hand jammed in the propellers. The average hand breadth for a child is used to size for the protective fence and

it is measured to be 16 cm.²¹ In the design, a square type mesh will be used, therefore the 16 cm breadth has to be considered as the diagonal of this square. Using simple trigonometry reveals that the mesh clearance is 10x10 cm. It means that for the current design, a cross suffices, since the diameter of the duct is 94 cm. In order to introduce some redundancy into the system, 5 spokes instead of the necessary 4 will be used to arrive at an immensely safe system. The schematic representation of the protective fence can be seen in Figure 7.18.



Figure 7.18: Protective fence with 5 spokes to be used on the top and bottom of the vehicle

As it can be seen in Section 5.1.2, the total loss in thrust is only 1.3 %, which does not have a significant effect on the performance of the system, therefore, can be considered negligible. It is not only important that the propellers are housed, it is also crucial to assess whether the fence can take up the occurring loads. The event of a fence failure would be fatal to the vehicle because the propellers would get jammed. It is assumed that the vehicle traverses through a room at 1.5 m altitude when suddenly power is lost and the UAV falls on the ground. Simple dynamics for the 533 gram drone reveals that the average force acting on the strut is 100 N.²² This value has to be used to calculate the tensile stress due to bending and the shear stress to find the required thickness of the fence elements. These scenarios are shown in Equation 7.50 and Equation 7.51. The cross-sectional shape of the fence is solid circular. The shear stress equation is identical to Equation 7.47.

$$\sigma_{fence} = \frac{M_{fence} r_{fence}}{I_{fence}} = \frac{F_{fence} L_{fence} r_{fence}}{I_{fence}} = \frac{100 * 0.094 * 0.002}{1.27 * 10^{-11}} = 1.47 * 10^9 Pa \quad (7.50)$$

$$\tau = \frac{F_{fence} r_{fence}^2}{I_{fence}} = \frac{100 * 0.002^2}{1.27 * 10^{-11}} = 3.15 * 10^7 Pa \quad (7.51)$$

The assessment of each material presented in Table 7.9 was carried out to come up with the optimum solution. The decision was made to choose the Aramid RA11 material of 2 mm radius (circular cross-section), which resulted in 7.5 grams of structural weight for each fence (top and bottom), which means that a total weight allocated for Occupational Health & Safety is 15 grams.

7.4 Vibrational Analysis

Moving parts such as motors and rotors, if out of balance, induce vibrations on the UAV. These vibrations can have undesirable effects on the payload and navigation instruments, negatively affecting the performance of the mission. Moreover, if the frequency of the input vibration is close to the natural frequency of the structure, resonance might compromise the structural integrity of the drone.

In the specific case of copters, vibrations are mainly induced by the motor, at the frequency it operates and its harmonics, and by the propellers, at frequencies equal to the motor frequency and its harmonics, or at frequencies equal to the motor frequency times the number of blades on the rotor, depending on the type of vibration. Two main vibration modes are present in copters, namely, lateral vibration and a vertical vibration. Lateral vibrations are caused by a mass imbalance of the propellers or improper alignment of the rotor shaft. Vertical vibrations are due to the blades producing different lift at a certain point of the rotation. This difference in lift can be caused by slight differences in the blade profile or by differences in the blade pitch due to unequal links to the swashplate.²³

In order to analyse the propagation of vibrations from the motors and propellers to the hull structure of the UAV, the model shown in Figure 7.19 was used. It consists of a mass representing the propellers and motors,

²¹URL:<http://www.censusatschool.ca/data-results/2004-05/average-hand-span-age/>

²²URL:<http://hyperphysics.phy-astr.gsu.edu/hbase/flobi.html>

²³URL:<http://www.helicoptermaintenancemagazine.com/article/rotor-blade-track-and-balance-past-and-present>

m_{prop} , a mass representing the hull structure and the payload, m_h , and a spring representing the struts that connect them. The spring has stiffness k , which is equal to the equivalent stiffness of the struts. Two input forces are applied at m_{prop} modelling the disturbances that induce the vibrations. Therefore, the total applied force on the propeller mass has two sinusoidal components. Two forces were used rather than one because the design has two different propellers, that might rotate at different speeds, and cause disturbances with different amplitude and frequency. The system of first order differential equations that define the model is given by Equations 7.52, 7.53, 7.54, and 7.55. The system variables are x_p , the displacement of m_{prop} , x_h , the displacement of m_h , and their derivatives \dot{x}_p and \dot{x}_h .

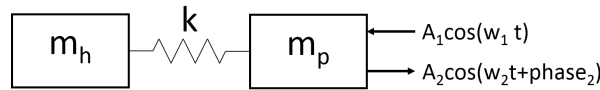


Figure 7.19: Model used to analyze the vibration behaviour of the UAV

$$\dot{\mathbf{x}} = \mathbf{A}\mathbf{x} + \mathbf{B}\mathbf{u} \quad (7.52)$$

$$\mathbf{x} = [\dot{x}_p \quad x_p \quad \dot{x}_h \quad x_h]^T \quad (7.53)$$

$$\mathbf{A} = \begin{bmatrix} 0 & \frac{-k}{m_{prop}} & 0 & \frac{k}{m_{prop}} \\ 1 & 0 & 0 & 0 \\ 0 & \frac{k}{m_h} & 0 & \frac{-k}{m_h} \\ 0 & 0 & 1 & 0 \end{bmatrix} \quad (7.54)$$

$$\mathbf{B} = [1 \quad 0 \quad 0 \quad 0]^T \quad (7.55)$$

$$\mathbf{u} = A_1 \cos(w_1 t) + A_2 \cos(w_2 t + phase_2) \quad (7.56)$$

The system was used to analyze both lateral and vertical vibrations. The equivalent stiffness of a single strut under vertical vibrations is given by Equation 7.57. In the UAV three struts are present, therefore the total vertical stiffness is 3 times that of a single strut.

$$k_v = \frac{3EI}{L^3} \quad (7.57)$$

In Equation 7.57, k_v is the equivalent vertical stiffness of a strut, E is the Young's modulus of the strut material, I is the moment of inertia of the strut around the horizontal axis, and L is the length of the strut.

For the case of lateral vibrations, the struts can be located at an angle with respect to the deflection direction and therefore finding the total equivalent lateral stiffness k_l is not straightforward. For a given displacement of the propeller mass Δx , every strut deforms axially and laterally as seen in Figure 7.20. The magnitudes of these displacements depend on Δx and on the angle Θ between the direction of the displacement Δx and the strut longitudinal axis. The axial displacement Δa is given by Equation 7.58 and the lateral displacement Δb is given by Equation 7.59.

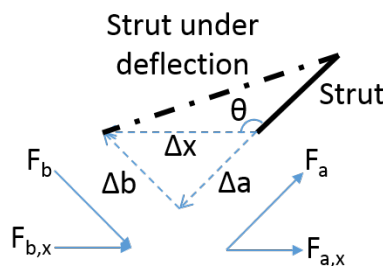


Figure 7.20: Axial and lateral deflections of a strut induced by a deflection Δx

$$\Delta a = \Delta x \cdot \cos(180 - \Theta) \quad (7.58)$$

$$\Delta b = \Delta x \cdot \sin(180 - \Theta) \quad (7.59)$$

In Equations 7.58 and 7.59, Θ is in degrees. The axial and lateral forces F_a and F_b that the displacements induce are proportional to the displacements and given by Equations 7.60 and 7.61.

$$F_a = k_a \Delta a \quad (7.60)$$

$$F_b = k_b \Delta b \quad (7.61)$$

The constants of proportionality k_a and k_b in Equations 7.60 and 7.61 are the equivalent stiffness of a strut under axial and lateral loads respectively. Due to the symmetry of the strut cross section, k_b is equal to k_v , given in Equation 7.57. The equivalent axial stiffness k_a is given by Equation 7.62.

$$k_a = \frac{EA}{L} \quad (7.62)$$

In Equation 7.62, A is the cross sectional area of a strut. The components of the forces F_a and F_b in the line of the displacement Δx are $F_{a,x}$ and $F_{b,x}$ respectively. Their expressions are given in Equations 7.63 and 7.64. The total force in the direction of Δx that a strut applies in one beam, F_x is given in equation 7.65, in which the relation of F_x , Δx and the equivalent stiffness in the direction of Δx , k_x is also presented.

$$F_{a,x} = F_a \cdot \cos(180 - \Theta) \quad (7.63)$$

$$F_{b,x} = F_b \cdot \sin(180 - \Theta) \quad (7.64)$$

$$F_x = F_{a,x} + F_{b,x} = k_x \Delta x \quad (7.65)$$

Combining the previous equations, an expression for k_x as a function of Θ can be obtained. The total stiffness in the lateral direction k_l is given by the summation of the k_x of every strut. The values of Θ for the struts differ by 120 degrees. This fact causes the total stiffness k_l to be constant, independently of the direction of lateral vibration, with the expression given by Equation 7.66.

$$k_l = \frac{3}{2}(k_a + k_b) \quad (7.66)$$

With the stiffness for both lateral and vertical vibrations defined, the system was simulated in Matlab using the *lsim* command. Different runs of the simulation were performed for the vertical and lateral vibration modes varying the amplitude of the input forces and their phase difference. The frequencies of the response of the system were investigated by means of a Fourier transform. The results show that the highest accelerations in the hull are present for phase differences of 180 degrees between the inputs, i.e. when both components act in the same direction at all times. The maximum deflections of the beam, given by the difference between x_h and x_p also happen at that value of phase difference.

When using the values for the structure design of iteration 11, an input amplitude of 10% of the hover lift, an input frequency range from 11500 to 13500 rpm, as given by the propulsion group, and a phase difference of 180 degrees, the maximum lateral deflection was found to be $(x_h - x_p)_{l,max} = 2.36 \cdot 10^{-6} mm$. Such a small deflection will not cause structural problems. On the other hand, the maximum g load on the hull under the same circumstances is $g_{l,max} = 0.51$. This is not a negligible acceleration, it could render the readings of the gyros and accelerometers located in the hull useless. However if the frequency spectrum of the acceleration on the hull is investigated, the Fourier transform presented in Figure 7.21 shows that only two peaks are present, at frequencies of 225.0 Hz and 485.8 Hz. The first one is the input frequency of the motors at 13500 rpm and the second one is the natural frequency of the struts under lateral vibration. In reality, harmonics of both this frequencies would also be present. Nevertheless, since all of these are high frequencies, a low pass filter can be used on the data collected by the accelerometers and gyros, and the acceleration due to vibrations will not influence the navigation performance of the UAV. In addition, since the sampling frequency of the IMU of the Navstik is 4000 Hz, vibration

frequencies up to 2000 Hz will be sampled correctly and aliasing will not occur. Higher frequency vibrations will have low enough amplitudes that will not pose a problem to the navigation, even if aliasing is present. Moreover, resonance due to the main input frequency will not be experienced in lateral vibrations due to the high natural frequency of the system and the limited input frequency of the motors and propellers. Regarding harmonics of the input frequency, the second harmonic of the input could induce resonance. However, the amplitude of the second harmonic would be lower than the amplitude of the base frequency, and the damping inherent to the strut, which was not considered in the analysis for simplicity, would prevent the hull vibration amplitude and the acceleration from growing past the point that would compromise the structural integrity of the drone.

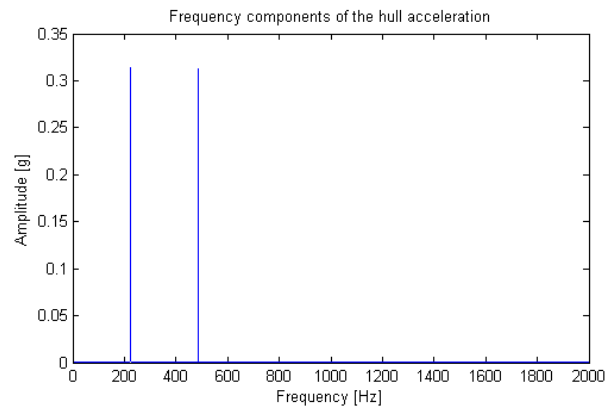


Figure 7.21: *Frequency components of the acceleration on the hull in the lateral direction*

When the same inputs were used to analyze the vertical vibrations, a maximum deflection $(x_h - x_p)_{v,max} = 1.21 \cdot 10^{-5} mm$ and a maximum g load $g_{v,max} = 0.008$ are found, at 11500 rpm. Both have a negligible impact on structural integrity and navigation capabilities. Also, the frequency spectrum of the acceleration, presented in Figure 7.22 shows two peaks, one at 26.7 Hz and one at 216.6 Hz. The first is the natural frequency of the system under vertical vibrations, and the second is the input frequency. As with the lateral vibrations, the input frequency is high enough to be filtered out. The vibrations on the natural frequency could probably be filtered as well, but the natural frequency is low enough that it may not be feasible. Either way, the amplitude of the acceleration is low enough that it will not have a noticeable impact on the navigation performance of the drone [20]. Regarding resonance, as long as the frequency of operation of the motors is maintained at a high enough level, no structural problems will arise.

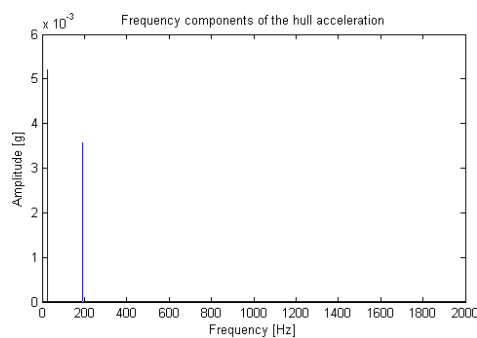


Figure 7.22: *Frequency components of the acceleration on the hull in the vertical direction*

Factors that generate a force that induces lateral or vertical vibrations, like propeller mass imbalance, can also induce moments on the propulsion subsystem mass. Similarly to the forces mentioned before, these moments would occur at the motor rotational frequencies of the UAV and its harmonics, and induce vibrations on the drone as well. In order to analyze the effect of these moments, a model equivalent to the one shown in Figure 7.19 was used. However, since these vibrations involve rotations, the masses m_h and m_{prop} were substituted by J_h and J_{prop} , the moments of inertia of the hull and the propulsion elements respectively. Moreover, the variables of the model were changed to θ_h and θ_{prop} , the rotation of the hull and the propulsion elements with respect to a horizontal frame of reference. Finally, the linear spring with stiffness k connecting both masses was substituted by a rotational spring with stiffness k_r .

The expression for the stiffness k_r was found following an equivalent process to the one outlined to determine k_t . This time, instead of axial and bending stiffness of the struts, torsional stiffness k_t and rotational stiffness due to bending $k_{r,b}$ were used. The expression for k_r is given in Equation 7.67.

$$k_r = \frac{3}{2}(k_t + k_{r,b}) \quad (7.67)$$

$$k_r = \frac{GJ}{L} \quad (7.68)$$

$$J = 2\pi R_{strut,inner}^3 t_{strut} \quad (7.69)$$

$$k_{r,b} = \frac{EI}{L} \quad (7.70)$$

$$F = \Delta m_{prop} \omega^2 L \quad (7.71)$$

As with k_t , the value of k_r is independent of the axis around which the rotation occurs, and so the vibrations analysis can be performed around any axis. The expression for k_t is given in Equation 7.68 [59].

In Equation 7.68, J is the torsional rigidity of the cross section. For the circular cross section of the struts, J is given in Equation 7.69.

The expression for $k_{r,b}$ as shown in Equation 7.70 was obtained rearranging the expression of the tip deflection of a cantilevered beam under a moment [70].

The force that a mass imbalance induces on the propeller shaft is given by Equation 7.71. This force times the distance from the propellers to the strut location gives the magnitude of the moment load that is used as input for the simulation of the vibrations due to bending.

In Equation 7.71, Δm_{prop} is the difference in mass between propellers, set to 5% in the analysis. The symbol ω stands for the angular velocity of the propellers, and is directly related to the rpm of the motor. As with the case of vertical and lateral vibrations, the highest rotations and accelerations occurred when the phase difference was 180 degrees. Using an input rpm range from 11500 to 13500 the maximum rotation of the hull was found to be $\varphi = 0.095 \text{ degrees}$, at an rpm input of 11500. The maximum angular acceleration occurred at the same input frequency, and resulted in a linear acceleration in the hull of 4.81 g. Similar to the vertical and lateral vibration modes, the deflection due to moments acting on the propulsion subsystem will not compromise the structural integrity of the UAV. However, the acceleration experimented by the hull in this vibration mode is considerable, and would not allow the use of the IMU data for navigation. Fortunately, the frequencies at which the UAV vibrates in this mode are 87.46 Hz and 191.7 Hz, as seen in Figure 7.23, both high enough to be filtered out. Moreover, as long as the minimum rpm of 11500 is not decreased, resonance will not occur in this vibration mode.

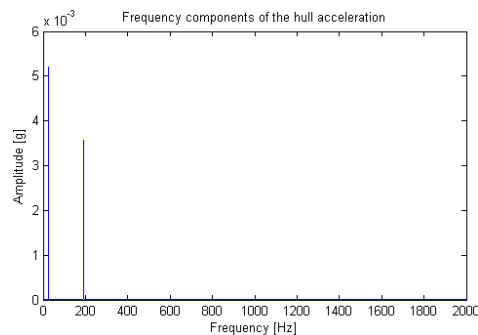


Figure 7.23: Frequency components of the acceleration on the hull in the bending mode of vibration

This section addressed the structural analysis of the vehicle's architecture. The reader got acquainted with the hull design in Section 7.1 and with the strut design in Subsection 7.1.2. The hull makes use of 1 mm thick walls on the all sides. The struts are hollow cylinders with 4.6 mm inner and 5.7 mm outer radii. Section 7.2 introduced impact resistance concepts. The employed design makes use of the foam finger paddings on the sides and full foam cover on the top and the bottom of the hull. Also, a protective fence was placed on the top and bottom of the duct to account for Occupational Health & Safety considerations. Lastly, the vibrational analysis of the structure concludes that resonance will not compromise the structural integrity and that vibrational accelerations on the payload (IMUs) either are negligible or can be filtered out.

8 | Data Handling & Hardware-Software Interaction

To ensure the proper interaction of the individual payload components, the software design needs to take care of the data flow through the complete system and the human-machine-interaction. In order to start with the software design, the complete airborne system needs to be split up into individual parts with a given functionality and clearly defined in- and outputs. The main subsystems to consider are the following:

1. Propulsion
2. IMU & Control
3. Visual recording
4. Additional World perception
5. Communications
6. Environment interaction

These subsystems together ensure the full operability of the system. The individual hardware components used have already been addressed in the previous chapter in Section 6.6. This chapter will focus on the individual interaction of these components and not on how and why they were chosen.

Section 8.1 will cover the internal data handling and data flows between the hardware components and also functions as an indication for the internal wiring. Section 8.2 will show the additional software needed to run the system aside from the off-the-shelf Paparazzi flight controller used by the Navstik by means of a software block diagram.

8.1 Data handling

The summary of the overall data handling structure is given in Figure 8.1. Two main processing units are in charge of handling all the drone's data: The Navstik for Flight control and the Gumstix Overo Earthstorm mostly in charge of video compression and forwarding; its additional computing power can be used to process additional flight control maneuvers if necessary in case the slower Navstik cannot handle all the sensor data.

Both the Navstik and the Gumstix are attached to a breakout board to add additional interfaces for connection of sensors and actuators. The Navstik is attached to the IvyPro interface board, which is equipped with a 16GB micro SD card to function as a flight-recorder/blackbox. The Gumstix Overo, which itself is already equipped with a 32GB micro SD card, is attached to its expansion board Summit to attach the IR camera and the transceiver unit.

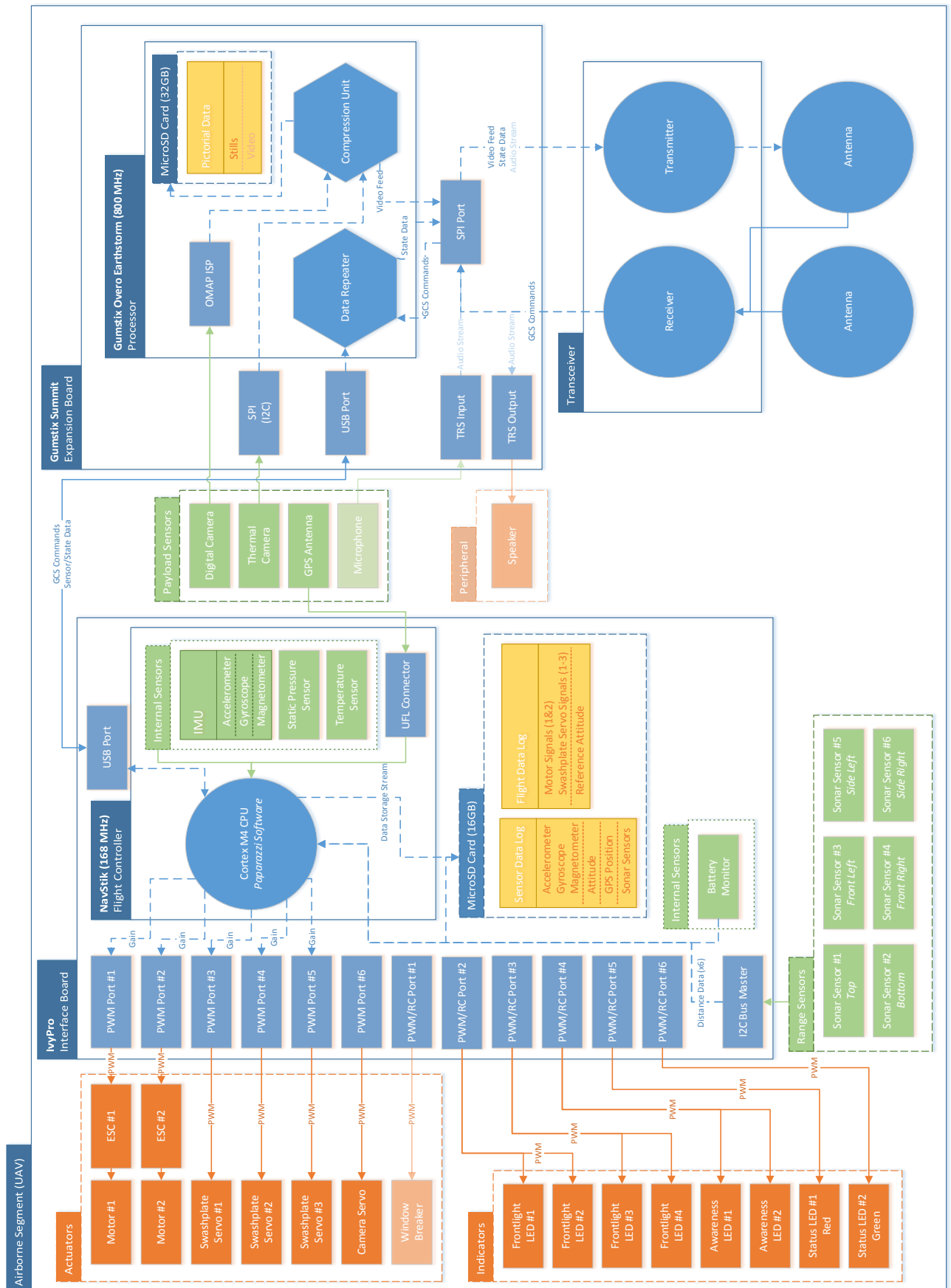


Figure 8.1: Data handling diagram of the UAV

Following the flow of data from the operator command through the system, back towards the GCS:

GCS Commands: Via the GCS, the operator sends commands towards the UAV in the form of gain values for roll, pitch, yaw and thrust; plus occasional commands to turn on/off the lights and/or change the flight mode of the UAV. This data is received by the transceiver and directly forwarded to the Gumstix summit via its SPI Port. Also, the processor on the Gumstix Overo decodes the received command data stream and sends it via the USB serial port towards the Navstik.

Navstik + IvyPro: The Navstik itself is a specialized flight control board, which does the control and stability calculations based on the pre-programmed layout of the UAV and the real-time received sensor data. It has a built-in IMU with an accelerometer, gyroscope and magnetometer as well as a static pressure and a temperature sensor ¹. The Navstik also receives additional sensor data directly and indirectly; a GPS signal is received via the dedicated UFL connector and the data of the 6 sonar sensors is received via the I2C bus of the IvyPro and forwarded to the Navstik. The IMU data together with the gathered sonar and GPS data is then merged via sensor fusion and together with the GCS commands used as input for the main control loop of the Paparazzi flight controller.

The paparazzi software will need to be altered to properly fuse all the additional sonar data to ensure the best possible ease of use for the operator, while still ensuring essential safety; this planned alteration will be addressed in the Section 9.3. In essence, the Paparazzi software converts all the sensor and command input data to a set of gains for the individual PWM ports connected to propulsion actuators, which in the present case are the 2 brush-less motors on port 1&2 and the 3 servos for the swash-plate tilt mechanism on ports 3-5. The sensor data and the results of the Paparazzi control algorithms are all stored in the micro SD card on the summit for flight path reconstruction and possible incident investigation in case of an unexpected failure or irregularity.

Besides the 6 dedicated PWM ports, the IvyPro interface board also has the possibility to use the 6 RC ports as PWM signal ports, these ports will be used to attach different kinds of LEDs for several purposes. In order to still be able to have a proper visual image in low lighting conditions, 4 high brightness LEDs are mounted to the front of the UAV in pairs of 2 to illuminate the area that is perceived by the cameras. A third PWM port is mounted to 2 auto-blinking LED's mounted on the side of the UAV for awareness of bystanders and enhanced visibility of the system at night or in dark indoor confinements. Due to the control of the LEDs via PWM ports all of them can be dimmed according to outdoor lighting conditions to save energy when high brightness is not required or contra productive e.g. blinding a subject of rescue inside a building. 2 PWM ports are connected to a red and a green status LED to display various information such as the flight controller status: e.g. 'Self-test completed', 'Ready for Takeoff', 'Battery low' or 'an Error occurred'. The last additional PWM port can be used to control the additionally attached window breaker mechanism, but since the design choice for this has not been finalized, this is merely an option.

Video Feed: Since 5 out of 6 dedicated PWM ports of the IvyPro are used for direct flight control, the remaining one is connected to the frontal servo used to pitch the 2 cameras: The e-CAM56-37x digital camera and the Flir lepton IR camera. These cameras are both connected to the Gumstix module, the digital camera is directly connected to the Overo processing unit via the OMAP ISP port, while the IR camera is connected to the SPI port on the Summit expansion board; both camera feeds are compressed by the compression thread on the Overos central processor to reduce the data rate that is send towards the GCS. Apart from the live video feed the cameras can also be used to take high quality single frame pictures to be stored on the micro SD card.

The compressed video streams together with general state- and sensor data received from the flight controller via USB will be combined to data packets that are being send via the SPI port and the transceiver to the ground station, to be processed on the GCS to be displayed in a comprehensible fashion on the GCS visual interface; in terms of video stream and flight instruments.

8.2 Software Design

Due to the design choice to use the Paparazzi hardware-software solution to control the UAV, the overall software that needs to be written to control, operate and communicate with the drone is rather marginal and most of the data flows in between the components and sensors are represented in Figure 8.1 and have just been explained. The more complex computations are the Paparazzi flight controller running on the Navstik and video compression running on the Overo; all other software functions are mostly direct data transfer via e.g.

¹URL: <http://wiki.navstik.org/doku.php?id=hw:ivypro>

sockets, sensor decoding and few smaller command loops to ensure e.g. the tilting of the camera, turning on and off the LEDs and possibly send the audio stream to the speakers.

There are 4 main computation blocks:

1. Flight Controller
2. Video compression
3. Communication
4. Sensor data pre-processing

The flight controller is an enclosed block handled by the external software; the internal processing of the Paparazzi system and possible alterations are addressed in Chapter 9.

The video retrieval is done via the build in ISP and SPI ports and compressed via the established h264 compression algorithm, this software functionality is described in Section 6.4.2.

The main task of the communications software is the merging of the individual sensor- and video data into a single compressed and encrypted data stream to be sent in packages towards the GCS, this system functionality is explained in Section 6.4.2.

The later sensor data processing is dealt with individually for the different sensor types: For example the voltage measurement of the sonar sensors needs to be translated to a distance via a calibration table/formula, the same holds for e.g. the accelerometer where the conversion is from voltage to acceleration; these are in essence one-liners executed during run time and do not require extensive computational power or attention.

In this chapter the interaction between the individual payload components and handling of data is depicted. Furthermore the operational software is explained.

9 | Control and Stability

The following chapter will introduce the theory on how to control the UAV. Since the flight control is taken care of by the paparazzi control software only the basis of the control method is addressed. The second half of the chapter will focus on what changes have or can be made to the existing software to enhance performance, optimize and ease the human-machine interaction.

9.1 Actuation flow

The IPD is in essence a tailless coaxial helicopter, so the control of such a drone is not trivial. Even though it will be handled by a third party software it is of utmost importance to understand the dynamics of existing system and not completely rely on the performance of a pre-programmed software.

Before going in depth looking at the actual control, it is needed to first get a better understanding of the characteristics and layout of the propulsion units and actuators that compose the overall physical control system. In the case of the IPD there are a total of 5 control actuators:

1. Engine #1
2. Engine #2
3. Swashplate Servo #1
4. Swashplate Servo #2
5. Swashplate Servo #3

All these actuators are controlled via the PWM ports on the IvyPro interface board. The control/actuation flow from the software output PWM signal towards the absolute drone state is depicted in Figure 9.1 and will be explained in the following section:

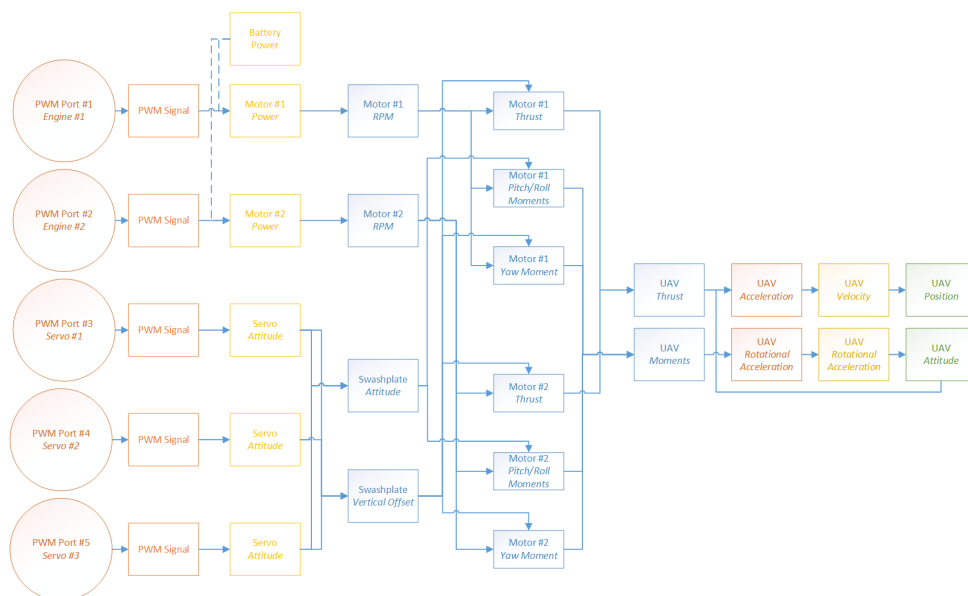


Figure 9.1: Control Flow of the UAV: Software output -> UAV final state

The PWM signals for the motors define the given throughput power to the motor, resulting in a given RPM based on the drag of the rotor blades, this RPM is translated to the thrust the propeller generates given its own induced velocity. The exact calculations on how to get from a given rotor RPM to the thrust are explained in Section 5.1.

Based on the specifications of the servos, the PWM signals sent into the servos will position the servo under a given angle based on the pulse length (for off-the-shelf servos the pulse length for the neutral position is around 1,5 ms). Hence the PWM signal send to the servos directly control their attitude and neither rotational velocity nor -acceleration. A rod is connected to the end of the servo arm and to both the upper and the lower swashplate, the upward deflection of the servo actuated rod is given based on Equation 9.1.

$$\Delta h_{servo} = r_{servo} \cdot \sin(\Delta \alpha_{servo}) \quad (9.1)$$

Since the rod connected to the servo is attached to the top- as well as the bottom swashplate, they are coupled and will behave both in a similar fashion, the 3 servos are all attached to a joint on the swashplates. Just as 3 points can form a plane, the three joint ends on the swashplate actuated by the servos form the swashplates' plane and define its attitude as well as its overall elevation; in terms of helicopter flight controls the attitude of the swashplate correspond to a cyclic input and the overall elevation corresponds to a collective input.

While the swashplates' outer ring is connected to the actuation rods of the servos, the inner part is freely rotating due to a ball bearing, yet maintaining the same attitude as the outer ring. The inner part is connected to the handles attached to the individual rotor blades. The pitch of the rotor blades is changed corresponding on the upward deflection of the rods based on the swashplate attitude and its current position in terms of heading in its own body reference frame (ψ_{ActRod}), corresponding to Equations 9.2 - 9.4.

$$\beta_{swash} = -\sin(\psi_{ActRod}) * \phi_{swash} - \cos(\psi_{ActRod}) * \theta_{swash} \quad (9.2)$$

$$\Delta h_{Act} = r_{swash_{inner}} * \sin(\beta_{swash}) + h_{swash} \quad (9.3)$$

$$\theta_{blade} = \arctan\left(\frac{\Delta h_{ActRod}}{r_{BladeArm}}\right) \quad (9.4)$$

The unsymmetrical pitch distribution results in an unsymmetrical lift distribution over the blade, creating a moment around the center of gravity to pitch and roll the UAV.

9.2 Flight Controller

The flight controller itself is handled by the NavStiks Paparazzi software, and is a complex universal flight controller. To properly understand how the system works it is best look at the top level control loop that is executed to stabilize the drone in a given reference attitude, this loop is illustrated in the lower half of Figure 9.2. The control of attitude is very easily executable due to the fact that the drones attitude is one of the properties that the internal sensors can measure with a low bias, therefore these values can be reliably used to minimize the control error. This is the most common form of control for rotorcraft drones.

In the case of attitude control the operator gives a reference attitude with the joystick and communicates this to the drone. The IMU of the UAV measures the attitude in pitch and roll of the drone and the rotational velocities around all its 3 axes. With these parameters known the error between the desired- and actual attitude, as well as the desired- and actual rotational velocity can be calculated (usually for the sake of stability $\omega_{ref} = 0$). These errors are then used as input for the PID controller calculating the desired gains for pitch and roll. For the present vehicle, the resultant control gains correspond to a given swashplate, which is then fed into the Servo Mixer that will translate a given swashplate attitude to the servo rod deflection and their corresponding PWM signal values.

To increase the user friendliness of the system and increase the Human-Machine-interface efficiency, a 'Corridor traverse mode' should be implemented as an optional flight mode that once engaged will enable the user to set a constant speed at which the UAV will traverse through a hallway, until it reaches an obstacle in front of it (end of the hallway, or corner) or the user specifically stops the traverse. The drone will keep itself in the middle of the corridor by accounting for the difference in sonar sensor distances in the calculations of the lateral and vertical control gains. Due to the limitations in velocity management it might be possible to use the GCS as an external computing source to perform an optical flow analysis on the received video feed to approximate the forward velocity.

3) 'Take a look around':

To make full use of the optional virtual reality component of the GCS, a flight mode should be implemented that enables the operator to inspect its surrounding area in an intuitive fashion, fully concentrating on the observation and less disturbed by the need to operate and stabilize the vehicle. To incorporate the use of the VR kit, the operator has the possibility to actually 'Take a look around' by tilting his head in the desired direction, the IMU in the VR headset and possibly an additional IR head tracker will measure the operators head movement and its absolute attitude, which can then be translated into the pitch angle of the camera servo and the control gain for the UAVs yaw axis. Therefore, the camera will indeed face into the direction of the operators eyes/head. This flight option is most useful in combination with the corridor traverse mode.

The biggest issue with this mode of operation is that since only one servo is used to control the camera the UAV has the yaw to look laterally and therefore does no longer face into the direction that is considered to be 'forward'. In terms of flight control this is easily solvable with a correction matrix on all the incoming data, transforming the data from the vehicle's body frame of reference to the flight controller flight coordinate system. But in terms of intuitive control by the operator, it might result in a few major issues. Imagine this: You're the operator and slowly traverse through a corridor and use the drone's camera to look for victims and suddenly to your left you see an unconscious individual lying on the ground, your initial reaction is to move forward towards that person to take a closer look; but remember, your specified forward direction is now to your right so as soon as you move your stick to the front suddenly you move sideways! To solve this problem an indication in terms of a head-up display style arrow shall always point your specified forward direction. Therefore as soon as you tilt your head sideways there's always a reminder present. Most importantly a reset button needs to be present that will reset the forward direction and/or end the 'Take a look around' mode, to enable a quick maneuvering as soon as you made a discovery. Coming back to the scenario that was just pointed out, the operator would press the reset button as soon as he made his important discovery and then engage in a quick forward maneuver resetting his forward direction and directly leading him towards his destination.

4) Connection-loss halt and landing:

In case of a connection loss with the GCS, the UAV shall engage in a 'Hold' mode that will minimize the systems acceleration, which can be directly translated to attitude, and possibly if measurable minimize absolute velocity to keep its initial position at the time of connection loss as accurate as possible and prevent a crash with the surroundings and/or a major uncontrolled drift around the perimeter.

In case the connection loss is not temporary and remains for a certain duration of time the system will be given 2 possible options: 1. Land and remain at the specified location to enable a possible rescue of the UAV in case humans will be entering the building after all. 2. Return to the GCS autonomously, aborting the mission, but saving the system itself to be reused in a follow-up mission after repairs have been performed. This second option is very complex and non-trivial, but will be addressed shortly.

5) Outdoor safety height:

To ensure no individuals will be harmed during the outdoor use of the system, the UAV shall, if requested, make use of the nadir pointed sonar sensor to measure it's height and always remain above a set safety height (approx. 2-3 meters); this will be very useful since the operator has no 'eyes' on the bottom of the vehicle and from a FPV point of view, its rather difficult to estimate your height above the ground and some possible obstacles can be overlooked. This mode is very similar to the proximity aided indoor flight, but in this case preventing crashes with ground based individuals and objects rather than walls and other objects.

Experimental Flight Modes

Besides these feasible and highly beneficial flight mode scenarios, a few other modes were also accounted for that require a significantly increased amount of work and computing power; these are not exactly trivial and quite experimental but very promising concepts.

6) Velocity control

Controlling a rotor-craft requires dual integration in the operators head, since the accelerations are controlled

essentially by means of throttle (vertical acceleration) and attitude (directional lateral acceleration). The only axis that is essentially controlled by means of (rotational) velocity is the yaw, as during a yawing input the UAV can directly measure the rotational velocity via the gyroscope and cancel it out via a PID controller, just as it does for the attitude. This form of control requires a lot of practice and precision by the pilot to properly maneuver such a vehicle especially via FPV. Therefore, every aid to ease the use of the system is very welcome, especially if every second counts. A control by means of a given reference velocity by the operator is the most intuitive form of operating any vehicle: Forward input \rightarrow forward flight; Zero input \rightarrow zero velocity (Hold).

In theory and for simulations, this method of control has been tested and been proven to be very effective and intuitive. This is similar to the control of a video game character and can be compared to the control of a car. Although, in a car, technically accelerations are the given input, but the quickly converging drag results in the intuitive feeling of velocity control. The problem arising though is the necessity for a very accurate measurement of the velocity. For an airborne vehicle without any external sensor, this is not trivial for small velocities. One possibility is to use a differential pressure sensor (pitot tube), the downside of this is that this measurement is only directional and only provides indicated airspeed and not ground speed.

The currently mounted sensors can give an indication of the drones state of velocity by means of fusing all sensor data together: For very short time-frames the IMU of the drone can give a reasonable estimation of the drones velocity by means of integration of the accelerometer data in accordance with the gyroscope. This method however is very prone to drift. A more direct measurement of velocity can be obtained by differentiating the distances measured by the sonar sensors, e.g. a decrease in distance can be translated to a velocity towards the wall, with the the drone can keep a constant distance from the wall. The excess computational power of the Gumstix Overo can be used to perform optical flow computations in lower resolution which can be used to calibrate the IMU velocity data: First the optical flow measurement is calibrated based on the knowledge on the rotational velocity of the drone from the gyroscope, hence any errors due to rotations can be reduced. If the resulting data if shows stationary behavior of the drone it can be used as fix point to reset the drones velocity to 0 hence nullifying the error caused by the IMU drift, on the other hand if the camera measures a optical flow not caused by the drones eigenmotion, but due to a dynamic object in front of the lens it can be distinguished due to the drones velocity measurement based on the IMU, hence if the drone was stationary and did not accelerate since the point of a dynamic optical flow measurement it can be assumed to a dynamic object rather than the drones eigenmotion. In anyway this control needs to be dealt with a lot of caution since exponentially growing errors can result in serious problems , therefore this method should only be used in situations when the probability of an erroneous measurement can be assumed to be small enough, hence when the sonar sensors give an absolute distance measurement for calibration. The best use of this flightmode is in cooperation with the corridor traverse mode where the walls are in close proximity and deliver adequate absolute distance measurement

Assuming the absolute velocity of the system would be exactly known at any point in time the control would be as follows: the error between the absolute velocity of the UAV and the reference velocity set by the operator, can be translated to a given reference acceleration based on a set proportionality factor defining the minimum settling time of the system. For example, with a difference velocity (V_{dif}) of $1 \frac{m}{s}$ and a gain $K=2$, the reference acceleration (a_{ref}) is given by: $V_{dif} \cdot K = 2 \frac{m}{s^2}$ resulting in a minimum Settling time ($t_{settling}$) of: $\frac{V_{dif}}{a_{ref}} = \frac{1}{K} = 0.5s$. This reference acceleration is then translated to a given reference attitude of the vehicle in the form of roll and pitch. This value is then fed into the regular PID attitude control system of the flight controller. The conversion from acceleration to attitude is performed by means of trigonometry, the current engine thrust setting and the known system mass.

If $a_{ref_z} = 0$ the formula is very straight forward and reduces to: $\theta = \arctan(\frac{a_x}{g})$.

A summary of this control algorithm given in the upper half of Figure 9.2.

All in all this flight mode can most probably not be implemented with sufficient accuracy, but can be used partially to prevent collisions: In case the operators flies to fast forward through the building and approaches a wall the differential measurement of the frontal sonar sensors translated to a velocity can be used to perform a quick breaking maneuver, a technology that is currently more and more adapted by car manufacturers to increase the vehicles safety.

7) Return to Base

As a last additional flight mode a 'return to base' function would significantly ease the use of the system. The main idea behind this flight mode is that the drone will be able to autonomously find its way back to the GCS, as soon as 1: the operator decides to abort the mission, 2: the UAV realizes that its battery power is below the critical value to make a safe return or 3: the communication with the GCS is lost for a prolonged time;

in this case the chances of a reconnection are enhanced.

As incredibly helpful this function might sound, its implementation requires a lot of ingenuity and computing power, as the current equipment of the vehicle does not allow for an absolute positioning while being indoors. To successfully implement and execute this functionality, the UAV requires extensive information about its surroundings, by this means the drone is in need to create a map of its perimeter while traversing through the building. Larger UAVs equipped with a Light Detection and Ranging (LIDAR) system can create very accurate maps of their surroundings, but not only are these systems very heavy but they are also power consuming and their processing the data requires a lot of (usually external) computing power. The system if implemented should be able to perform this task, while disconnected to the GCS, hence without external computing power. A solution for this would be to track to the position of the UAV via GPS while outdoors to enable safe return to the GCS and indoors a sophisticated sensor fusion is necessary that makes use of the local tracking of the UAVs movement using the IMU data and cross-check of speed with the sonar sensors and optical flow based on the camera data. A means of breadcrumbs navigation can be implemented based on a quick pattern recognition software, spotting and re-identifying of particular structures inside the building.

9.4 Summary

To summarize the findings on the UAV's control system, it is safe to assume that the well established Paparazzi autopilot software will take care of the overall control and stability of the dual swashplate actuation system. The tasks left to be performed are the optimization of the original code and the integration of additional flight modes as stated in the previous section. These flight modes except for mode #7 & #8 are pure software solutions and no changes in the hardware design are needed to implement them and make them reality.

10 | Verification and Validation

In this chapter, the calculations of the system properties will be verified and validated and the methods to do this will be explained. In Section 10.1, the propulsion calculations will be verified and in Section 10.2 validation methods are proposed for the results. In Section 10.3, the verification and validation for the structural calculations are performed. In Section 10.4, verification and validation for the communication subsystem is shown.

10.1 Verification of Propulsion Calculations

The theory used to perform the propulsion calculations as shown in Chapter 5 is already verified as it has been taken from articles and known helicopter dynamics. However the program used for the calculations needs to be verified. This verification will be done in the same order as the theory is explained in Chapter 5.

10.1.1 Verification of Thrust Calculations

The calculations described in Section 5.1 have been revised by analytical performing the calculations. This resulted in exactly the same values as the program directly uses the analytical method to calculate the values. However, as a special note, the drag coefficient for the design could only be approximated. This approximation is performed at a Reynolds number of 10000 while the drone itself has a Reynolds number of 200000. This discrepancy is very large as there was no accessible data on higher Reynolds numbers. Thus, it is important to validate the drag coefficient using tests when the prototype is developed.

10.1.2 Verification of Coaxial Rotor Calculations

The integrals shown in Section 5.2 are too complicated to be performed analytically. Therefore, this part of the program can not be verified using an analytical method. Instead, the code was evaluated for convergence as the step size used to calculate the integrals increased. At first, the value from the integral increased in the same order as the step size was increased. This error was investigated and solved to have the integral converging. Tests were also performed by varying the initial guess of the Prandtl tip loss factor, however, convergence was found for values between 0 and 1 in varying step sizes.

10.1.3 Verification of Propeller Design

The twist distribution calculations in Subsection 5.4.2 have been verified by taking random points along the propeller and comparing the numerical values to analytical values for the velocities the propeller sees. These were either exactly the same or insignificantly different due to rounding errors. Using these velocities, the angles were plotted over the length of the propeller as seen in Figure 5.7 and the twist distribution was fitted over this plot for visual inspection. The twist distribution was smooth enough for production and did not differ from the angle it was set to be either exactly the same or only different due to rounding errors. The tip displacement was verified using several assumptions. The formulas are too computationally intensive due to the blade twist and distributed force. Therefore by using a constant inertia and an uniform distributed load it could be verified that the values are in the right order of magnitude, but could not be used to verify the exact number. The stresses were verified analytically and found to be exactly the same as the numerical program.

10.1.4 Verification of Power Calculations

The calculations described in Section 5.5 have been confirmed by additional analytical calculations. This resulted in exactly the same values as the program directly uses. However, the Figure of Merit can also be

checked against known values from existing designs. For a standard helicopter design, the FM is in the range of 0.6 to 0.65.[7] As the drone design mostly uses helicopter dynamics theory, the FM of 0.58 is very plausible.

10.2 Validation of Propulsion Design

As mentioned in Subsection 10.1.1, the drag coefficient of the drone should be validated using tests such as wind tunnel testing. Although, the effects of a duct and coaxial rotors have been studied extensively little is known about the combination of these two parts. As such tests need to be performed to validate the combination of the theory used to calculate the effect of the duct and the theory used to calculate the thrust of the coaxial rotors.

Regarding the effect of the duct, it is known that blade tip clearances of $1m$ or less are preferable. [4] However, due to impact constraints, a larger blade tip clearance of $5mm$ is chosen for the design and the effect of a larger blade tip clearance is not present in the theory and needs validation from experiments. For the effect of the coaxial rotor wake analysis needs to be performed to see what the wake contraction of the upper rotor and thus validate the assumption that the wake of the upper rotor is fully contracted. The tip displacement of the blades can be validated by manufacturing a model and applying the right force to it. In this way, the tip displacement can be measured. The tensile and bending stresses should be validated using strain gauges on the model.

10.3 Verification and Validation of the Structural Design

Verification of the models used to simulate structural behaviour was conducted to ensure the results obtained agreed with the theoretical models used. The choice of theoretical model has already be discussed in the respective sections, however, this section describes the verification of code implementation.

10.3.1 Buffer Design Response Analysis Tool

The *MATLAB* tool designed to simulate the loads on the spring and viscoelastic buffer design was verified against similar implementations of a conventional spring mass and spring-damper mass system. The fundamental equations of motion used to simulate the systems as described in Sections 7.2.1 and 7.2.2 do not need to be verified as they are widely adopted equations to model the system.[62] The coding was checked using simple spring constants and damping coefficients to ensure the correct response, including period and frequency, was computed by theory of vibrations [62]. Individual functions of the code were verified by ensuring correct implementation in code and computing results by hand to check agreement. Bugs in the code were rectified before it was used for design. As described in Sections 7.2.1 and 7.2.2, the average force computations were verified against simplified theory based on change of linear momentum using the rebound velocity and time. Given the highly non-linear behaviour of viscoelastic material [64], it is recommended to validate the results with experiments to get realistic behaviour of the material under impact.

10.3.2 Stiffening Ring Calculator Tool

It is of primary importance to ensure that the tool that is used for the Stiffening Ring concepts is properly verified. Therefore, a verification procedure was carried out on the Stiffening Ring calculator tool. Firstly, the so-called code verification has to take place which is the systematic checking and re-checking of the code while fixing syntax errors. It can be reported that all syntax errors were properly fixed and the software is error free. The next step in the process is calculation verification where the parts of the code are examined, several inputs are being run on it and the results are compared with analytical solutions. The moment of inertia calculation comparisons can be seen in Table 10.1.

Table 10.1: Verification of the inertia calculator of the Stiffening Ring Calculator tool

Height [mm]	Thickness [mm]	Numerical I_{yy} [m^4]	Analytical I_{yy} [m^4]	% Difference
4.5	4	$3.04 \cdot 10^{-11}$	$3.04 \cdot 10^{-11}$	0
5	4.5	$4.69 \cdot 10^{-11}$	$4.69 \cdot 10^{-11}$	0
5.5	5	$6.93 \cdot 10^{-11}$	$6.93 \cdot 10^{-11}$	0
6	5.5	$9.9 \cdot 10^{-11}$	$9.9 \cdot 10^{-11}$	0
6.5	6	$1.37 \cdot 10^{-10}$	$1.37 \cdot 10^{-10}$	0

The verification of each equation and loop was carried out in the same fashion and it was concluded that the difference between the numerical and the analytical solutions does not exceed 1 %. Also, the final results of the code have to be verified, this is done by using the same values as in Table 10.1 for the compressive stress calculations presented in Equation 7.46. The results can be seen in Table 10.2.

Table 10.2: Verification of the compressive stress calculations

Height [mm]	Thickness [mm]	Numerical σ [m^4]	Analytical σ [m^4]	% Difference
4.5	4	$8.66 \cdot 10^8$	$8.65 \cdot 10^8$	0.1
5	4.5	$6.23 \cdot 10^8$	$6.23 \cdot 10^8$	0
5.5	5	$4.64 \cdot 10^8$	$4.64 \cdot 10^8$	0
6	5.5	$3.54 \cdot 10^8$	$3.54 \cdot 10^8$	0
6.5	6	$2.77 \cdot 10^8$	$2.77 \cdot 10^8$	0

The rest of the code was also verified and it was concluded that the maximum difference between the analytical and the numerical solution was 0.1 %. These results are not presented in this document due to the limited amount of space allowed for reporting. Due to the limitations of the Design Synthesis Exercise, it is not possible to collect real-life data for the validation of the software, therefore the validation procedure is disregarded. However, assessing code validation is recommended for future work in order to ensure that the calculated results are accurate and accurately represent reality.

10.3.3 Hull cross section stress calculations

The Matlab script used to calculate the stresses in the hull cross section was verified as follows. Firstly, the dimensions of the cross section were set to be such that the cross section was symmetric around two axis. The first verification step was then to calculate the location of the centroids of the cross section elements, and their moments of inertia. This values were compared with the calculated values in the script, and they were found to match. The next step involved the location of the centroid and the shear centre. For such a cross section the location of these points coincides with the point where the symmetry axes meet. While the centroid was in the expected location, and the x location of the shear centre was correct, a small error of 1.29% was found in the vertical location of the shear centre. This error was attributed to the imperfection of the integrals performed to obtain the value. Moreover, since the error was so small, it was deemed negligible. Next, the bending stresses and shear flows at certain locations were calculated analytically and compared with the stresses calculated by the tool. This was the main verification procedure, and when it was performed, the stresses were found to be in agreement. Other procedures were followed as well, making use of theoretical knowledge of the stresses in a cross section. For one of these steps, a single vertical shear force was applied through the centre. The constant shear flow due to shear forces calculated by the tool was found to be zero, as should be the case. For another verification activity the von Mises stresses caused by a vertical force not acting through the shear centre were compared to the stresses of a fore of the same magnitude acting through the shear centre and an additional equivalent moment around the z axis. The stresses were found to match perfectly in both cases. More of these activities were performed but are not included here due to page limit constrains.

10.3.4 Vibrations calculations

The main functions used in the vibration analysis script are *lsim* and *fft*. Since these are standard Matlab functions they were not verified. What was checked was the inputs. It was made sure that the moment of inertia, Young's modulus, and area of the strut were correct, as well as the masses of the propulsion system and the hull. In addition, the derivation of the state-space system was double checked, in order to assure the

correct system was being solved, and that the model would accurately represent the system. All these processes were performed without incidents, and the script was deemed verified by the team.

10.4 Verification and Validation of Communication Calculations

The link budget calculations presented in Section 6.4.6 and example performance analysis in Section 6.4.8 were based on theory widely adopted and well documented by many scholars. References have been provided to justify the theory and the method so only its implementation was verified. The program analytically computed results and was verified by computing the link budget by hand and confirming the results of the program. As both methods are analytical, there were no differences in the results obtained using both approaches. Unit tests were performed to check whether the correct functions for the atmospheric and wall attenuation were implemented by comparing plots against those available from the referred literature. To validate the results, it would be necessary to produce the system and conduct experiment in actual operational conditions. This would require a thorough study of the signal propagation in built-up indoor and outdoor environment over varying range using actual walls and obstacles to check power losses. It is also advised to test the antennae gains when integrated with the rest of the UAV to see how its performance is affected by interferences, placement and the quality of components.

11 | Sustainable Solutions

This chapter primarily deals with the sustainability of the developed system. It is of primary importance to develop a product that is both environmentally friendly and socially acceptable and economically favourable. Firstly, social considerations, such as influence of the system on human perception, occupational health and safety and user friendliness are considered in Section 11.1. This is followed by economical considerations in Section 11.2. Lastly, environmental considerations such as material selection, production techniques and recyclability are considered in Section 11.3.

11.1 Social sustainability

One of the primary concerns of UAVs is the perception by humans. Due to the lack of information of the public on UAVs, it is fair to assume that meeting with drones might cause either aggressive or unpredictable behaviour [71]. Therefore, it is of primary importance to make the people involved in such an operation aware of the drone's presence and its behaviour. One of the solutions is to apply painting on the vehicle that defines the intended user or the purpose. Such an example is the application of distinctive colours of the Dutch fire department (Brandweer). In this way, the victims to be rescued from a building on fire are warned that a rescue operation is being carried out. Operating in a smoky environment is also highly likely, so it is crucial to equip the vehicle with pulsating (LED) lights. For the fire department edition of the system, blue and red colours can be used to further emphasise that the operation being carried out serves the involved. Of course, the vehicle's outlook can be fully customised based on customer needs.

One of the advantages of the system is that it can be used for multiple purposes such as rescue operations and inspection activities as mentioned in Section 2. Since all of these operations might have human involvement, it is critical to prevent the system from being harmful to people in any way. One of the ways to prevent accidents is to make the system exhibit an equivalent level of safety (ELOS) to Conventionally Piloted Aircraft (CPA). It means that the pilot of the vehicle shall be equipped with a "RPAS Operator License" to operate the system. This law will be enforced by the Dutch Ministry of Infrastructure from the 1st of July 2015 and is mentioned in "Regeling op afstand bestuurd luchtvaartuigen". Unfortunately, that still does not necessarily convince the public of the reliability of such a system due to the fact that there are differences between conventional aircraft operations and UAV operations in perceived level of benefit or voluntariness of exposure [71]. Unfortunately, this is a consideration that cannot be designed for or mitigated and will only change over time when drone applications will be more present in everyday life. A way to improve public opinion is to have demonstrations of drone deployment in practice, for example during a fire drill.

It is not only important to create a product that complies with the regulations as imposed by authorities and that can be perceived as a non-harming product, but it is also important to make sure that in case of a system failure, the vehicle does not cause any trauma to the people involved. The most critical part of the body in terms of injury is the head. Head injuries are assessed using the so-called Head Injury Criterion [72]. Section 7.2.2 shows that the total duration of impact is approximately 18 ms. Also, Table 11.1 shows the allowable HIC values for different age groups.

Table 11.1: Head Injury Criterion for different people

Person Type	Large-sized Male	Medium-sized male	Small-sized male	6-year-old Child	3-year-old Child	1-year-old Infant
HIC Limit	700	700	700	700	570	390

This information can be used to calculate the impacting g load on the human body. Equation 11.1[72] shows the way the maximum allowable impact g-load on the head can be obtained.

$$A_{head} = 2.5 \sqrt{\frac{HIC}{t_{impact}}} = 2.5 \sqrt{\frac{390}{0.036}} = 41 \text{ "g forces"} \quad (11.1)$$

It has to be noted that infants might be involved in rescue situations, therefore they have to be considered as worst-case scenario targets. Therefore, the maximum allowable g load on their head is approximately $41 g$'s. Since it is already known that the vehicle will have a maximum impacting force of $111N$ (Subsection 7.2.2), one also needs to investigate whether the total force acting on the person's head due to collisions exceeds this value. The mass of an average 1-year-old's head is approximately $9kg^1$, so the maximum force that can act on their head can already be calculated using Equation 11.2 where m_{head} is the mass of the head and A_{head} is the g -load.

$$F_{allowable} = m_{head}A_{head} = 9 \cdot 41 = 369N \quad (11.2)$$

As it can be seen, the drone's impact force is significantly lower ($111 N$), so the vehicle does not cause head trauma upon impact. It is also essential to make sure that the vehicle does not cause lacerations. Due to the two counter rotating blade system, the UAV is a potential threat, however the payload housing hull covers most of the exposed area preventing injuries. Unfortunately, the top and bottom of the vehicle are not covered, therefore they introduce risk of injuries. This problem can be solved with the protective fence solutions presented in Section 7.3. In this way, the propellers of the drone are essentially fully housed and guarded from the environment, which means that lacerations are eliminated.

11.2 Economical Sustainability

This section contains information and elaboration on the economical sustainability of the UAV. To achieve economical sustainability, the target market is assessed to establish an estimate on the size of the demand. A customer with high interest in the product would be the Dutch fire departments. With about 900 fire stations, 400 of which in urban areas, this may generate a sizable demand². Since the national fire department's costs amounts to 1.1 billion euros annually, their budget is deemed sufficient to purchase the system as a new piece of standard equipment³. Other possibly interested parties are construction companies, building inspection services and emergency services other than the fire department.

A second point of interest for assessing economical sustainability are the production costs. Since most subsystems consist of off-the-shelf components, production costs can be directly translated into purchasing costs. Self produced components are the airframe and the propellers, and highly depend on the manufacturing method and materials used. Another factor is the batch size in which the components are produced. For example, using a 3D-printer might be cheaper than using a mold when only small batches are required. It is the Selective Laser Sintering (SLS) technique that will be used to produce the airframe of the vehicle. Although, this process has higher material costs per product, this process is still more economical when small batch sizes are considered than the conventional Injection Moulding [73]. This phenomenon can be clearly seen in Figure 11.1.

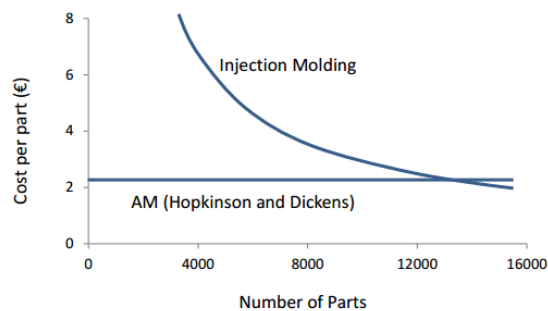


Figure 11.1: Comparison of production costs of the Selective Laser Sintering and the Injection Moulding processes[73]

This figure shows a significant decrease in price for the design at hand. Since the amount of parts to be manufactured are in the order of a few thousand, total manufacturing cost per part is decreased by at least 75%. (see Figure 11.1)

¹URL:http://www.babycenter.com/0_your-childs-size-and-growth-timeline_10357633.bc

²URL:<http://www.brandweer.nl/organisatie/brandweer-buurt>

³URL:<http://statline.cbs.nl/StatWeb/publication/?PA=37511>

A third important contributor is the durability of the components. For the end user, it is important that individual components do not need constant replacement, not only in terms of convenience but for the constant negative cash flow this would represent. If this cannot be guaranteed, the buyer might switch to a competitor's product. To gain an accurate estimate of the durability of the design as a whole, tests will have to be performed. For the purchased components, the manufacturer gives an indication of expected durability per part. This will have to be verified with real-life application of the component. For the self-made parts, durability assessment is slightly more difficult. It depends on the material and the manufacturing method employed. The three self-made components (airframe, rotor blades and hull protection), due to different imposed requirements, are made from different materials using different production methods. The airframe will be made out of two materials: the struts are made from HDPE, a High Density Polystyrene Blend [74]. Since this material is both chemical and corrosion resistant, non water-absorbing, has a high tensile strength and is very impact resistant, it is considered highly durable. The hull itself is made from PA 640-GSL, a very light-weight Nylon 12 Laser Sintering Material [75]. With a high strength-to-weight ratio, this is also considered a durable material. However, the hull is fitted with a protective rim, so the durability of the combination should be assessed to attain a good insight. This protective rim is made from MP15FR, a fire-retardant and water resistant polyethylene [69]. Although often used as an impact-resistant UAV material, few information on durability is given. However, the low price and easy of replacement of this specific part make up for any durability deficiency.

11.3 Environmental sustainability

This section contains information and elaboration on the environmental sustainability of the system. To achieve environmental sustainability, the entire life of the UAV must be analysed to identify potential polluting factors. This can be split up into production methods applied (for self-made components), shipping method used for purchased and self-made components, efficiency of power consuming components, and recyclability.

The first subject for analysis is the production methods used. Various production methods exist, each with their own benefits and drawbacks. The hull and struts, although made from different materials, will be shaped using the same method: Selective Laser Sintering. This method is very sustainable in terms of material usage, because almost all waste material is instantly recycled. It is also efficient in terms of power consumption, especially for small component batch sizes [76]. For the protective hull component, the production method to be used is thermoforming. Again, the waste material can be immediately recycled to serve as basis material for new parts. Moreover, in terms of power consumption, thermoforming offers low-power options⁴.

The second point of interest is the method of shipping. A distinction is made between four modes of freight transportation: maritime, aerial, rail and road. All of these cause environmental pollution, both by generating waste material (e.g. greenhouse gasses) and noise. Noise pollution has been a factor of influence for a long time, whereas awareness of environmental pollution has only been considered for the past few decades. Even now there is still a large group that does not believe in the predicted effects of environmental change due to pollution. To assess the impact of certain sources of pollution to determine what needs improvement, the European Environment Agency has performed widespread research. Part of this research was aimed toward determining emission of certain polluting materials (mostly gasses and some liquids) by transportation methods for both freight and person transport. Their report [77] indicates a large difference in emissions generated between the aforementioned transportation types. The conclusion is drawn that transport by rail is the least polluting means of transporting large quantities. Maritime transport takes second place in this ranking. This means that transportation should be planned so that railroads are used as primarily, with maritime transport when necessary, when no rail connection is possible. Transportation on the road should be avoided at all cost, since this has the largest pollution to cargo ratio. Of course, the individual efficiency of a vehicle depends on the level of technology used to make that specific vehicle. However, it is safe to assume that a company or country still operating old vehicles of one type also operates vehicles from the same era in the three other classes. The report also shows the change in total emission over the years per transportation type, which indicates that rapid developments are taking place. This is good to know, and re-assessment of transportation methods might be necessary in the future to accommodate the new emission figures.

A third facet is the efficiency of power-consuming components. Since the UAV is designed to have a balance between weight and flight time, energy density is an important factor for the batteries. This includes the decay of total capacity over time. The chosen batteries, when treated with care, have an average loss in capacity of 2% per year. This means storing the battery in a cold location at 40-50% charge. When considering the mission, the specific treatment necessary to attain this is not feasible, since the drone has to be ready to go as soon

⁴URL:<http://www.thermoformer.biz/know-how/newsdetail/id/196/?L=1&Hash=bf2768de9ff99257f91c95e593c53c73>

as an emergency situation occurs. Therefore, the batteries have to be kept at 100% charge at all times. Storing the batteries in a cold location is still possible, and this would lead to an average loss in capacity of 6% per year. These percentages exclude capacity loss introduced by load cycles, since this depends on the number of times the vehicle is employed per year. When comparing this battery degradation to other batteries, this turns out to be the lowest of all common battery types, making the lithium-polymer the optimal choice in terms of sustainability. As for the actual power consumption by the system, the efficiency is expressed as a Figure of Merit. This is 58.6% for the UAV, which seems very low at first glance. Considering that common helicopter attain a value around 60%, perspective is changed drastically, and the total system efficiency is actually acceptable. An improvement can be achieved by reducing the drag on the rotorblades (the main source of energy loss), but this would require a drastic change in other system properties such as total weight or thrust generated. Doing so would most likely break primary requirements on the UAV design, and is therefore not an option.

Lastly, recyclability is an important indicator of environmental sustainability. Since recycling of materials during production is already discussed in the paragraph on production methods, this paragraph focuses on recycling of components at end-of-life. The design features different components made from many different materials, which therefore have to be assessed individually. First of all, the circuitry of the UAV is assessed. Since circuit boards and components contain precious metals such as gold, silver and platinum, the circuits and computer parts are considered very lucrative for recycling [78]. Therefore, these boards are highly recyclable, and the same applies to wiring. Secondly, the body frame of the drone is assessed. This consists of three materials, the first of which to be analyzed is the protective foam. The datasheet, being outdated, states methods of recycling this type of foam are under development. Nowadays, this type of foam is 100% recyclable.⁵ The second material is a nylon laser sintering material. This falls under the thermoplastic material family, and thermoplastics are easily recycled by simple reshaping the structure at high temperatures. The last material used in the body is High-Density Polyethylene, the same material used in plastic drinking bottles. This material is also very recyclable, either in the current shape or as shards for 3D printing purposes [79].

Thirdly, the engines of the UAV are assessed. These mainly consist of different metals, and are therefore highly recyclable. Lastly, the batteries have to be assessed. Batteries are notorious for containing hazardous materials and acids, and disposal and recycling of these materials has been a challenge for a long time. As far as the components are concerned, lithium polymer batteries are a lot like lithium ion batteries. The main difference lies in the electrolyte being a polymer instead of a lithium-salt solution. Recycling of lithium-ion batteries is a well-practiced operation nowadays, and uses most parts of a battery for re-purposing⁶. The polymer electrolyte is also largely recyclable. In total, about 25% of the battery system will have to be land-filled, but this number can reduce in the future as the lithium battery technology develops further.

⁵URL:<http://www.dow.com/en-us/markets-and-solutions/products/impaxx/impaxxenergyabsorbingfoams/>

⁶URL:<http://www.teslamotors.com/blog/mythbusters-part-3-recycling-our-non-toxic-battery-packs>

12 | Systems Engineering

In this chapter, the systems engineering approach utilized to achieve a feasible product is described. Firstly, the resource allocation and budgeting is described in Section 12.1. A risk assessment is performed in Section 12.2, and after that the payload placement is explained in Section 12.3. Section 12.4, gives a summary of all the iterations of the design, and the chapter is ended with the final design in Section 12.6.

12.1 Resource Allocation and Budget Balance

This section describes how the technical budgets have been set up and managed over the course of the design process. Contingencies were reduced over time and budgets finalised. For each budget a short summary is given here.

12.1.1 Mass Budget

In the design process of the vehicle at hand, it is important to develop a contingency plan and see how the system evolves over time. Unfortunately, as a natural tendency, the mass of a system always increases over the development time. [80] It is also important to realise that as the design is maturing, its subsystem and total mass should stay within the pre-defined limitations to avoid a so-called snowball effect. It is set by a customer requirement, that the mass of the vehicle shall not exceed 500 g as mentioned in Section 2.3. This value can be considered as the baseline of the mass budget analysis. However, it has to be mentioned that it is a secondary requirement, since the customer's reasoning behind the 500 g mass was to create a system that is easily transportable. The next step is to set a mass budget and a corresponding redundancy to keep the design process within acceptable bounds. The contingency for the total mass is defined based on currently existing similar design masses and the 500 g criterion. The summary of the structural masses of similar designs can be found in Table 12.1.

Table 12.1: *Mass of similar designs*

Name of design	Total mass [g]
Gimball project ¹	500
Phantom 1 ²	1280
Phantom 3 ³	1200
Average mass	745

Additionally, the concurrent design process that will be mentioned in Subsection 12.4 has to be divided into 3 segments. Namely, design iteration step 1 is called Design for Flight (Phase 1), design iteration step 2 is called Design for Robustness (Phase 2) and design iteration step 3 is called Optimisation (Phase 3). In order to set a starting point to the design process, the average of the weights of these designs was taken as a starting point. It means that the average is approximately 50 % heavier than the mass of 500 grams set in the requirements. Therefore, this 50 % will be taken as the contingency for the "Design for Flight" phase. It is also vital to set the contingency for phase 2 and 3 accordingly. A contingency of 35 % for phase 2 is set and a contingency of 20 % for phase 3 was appointed. The reason for determining such high contingencies is the fact that the presented designs (Table 12.1) that are able to cope with high impact loads is limited. Also, the currently designed system has to deal with high impact loads, therefore there is an expected increase in structural mass due to the feature of impact resistance. In Section 12.4, the change in the mass of the system is clearly shown per iteration. This figure can again be seen in Figure 12.1 along with the applied contingency plan.

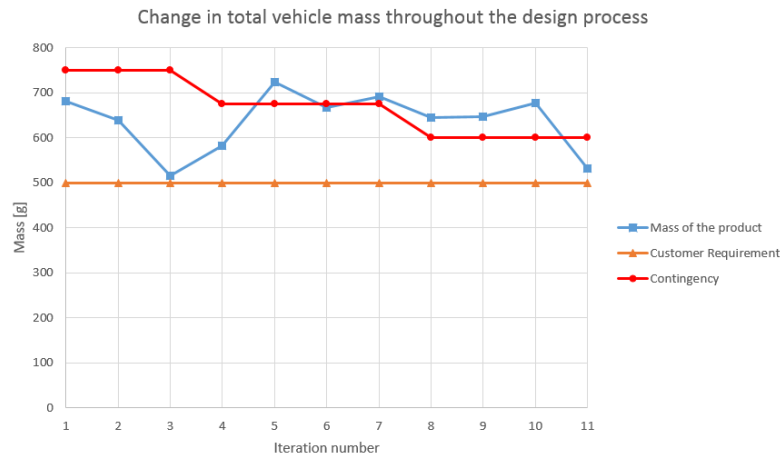


Figure 12.1: Variation in total mass as a function of the design iteration steps

As one can clearly see, the customer requirement of 500 grams was not met in any of the cases. The final mass of the vehicle is 533 grams, which is 6.6 % more than anticipated by the customer. The reasoning for that can be the fact that no other similar system was design to the writing of this report. Moreover, the customer requirement might not be precise, it can be considered as an indication of the desired range of mass that has to be achieved. However, one has to make sure that the design does not diverge significantly away from the goal at hand. As it can be seen in Figure 12.1 and in Section 12.4, the mass of the vehicle changes abruptly several times in the process. It is a consequence of the fact that the design was built in phases and during each phase a new function or feature of the system was presented. It has to be mentioned that this design strategy is not favourable, was harmful in the design process and lead to unpredictability. The predictability of the design growth is unclear, and it is impossible to draw conclusions based on the mass pattern after each iteration. Additionally, as it was mentioned earlier, it is a natural tendency that the design increases in weight as the delivery deadline is approached, but due to the lack of proper information the behaviour shown in Figure 12.1 follows a pattern opposite to the natural tendency. All in all, a rather pessimistic concurrent design approach was chosen where firstly the essential requirements were met and then additional features such as impact resistance were included. It is recommended that more research is to be carried out about the currently existing designs. Likewise, it is important to consider all the essential features of the system at the beginning of the design and to add extra characteristics only in case they have a minor influence or if there is enough room to accommodate that component.

12.1.2 Power Budget

To check if the power budget is on track a contingency strategy has to be made. From previous designs the mass of a small UAV can be linked to the required power. By using the values for the contingency for mass the contingency for power can be set up. This can be seen in Figure 12.2. This contingency was based on data that comes from open rotor UAVs, therefore it was multiplied by a factor one and a half, to account for the duct (for more details on the duct effect see Chapter 5 about Propulsion).

The power budget is mostly dictated by the propulsion subsystem. To fly the motors need a certain amount of energy that must be supplied by the battery. The payload only needs a little additional power with respect to the propulsion. With each iteration the required lift and thrust changes, and thus the power required from the batteries. The payload power requirement is taken into account and fixed at a value of seven watt. This also includes a safety factor for if some additional payload is implemented in the drone. Even if this excess power is not needed it provides some contingency on mission duration. The total power budget required is than the power required by the propulsion group and the payload group together. The development of the power budget over time can be seen in Figure 12.2. The significant drop in power from iteration two to three comes from the fact that for the first two iterations it was assumed that the entire mission is flown with full power. This leads to a lot of contingency for the available energy, which increases the endurance. This led to heavy batteries, so a better estimate of the flight profile was made. The steep increase for iteration four and five follows from the development of the structure for collision resistance, which increased the weight. More weight means more lift required which means more battery power required. Further finalising the design yielded the general decrease towards the final iteration. After this was done a bug was found in on of the codes that resulted in a massive weight reduction, and as a consequence

a significant power drop. This power drop caused the required power to almost match the budget power. As said before, of these numbers only seven watt is required for the payload, the rest is required for the propulsion.

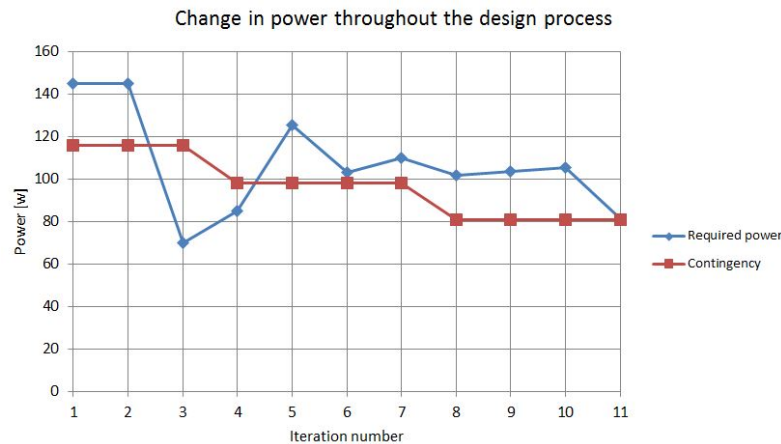


Figure 12.2: The power budget during the several iterations

12.1.3 Data Budget

The data link budget is treated in detail in Section 6.4.2 when designing the Communication subsystem with the budget breakdown given in Table 6.10. The initial calculations for the communication module were based on a maximum 850kbps directional data rate budget. However, further analysis of the data flows as described in Section 8.1 showed that the budget would have to be increased to allow a 910kbps maximum directional data rate (downlink from UAV) to accommodate for additional sensors. The budget was mainly driven by the downlink from the UAV to the GCS as a result of the live video feed requirement. The chosen module had a maximum 1Mbps directional data rate which meant the data flows to and from the UAV were within the maximum limit.

12.2 Risk Assessment

As the design is in the detailed phase where all individual components and subsystems are defined and their relations are properly determined, the risk of the entire system is assessed as documented in this chapter. When an overview of the most risky elements of the system and its behaviour is created, eventual risk mitigation and management can be initialized.

12.2.1 Risk identification

Technical and non-technical risk is assessed using an identical method. The risk assessment is performed by starting at the top-level of the FFD and working towards the lower, more detailed levels of functionality. The procedure for technical risk assessment follows the failure mode and effects analysis (FMEA) method ⁴. The list below defines the necessary steps towards assessing the functional and technical risk of the UAV system.

1. Identification of the top-level system functions by defining the system, system functions and flow of functions (using the FFD)
2. Identification of the different failure modes at a detailed level of functionality.
3. Analysis of the risk by qualitatively (quantitatively if possible) assessing the likelihood and consequence of the failure.
4. Organisation of failure modes by risk level (high, medium and low risk items) by means of a risk map.
5. Identification of high risk items, the type of risk and possible risk mitigation strategies.

⁴URL:<http://asq.org/learn-about-quality/process-analysis-tools/overview/fmea.html>

12.2.2 Types of risk

For use in the risk assessment of the final product, three risk categories are identified:

1.) Environmental risk

This category contains risk elements caused by environmental circumstances and their impact on the behaviour and performance of the system. This can include weather, bystanders, traffic and other uncertainties the surroundings might pose while the system is operated.

2.) Operational risk

Operational risk elements directly relate to the risk posed by the way the system is operated and reacts to its surroundings. Risks related to handling and logistics of the system are taken into account as well.

3.) Technical risk

The technical risk items relate to the reliability of all components and internal functionality. The technical risk items are categorized for each subsystem for easy identification.

12.2.3 Risk quantification and mapping

The risk of a specific failure mode is determined by assigning each risk item with a probability of occurrence of the respective failure and its impact on the mission or the environment. The probability of occurrence is given by an estimation of number of occurrences per number of mission cycles, ranging from (1:1), almost certainly occurring every mission up to (<1:1000), meaning that the failure occurs in less than one in a thousand mission cycles. An overview is provided in Table 12.2.

Table 12.2: *Probability levels of failure occurrence*

Level	Likelihood of occurrence	Description
1. Rare	<1:1000	The probability of failure occurrence during the mission is very low.
2. Unlikely	1:100 - 1:1000	There is a remote probability of failure occurring in lifetime of system.
3. Likely	1:10 - 1:100	There is a significant probability of failure occurring in lifetime of system.
4. Very Likely	1:1 - 1:10	There is a high probability of failure occurring in lifetime of system.
5. Almost certain	1:1	The probability of failure occurring in lifetime of system is almost certain.

Considering the impact of failure modes on the mission and the environment, the categories are as defined in Tables 12.3 and 12.4 for the environmental and operational risks and technical risks respectively

Table 12.3: *Impact levels of failure on mission performance and environment for environmental and operational risk items*

Consequence of failure	Description
1. Negligible	The mission success is not affected. Failure has a negligible or non-operational impact and/or no compromised safety for the mission environment.
2. Marginal	Degradation of success of secondary mission goals or small reduction in technical performance and/or minor safety consequences for the mission environment.
3. Moderate	Failure of secondary mission goals and degradation of success of primary mission goals. Significant reduction in technical performance. Significant induced safety consequences for the mission environment.
4. Major	The overall mission success is questionable or leads to imminently high decrease in technical performance and/or severe safety consequences for the mission environment.
5. Extensive	Catastrophic for mission or inducing severe and unacceptable safety consequences for the mission environment.

Table 12.4: Impact levels of failure on mission performance for technical risk items

Consequence of failure	Description
1. Negligible	The mission success is not affected. Failure has a negligible or non-operational impact.
2. Marginal	Degradation of success of secondary mission goals or small reduction in technical performance.
3. Moderate	Failure of secondary mission goals and degradation of success of primary mission goals. Significant reduction in technical performance.
4. Major	The overall mission success is questionable or leads to imminently high decrease in technical performance
5. Extensive	Results in overall mission failure or very high decrease in technical performance.

The considered risk items and their failure probability and impact, as based on the earlier tables, are listed in Figures 12.3, 12.4 and 12.5 for respectively the environmental risk, operational risk and technical risk.

Environmental risks	Risk ID	Total Failure P (1-5)	Impact (1-5)	Total Risk
Unforeseen environmental disturbances: aligned with flight di	EV-1	4	1	4
Unforeseen environmental disturbances: not aligned with flight	EV-2	4	1	4
Collision with person	EV-3	2	2	4
High environment temperature > 80 C	EV-4	3	3	9
Heavy rain conditions	EV-5	2	2	4
High wind conditions	EV-6	3	2	6
Operation in densely populated area / high bystander density	EV-7	3	2	6

Figure 12.3: Environmental risk items, failure probability, impact and resulting risk

Operational Risks	Risk ID	Total Failure P (1-5)	Impact (1-5)	Total Risk
Attitude disturbance due to collision by UAV body	OP-1	5	1	5
Rotor blade obstruction / impact	OP-2	2	4	8
Collision with object to side of UAV	OP-3	5	2	10
Collision with object to top/bottom of UAV	OP-4	4	2	8
Crash landing	OP-5	1	5	5
Opening smaller than 50 x 50 cm	OP-6	2	4	8
Communication signal interference / jamming	OP-7	4	3	12
Overdraining of battery	OP-8	2	3	6
Disassembly obstructed	OP-9	1	3	3
Unachievable regulatory requirements	OP-10	2	5	10
No available opening for UAV entry	OP-11	3	4	12
Pilot error resulting in crash	OP-12	2	5	10
Conflict with other traffic	OP-13	1	5	5

Figure 12.4: Operational risk items, failure probability, impact and resulting risk

	Technical risks	Risk ID	Component depende	Total Failure P (1-5)	Impact (1-5)	Total Risk
<i>Deployment</i>	Battery mount failure	TE-D-1	ST-1, PW-1	1	5	5
<i>Propulsion / flight control</i>	Motor failure during flight	TE-P-1	PR-1	1	5	5
	Servo failure during flight	TE-P-2	PR-4	1	4	4
	ESC Failure	TE-P-3	PW-1	1	5	5
	Swashplate failure	TE-P-4	PR-3	2	4	8
	Rotor failure	TE-P-5	PR-2	1	5	5
	Rotor mount failure	TE-P-6	PR-2	1	5	5
<i>Electronics / SW</i>	Main on board computer failure	TE-E-1	OBC-1	1	5	5
	Breakout board failure	TE-E-2	OBC-2	1	5	5
	Failure in image processing COM	TE-E-3	OBC-3	1	4	4
	Signal loss between UAV and GCS	TE-E-4	C-1	3	4	12
	Communication flow interruption / noise	TE-E-5	C-2, C-1	4	2	8
	Short circuit in UAV	TE-E-6	OBC-2, OT-1	1	5	5
	Battery connection failure	TE-E-7	PW-2, OT-1	1	4	4
	Sonar sensor failure	TE-E-8	PL-2	2	2	4
	Camera failure	TE-E-9	PL-1	2	5	10
	Video data transmission failure	TE-E-10	OBC-3 -> C-1 -> C-2	3	4	12
	IR Camera failure	TE-E-11	PL-3	2	3	6
	Transceiver failure	TE-E-12	C-1	1	5	5
	IMU failure	TE-E-13	OBC-1	1	5	5
	Erroneous attitude determination	TE-E-14	OBC-1	2	4	8
	GPS positioning failure	TE-E-15	PL-4	3	2	6
	Electrical connector / wiring failure	TE-E-16	OT-1	1	4	4
	OBC boot/initialization failure	TE-E-17	OBC-1 -> OBC-3	2	5	10
	Short circuit in UAV	TE-E-18	OT-1 -> OBC-2	1	5	5
	Corrupted on-board stored data	TE-E-19	OBC-3, OBC-2	1	2	2
	Software error	TE-E-20		1	4	4
<i>Structures&Materials</i>	Structural failure of propulsion system strut	TE-S-1	ST-1	1	4	4
	Structural failure of hull due to impact	TE-S-2	ST-2	1	3	3
	Fuselage parts connection failure	TE-S-3	ST-1, ST-2	2	4	8
	Structural failure of foam padding due to impact	TE-S-4	ST-2	3	1	3
	Payload mount failure	TE-S-5	ST-1, ST-2	1	5	5
<i>Ground Station</i>	GCS computer failure	TE-G-1		1	5	5
	GCS screen failure	TE-G-2		1	5	5
	GCS interface hardware failure	TE-G-3		1	5	5
	GCS software failure	TE-G-4		1	5	5
	GCS deployment obstructed or defunctional	TE-G-5		2	4	8
	GCS communication system failure	TE-G-6		1	5	5
	Head motion tracker failure	TE-G-7		1	4	4
	Video glasses failure	TE-G-8		1	4	4

Figure 12.5: Technical risk items, dependent components, failure probability, impact and resulting risk

Resulting from this risk assessment, the risk items can be mapped in the risk maps as shown in Figures 12.6, 12.7 and 12.8.

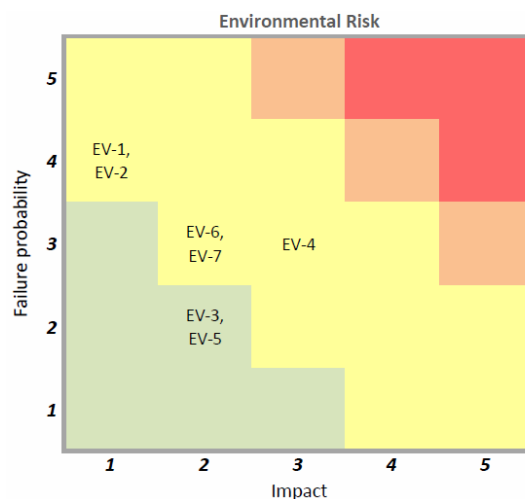


Figure 12.6: Risk map containing the environmental risk items

Considering environmental risks, the most riskful items include encountering high environment temperatures during the mission, based on the initial mission scope of providing aid in firefighting missions. Substantial exposure to temperatures higher than 80 degrees can damage the on-board electronics and structural elements. Furthermore, very strong wind conditions, for instance in case of extreme weather, might cause the drone to not

be able to cope with the disturbances or collide with its surroundings. In case the operation takes place in densely populated areas or places with many bystanders, operating the drone carries higher risk on colliding with a person.

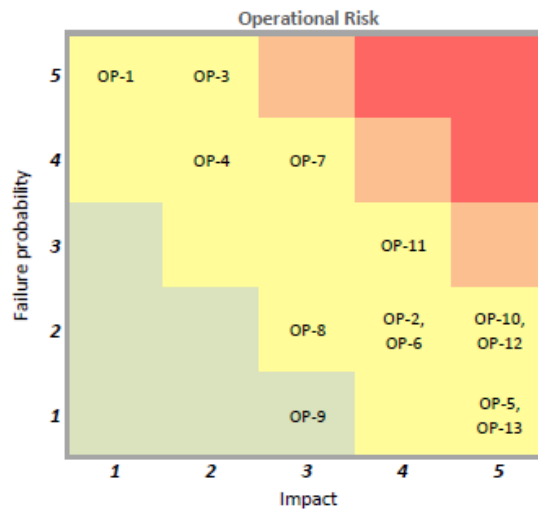


Figure 12.7: Risk map containing the operational risk items

With respect to operational risk, the most risk carrying items include that there is no available opening for the drone to make the transition from outdoors to indoors. Collisions with objects to both the side and top or bottom of the UAV pose a risk. However the design is built for withstanding impacts, their almost certain probability of occurrence during a mission induces frequent checking for possible damage. Furthermore, pilot errors might result in unexpected and unwanted damage resulting in the system being unable to further complete the mission. Besides in-operation risks, regulatory requirements pose a risk as well, related to when and where the system can be deployed.

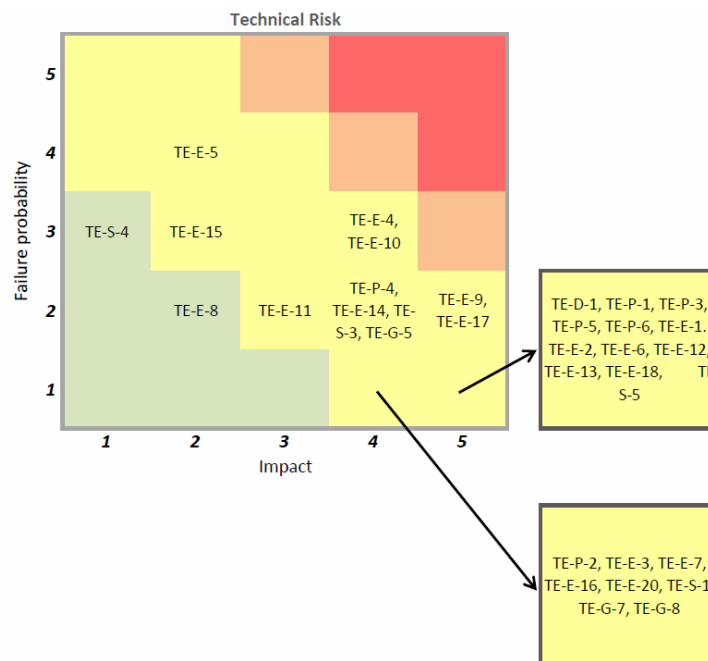


Figure 12.8: Risk map containing the technical risk items

Most risk items in the Technical Risk category belong to the high-impact, low-probability area of the risk map, as they are related to the failure of certain components. The most riskful items in the technical risk category relate to signal obstruction or loss of communication link between the UAV and the ground station. Besides the fact that the UAV is designed to, in case of a signal loss, hold its position, it does affect the further

mission completion until the connection is re-established. Furthermore, both the normal and thermal camera are sensitive components which in case of failure have a large impact on mission success.

12.2.4 Risk Mitigation

As can be seen in the risk maps, no risk items fall within the areas of very high and unacceptable risks. Therefore, there is no urgent need to introduce risk mitigation measures. However, in future development phases special care and resources should be assigned to ensuring the reliability and functionality of the communication link between the UAV and the ground station by means of extensive testing and introducing measures for redundancy. This currently poses the highest technical risk related to the system. For further development, regulatory challenges affect the success and applicability of the UAV system as well. Careful notion should be taken in changes in these regulations related to the flight and certification of unmanned aerial systems. This is also addressed in Section 3.5.

12.3 Subsystem Allocation

This section presents the choices made on the absolute positioning of each subsystem on the UAV airframe. Firstly, the general overview of the subsystem locations will be presented which will be followed by a center of gravity location analysis. Also, the reasoning behind the payload placement will be presented. It is important to collect all the subsystems that are present in the vehicle to a complete list. This can be seen below with an additional identifier for each subsystem.

- 1, eCam56 Camera
- 2, Navstik Main board
- 3, IvyPro interface board
- 4, Gumstix Overo Earthstorm
- 5a-b, System batteries
- 6, Vehicle on-off switch
- 7, Gumstix Summit expansion board
- 8a-b, ECSs
- 9, Wires
- 10, Propulsion subsystem
- 11a, SiFlex Transceiver
- 11b-c, Antennas
- 12a-f, Sonar sensors
- 13, FLIR Lepton Thermal camera
- 14a-f, LED lights
- 15 GPS antenna

The subsystem allocation procedure is based on several influencing factors. The most important one is to allocate the payload in such a way that the mission objective is accomplished to the fullest. Secondly, systems that are in a close interaction shall be placed close together to decrease the length of cabling. Also, subsystems that are directly connected to the motors and servos shall be placed close to the load carrying struts, since these stiffeners provide room for cable lead. Determination of the position of the subsystems was based on the co-operation of several divisions, namely the payload division, the power division, the communications division and the structural solutions division. The resulting subsystem allotment can be seen in Figure 12.9. The arrow represents the inspecting and forward translating direction of the vehicle. The angle β presents the clockwise rotation around the centroid of the vehicle to help determine the position of each subsystem.

The subsystems are attached to the structure using rubber clamps. These clamps are glued to the structure and use friction to hold the subsystems in place. The clamps reduce vibrations for the subsystems as well. Important to note is that the IvyPro interface board is instead fastened using screws on top of rubber padding as this board does not have the space for rubber clamps. Next to that the struts of the propulsion subsystem are attached to the hull by sliding these into custom sockets and then using screws to fasten the struts to the sockets.

As it can be seen, the inspection camera is placed in the front of the vehicle along with the thermal camera plus a green and a red LED light to allow for inspection in smoky or dimmed lighting conditions. One can also find sonar sensors on both the left and the right side of these subsystems. Sonar sensor 12a and 12c are pointing to the front under a 45 degree angle from the flight direction (in the horizontal direction) and trace the path of and distance of the drone from its surrounding. Additionally, sonar sensor 12b points downwards to assess distance between the drone and the object below it. Sonar sensor 12d does the same job accordingly, but in the upwards direction. The remainder of the sonar sensors (12e and 12f) are placed on the left and right-hand side (90 and

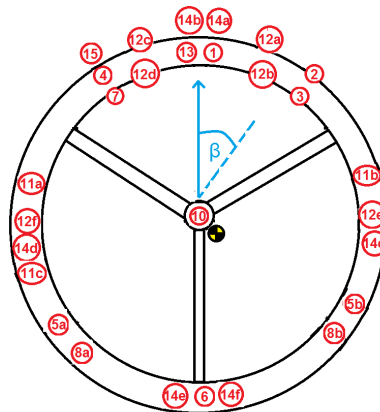


Figure 12.9: Top view of the Inspection Pocket Drone with subsystem allocation

270°) of the vehicle to sense sideways distances. Indicator LEDs 14c and 14d are also placed on the sides to provide full visibility by people of the vehicle in all rotational conditions. One can also notice that the Navstik Mainboard (2) and the IvyPro breakout board are attached together as it was requested by the payload division. Furthermore, the Gumstix Overo Earthstorm COM, the Gumstix Summit board and the GPS antenna are also attached and placed symmetrically on the other side of the vehicle. It is also visible that the Siflex transmitter (11a) is placed at approximately 280 degrees. The two antennas (11b and 11c) are placed as far as possible from each other to provide all-time communication coverage and to avoid interference. Their respective positions are at 90° and 270°. The batteries and the electronic speed controllers (ESC) are placed closely together as requested by the power division. These are also located close to the strut at 180° in order to reduce the cable length. Finally, 2 LEDs for system initialisation are placed also at the 180° position along with the on-off switch of the vehicle (6). Figure 12.9 does not show element 9, namely the cables due to the fact that it was assumed that the cables are equally distributed and their center of gravity lies in the centroid of the system. It is also essential to mention that the placement of the subsystems was also driven by the fact that there is a significant amount of vibrations originating from the engines as it was mentioned in Section 7.4. Therefore, one has to make sure that no subsystems are placed directly at or at the close proximity of the struts. It is clearly visible that near the struts, subsystem placement is avoided. Only the on-off switch with 2 LED lights are placed at the 180° strut, however, these subsystems are not affected by the above mentioned vibrational loads.

The subsystems are already allocated according to the requests of the involved divisions, but it is also vital to take stability considerations into account. The system achieves maximum stability when the center of gravity lies as close as possible to the geometrical center of the vehicle. The center of gravity of the vehicle is calculated using Equation 12.1 and Equation 12.2 The x and y locations of the center of gravity are mainly determined by the subsystem positions since the structure around them is highly symmetric.

$$x_{cg} = \frac{\sum x_i m_i}{\sum m_i} = 1.8 \text{ mm} \quad (12.1)$$

$$y_{cg} = \frac{\sum y_i m_i}{\sum m_i} = -3.5 \text{ mm} \quad (12.2)$$

It is visible that the center of gravity location is 1.8 mm right of and 3.5 mm below the centroid of the vehicle as shown in Figure 12.9. These distances can be considered negligible since their effect on the stability of the vehicle are not influencing. Allocation of subsystem positions is a critical step in the design process. Once all the positions are settled, it is time to build the vehicle around the subsystems. This procedure is presented in the section below.

12.4 Design Iteration Summary

This section primarily deals with the development history of the design. In total, 11 iterations were carried out as presented below. As a usual behaviour of the design process, one would expect that the mass of the design increases over time, however as it will be seen, it was not achieved during this design process. [80] It has to be mentioned that the mass of the payload, OBC and communications subsections was set in the first

iteration to be 100 grams and did not change in the design process up until iteration 10 where it increased to 118. The rest of the parameters were constantly changing and finally a feasible design is achieved.

The design process was divided up into 3 phases, namely phase 1 dealt with "Design for Flight", phase 2 considers "Design for Robustness" and phase 3 addresses "Optimisation". As it will be seen later on, the first phase comprised of 3 iterations, phase 2 contained 4 iterations and phase 3 consists of 4 optimisation iterations. A simple schematic of the iteration process can be seen in Figure 12.10.



Figure 12.10: The division and the order of the utilised design phases for the IPD project

In order to give the reader a proper overview of the iteration steps that were taken, Figure 12.11 shows all the 11 steps along with the mass and additional features of each design. The colouring of the figure was based on the previously mentioned 3 phase system. In this way, one can again clearly see that phase 1 consists of 3 iterations, phase 2 consists of 4, while phase 3 contains 4 optimisation iterations.

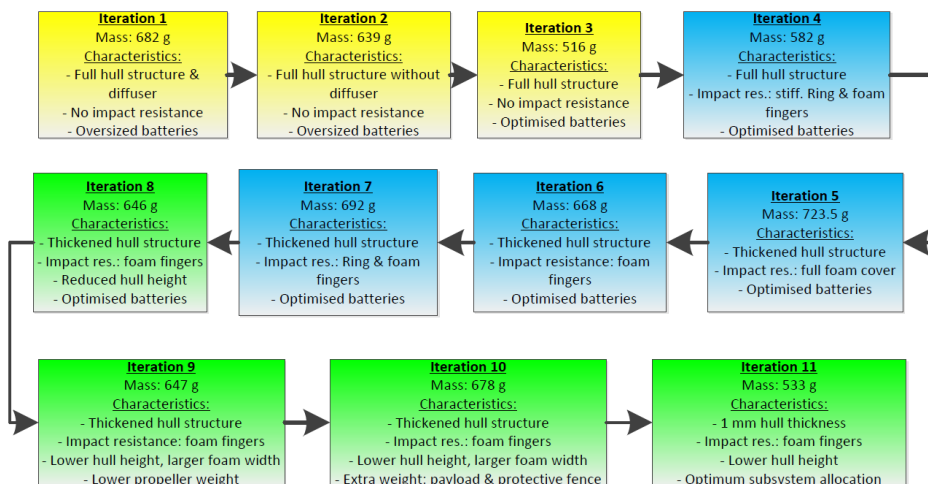


Figure 12.11: Flow diagram with detailed description of the iteration steps with the 3 distinctive iteration phases

12.4.1 Phase 1: Design for Flight

In this first part of the design process the basic features of the UAV were designed for. Namely, the vehicle shall be able to fly, cope with the -dynamic and static- internal and external loads and to house the payload. In this design process, the results and solutions could be considered sufficient in case an outdoor drone were to be built. The electronics mass of the system was already fixed to be 100 grams, therefore the power and propulsion subsystem along with the load carrying structure still had to be decided on. These 3 divisions had to work in close co-operation during the design process, since a change in mass in one of them leads to a completely different result than the previous one. An additional general remark is that the iteration loops had a converging behaviour, therefore with the enough amount of tries, a feasible design was produced. Figure 12.12 shows the iteration procedure and the interaction between the 3 divisions (design teams). At the end of this section, a summary of all the important general parameters of the vehicle for all iterations are listed in Table 12.5.

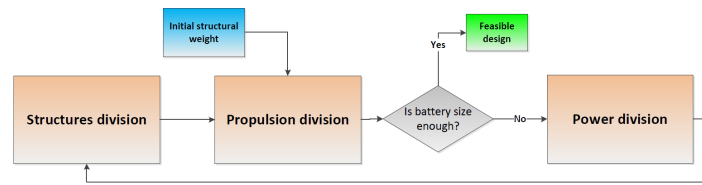


Figure 12.12: General outlook of the iteration loop used for the IPD project

Iteration 1

The main purpose of iteration 1 was to come up with a design that is able to fly and that can house all the payloads and protect them from the environment. The theories used to design the concepts presented below were all presented in Chapter 7. The cross-sectional area of the hull structure can be seen in Figure 12.13a, where the payload is mounted in the hull structure. Unfortunately, additional material has to be placed below the payload, because this design makes use of a diffuser mentioned in Section 5.1.1. As it can also be seen, the payload is covered with a protective cover against environmental effects such as wind, dust and water. An additional feature of this hull shape is that it is able to cope with the experienced manoeuvring acceleration loads. The thickness of all the walls is 1 mm and will not be changed in the iteration process unless stated otherwise. Additionally, the diameter of the rotor housing duct is set to be 204 mm and will not be changed in the iteration process unless mentioned. Furthermore, a huge amount of contingency was put on the design when it comes to power management. It was assumed that the vehicle has to be able to cope with maximum wind speeds of 21 m/s as it was stated in requirement IPD-AAoI-Reach-A-8-A in Section 2.3. This means that the vehicle is over sized. Unfortunately, this decision resulted in heavier batteries, which greatly contributed to a weight increase. The mass of the vehicle is 682 grams, which is 36 % above the one requested by the customer.

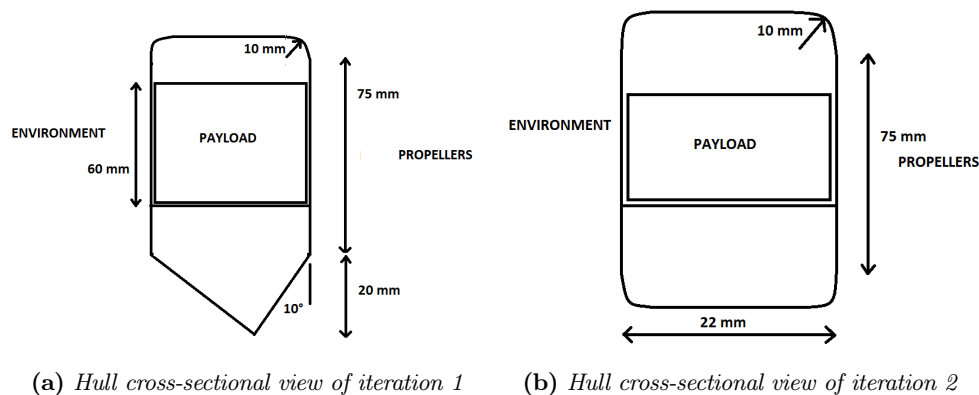


Figure 12.13: Hull cross-sectional views of iterations 1 & 2

Iteration 2

Iteration 2 still makes use of the 100% maximum thrust for the full mission profile just as iteration 1, however, due to a more detailed research, it was found that the diffuser can be discarded from the design, since its added aerodynamic benefit results in significant weight increase. The only difference between iteration 1 and the current model is that the diffuser is discarded (Subsection 5.1.1) which allows for a symmetric hull cross-section as it can be seen in Figure 12.13b. This update to the design resulted in a total mass of 639 grams which means that 43 grams of weight was removed.

Iteration 3

In order to decrease the weight of the vehicle, the attributes of the propulsion subsystem had to be reconsidered. It was determined that 4 minutes of full throttle in $11 \frac{m}{s}$ of wind (outdoors) with $3 \frac{m}{s}$ will be used along with 6 minutes of translation with $3 \frac{m}{s}$ in zero wind conditions (indoors). This assumption represents the mission profile in a more accurate way and also mainly concerns the primary requirement IPD-AAoI-Reach-A-3-A which is mentioned

in Section 2.3. As it was expected, the weight of the vehicle decreased drastically, since the total required power is halved (see Table 12.5). The cross-section of the hull is left unchanged and is identical to the one shown in Figure 12.13b. However, the diameter of the duct could be decreased to 179 mm since the vehicle weighs less, therefore smaller propellers suffice. This design solution closes down the first phase of the design procedure, namely the "Design for Flight" phase. The next iteration, iteration 4 will directly begin with the "Design for Robustness" phase.

12.4.2 Phase 2: Design for Robustness

Iteration 3 concluded the "Design for Flight" phase, which means that the vehicle is able to take-off, traverse and manoeuvre in- and outdoors. These abilities result in the fulfillment of most of the primary requirements set in Section 2.3. Unfortunately, the ability that makes this vehicle so unique, namely to fly indoors safely without structural failure upon impact is still lacking. Hence, phase 2 aims at developing an impact resistance system to ensure a robust design. This phase consists of 4 iterations where several ideas will be developed and presented. At the end of the iteration process, a final concept is chosen and will be sent to phase 3 for optimisation.

Iteration 4

Iteration 4 is included in phase 2, namely "Design for Robustness". The 516 grams obtained in the previous iteration look very attractive, however, it has to be noted that impact resistance is still not accounted for in the design. In its current state, the vehicle would fail in case an impact would occur at its maximum translational speed of $3 \frac{m}{s}$. This design makes use of the stiffening ring concept introduced in Subsection 7.2.4 with stiffening struts. Both of these stiffeners are made out of Carbon Fibre reinforced Polymer (CFRP). This results in 25 grams of additional weight due to the impact resistance. Besides, the vertical distance between the propellers had to be increased due to the accommodation of the detailed swashplate design as shown in Section 5.3, therefore the height of the hull had to increase to 115 mm. Furthermore, the diameter of the duct is increased again to 188 mm, but will remain unchanged for the remaining iterations. It is also important to mention that the width of the hull increased by a total of 5.5 mm since the stiffening ring had to be housed. This also leads to an increase in structural mass. All of these resulted in a total of 66 gram increase in the total vehicle mass which lead to a total mass of 582 grams. The cross-sectional area of this design can be seen in Figure 12.14.

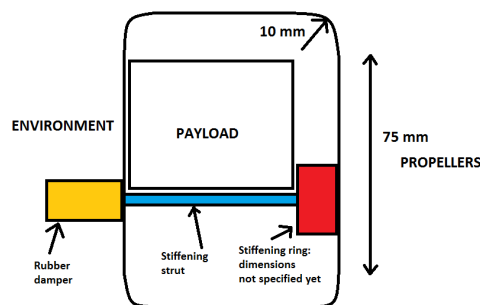
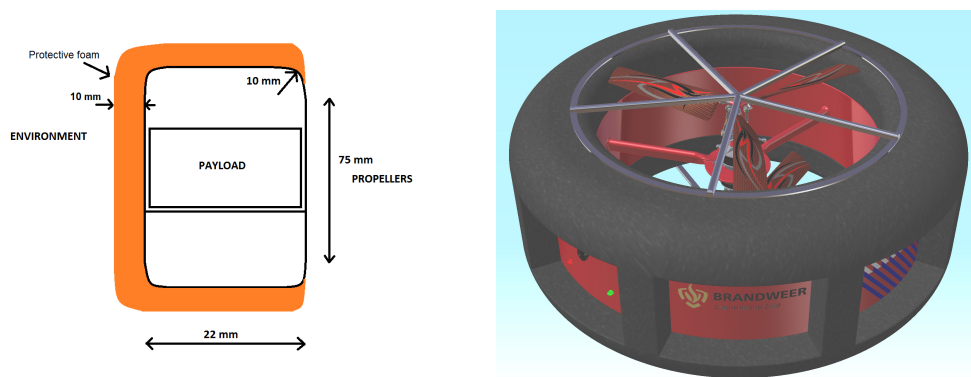


Figure 12.14: Cross-sectional view of the payload carrying hull (symmetric) of the vehicle for design iteration 4

Iteration 5

Iteration 5 introduces a new solution for impact resistance. The vehicle is fully covered with a protective foam cover as mentioned in Subsection 7.2.2. The stiffening ring concept in this case is excluded, so the hull structure has to take up the load dampened by the foam. The thickness of the top wall of the hull has to be increased from 1 mm to 1.5 mm, on top of the increase in mass due to the addition of the foam cover of 40 grams using the theory of Section 7.1 and Subsection 7.2.2. As it was expected, due to all these weight increases, the propulsion subsystem could not produce enough thrust, therefore the rpm of the propulsion subsystem had to be increased. Interestingly, the absolute height of the vehicle remains unchanged (115 mm), so the addition of 10 mm foam to the top and bottom reduces the hull height leading to some degree of weight reduction. Unfortunately, that is still not enough to prevent the vehicle mass from exceeding 700 grams to end up on 724 grams. The cross-section of this concept can be seen in Figure 12.15a.



(a) Cross-sectional view of the hull of design iteration 5 (b) Cross-sectional view of the hull of design iteration 6

Figure 12.15: Main geometric considerations of iterations 5 & 6

Iteration 6

Iteration 6 makes use of a similar concept to the one mentioned in iteration 5, however, the side of the vehicle will not be fully covered with foam. Eight so-called foam fingers will be utilised on the outside of the vehicle. This results in a small amount of weight decrease. This weight decrease resulted in a lower rpm for the motors which is interestingly just enough to opt for a smaller, hence lighter battery. The vehicle mass is decreased by 19 grams (due to partial foam removal) and by an additional 36 grams (decreased battery weight) and stopped at 668 grams. The general outlook of this concept can be found in Figure 12.15b.

Iteration 7

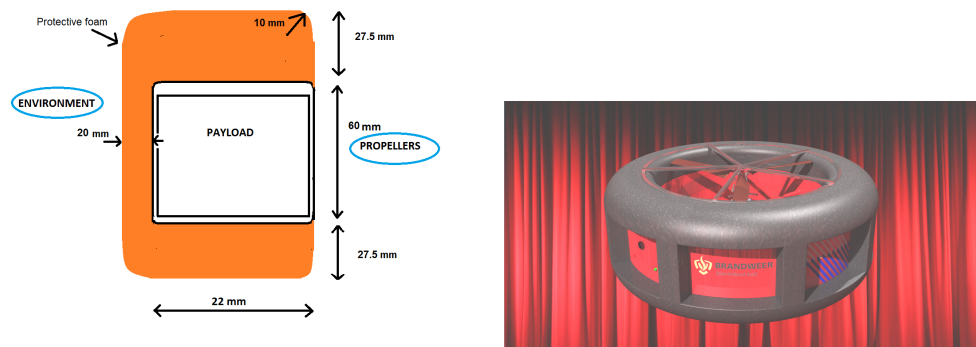
Iteration 7 makes use of the same concept that was considered for iteration 4, however applied for a higher absolute mass (Figure 12.14). The reason behind this choice is the differences between a fully impact resistant system compared to a system that is only impact resistant on the sides (Iteration 7). As it can be seen, there is an additional weight due to the stiffening ring with struts component of 24 grams. This means that the vehicle mass would increase for no reason. Design iteration 7 concludes the "Design for Robustness" phase which means that the "Optimisation" phase can commence. Before that could happen, it is essential to choose a final concept that will further be optimised. The chosen concept (based on impact resistances) is iteration 6.

12.4.3 Phase 3: Optimisation

Design iteration 6 was favoured in the conclusion of phase 2, which means that this concept is the one to be further developed and optimised. Phase 3 consists of 4 major optimisation steps, which are presented as iterations 8-11. Iteration 10 is somewhat of an outlier since a late update from the payload design team altered the design. It means that iteration 10 is not a classical optimisation step, but is included here as part of the iteration process.

Iteration 8

Iteration 8 entertains the idea of thickening the top of the hull structure again to 1.5 mm and covering it with foam. The top and the hull would be fully covered while there would be 8 foam fingers of 20 mm length. The major difference between iteration 5 and the current one is that while the absolute vehicle height is still 115 mm, the hull height is decreased to 60 mm. The remaining 55 mm will be replaced with foam, which results in a weight reduction of the hull of 28 grams. As a positive side effect, the use of lighter batteries is possible which also leads to a mass reduction of 18 grams totalling a 46 gram weight reduction. In this way, the finalised mass is 646 grams. The cross-section of iteration 8 can be seen in Figure 12.16a.



(a) Cross-sectional view of the hull of design iteration 8 (b) The optimised and finalised iteration 9 concept of the IPD project

Figure 12.16: Main geometric considerations of iterations 8 & 9

Iteration 9

Iteration 9 aims at improving on iteration 8 by reducing the mass of the vehicle. The propeller mass could be decreased by 11.5 grams as the rpm of the motors was increased as much as possible without having to choose a larger battery. This increase in rpm resulted in a reduced chord length for the propeller blades. Unfortunately, a calculation mistake was made in iteration 8, since due to the decrease in hull height, the width of the foam fingers had to increase from 15 mm to 23 mm. This led to a weight increase of 12.5 grams which resulted in a total of 1 gram increase compared to iteration 8. The outlook of the cross-section can be seen in Figure 12.16a, while the general outlook of iteration 9 is seen in Figure 12.16b.

Iteration 10

A change in the design of the payload system caused the mass to increase by 18 grams. Also, the top and bottom protective fences were added to the design which resulted in 15 grams of additional structural weight. Therefore, the total added mass was 33 grams. These decisions clearly interrupt the optimisation procedure and have to be dealt with in a way that a snowball effect in the mass increase is avoided. The design team came to the decision to reduce the translational speed of $3 \frac{m}{s}$ at full wind speed conditions to $2 \frac{m}{s}$. It resulted in more redundancy and range in the usable power, thus weight increase due to the employment of heavier batteries is prevented. It also has to be indicated that the indoors (no wind conditions) translational speed of $3 \frac{m}{s}$ is left unchanged. The only weight optimisation procedure was a 2 gram weight reduction in the foam weight. The possibility of foam reduction on the outer edges of the drone on the top and bottom was probable and accounted for. The general cross-sectional look of this design is also seen in Figure 12.16b. The weight of iteration design 10 is 678 grams.

Iteration 11

The re-evaluation of the subsystem locations and dimensions revealed that a significant amount of mass can be saved by means of reduction in the height of the load carrying hull. The locations of the subsystems can be seen in Figure 12.17b. The hull height could be decreased by a significant 18 mm while the width of the hull is changed to 28 mm. However, the absolute height of the drone still had to stay 115 mm, therefore, the resulting gap also had to be filled up with the impact resistant foam. An overview of the new cross section can be seen in Figure 12.17a. It resulted in a 120 gram weight reduction in the structural mass. Additionally, the required thrust and power are significantly reduced as a result of the previous discussion. So, new battery mass of 124 was achieved resulting in a 20 gram reduction. Even though, the shape of the hull is drastically changed, the only change in absolute dimensions is the diameter of the vehicle which is 278 mm. It has to be mentioned that this configuration is chosen to be the finalized design solution and it is elaborated on in Section 12.6. The location of the centre of gravity is at $x_{cg} = 8.5 \cdot 10^{-7} m$, $y_{cg} = 3.9 \cdot 10^{-3} m$.

Table 12.5: Summary of the important design parameters per iteration

	1	2	3	4	5	6	7	8	9	10	11
Total Mass [g]	682	639	516	582	724	668	692	646	647	678	533
Hull Mass [g]	209	151	136	207	248	229	235	195	207	207	87
Propulsion Mass [g]	150	150	147	133	133	133	133	133	122	122	122
Payload Mass [g]	100	100	100	100	100	100	100	100	100	118	118
Battery Mass [g]	210	210	108	124	180	144	162	144	144	144	124
Height [mm]	105	95	95	115	115	115	115	115	115	115	115
Drone Diameter [mm]	248	248	234	265	299	299	299	299	299	299	278
Duct Diameter [mm]	204	204	180	188	188	188	188	188	188	188	188
Average Power [W]	145	145	70	85	126	103	110	102	102	105	81
Motor RPM [rpm]	10000	10000	10000	12000	14000	12500	13000	13000	15000	15000	13500
Maximum Thrust [N]	11.4	10.8	6.1	8.2	10.8	8.8	9.4	9	9.4	8.5	7.6

vary linearly with changing mass. The problem is however that for the power increase created by a mass increase different batteries might be necessary. This results in a change in battery mass which triggers the snowball effect. Figure 12.20 shows the required battery mass with increasing mass. As can be seen a certain battery has a window of masses in which it can fulfill the mission requirements. Over this window the maximum achievable flight time decreases with increasing mass, because more of the energy in the battery is needed to provide the required power.

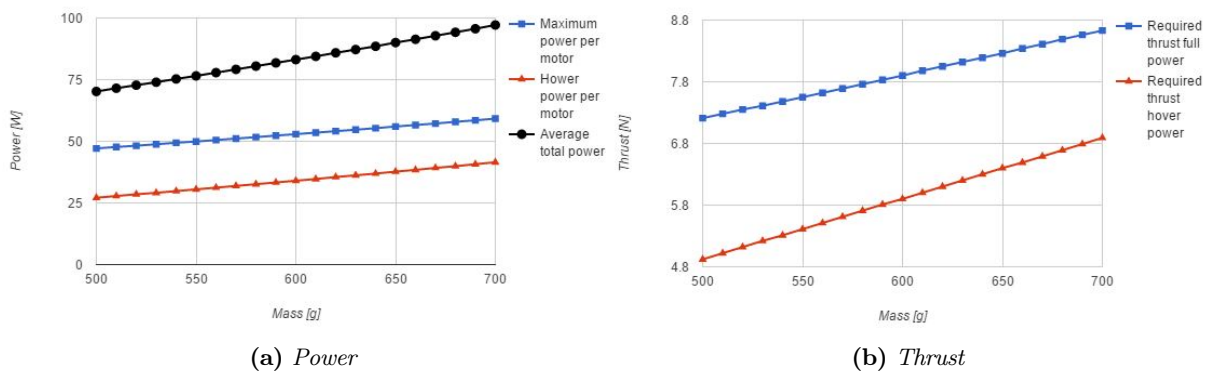


Figure 12.19: Power and required thrust variations due to changing mass

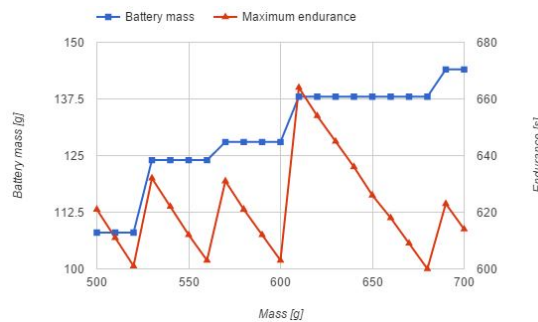


Figure 12.20: Battery mass and maximum endurance due to changing mass

Another parameter that can be checked for sensitivity is the rotor RPM in full power flight. This is done with a fixed mass of 650 gram and the same propeller for each RPM. As such the required power and the delivered thrust will go up with increasing RPM. This can be seen in Figure 12.21. An increase in RPM is undesired, since it requires more power which will lead to heavier batteries which will show the behaviour as shown in Figure 12.20, except now as a function of RPM instead of mass. However, as can be seen in Figure 12.21b, there is a certain minimum RPM that must be achieved to meet the requirements. This limit will only go down with a more aerodynamic design that will reduce drag or a lighter design that will reduce the weight. The other option is to change the propeller so that it generates more lift. Since less RPM means less power required, the battery can be smaller, which reduces mass, which again reduces the required thrust, so a snowball effect is to be expected here as well.

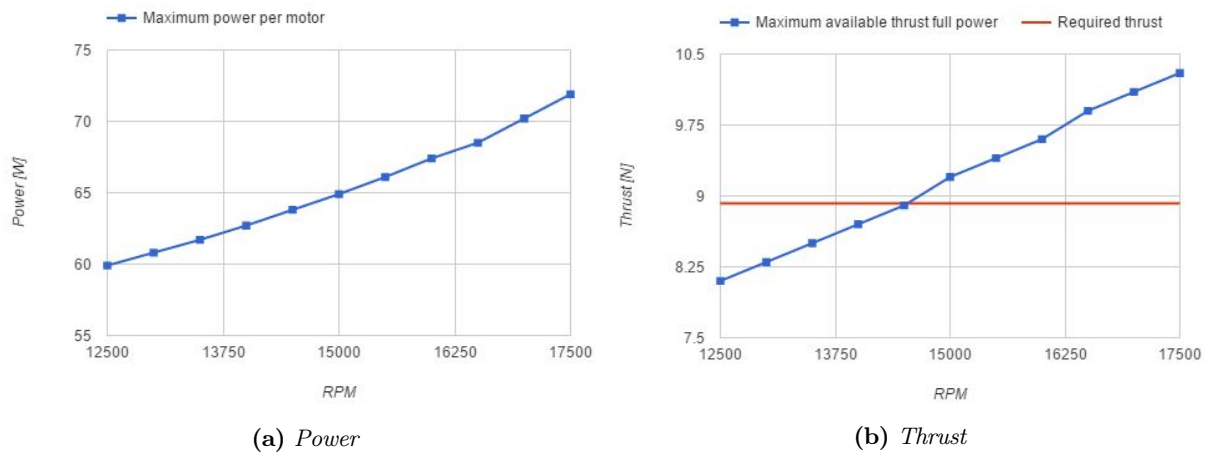


Figure 12.21: Power and required thrust variations due to changing RPM

12.6 Inspection Pocket Drone: description of the integrated system

The previous chapters discussed the theories and method necessary to design the Inspection Pocket Drone. This section summarizes all design choices and provides a brief description of the entire Inspection Pocket Drone system.

12.6.1 Propulsion technology

The propulsion subsystem consists of a coaxial rotor inside a duct. The rotors are made from carbon fiber and have a radius of 89mm , a cut-off radius of 13mm , and a constant chord length of 15mm . Due to the effect of the upper rotor on the lower rotor the twist distribution is different per rotor and can be found in Figure 5.7. Between the rotors and the duct is a blade-tip clearance of 5mm . In full thrust setting the rotors have a RPM of 13500. The duct is modelled as a straight diffuser with a length of 95mm and with an inlet and outlet tip radius of 10mm .

12.6.2 Payload and On Board Computing

The On Board Computing architecture is the Paparazzi framework, which is a combination of open-source hardware & software modules. The NavStik flight controller board is the basis, plus the IvyPro interface board which connects the servos, electronic speed controllers and 6 MaxBotix sonar sensors for ranging. To enable FPV flight and perform the recognition mission, a video feed is included by the eCam56 5MP camera in the payload which is able to generate VGA quality video at 30fps and 5MP stills at 7fps. A FLIR Lepton 80 x 60 pixels thermal camera is included for recognition of fire hotspots and persons in reduced visibility environments. To add processing power for compression of the video data, the Gumstix Overo Earthstorm COM is used, adding 1GHz of CPU power. The Gumstix Overo Earthstorm is combined with a Gumstix Summit breakoutboard adding the required connectivity options.

12.6.3 Communication technology

To achieve live video streaming and transmission of command and control data for a 150m range through reinforced concrete, a robust and powerful subsystem was designed. The UAV will be equipped with two Random Wire Antennae which have near omnidirectional transmission in the plane perpendicular to the wire. The wires are placed on opposite ends of the vehicle on a slanted face that faces ground on the perpendicular as shown in Figure 6.9. Two 1.25 wavelength dipole antennae are used on the GCS as will be described in Section 12.6.5. Two customisable SiFLEX02-R2-HP dual antennae transceiver module, one on the UAV and the other on the GCS, will interface with the host to handle data flow, antennae switching and signal amplification. The maximum range through concrete wall on 868MHz and 908MHz is 278.3m and 263.2m. The module is customisable and available to operate on either frequency band. The maximum supported data rate would be 1Mbps directional which is sufficient for timely data transmission as analysed in Section 6.4.8.

12.6.4 Power solutions

To provide enough power while staying lightweight, the battery system consists of two LiPo batteries, that are connected in parallel. Using two batteries has an advantage over using one bigger battery, since the two batteries can balance each other around the center of gravity. The batteries are placed in compartments inside the hull that can be opened, so they can be changed on site to extend the mission.

12.6.5 Ground Control Station and the User

The user has a handheld controller device to control the movement of the UAV. It is linked to a tablet computer and the antenna system to relay the instructions and get a video feed. The video feed can be watched on the tablet, or using virtual reality goggles which immerse the operator in what the drone sees, with a motion tracker so that the motions of the head can be used to control the vision of the drone.

12.6.6 Structural solutions

Structural considerations were conducted on the vehicle itself and were not assessed for the Ground Control Station. The vehicle contains a ring shaped hull which houses the payload and other subsystems, protects the environment from the propellers and vice versa. The hull is fully covered on the top and the bottom with a protective foam which is multifunctional: it protects the structure from failure upon impact, it reduces impact forces upon collision with people and it also defines the required aerodynamic shape. There are 10 foam fingers connecting the top and the bottom foam layers together to ensure sideways protection of the hull, the camera and other sensors. The hull is a 1 mm laser printed carbon fibre reinforced Nylon 12 material. The height of the hull is 42 mm which is covered by 36.5 mm of foam on the top and the bottom equaling an absolute hull height of 115 mm. The width of the hull is 28 mm, the length of the foam fingers is 17 mm equaling a total of 45 mm hull width. The diameter of the vehicle takes into account the diameter of the propeller housing duct (Subsection 12.6.1) which is 188 mm plus the above mentioned 45 mm two times. This gives a total vehicle diameter of 278 mm. To facilitate fast battery replacement, the outer wall of the hull at the battery locations is possible. The hull is connected to the propulsion subsystem with 3 stiffening struts that are made out of High Density Polyethylene (HDPE). These struts can survive impact loads and provide stiffness to reduce the impact of vibrations on other subsystems. The struts are circular with a hollow inner radius of 4.6 mm and an outer radius of 5.7 mm to allow for the placement of cables that connect the motors to the electric speed controllers and the batteries. Additionally, a protective fence of 5 spokes is placed on both the top and the bottom of the vehicle. They are 94 mm in length and 4 mm in diameter and made out of Aramid RA11 (Table 7.9). The total mass of the vehicle is 533 grams.

13 | Requirement Compliance Matrix & Feasibility Analysis

In this chapter, the Requirement Compliance Matrix and Feasibility Analysis will be described. The Requirement Compliance Matrix will be shown and explained in Section 13.1 and the Feasibility Analysis of the design will be discussed in Section 13.2.

13.1 Requirement Compliance Matrix

The Requirement Compliance Matrix is shown in Table 13.1. The first column of the matrix contains the code of the requirements listed in Section 2.3. The second column contains the value each requirement specifies the design must meet. The third column shows the actual value the design meets and the fourth column shows with either a tick-mark or a cross if the required value has been met or not. For requirements that have no concrete value it will be said that it's not applicable (n.a.) and qualitative assessments have been performed for those requirements to see if they are met or not. The requirements that are not met according to Table 13.1 will be elaborated on in Section 13.2.

13.2 Feasibility Analysis

Several requirements that were set have not been met. Mostly these requirements are not met as they would conflict with other requirements. The exact reason why these requirements are not met and what reasoning is used to justify this will be explained per requirement in the list of failed requirements. Also requirements stating a value that need to be met and have no value given but are fulfilled will be explained in the list of special requirements for the sake of clarity.

List of failed requirements

- IPD-AAoI-Transport-A [2,D,K]: The maximum stored size of the total system shall be $35 \times 25 \times 10 \text{ cm}$. The original transport size requirement defined a rectangular shape that fits inside a conventional backpack. The circular drone design does not fit into this rectangular shape but does fit inside conventional backpacks for easy transport.
- IPD-AAoI-Transport-B [3,D]: The maximum total system mass shall be 2 kg . The 2 kg mass requirement on the total system mass was an initial estimate made by the design team as the first impression was to design a system weighing around the same as a laptop. After more research into a ground station it was found that the required components together already weighed more than 2 kg . And as such it was not possible to go below the 2 kg requirement without sacrificing required functionality.
- IPD-AAoI-Reach-A-8 [2,D,KL]: The system shall be able to operate in 75% of Dutch weather conditions at an altitude of 100 meters. This requirement is not met as the two child requirements IPD-AAoI-Reach-A-8-B [2,D,KL] and IPD-AAoI-Reach-A-8-D [2,D,KL] are not met.
- IPD-AAoI-Reach-A-8-A [2,D,KL]: The vehicle shall be able to perform its mission in maximum wind speeds of $21 \frac{\text{m}}{\text{s}}$. The first two iterations of the design met this requirement. However this pushed the drone to fail other requirements. As such it was decided by the design team to reduce the speed the drone could fly at as it was known that this requirement was a secondary killer requirement.
- IPD-AAoI-Reach-A-8-B [2,D,KL]: The vehicle shall be able to perform its mission in maximum gust speeds of $24 \frac{\text{m}}{\text{s}}$.

Table 13.1: Requirement Compliance Matrix

Requirement code	Req. Value	Design Value	Tick	Requirement code	Req. Value	Design Value	Tick
IPD-AAoI-Transport [1,D,K]	n.a.	n.a.	v	IPD-GI-Maneuver [1,D]	n.a.	n.a.	v
IPD-AAoI-Transport-A [2,D,K]	35x25x10 cm	D28x11.5cm	x	IPD-GI-Maneuver-A [1]	n.a.	n.a.	v
IPD-AAoI-Transport-B [3,D]	2 kg	5 kg	x	IPD-GI-Maneuver-A-1 [1]	n.a.	n.a.	v
				IPD-GI-Maneuver-B [1]	n.a.	n.a.	v
IPD-AAoI-Deploy [1,D]	n.a.	n.a.	v	IPD-GI-Maneuver-B-1 [2,D]	0 cd/m ²	n.a.	v
IPD-AAoI-Deploy-A [1,D,K]	60 sec	n.a.	v	IPD-GI-Maneuver-B-2 [1]	n.a.	n.a.	v
IPD-AAoI-Deploy-B [3]	n.a.	n.a.	v	IPD-GI-Maneuver-B-3 [1]	n.a.	n.a.	v
IPD-AAoI-Deploy-C [3]	n.a.	n.a.	v	IPD-GI-Maneuver-B-4 [2]	n.a.	n.a.	v
IPD-AAoI-Deploy-D [2]	60 sec	n.a.	v	IPD-GI-Maneuver-B-5 [1]	n.a.	n.a.	v
				IPD-GI-Maneuver-B-6 [3]	n.a.	n.a.	v
IPD-AAoI-Reach [1,D,K]	n.a.	n.a.	v	IPD-GI-Maneuver-C [1,D,K]	n.a.	n.a.	v
IPD-AAoI-Reach-A [1,D]	n.a.	n.a.	v	IPD-GI-Maneuver-C-1 [1]	n.a.	n.a.	v
IPD-AAoI-Reach-A-1 [1]	n.a.	n.a.	v	IPD-GI-Maneuver-C-2 [1,D,K]	n.a.	n.a.	v
IPD-AAoI-Reach-A-1-A [1]	n.a.	n.a.	v	IPD-GI-Maneuver-D [1,D]	n.a.	n.a.	v
IPD-AAoI-Reach-A-2 [1]	n.a.	n.a.	v	IPD-GI-Maneuver-D-1 [2,D]	n.a.	n.a.	v
IPD-AAoI-Reach-A-2-A [1]	n.a.	n.a.	v	IPD-GI-Maneuver-D-2 [1,D]	n.a.	n.a.	v
IPD-AAoI-Reach-A-3 [1,D,K]	n.a.	n.a.	v	IPD-GI-Maneuver-D-3 [2,D]	n.a.	n.a.	v
IPD-AAoI-Reach-A-3-A [1,D]	11 m/s	13 m/s	v	IPD-GI-Maneuver-D-4 [3,KL]	400°C	55°C	x
IPD-AAoI-Reach-A-3-B [1,D]	17 m/s	13 m/s	v	IPD-GI-Maneuver-D-5 [3]	n.a.	n.a.	v
IPD-AAoI-Reach-A-3-C [1,D]	n.a.	n.a.	v	IPD-GI-Maneuver-E [2]	n.a.	n.a.	v
IPD-AAoI-Reach-A-3-D [1]	-5°C	0°C	v	IPD-GI-Maneuver-F [3]	n.a.	n.a.	v
IPD-AAoI-Reach-A-3-E [1]	25°C	55°C	v	IPD-GI-Maneuver-F-1 [3]	n.a.	n.a.	v
IPD-AAoI-Reach-A-4 [1]	n.a.	n.a.	v	IPD-GI-Maneuver-F-2 [3]	n.a.	n.a.	v
IPD-AAoI-Reach-A-4-A [1]	n.a.	n.a.	v	IPD-GI-Maneuver-F-3 [3]	1 sec	n.a.a	x
IPD-AAoI-Reach-A-4-B [1]	n.a.	n.a.	v	IPD-GI-Maneuver-G [1]	n.a.	n.a.	v
IPD-AAoI-Reach-A-4-C [1]	n.a.	n.a.	v	IPD-GI-Maneuver-G-1 [1]	n.a.	n.a.	v
IPD-AAoI-Reach-A-5 [1]	n.a.	n.a.	v	IPD-GI-Maneuver-G-2 [1]	n.a.	n.a.	v
IPD-AAoI-Reach-A-5-A [1,D]	n.a.	n.a.	v	IPD-GI-Maneuver-G-3 [1]	n.a.	n.a.	v
IPD-AAoI-Reach-A-5-B [1,D]	n.a.	n.a.	v				
IPD-AAoI-Reach-A-5-C [1]	n.a.	n.a.	v	IPD-Communicate-A [1]	n.a.	n.a.	v
IPD-AAoI-Reach-A-6 [1]	n.a.	n.a.	v	IPD-Communicate-B [3]	n.a.	n.a.	v
IPD-AAoI-Reach-A-6-A [2,D]	0 cd/m ²	n.a.	v	IPD-Communicate-C [3]	n.a.	n.a.	x
IPD-AAoI-Reach-A-6-B [1]	n.a.	n.a.	v	IPD-Communicate-D [2,K]	96000 cd/m ²	n.a.	v
IPD-AAoI-Reach-A-6-C [1]	n.a.	n.a.	v	IPD-Communicate-E [1,D]	n.a.	n.a.	v
IPD-AAoI-Reach-A-6-D [2]	n.a.	n.a.	v	IPD-Communicate-E-1 [2]	0.1 sec	0.1 sec	v
IPD-AAoI-Reach-A-6-E [1]	n.a.	n.a.	v	IPD-Communicate-E-2 [2]	n.a.	n.a.	v
IPD-AAoI-Reach-A-6-F [3]	n.a.	n.a.	v	IPD-Communicate-E-3 [1]	n.a.	n.a.	v
IPD-AAoI-Reach-A-7 [1,D,K]	n.a.	n.a.	v	IPD-Communicate-E-4 [2]	n.a.	n.a.	x
IPD-AAoI-Reach-A-7-A [1]	n.a.	n.a.	v	IPD-Communicate-E-5 [2]	n.a.	n.a.	v
IPD-AAoI-Reach-A-7-B [1,D,K]	n.a.	n.a.	v	IPD-Communicate-E-6 [2]	n.a.	n.a.	x
IPD-AAoI-Reach-A-8 [2,D,KL]	n.a.	n.a.	x	IPD-Communicate-F [1,D]	n.a.	n.a.	v
IPD-AAoI-Reach-A-8-A [2,D,KL]	21 m/s	13 m/s	x	IPD-Communicate-F-1 [3]	n.a.	n.a.	v
IPD-AAoI-Reach-A-8-B [2,D,KL]	24 m/s	13 m/s	x	IPD-Communicate-F-1-A [3]	10 Hz	10 Hz	v
				IPD-Communicate-F-1-B [3]	n.a.	n.a.	v
IPD-AAoI-Enter [1,D,K]	n.a.	n.a.	v	IPD-Communicate-F-1-C [3]	n.a.	n.a.	v
IPD-AAoI-Enter-A [2,D]	n.a.	n.a.	v	IPD-Communicate-F-1-D [3]	n.a.	n.a.	v
IPD-AAoI-Enter-A-1 [2,D]	n.a.	n.a.	x	IPD-Communicate-F-1-E [3]	n.a.	n.a.	v
IPD-AAoI-Enter-A-2 [2,D]	n.a.	n.a.	v	IPD-Communicate-F-1-F [3]	0.1 sec	0.1 sec	v
IPD-AAoI-Enter-B [1,D,K]	n.a.	n.a.	v	IPD-Communicate-F-2 [1,D]	n.a.	n.a.	v
IPD-AAoI-Enter-B-1 [2]	n.a.	n.a.	v	IPD-Communicate-F-2-A [2]	0.1 sec	0.1 sec	v
IPD-AAoI-Enter-B-2 [1,D,K]	61x60 cm	28x11.5 cm	v	IPD-Communicate-G [2]	n.a.	n.a.	v
IPD-AAoI-Enter-B-3 [1,D]	n.a.	n.a.	v	IPD-Communicate-H [2,D]	150 m	263 m	v
IPD-AAoI-Enter-B-3-A [2,D,KL]	21 m/s	13 m/s	x	IPD-Communicate-H-1 [2,D]	100 m	263 m	v
IPD-AAoI-Enter-B-3-B [2,D,KL]	24 m/s	13 m/s	x	IPD-Communicate-H-2 [2,D]	100 m	263 m	v
IPD-AAoI-Enter-B-4 [1,D]	n.a.	n.a.	v				
				IPD-Misc-A [2,D,K]	500 g	533 g	x
IPD-GI-Payload [1,D,K]	n.a.	n.a.	v	IPD-Misc-B [2]	200 m	263 m	v
IPD-GI-Payload-A [1]	n.a.	n.a.	v	IPD-Misc-C [2]	100 m	n.a.	x
IPD-GI-Payload-B [1,K]	n.a.	n.a.	v	IPD-Misc-D [2,K]	600 sec	628 sec	v
IPD-GI-Payload-B-1 [2,K]	n.a.	n.a.	v	IPD-Misc-E [2,K]	€15000	€1500	v
IPD-GI-Payload-B-1-A [2,K]	n.a.	n.a.	v	IPD-Misc-F [2,K]	n.a.	n.a.	v
IPD-GI-Payload-B-1-B [3]	24 fps	30 fps	v	IPD-Misc-G [2,D,K]	80%	93%	v
IPD-GI-Payload-B-2 [1,K]	n.a.	n.a.	v	IPD-Misc-H [2]	n.a.	n.a.	v
IPD-GI-Payload-B-2-A [1,K]	n.a.	n.a.	v	IPD-Misc-H-1 [2]	n.a.	n.a.	v
IPD-GI-Payload-B-2-B [2,K]	3 MP	5 MP	v	IPD-Misc-H-2 [2]	n.a.	n.a.	v
IPD-GI-Payload-B-3 [3]	80 degrees	n.a.	v	IPD-Misc-I [3]	20 Sy/year	n.a.	v
IPD-GI-Payload-C [2,K]	0 cd/m ²	n.a.	v	IPD-Misc-J [3]	n.a.	n.a.	v
IPD-GI-Payload-D [2]	n.a.	n.a.	v	IPD-Misc-K [3]	n.a.	n.a.	v
IPD-GI-Payload-E [2]	n.a.	n.a.	v	IPD-Misc-L [3]	85 dB	n.a.	v
IPD-GI-Payload-E-1 [2]	5 pixels	n.a.	v				
IPD-GI-Payload-E-2 [2]	12Hz	26.7Hz	x	IPD-DSE-A [1,K]	n.a.	n.a.	v
IPD-GI-Payload-E-3 [2]	n.a.	n.a.	v	IPD-DSE-B [3]	n.a.	n.a.	v
IPD-GI-Payload-F [2,K]	n.a.	n.a.	v	IPD-DSE-C [3]	n.a.	n.a.	v
IPD-GI-Payload-G [2,D]	n.a.	n.a.	v				
IPD-GI-Payload-H [2,K]	n.a.	n.a.	x				

To meet this requirement the drone had to be designed in such a way it would fail most other requirements. As such the same decision was reached as with requirement IPD-AAoI-Reach-A-8-A [2,D,KL].

- IPD-AAoI-Enter-A-1 [2,D]: The vehicle shall be able to break a tempered double-glass window.
Due to time constraints and prospectively high mass increase the option to break windows by using the drone has been postponed. It is still possible for users to open windows for the drone to use to enter the building.
- IPD-AAoI-Enter-B-3-A [2,D,KL]: The vehicle shall be able to enter the area of interest in maximum wind speeds of $21 \frac{m}{s}$.
See IPD-AAoI-Reach-A-8 [2,D,KL].
- IPD-AAoI-Enter-B-3-B [2,D,KL]: The vehicle shall be able to enter the area of interest in maximum gust speeds of $24 \frac{m}{s}$.
See IPD-AAoI-Reach-A-8-B [2,D,KL].
- IPD-GI-Payload-E-2 [2]: The frequency of the vibration of the payload cameras shall not exceed half of the video frame rate.
The lowest frequency of the system is $26.7Hz$ this is more than twice the set requirement. However the amplitude of the vibrations is in the order of $10^{-5}m$ and as such the frequency poses no problem.
- IPD-GI-Payload-H [2,K]: The payload shall gather gas concentration data of the surroundings.
Due to constraints on the mass and size of the drone it was decided to leave out sensors that can measure the concentration of toxic gasses. As this was a second requirement it is not vital to the mission.
- IPD-GI-Maneuver-D-4 [3,KL]: The vehicle shall be able to perform its mission in maximum indoor temperatures of $400^{\circ}C$.
The highest operational temperature of one of the components is $55^{\circ}C$. This is far below a temperature of $400^{\circ}C$. However it is assumed that by moving quickly through the high temperature areas the drone should be able to perform its mission without increasing its internal temperature past the operational temperature of the components.
- IPD-GI-Maneuver-F-3 [3]:
It is not known yet whether or not this requirement is actually met. This is due to no hardware or software testing during the design phase. Thus it can't be known what the settling time is with the paparazzi software.
- IPD-Communicate-C [3]: The system shall be able to communicate with persons inside the building.
Tests were performed to find out if the noise of the propellers could be filtered out of an audio sample if the propellers were in the vicinity of the microphone. It was found that this was not possible and as such direct communication with persons inside the building was scrapped.
- IPD-Communicate-E-4 [2]: The vehicle shall transmit sound data to the GCS.
As it was decided to scrap direct communication with persons inside the building this requirement automatically fails.
- IPD-Communicate-E-6 [2]: The vehicle shall transmit gas concentration data of the surroundings to the GCS.
As it was decided to leave out sensors that can measure the concentration of toxic gasses this requirement automatically fails.
- IPD-Misc-A [2,D,K]: The vehicle shall have a maximum weight of 500 grams.
The mass of the drone is over the $500g$ requirement. The drone is designed to be able to perform the mission while being as light as possible. However to perform its mission the drone is heavier than required.
- IPD-Misc-C [2]: The vehicle shall have an operational ceiling of 100m.
According to requirement IPD-AAoI-Reach-A-8-B [2,D,KL] the drone is not capable of flying at $100m$ altitude in certain wind conditions. However in lower wind conditions of $13 \frac{m}{s}$ it is possible to fly at $100m$ altitude.

List of special requirements

- IPD-AAoI-Deploy-A [1,D,K]
It was specified that the drone is deployed in 1 minute, however without an actual prototype it is not possible to test this. Thus to meet the requirement the drone is designed to have no assembly and be able to start directly after switching on.

- IPD-AAoI-Deploy-D [2]
There are two doors on the drone that can be opened up to reach the subsystems. To replace the batteries you can quickly open up the drone replace the batteries and close up. Due to this simple design it is assumed that this requirement is met.
- IPD-AAoI-Reach-A-3-B [1,D]: The vehicle shall be able to perform its mission in maximum gust speeds of $17 \frac{m}{s}$.
This requirement specifies that the drone shall be able to perform its mission in gusts of $17 \frac{m}{s}$. Any wind speed over $14 \frac{m}{s}$ will push the drone away. However gusts are short in duration and as such the drone will be moved a small distance but as long as it maintains stability it can continue the mission after the gust is over.
- IPD-AAoI-Reach-A-3-D [1]: The vehicle shall be able to perform its mission in minimum temperatures of $5^{\circ}C$.
One of the payload components has a lower operational temperature of $0^{\circ}C$. However the component is encased inside a hull generates heat by itself when operational. As such it is assumed that the component will not fall below the $0^{\circ}C$ mark. A test run in an environment of $-5^{\circ}C$ would be necessary to provide a final conclusion.
- IPD-AAoI-Reach-A-6-A [2,D]
This requirement specifies that the drone shall be able to sense its state properties when there is no light. The sensors used do not require any light to sense its state properties as such there is no value but the requirement is met.
- IPD-GI-Payload-B-3 [3]
The minimum view angle is set to be 80 degrees, the camera used has a view angle of 70 degrees.
- IPD-GI-Payload-C [2,K]
In lighting conditions of $0 \frac{cd}{m^2}$ a LED Will be used to shine light on the surroundings at which point the lighting condition will no longer be $0 \frac{cd}{m^2}$ and the camera can be used.
- IPD-GI-Payload-E-1 [2]
The amplitude of the vibrations of the entire drone have been calculated to be in the order of $10^{-5}m$. This is so low that is assumed that the camera vibration amplitude does not exceed 5 pixels.
- IPD-GI-Maneuver-B-1 [2,D]
See requirement IPD-GI-Payload-C [2,K].
- IPD-Communicate-D [2,K]
The design uses Cinemizer OLED glasses which covers the eyes completely. Thus outside lighting conditions have no effect on the user interface.
- IPD-Misc-I [3]
No radioactive materials are used in this design. Thus this requirement is met.
- IPD-Misc-L [3]
Testing of the propulsion unit would give a value of how much noise the drone generates at the source. However from experience with existing drones it is assumed the noise will not reach the level of 85db.

14 | Further Development

In this chapter the further development and usage about the IPD project is discussed. First an overview is given in Section 14.1 about the tasks that have to be performed to further develop the UAV and come to the first sale. In Section 14.2 the tasks that have to be performed are plotted in a Gantt Chart with an estimation of the time that the tasks will take. The estimated cost of further testing, development and production is presented in the form of a Cost Breakdown Structure in Section 14.3. Finally in Section 14.4 the operations and logistics concept of the actual mission is discussed.

14.1 Project Design and Development Logic

In this section the project design and development logic of the IPD project after the detailed design phase is explained. The logic is split up in to five separate phases, which are the prototyping, testing, certifications, sales and after sales. From which the prototyping phase and testing phase will start in parallel. The logic is visualized in a block diagram in Figure 14.1.

Prototyping

The first step in the development logic is to actually make a prototype of the UAV and start the development of the software. The development of the software and the prototype of the UAV itself will start simultaneously. For the prototyping the custom parts, like the rotor blades, have to be manufactured. Once these are finished and the off the shelf components are ordered the first prototype can be assembled. Although before assembling all parts should be measured and compared to the theory. Doing this will make sure everything fits as designed for, if not some changes in the design might be necessary. It has to be noted that most likely multiple prototypes are necessary, because the first one might not be perfect and some will probably break during the testing phase.

Testing

The testing phase will start simultaneously with the prototyping phase. It is common practice that after a day of software development a day of testing is done. Also once the first UAV assembly is done the first structural tests can be performed, since the software is not necessarily needed for this. First tests to be performed are tests on the duct and the optimization off this component. With flow visualization and with measurements it is possible to check how well the duct performs and what the drag coefficient of the duct is. Next are the structural tests like, crash testings, stress testing of the hull and vibration tests. Heat resistance and water tightness of the UAV will also be tested here. During the safety tests it will be checked whether the UAV will not cause trauma on impact and failure modes will be investigated. Once all tests are done the actual fly testing will be done, first inside and then outside. During all tests the results will be validated with the theoretical values.

Assessment

After all prototyping and testing there will be a working product which now has to be assessed to comply with the Dutch regulations. For this an operational manual has to be written first. This will take quite sometime, because the document will constantly be checked by an external company until it complies with all laws. Once the operational manual is done an external company can assess the UAV and give the clearance.

Sales

Now everything is in place to sell the actual product it is time to find some customers and sell the product. Of course the client will need time internally to make the decision to buy the product.

After Sales

Once the customer signed the contract it is time to deliver the product. First the certification for the customer will be started. When the certification is done the UAV will be manufactured. Also a user training will be provided.

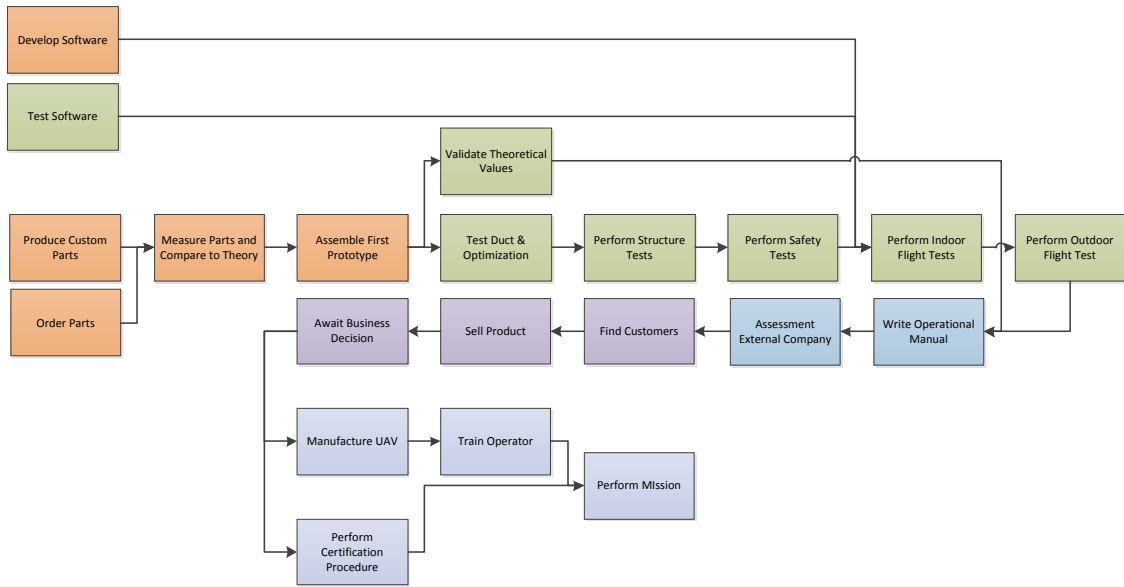


Figure 14.1: Project Design & Development Logic Block Diagram

14.2 Development Gantt Chart

In this section the Gantt Chart of the project is shown, as can be seen in Figure 14.2. All activities discussed in Section 14.1 and their duration are plotted in the Gantt Chart. It is likely that the duration may be grossly under- or overestimated as the actual time it takes depends on unknown factors. For example the regulations regarding UAV's are changing in a rapid fashion and this might slow down or speed up the process.

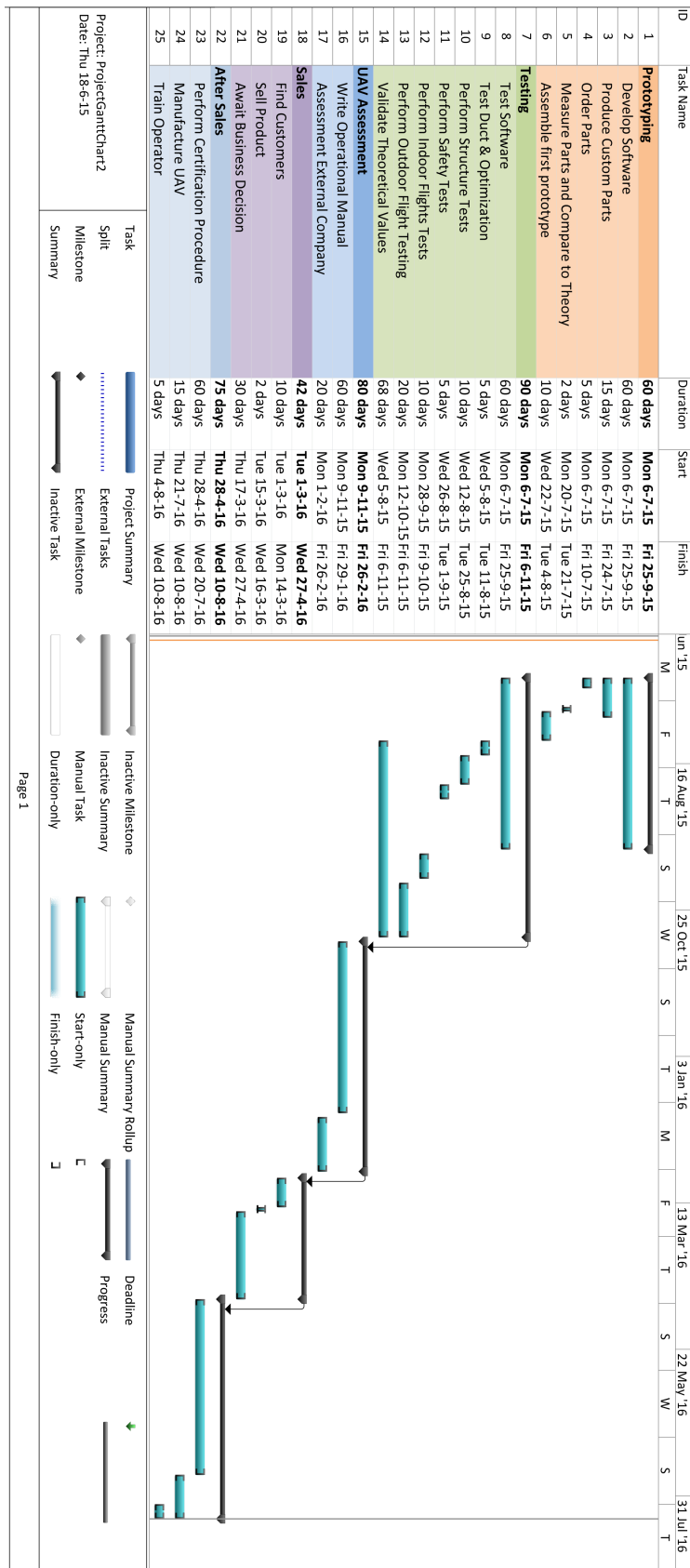


Figure 14.2: Project Gantt Chart

14.3 Cost Breakdown Structure

This section presents an overview of the estimated cost for further development of the system. It follows the logic of Section 14.1 and the components of the Gantt Chart in Section 14.2. Some of the components have been merged for brevity: in the Gantt chart they were on different timelines and hence needed to be mentioned separately, but since the purpose of this structure is not to show the timing but the cost, some were taken together.

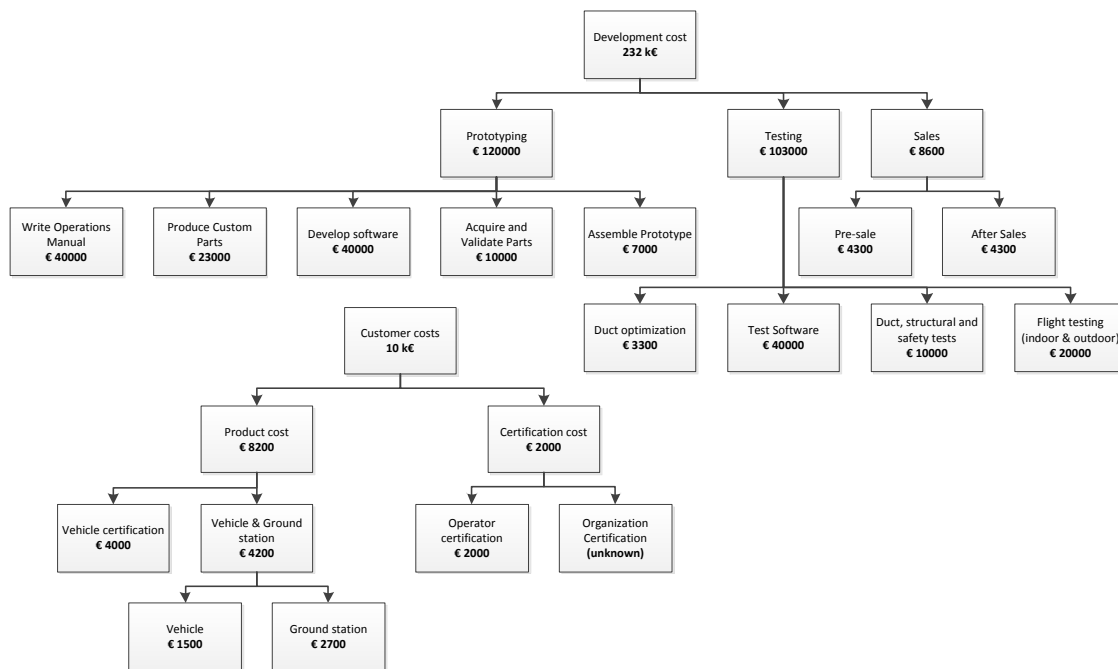


Figure 14.3: Cost Breakdown Structure

This rough estimation of the costs required to continue develop the product was based on calculating the required man hours by taking the time from the Gantt chart and assigning the expected number of persons to it (for instance, software development: 60 days by 2 persons), and multiplying by the hours in a day (8) and the average cost for this type of labour (€41.57¹). Additionally, some equipment costs (for instance, the 3D printer) and costs for external parties (for certification) are included. The development cost up to the point where there is a working prototype is estimated to be €232 thousand, and the customer cost is estimated at €10 thousand.

14.4 Operations and Logistics Concept

This section describes the operations and logistics concept for the use of the IPD. It is set up so that it gives an overview of all the actions that the user has to do while using the drone. Starting from the moment the operator is notified that the UAV is required to inspect something somewhere, it stretches all the way till the drone is back in storage. In Figure 14.4 the general flow of operations is shown during the course of one mission. There are five main phases in the operations and logistics, being the pre-mission phase, the deploy phase, the mission phase, the pack phase and the after-mission phase. They are explained in more detail below.

Pre-mission phase

After the operator has received a notification that the IPD is needed somewhere, it must be taken from storage. The batteries must be taken from their cool storage and put in the systems ground control station casing in their respective spot. The batteries that are going to be used for the first flight are placed in and connected to the drone. The battery compartments must be shut so the system is ready to fly when arrived at the site. A quick check must be done to ensure that everything is properly secured in the ground control casing. The

¹Centraal Bureau voor de Statistiek, Cost of labour per hour, sector Business Services.

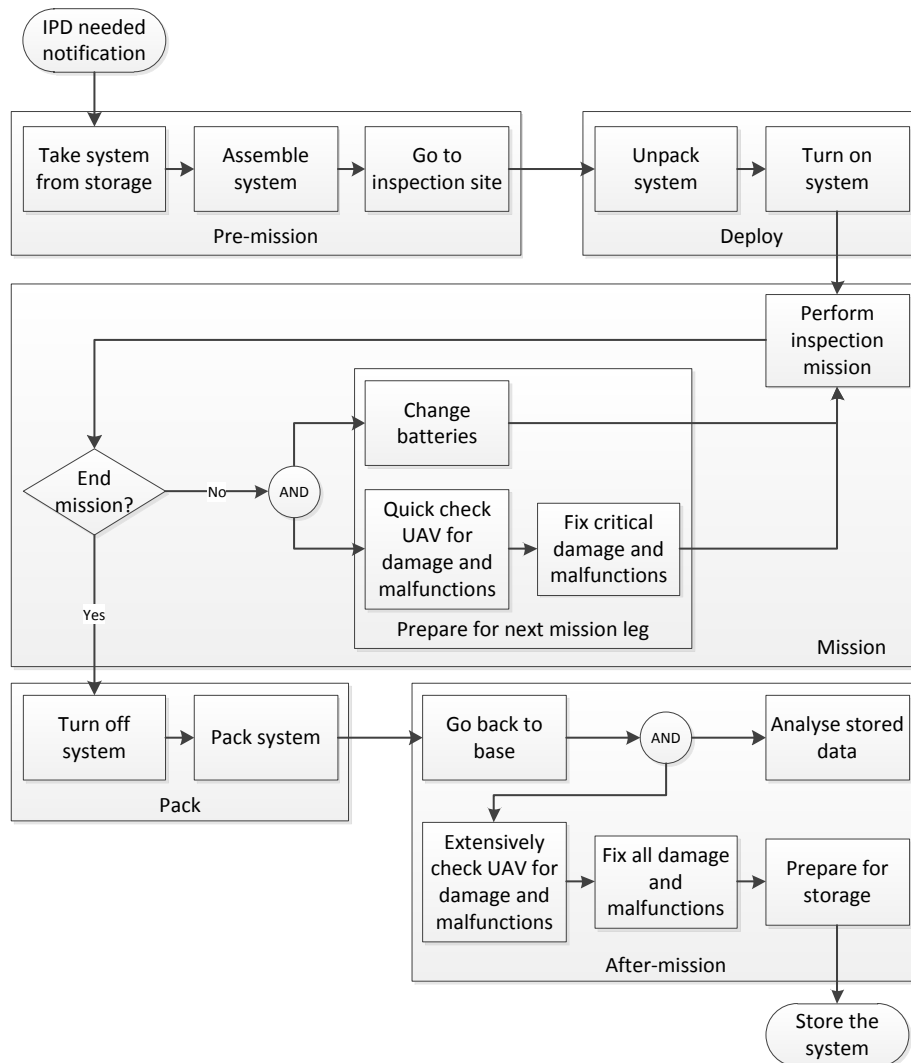


Figure 14.4: *The operations and logistics concept flow chart*

system must then be transported to the inspection site to perform its mission. It may be desirable for the operator to walk closer to the inspection site if the transportation vehicle cannot come close enough.

Deploy phase

When the system arrives at the site it must be unpacked. The ground control case is placed on it back and folded open. The UAV, the remote control and the goggles must be taken out, after which the ground station can be turned on. The drone is turned on next and when a connection between GCS and UAV is established a quick systems check must be done. During this check the operator must check that the UAV responds correctly to the control inputs and that the video feed is transmitted properly. When this is the case he can put on the goggles and the mission can start. If an observer, for example the commander, also wants to follow the operation he can take the tablet out of the casing and follow the mission on that.

Mission phase

In the mission phase the actual inspecting is done. After take off the drone is flown to an entrance of the building. After entering the flight mode must be switched from outdoor to indoor flying. In indoor mode the drone will fly slower than in outdoor mode, which will both feel more natural to the pilot and also reduces the chance and severity of impacts. When the batteries are running low the drone must return to the ground station, and the flight mode can be switched back to outdoors once the drone is outside. Back at the GCS there is a choice to be made. If there are still unexplored reachable areas of interest the mission can be extended. There are two things that need

to be done to prepare the UAV for its next mission leg. The first thing is to quickly check the craft for damage and malfunctions, for example a damaged or broken rotor blade or a stuck servo. Minor damages and malfunctions that do not hinder the systems performance to a large extent do not have to be fixed in emergency situations where every second counts, but critical damages must be fixed immediately. If the IPD is used in a non-emergency situation it is up to the operator to decide on what to do in case of minor damages found in between two mission legs. Next to this quick inspection the battery of the UAV must be changed. Even in the case that the drone is back at the ground station after only a very short flight due to for example dead ends this has to be done, so that the range for the next mission leg is not compromised because of low power. To do this the drone must be turned off, after which the battery compartments can be opened. Next the old batteries can be taken out and be replaced by new ones. When these are connected and placed properly inside the drone the compartments can be closed again. The drone can be turned on again and the quick system functionality check must be performed before flying again. This process is repeated until the mission is completed, after which the operator can move on to the pack phase.

Pack phase

When the mission phase has come to an end the system must be packed again. To do this the UAV must be turned off and then the ground control station. Everything must be placed in its respective location inside the case, and secured properly to ensure safe transport.

After-mission phase

After the mission the system must be transported back to base. After arriving there are two things to be done. The UAV must be extensively checked for damage and malfunctions. This may require disassembling the drone completely, to gain access to deeply embedded subsystems and parts. Every error must be fixed and the drone must also be cleaned if necessary, to ensure it is fully functional for its next flight. The batteries must be taken out and charged before they go in their cooled storage. The batteries required for the ground station systems must be charged. The ground station case inventory must be checked and refilled if necessary. When these activities are done the system is packed and stored so that it is ready to repeat the aforementioned cycle. Next to these fixing and packing actions the stored data achieved during the mission must be analyzed and documented.

In this chapter the further development of the project was explained. First, the Project Design and Development Logic was described and then depicted with a time schedule in the Project Gantt Chart. Second, the Cost Breakdown Structure was shown and the cost for the project was estimated. Third, the Operations and Logistics Concept was explained.

15 | Conclusion

In this chapter, a conclusion of the report is discussed to give the reader a clear overview of achievements and processes treated during this design phase.

First of all, the mission is described using a Functional Flow Diagram and a Functional Breakdown Structure. This provides a clear overview of what tasks need to be fulfilled, what subtasks this entails and in which order the work should be performed. Having defined the mission, a market analysis was performed to identify potential end users and indicate the demand for this new design. It includes an overview of laws that apply to this design and have to be accounted for.

Having established the boundaries of the design space, the subsystems can be designed. The propulsion subsystem is discussed first, separated into the different components of the subsystem. The final design makes use of two electric motors with two swashplates, and incorporates two propellers with three rotorblades each. These rotorblades are specifically designed for this mission, and have to be custom-made. The entire system is placed in the middle of the UAV, and makes use of the duct-shape of this section to increase the thrust it generates. This propulsion system enables the operator to control the UAV in all four degrees of freedom.

To perform the mission, a multitude of electrical components have to be implemented into the UAV. The first and foremost is the payload, a group of many components. The chosen camera is the eCam56 5MP Gumstix Overo, which fits the video requirements perfectly. To provide visibility to and of the drone, LEDs are added. The next component is the Inertial Measurement Unit, which is already integrated in the NavStik Flight Controller. For ranging, Maxbotix EZ sonar ranging sensors are chosen to support navigation. Other components of the payload are temperature sensors and thermal camera modules. The FLIR Lepton thermal camera will be used in combination with basic temperature sensors to make flight possible in reduced visibility conditions. For location determination during the outside mission phase, a uBlox module with a Sangshin 1580MHz RF 18mm Antenna patch will make use of GPS signals to determine its exact location. Finally, to interact with victims once located, the UAV is outfitted with speakers. Other optional payload components and peripherals not included in the final design include a gas detector and window breaking mechanisms.

The second electrical component is the On-Board Computer. This is another collective term, and contains four distinct OBC boards. These are the NavStik, IvyPro, Gumstix Overo Earthstorm and Gumstix Summit boards, each with their own defined task. The NavStik, functioning as the main board, is based on the Paparazzi platform. The third electrical component is the Communication subsystem. This subsystem consists of a transceiver board and a set of antennae. For this design, a communication frequency of 868MHz was chosen, and the SiFlex02 transceiver module turned out to be the ideal component to serve in this design. Using two quarter wavelength wire antennae, the system is capable of receiving control inputs and transmitting video as well as housekeeping data.

The fourth electrical component is the Power subsystem. A decision was made to use Lithium-Polymer batteries, as is common in RC applications due to its favorable properties. Two Zippy Flightmax 1000 mAh packs are needed in parallel to guarantee sufficient flight time.

Finally, an overview of the hardware interface of the electrical components is provided to clarify power, data and control links between systems.

After determining the loads imposed on the UAV by the propulsive and electrical subsystems, the structure of the UAV was designed. During the design, not just the performance but also occupational health and safety was taken into account. The propulsive and electrical subsystems induce loads in terms of weight and vibrations. The impact of both of these on the structure were assessed, and a structure was designed to cope with the highest possible imposed loads including a safety factor. Finally, the shape of the drone with according material properties necessary to cope with the maximum load case was determined. The final design features struts to support the mounting of the propulsion subsystem, and features a protective foam layer to protect the contents as well as possible victims from damage caused upon impact. For further protection, a 5-spoke fence was added to the open sections of the UAV so that no hands can accidentally get into the propeller area. The final diameter of the vehicle is 278mm with a height of 115mm.

Having acquired a clear definition of all the hardware that will be implemented, the data generated or required by each subsystem must be handled properly. To this end, data handling and hardware-software interaction

was analysed. The results of this are portrayed in a Data Handling Diagram, which shows where information is generated and where it should go.

The software needed to handle this process of collecting and redistributing information is such an intricate and integral part of the UAV that it's handled in a separate section. The main software part needed to fly the UAV is a flight controller, which is responsible for translating control inputs to movement and is constantly controlling the actuators to compensate for external influences. To make this work, alterations have to be made to the existing Paparazzi system.

To assure the validity of the final design, all subsystem designs are validated and all the formulae and calculation methods used during the design are verified. This is not just an error check, but serves to show that the final design is based on correct models, and the correct design method was applied. Having confirmed the validity of the final product, the sustainability can be analysed. This is done by taking three different points of view: social, economical and environmental. These all take different aspects of the final design into account, from shape to materials used and from flight time to design costs. The final design is considered to fulfill its sustainability demands in all three fields. If a design change is applied, this assessment will have to be re-evaluated.

The final design was achieved using a structured design process, based on an iterative approach. Time and manpower was allocated to the separate subsystems according to necessity, and mass and power budgets were continuously checked to make sure the design did not go to extremes. A risk assessment was performed to identify potential hazards, which granted insight as to which parts of the design needed more attention. Having established which hardware would be used in the UAV, the placement of each component was decided so that the center of gravity would lie as close to the ideal location as possible. Of course, design alterations either to improve the design in one way or another or due to unforeseen reasons occurred. To accommodate these changes, a total of 10 iterations was performed, each analyzing the system configuration at that point to identify points of improvement. Of course, changes in design lead to changes in system mass. To determine the impact of an increase or decrease in system mass in terms of power and thrust, a sensitivity analysis was performed. Finally, a description of the integrated system as a whole is given to clarify the theories and technology used and how this will have a positive influence on the design as a whole. This included the user-system interaction at the Ground Control Station as well.

At the start of the UAV design, requirements were identified and analyzed to determine which were driving or key requirements, and subsequently subdivided into primary, secondary and tertiary requirements. These are split into the requirements that are fulfilled and those that could not be fulfilled by the final design, and a feasibility analysis is performed to determine the cause and impact of failing certain requirements.

After the design phase, the product is not yet ready to be deployed. To clarify what needs to be done next, a chapter on further development was written explaining further project design and development such as prototyping and testing, but also sales and after-sales. A Gantt chart indicating expected time needed to fulfill certain aspects is shown to clarify the extent of work still to be performed, and a cost breakdown is shown containing estimates of further costs per segment shown in the Gantt chart. Finally, a concept of the operations and logistics is included to describe how the UAV would be employed before, during and after a mission, to clarify the suggested approach taken by any end user of the device.

16 | Recommendations

In this chapter recommendations per subsystem are specified. These recommendations follow from challenges encountered in the design of the UAV.

Propulsion

In Section 5.1 the drag coefficient was approximated using Figure 5.1. This approximation is very rough and should be analyzed after testing for the drag. Furthermore it is recommended to perform analysis on the effect of the duct and blade tip clearance on the blade tip losses.

In the current design the UAV is controlled by three servos actuating both swashplates. However it has to be investigated whether this is actually possible due to the phase lag of the control input. Phase lag refers to the angular difference between the point at which a control input to a rotor blade occurs and the point of maximum displacement of the blade in response to that control input, said displacement occurring in the direction of rotor rotation. In ordinary helicopter this phase lag is 90 degrees, so it has to be investigated what the phase lag is on a small RC coaxial helicopter with high stiffness blades. If the the conclusion is that the phase lag is not cancelled out by using a coaxial system, then three extra servos have to be added or only control the top or lower rotor.

Payload and On-Board Computer

The current configuration of on-board computer and payload hardware is designed with the outlook in mind to add additional payload and OBC functionality in the future. Recommended is to pay special attention in future development phases to the following items. Testing needs to be done on including a microphone and speaker on the UAV. The current expectation is that due to the noise and vibrations from the propulsion system including a speaker and microphone is not feasible as there are no ways to filter out the noise and get a usable audio stream. However, if there is a way to include this functionality, it will greatly enhance the usability and applicability of the UAV in emergency situations. For the camera, it is recommended to include a tilting mechanism with servo in order to increase the vertical view angle and make control easier in case the UAV has a pitch angle. Furthermore, it is recommended to develop a custom breakout board for the Gumstix Overo module. The currently used Gumstix Summit breakout board includes connectivity options which are not needed in the current design, resulting in redundant mass.

Communication

There is usually a significant discrepancy between theory and practice regarding communication as empirical models are used to model electromagnetic propagation. The empirical model utilised for path loss also had a large uncertainty in the conclusions drawn as explained in Section 6.4.6. Also, the antennae placement should be investigated for coverage and especially blind spots to optimise their placement. Therefore, it is advisable to conduct field tests of the communication subsystem using the selected components. This test will help identify possible interference sources, and unforeseen factors that were not accounted for in the model resulting in a more accurate estimate of the performance characteristics, and limits of the subsystem.

Power

Regarding the battery system, the most important recommendation is to go for a fully customized tailor made batteries. These will be fully optimized only for this UAV and therefore be lighter than any of the shelf component can be. It can also increase the integration of the batteries, because of the large flexibility in cell shape. Similar custom designs can be made for the motors. The current motor choice has about seventy percent excess power and eighty percent excess RPM, so that can be a lot closer to the requirement values. The ESCs can be custom design as well, to achieve better part integration.

Structures

Although Chapter 7 elaborated on the internal and external loads acting on the vehicle, there are still some necessary fundamental analyses to guarantee the delivery of a complete system. The first recommendation would be to implement the analysis of cut-outs on the structure at the locations where the cameras and the sonar sensors are located. Stress concentrations will be present at these locations, but due to time constraints, these were not accounted for. Additionally, cut-outs for the ease of battery replacement have to be treated alike. Furthermore, the mounting of payload to the hull was not designed for. Mounting the payloads and measurement systems while accounting for the damping the vibrations on them is indispensable for correct manoeuvrability and proper functioning of subsystems. Therefore, further research is highly advised in the future. Unfortunately, there were no time and material resources available for testing the system during the DSE period. It is advised to utilise stress tests, impact tests and crash tests on the vehicle for a proper validation. Lastly, the hull structure and the stiffening struts are produced from different materials. During the assembly of the system, it was assumed that these two components can easily be mounted together. However, this assumption is yet to be validated. Accordingly, it is recommended to investigate how these two materials behave, how can they be attached and whether the load carrying properties diminish due to the manner attachment.

Bibliography

- [1] United Nations OCHA, *Unmanned Aerial Vehicles in Humanitarian Response*, OCHA, 2014.
- [2] Ben Franzluebbers, "Drag Coefficients of Inclined Hollow Cylinders: RANS versus LES," Tech. rep., Worcester Polytechnic Institute, April-2013.
- [3] Heinrich Jacques Geldenhuys, "Aerodynamic Development of a Contra-Rotating Shrouded Rotor System for a UAV," Tech. rep., Stellenbosch University, Maart-2015.
- [4] Jason L. Pereira, "Hover and Wind-Tunnel Testing of Shrouded Rotors for Improved Micro Air Vehicle Design," Tech. rep., University of Maryland, 2008.
- [5] D. L. Valera*, A. J. A. and Molina, F. D., "Aerodynamic analysis of several insect-proof screens used in greenhouses," *Spanish Journal of Agricultural Research*, Vol. 4, No. 4, 2006, pp. 273–279.
- [6] E. Brundrett, "Prediction of Pressure Drop for Incompressible Flow Through Screens," Tech. rep., University of Waterloo, 1993.
- [7] Seddon, J., *Basic Helicopter Dynamics*, BSP Professional Books, 1st ed., 1990.
- [8] W.J. McCroskey, K.W. McAlister, L.W. Carr, S.L. Pucci, "An Experimental Study of Dynamic Stall on Advanced Airfoil Sections Volume 1. Summary of the Experiment," Tech. rep., NASA, 1982.
- [9] W. Kania, W. Stalewski, B. Z., "Design of the Modern Family of Helicopter Airfoils," Tech. rep., Prace Instytutu Lotnictwa, 2007.
- [10] William D. Callister, D. G. R., *Materials Science and Engineering*, John Wiley & Sons, 8th ed., 2011.
- [11] Peter Henry, Michael Krainin, E. H. X. R. D. F., "RGB-D Mapping: Using Depth Cameras for Dense 3D Modeling of Indoor Environments," *12th International Symposium on Experimental Robotics (ISER)*.
- [12] Zheng Fang, S. S., "Real-time Onboard 6DoF Localization of an Indoor MAV in Degraded Visual Environments Using a RGB-D Camera," *2015 IEEE International Conference on Robotics and Automation*.
- [13] "OV5640 5-megapixel Product Brief," http://www.ovt.com/download_document.php?type=sensor&sensorid=177, Product data sheet.
- [14] Jorge Sales, Raul Marin, E. C. S. R. and Perez, J., "Multi-Sensor Person Following in Low-Visibility Scenarios," *Sensors 2010*.
- [15] "I2CXL-MaxSonar-EZ Series," http://www.maxbotix.com/documents/I2CXL-MaxSonar-EZ_Datasheet.pdf, 2012, Product data sheet.
- [16] "u-Blox 6 GPS Modules Data Sheet," [https://www.u-blox.com/images/downloads/Product_Docs/MAX-6_DataSheet_\(GPS.G6-HW-10106\).pdf](https://www.u-blox.com/images/downloads/Product_Docs/MAX-6_DataSheet_(GPS.G6-HW-10106).pdf), 2012, Product data sheet.
- [17] C. De Wagter, S. Tijmons, B. R. and de Croon, G., "Autonomous Flight of a 20-gram Flapping Wing MAV with a 4-gram Onboard Stereo Vision System," 2014.
- [18] Pierre Collet, P. G., "Intel Edison for Smart Drones," Tech. rep., Intel, 2014.
- [19] Guermonprez, P., "Internet of Things with Intel Edison," 2014, Powerpoint Presentation.
- [20] "MPU-6000 and MPU-6050 Product Specification," http://store.invensense.com/datasheets/invensense/MPU-6050_DataSheet_V3%204.pdf, 2013, Product data sheet.
- [21] "I2CXL-MaxSonar-EZ Series," <http://media.gumstix.com/docs/gs3703e.pdf>, 2012, Product data sheet.
- [22] Amerasinghe, K., "H.264 For the rest of us," Adobe, 2009.
- [23] Zyren, J. and Petrick, A., "Tutorial on Basic Link Budget Analysis," Tech. rep., Intersil, June 1998.
- [24] Triantaphyllou, E. and S˜anchez, A., "A Sensitivity Analysis Approach For Some Deterministic Multi-Criteria Decision Making Methods," 2010.
- [25] Faria, D. B., "Model Signal Attenuation in IEEE 802.11 Wireless LANs," Tech. rep., Stanford University.
- [26] Faison, K., "Understanding noise figures in radio receivers," http://www.eetimes.com/document.asp?doc_id=1272302, 2006, [Online; accessed 02-Jun-2015].
- [27] Assembly, I. R., "Attenuation by atmospheric gasses," Tech. rep., ITU Radiocommunication Assembly, 1997.

BIBLIOGRAPHY

- [28] Stone, W. C., "Electromagnetic Signal Attenuation in Construction Materials," Tech. rep., National Institute of Standards and Technology, October-1997.
- [29] Feick, R., Hristov, H. D., and Grote, W., "Attenuation Measurements for Double-Mesh Reinforced Concrete Walls at the 900-MHz Cellular Band," Tech. rep., Universidad Técnica Federico Santa Maria.
- [30] European committee for standardization, "Eurocode 2: Design of concrete structures," Dec-2004.
- [31] VDAB, "Ijzervlechten," Jun-2003.
- [32] Ministerie van Economische Zaken, "Nationaal Frequentieplan 2014," Nov-2014, Dutch government.
- [33] Frenzel, L., "The Difference Between Bit Rate And Baud Rate," <http://electronicdesign.com/communications/what-s-difference-between-bit-rate-and-baud-rate>, 2012, [Online; accessed 03-Jun-2015].
- [34] Atayero, A. A., Sheluhin, O. I., and Ivanov, Y. A., "Modeling, Simulation and Analysis of Video Streaming Errors in Wireless Wideband Access Networks," IAENG Transactions on Engineering Technologies World Congress on Engineering and Computer Science 2011, Springer.
- [35] Sharma, D. K., Mishra, A., and Saxena, R., "Analog and digital modulation techniques: an overview," *International Journal of Computing Science and Communication Technologies*, Vol. 3, No. 1, Jul-2010, pp. 551–561.
- [36] Joung, J., Ho, C. K., and Sun, S., "Spectral Efficiency and Energy Efficiency of OFDM Systems: Impact of Power Amplifiers and Countermeasures," *IEEE Journal on selected areas in communication*, Vol. 32, No. 2, Feb-2014, pp. 208–220.
- [37] Stanciu, A. E., mihaela Nemptoi, L., and MOISE, I. M., "Considerations regarding the spectral efficiency of orthogonal frequency division multiplexing," *11th International Conference on development and application systems*, May-2012, pp. 128–134.
- [38] Zhang, H., Ruyet, D. L., and Terre, M., "Spectral Efficiency Analysis in OFDM and OFDM/OQAM based Cognitive Radio Networks," Tech. rep., Electronics and Communications Laboratory, CNAM, 2009.
- [39] Kocher, P. C., "Timing Attacks on Implementations of Diffie-Hellman, RSA, DSS, and Other Systems," Tech. rep., Cryptography Research, Inc.
- [40] Josang, A., Maseng, T., and Knapskog, S. J., "Identity and Privacy in the Internet Age," 14th Nordic Conference on Secure IT Systems, NordSec 2009, Springer, 2009.
- [41] Paul, R., Saha, S., Sau, S., and Chakrabarti, A., "Design and implementation of real time AES-128 on real time operating system for multiple FPGA communication," Tech. rep., University of Calcutta, Date unknown.
- [42] Elkilani, W. S. and Abdul-Kader, H. M., "Performance of Encryption Techniques for Real Time Video Streaming," Tech. rep., Minufya University, 2009.
- [43] Haykin, S. and Moher, M., *Modern Wireless Communications*, Pearson Education, international ed., 2005.
- [44] Goldsmith, A., "EE 359 Signal Propagation and Path Loss Models," Lecture notes, Stanford University.
- [45] Seidel, S. Y., "914 MHz Path Loss Prediction Models for Indoor Wireless Communications in Multifloored Buildings," *IEEE Transactions on Antennas and Propagation*, Vol. 40, No. 2, 1992, pp. 207–217.
- [46] Rappaport, T., *Wireless Communications Principles and Practice*, Prentice Hall, 1996.
- [47] Mulder, M. and Tiberius, C., "AE2235-II Instrumentation and Signals Noise," Lecture notes, Delft University of Technology.
- [48] Tranzeo, "Wireless Link Budget Analysis," *Decision Sciences*, Vol. 28, No. 1, Winter 1997, pp. 151–194.
- [49] Freaklabs, "Freakduino-900 v2.1a," http://www.freaklabsstore.com/index.php?main_page=product_info&products_id=205, 2013, Device datasheet.
- [50] Instruments, T., "CC1101: Low-Power sub-1 GHz RF Transceiver," <http://www.ti.com/product/cc1101>, 2015, Device datasheet.
- [51] Solutions, A. N., "@ANY900-2 RF MODULE: 868/915 MHz Modules for IEEE 802.15.4/ZigBee Wireless Mesh Networking Applications," <http://www.an-solutions.de/>, 2010, Device datasheet.
- [52] LSR, "SIFLEX02-R2-HP transceiver module: Integrated Transceiver Modules for ZigBee / 802.15.4 (900 MHz)," <http://www.lsr.com/embedded-wireless-modules/zigbee-module/siflex02-hp#docs>, 2014, Device datasheet.
- [53] Weiner, M. M., *Monopole Antennas*, Taylor & Francis, 2003.
- [54] Macnamara, T., *Introduction to Antenna Placement and Installation*, Wiley, 2010.
- [55] Crane, R. K., *Propagation Handbook for Wireless Communication System Design*, CRC Press, Jul-2003.

BIBLIOGRAPHY

- [56] Atmel, "AT86RF212B Low Power, 700/800/900MHz, Transceiver for ZigBee, IEEE 802.15.4, 6LoWPAN, and ISM Applications," http://www.atmel.com/images/atmel-42002-mcu_wireless-at86rf212b_datasheet.pdf, 2015, Device datasheet.
- [57] Basta, P. O., "Quad Copter Flight," Tech. rep., California State University, May-2012.
- [58] Buchmann, I., "Basics about Batteries," Training Series, Cadex Electronics Inc., 2014.
- [59] Megson, T., *Aircraft Structures for Engineering Students*, Butterworth-Heinemann, 4th ed., 2007.
- [60] R. v. Mises, "Mechanik der festen K rper in plastisch-deformablen Zustand," Tech. rep., K nigliche Gesellschaft der Wissenschaften zu G ttingen, 1913.
- [61] Nise, N. S., *Control Systems Engineering*, John Wiley & Sons, Inc., 6th ed., 2011.
- [62] Inman, D. J., *Engineering Vibrations*, Pearson Prentice Hall, 2009.
- [63] Hibbeler, R., *Mechanics of Materials*, Pearson Education, 8th ed., 2011.
- [64] Lakes, R., *Viscoelastic Materials*, Cambridge University Press, 2009.
- [65] de Silva, C. W., *Vibration Fundamentals and Principles*, CRC Press Taylor and Francis Group, 2007.
- [66] Chen, C. and Lakes, R., "Design of Viscoelastic Impact Absorbers: Optimal Material Properties," *International Journal on Solid Structures*, Vol. 26, No. 12, pp. 1313.
- [67] Ashby, M., "On The Engineering Properties of Materials," *Acta Metallurgica*, Vol. 37, No. 5, pp. 1273.
- [68] The DOW Chemical Company, "IMPAXX 300 Energy Absorbing Foam," Datasheet.
- [69] Zotefoams, "Plastazote MP15 FR: Flame Retardant, Metallocene Polyethylene Foam Data Sheet," Aug-2005, Datasheet.
- [70] Hibbeler, R., *Mechanics of Materials*, Pearson Prentice Hall, 8th ed., 2010.
- [71] Clothier, R. A., "Risk Perception and the Public Acceptance of Drones," Tech. rep., Delft University of Technology, 02-2015.
- [72] Brian G. McHenry, "Head Injury Criterion and the ATB," 2004, McHenry Software, Inc.
- [73] Douglas S. Thomas, "Costs and Cost Effectiveness of Additive Manufacturing," Tech. rep., Applied Economics Office Engineering Laboratory, December-2014.
- [74] Plastics International, "HDPE (High Density Polyethylene)," Datasheet.
- [75] Advanced Laser Materials, LCC, "PA 640-GSL: Extremely Light Weight Nylon 12 Laser Sintering Material," Datasheet.
- [76] Telenko, C. and Seepersad, C. C., "A Comparative Evaluation of Energy Consumption of Selective Laser Sintering and Injection Molding of Nylon Parts," Tech. rep., University of Texas, Date unknown.
- [77] European Environment Agency, "Specific air pollutant emissions (TERM 028)," .
- [78] S, S. and M.H., W., "Handling e-waste in developed and developing countries: Initiatives, practices, and consequences," *Elsevier*, Vol. Science of the Total Environment, 2012.
- [79] Baechler, C., Devuono, M., and Pearce, J. M., "Distributed recycling of waste polymer into Rep Rap feedstock," *Rapid Prototyping Journal*, Vol. 19, 2013.
- [80] Curran, D. R., "Risk Management & Reliability," Lecture notes, Delft University of Technology, 2015.

A | Work distribution

The work distribution of the final report can be found in Table A.1. The table gives both an overview on who wrote which section in the report it self but also who actually worked on what. An I in the table means the person worked on it, but did not do the reporting in this report. And X means the person both worked on it and did the reporting.

Table A.1: *Work distribution for the Final Report*

Group members	Henricus	Douwe	Ricard	Gergely	Stephen	Erik	Victor	Nikhil	Christian	Salomon
Project Management		I								
Systems Engineering					I					
Logbook						I				
Catia Sketches	I									
Preface		x		x						
Summary				x						
1. Introduction		x								
2. Mission Description										
2.1 Functional Flow Diagram		x								
2.2 Functional Breakdown Structure		x			x					
2.3 Mission Requirements			x	x						
3. Market Analysis										
3.1 General Market Description		x					x	x		
3.2 Applications and End Users of UAV Systems		x					x	x		
3.3 Market Structure		x					x	x		
3.4 Product Differentiation and Market Gap		x					x	x		
3.5 Legislation										x
4. Design and Iteration Strategy		x	I							
5. Subsystem Design: Propulsion										
5.1 Thrust Calculations		I			I	x				
5.2 Coaxial Rotor Design		I			I	x				
5.3 Rotor Head Design	I	x								
5.4 Propeller Design		x			I	x				
5.5 Power Calculations		I			I	x				
6. Subsystem Design: Electronics										
6.1 Payload							x			x
6.2 On Board Computer							x			
6.3 Payload and OBC hardware configuration							x			
6.4 Communications								x	x	
6.5 Power			I		x					
6.6 Hardware Interface							x	x		
6.7 Ground Control Station					I				x	x
7. Subsystem Design: Structures										
7.1 Sizing for Loads			x	I						
7.2 Impact Resistance				x				x		
7.3 Occupational Health & Safety considerations				x						
7.4 Vibrational Analysis			x							
8. Data Handling & Hardware-Software Interaction										
8.1 Data Handling	x						I			
8.2 Software Design	x									
9. Software/Control and Stability										
9.1 Actuation flow	x									
9.2 Flight Controller	x									
9.3 Paparazzi Alterations	x									
10. Verification and Validation										
10.1 Verification and Validation of Propulsion Calculations		x			x	x				
10.2 Verification and Validation of Structural Design			x	x				x		
10.3 Verification and Validation of Communication Calculations								x		
11. Sustainable Solutions										
11.1 Social Sustainability				x					I	
11.2 Economical Sustainability									x	
11.3 Environmental Sustainability				x					x	
12. Systems Engineering										
12.1 Resource Allocation and Budget Balance				I	x			x		
12.2 Risk Assessment							x			
12.3 Subsystem Allocation				x			I	I	I	
12.4 Design Iteration Summary				x		x				
12.5 Sensitivity Analysis					x	x				
12.6 Inspection Pocket Drone: description of the integrated system				x	x	x	x	x		
13. Require Compliance Matrix & Feasibility Analysis										
13.1 Requirement Compliance Matrix						x				
13.2 Feasibility Analysis						x				
14. Further Development										
14.1 Project Design and Development Logic		x				I				
14.2 Development Gantt Chart		x								I
14.3 Cost Breakdown Structure		I								x
14.4 Operations and Logistics Concept					x					
15. Conclusion									x	
16. Recommendations				x	x	x	x	x		

B | Propulsion Example Calculation

In this appendix sample calculations of the theory in Section 5.2 are shown. For brevity the number of steps is set to 10. For the actual calculation used during the design phase a 1000 steps was used for accuracy. Table B.1 shows the values of the Prandtl tip-loss factor (F), inflow ratios (λ), twist (θ) and blade solidity (σ) for both upper and lower rotors. The values for the inflow ratio of free stream velocity, thrust coefficients, and thrust generated by upper and lower ratio are single values and are given to be 0.197, $3.7 \cdot 10^{-3}$, $3.2 \cdot 10^{-3}$, 1.8, 1.52 respectively.

Table B.1: Calculation values over the radius of a propeller in 10 steps

r [m]	0.0089	0.0178	0.0267	0.0356	0.0444	0.0533	0.0622	0.0711	0.0800
F_{upper} [N]	0.9993	0.9975	0.9954	0.9912	0.9824	0.9643	0.9268	0.8480	0.6741
λ_{upper} [-]	0.1971	0.2168	0.2129	0.2105	0.2091	0.2083	0.2079	0.2081	0.2102
θ_{upper} [°]	0	41.7703	32.5761	27.1257	23.8818	21.7545	20.1005	18.7236	17.8745
σ_{upper} [-]	0	0.0358	0.0239	0.0179	0.0143	0.0119	0.0102	0.0090	0.0080
F_{lower} [N]	0.9793	0.9573	0.9432	0.9221	0.8909	0.8451	0.7774	0.8461	0.6744
λ_{lower} [-]	0.3942	0.4440	0.4343	0.4279	0.4239	0.4215	0.4201	0.2099	0.2099
θ_{lower} [°]	0	44.8534	34.6769	27.4679	22.4572	18.8757	15.9542	12.9236	9.0147
σ_{lower} [-]	0	0.0358	0.0239	0.0179	0.0143	0.0119	0.0102	0.0090	0.0080